THE UNIVERSITY OF CHICAGO

SEARCHING FOR LIGHT DARK MATTER WITH DAMIC AT SNOLAB AND DAMIC-M: INVESTIGATIONS INTO RADIOACTIVE BACKGROUNDS AND SILICON SKIPPER CHARGE-COUPLED DEVICES

A DISSERTATION SUBMITTED TO
THE FACULTY OF THE DIVISION OF THE PHYSICAL SCIENCES
IN CANDIDACY FOR THE DEGREE OF
DOCTOR OF PHILOSOPHY

DEPARTMENT OF PHYSICS

BY
ARIEL YECHEZKEL MATALON

CHICAGO, ILLINOIS
DECEMBER 2021

I dedicate this work to my family, with love:

Joseph Matalon

Gila Matalon

Netalie Matalon

Danielle Matalon

אני מקדיש את העבודה הזאת למשפחתי באהבה:

יוסף מטלון (זכרונו לברכה)

גילה מטלון

נטעלי מטלון

דניאל מטלון

TABLE OF CONTENTS

LIST OF FIGURES

LIST OF TABLES

ACKNOWLEDGMENTS

About a decade ago, I began my journey working in experimental physics research. It would have been impossible to reach the point where I am today without the support of so many people dear to my heart.

First and foremost, I would like to thank my supervisor Paolo Privitera for his unwavering support. I have had the great fortune to be a part of Paolo's group for nine years, during my time as an undergraduate and graduate student at the University of Chicago. Paolo is the best researcher, teacher, and mentor that I have ever encountered. In the spring of 2013 I attended an event highlighting research at the university, and entered my name in a lottery to have lunch with a faculty member. I won the draw that day: I did not know it at the time, but that first meeting with Paolo would be the single most important moment in shaping my academic career. He has always been there to guide my work and to listen to my interests, preferences, and struggles. He is one of only a few principal investigators who enable their students to participate in the numerous activities required to develop experiments from start to finish, keeping them constantly excited and engaged with new work opportunities.

Paolo has helped me become a well-rounded scientist, but perhaps more importantly he has influenced my leadership, empathy, and collaborative spirit. It is this set of traits, among others, that enabled me to pursue the first-ever international dual-PhD in physics from the University of Chicago, working jointly with Sorbonne Université. There's an Italian saying I learned from Paolo: "il buon giorno si vede dal mattino," which describes a feeling that lets you tell from the very beginning whether something is destined to have a positive outcome. When you meet Paolo, when you work with him, you'll only have one feeling ... that you've just won the lottery. Grazie mille.

I have been lucky enough to have two supervisors during my PhD. I have spent the last three years working with and learning from Antoine Letessier Selvon. Antoine is a remarkable scientist: his analytical prowess, attention to detail, and direct communication

style help to drive any project forward. Antoine welcomed me into his group with open arms, and provided me the support I needed to successfully deliver key results for DAMIC on short timelines. Matching Antoine's energy means voicing your opinion during problem-solving sessions; it means a no-nonsense approach to prioritizing tasks, finding the most efficient way to getting them done, and then tackling them head-on; importantly, it means simultaneously having a thick skin and good sense of humor in the face of adversity. I am happy to have integrated these elements into my work style. Merci beaucoup.

I am very grateful to my UChicago and Sorbonne Université committee members for their time, presence, and feedback: Robert Rosner, Abigail Vieregg, David Awschalom, Ranny Budnik, Christophe Balland, and Lucia Di Ciaccio. It has been an honor to have had these extraordinary people involved throughout this process. A special thanks to Ranny for all he did to energize my interest in physics even from high school, everything from weekend discussions to visits to Columbia University's Nevis Labs. And a big thanks to Robert, Abby, and David, all three of whom taught some of my favorite courses at UChicago.

I would like to thank several current and former members of Paolo's UChicago KICP group and Antoine's LPNHE group, as well as some DAMIC and DAMIC-M collaborators from other institutions, for being such terrific and helpful colleagues over the years: Karthik Ramanathan, Ryan Thomas, Alvaro Chavarria, Dan Baxter, Toshihiro Fujii, Max Malacari, Pavel Motloch, Pitam Mitra, Elise Darragh-Ford, Danielle Norcini, Romain Gaiör, Joao Da Rocha, Michelangelo Traina, and others.

I am very appreciative of Alessandra Tonazzo and Sophie Trincaz-Duvoid, Anna Mukhurtova and the PNF staff, UChicago Department of Physics members Tiffany Kurns, Van Bistrow, Shadla Cycholl, Amy Schulz, and Putri Kusumo, LPNHE teams (electronics, mechanical, IT, etc.), as well as Briana Konnick, Meredith Daw, and Michael Tessel for providing invaluable technical, administrative, and career support. Thanks to Michael S. Turner, Philip Kim, and Jamal Ali for their mentorship at early stages in my research career.

To my friends from my time in Paris and Chicago: Michele Ronco, Serena Sabatucci, Letizia Robbiani, Tara Shreve, Elodie Périé, Malte Lange, Feven Jembere, Jai Brunner, Vladimir David, Johnny Antos, Skomantas Pocius, Tiana Pyer-Perreira, Katrina Miller, Matt Luchins, and more, thank you for some wonderful memories, and for entertaining my love of football (soccer), biking, cards, crossword puzzles, and good food. Thanks to Julianna Vittoria Stermer for 5th floor tea breaks and exploring some of the best parts of Paris.

To some of my closest friends: Horia (Lee) Popa, Graham Carling, Jamie Oliver, Will Haack, Chris Haack, and Rolando Schneiderman, thank you for always having my back, and for being like a second family to me. Thanks to Hillary Child for making my first years in Chicago so special, and for helping in navigating so many of life's complexities.

Most of all, thank you to my family for their love and support. Thank you to my sisters Dani and Netalie for being there to celebrate the good moments, for lifting me up when times are tough, and for giving me new perspectives. I am especially grateful to my parents, Joseph and Gila, for their hard work, sacrifice, and support throughout. I am grateful to them for passing on to me their strong work ethic, resiliency, creativity, and caring. My family inspires me – my achievements are theirs, and I dedicate this thesis to them.

This material is based upon work supported by the National Science Foundation Graduate Research Fellowship Program under Grant DGE-1144082, and by the National Science Foundation Graduate Research Opportunities Worldwide Program (2018, 2019). This material is based upon research supported by the Chateaubriand Fellowship of the Office for Science & Technology of the Embassy of France in the United States.

ABSTRACT

The dark matter community has reached an inflection point. Strong limits have been placed on $O(100\,\mathrm{GeV})$ WIMPs, and attempts to produce dark matter at accelerators have not yet been successful. As such, there has been a shift towards exploring new parameter space, specifically that of light dark matter, and looking for hidden photons or dark matter-electron interactions.

The DAMIC (Dark Matter in CCDs) program employs the bulk silicon of scientific CCDs to search for ionization signals produced by interactions of particle dark matter from the galactic halo of the Milky Way. By virtue of the low noise (~ 2 e$^-$) and small pixel size ($15\,\mu$m) of conventional DAMIC CCDs, as well as the relatively low mass of the silicon nucleus, DAMIC is sensitive to small ionization signals from recoiling nuclei or electrons following the scattering of dark matter particles, and especially to low-mass WIMPs with m_χ in the $1-10$ Gev/c^2 range. A decade-long deployment of such detectors at the SNOLAB underground laboratory has demonstrated CCDs as successful dark matter detectors.

There are two major themes of this thesis: first, understanding backgrounds that limit the sensitivity of silicon CCD direct-detection searches, and second, improving the resolution of CCDs using Skipper technology in order to drive next-generation searches for dark matter.

A major contribution of this thesis is the development of a powerful technique to distinguish and reject background events in the DAMIC at SNOLAB detector. Utilizing the exquisite spatial resolution of CCDs, discriminating between α and β particles, we identify spatially-correlated decay sequences over long periods. We report measurements of radiocontaminants in the high resistivity CCDs from the DAMIC at SNOLAB experiment, including bulk ^{32}Si and surface ^{210}Pb; we also set limits for radiocontaminants along the ^{238}U and ^{232}Th chains. This technique will enable future silicon-based dark matter programs to optimize silicon ingot selection in order to minimize what may otherwise become a dominant and irreducible background.

We also present a direct experimental measurement of the cosmogenic activation of silicon, following the irradiation of DAMIC CCDs at the LANSCE beam of the Los Alamos National Laboratory. Beyond measurements of key problematic backgrounds, we present the first-ever radioactive background model constructed for a dark matter CCD detector, which revealed the existence of a partial charge collection region in DAMIC CCDs. We outline fabrication efforts of the core element of CCD devices, with steps that can address this problematic partial charge collection layer.

Finally, this work presents results from the successful deployment of novel Skipper CCDs. These CCDs are able to reach sub-electron resolution by performing non-destructive, multiple measurements of pixel charge. DAMIC-M, a record mass, kg-size CCD experiment under development, will feature such devices. A resolution of $0.07\,\mathrm{e}^-$ has been demonstrated in a DAMIC-M prototype CCD. We present the work to fully characterize and integrate these detectors via the construction of automated test chambers, and outline the projected sensitivity both of DAMIC-M and its prototype, the Low Background Chamber.

CHAPTER 1

INTRODUCTION TO DARK MATTER

1.1 Evidence for Dark Matter

Dark Matter (DM), an essential component of the standard cosmological model and a driver of cosmic structure, remains a scientific mystery; determining its nature has driven decades of theoretical and experimental work. Current analyses constrain the energy densities of the Universe, with a component of nonbaryonic dark matter contributing roughly five times that of baryons [1], implying a staggering amount of knowledge left to be revealed.

The term "precision cosmology" may have been considered an oxymoron for many years, but a vast array of technological development in the field has dispelled such a notion. And today there is overwhelming astrophysical and cosmological evidence for the existence of dark matter. The historical starting point for such evidence is typically aligned with the work of Fritz Zwicky, who, in 1933, when applying the virial theorem in examining the dynamics of the Coma galaxy cluster, reported a significant missing matter component after relating the cluster's kinetic and potential energies [2]. This result did not come without significant skepticism within the astronomy community. Although further studies over the next two decades that exploited mass-to-light ratios of galaxy clusters showed continued evidence for a missing, "dark" matter, there were consistent concerns raised regarding systematics and assumptions of those studies [7]. The community could all but agree that they needed better precision and more information, a theme relevant even today.

One of the most significant advancements in the field of dark matter came from the 1970's work of Vera Rubin and collaborators, in which they studied rotation curves [3] – velocity profiles of luminous matter in galaxies as a function of their distance from galactic centers – of high-luminosity spiral galaxies. They demonstrated a significant deviation between the expected and observed profiles: in particular, expected calculations should have provided

profiles featuring a drop in velocity with increasing radius. This comes from application of Gauss' theorem to obtain stellar velocity v at distance R from the center:

$$v(R) = \sqrt{\frac{GM(R)}{R}} \tag{1.1}$$

where $M(R)$ is the total mass contained in a radius R. Far from the galactic disk, the star density decreases so the total mass within R becomes roughly constant, giving $v(R) \propto R^{-1/2}$.

Instead, Rubin et al. found that they were flat out to the outermost radius measured. An example of one such rotation curve from NGC 6503 can be seen in Fig. 1.1. A larger catalog of more precise measurements, all showing such an observed plateau, strengthened the consensus for the existence of a matter component beyond the visible one in galaxies.

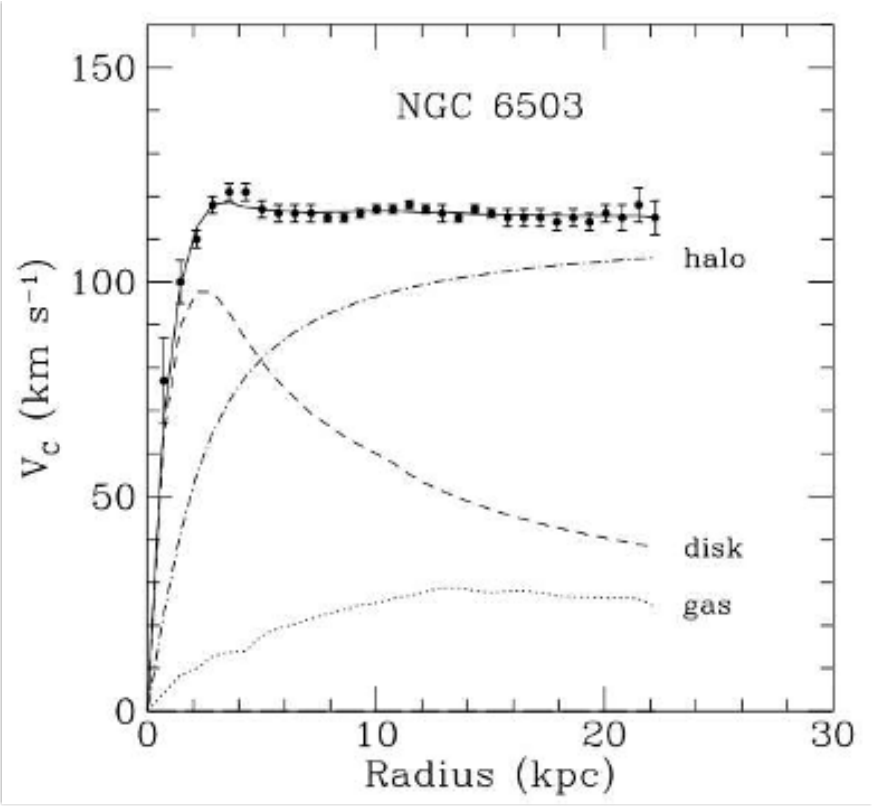

Figure 1.1: Galactic rotation curve of NGC 6503 taken from Ref. [4], showing that a dark matter halo distributed in the galaxy is necessary along with normal matter in order to reproduce the profile shape.

In 2006, a pair of merging clusters known as the "bullet cluster" was observed. By relying on the distortion of light due to the presence of matter, one can use weak and strong lensing to reconstruct the gravitational profile of galaxy clusters. Application of such gravitational lensing by a group of astronomers provided yet another source of evidence for the presence of dark matter [6]. A notable discrepancy was observed in mapping out the weak lensing and X-ray profiles of the bullet cluster – this can be seen in the contour plot of Fig. 1.2. The baryonic matter of the merged cluster does not dominate the system; rather, it is dark matter that is empirically interpreted to do so.

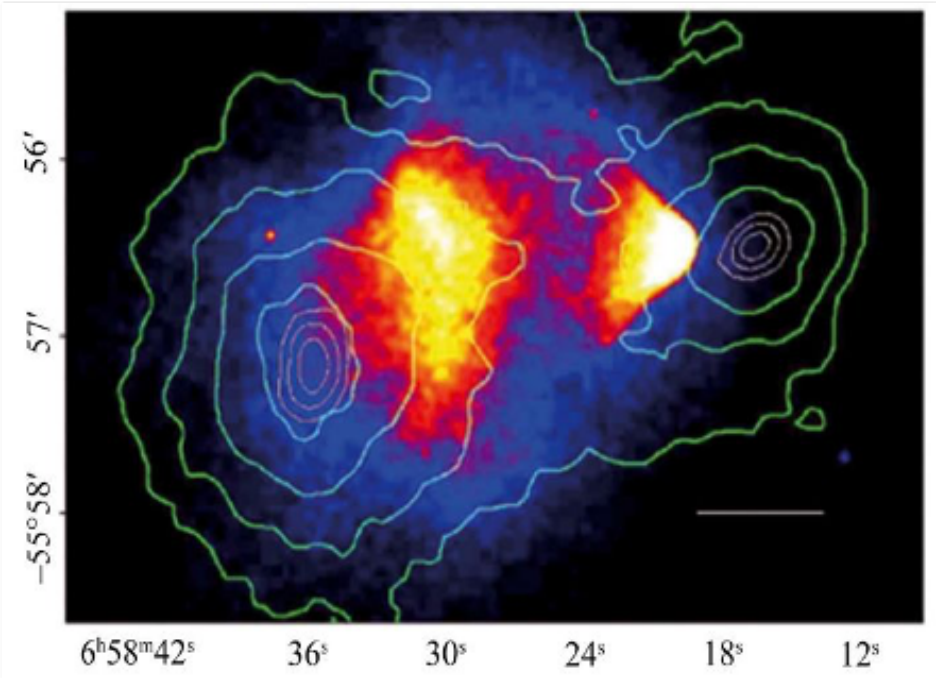

Figure 1.2: Reconstruction of the bullet cluster from weak lensing (green contours), including an X-ray overlay, with a visible discrepancy in lensed mass position; taken from Ref. [6].

The Cosmic Microwave Background (CMB) [5] provides yet another avenue of evidence for dark matter. The CMB is the relic radiation from photon last-scattering occurring roughly 300,000 years after the Big Bang; it refers to the time when an opaque universe had cooled sufficiently to become transparent. The features of the CMB contain information about the gravitational structure of the early universe: its temperature anisotropy maps out

the distribution of matter at that time, and fitting its angular power spectrum to cosmological models (e.g ΛCDM) enables extraction of the aforementioned abundances for the Universe's energy-density components. The CMB closely matches a blackbody spectrum with temperature 2.725 K, and has micro-Kelvin level anisotropies. The most recent Planck results for baryonic and cold dark matter densities, respectively, are: $\Omega_b h^2 = 0.02233 \pm 0.00015$ and $\Omega_c h^2 = 0.1198 \pm 0.0012$ [1].

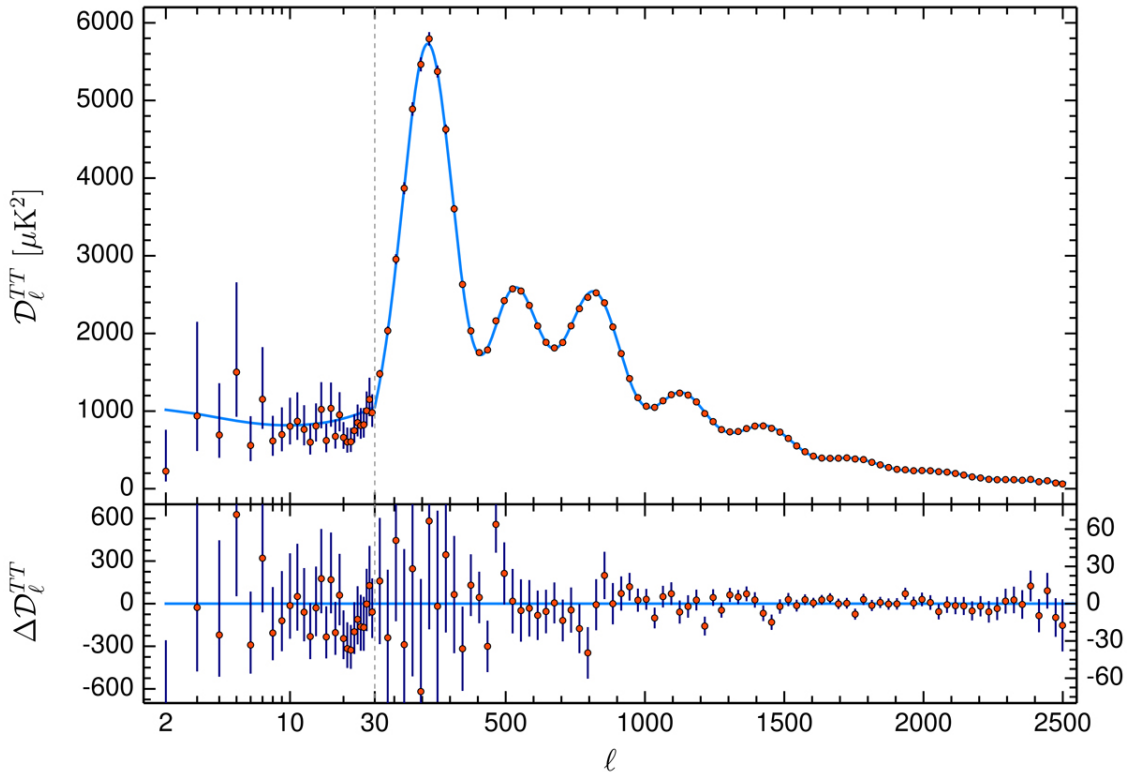

Figure 1.3: The CMB power spectrum fit to a ΛCDM cosmological model, with residuals shown; taken from Ref. [1].

More techniques have been used to infer the presence of dark matter, including studies of hot gas in clusters [8], Big Bang nucleosynthesis [9], and large-scale structure; for additional reading on the history and evidence of dark matter, the reader can turn to Ref. [7].

1.2 Dark Matter Candidates

Despite independent measurements indicating the existence of dark matter, it is still not clear as to what dark matter exactly is; observations indicate that dark matter would be massive, stable over billions of years, and gravitationally-interacting [17]. The Standard Model (SM) of particle physics does not include an obvious dark matter candidate; we know that dark matter does not consist of baryons unless created through phase transitions in the early Universe. We then turn to a composition from new particles or objects, more generically identified by "hot" and "cold" thermal velocities, the latter corresponding to non-relativistic speeds. Hot dark matter would consist of massive and high velocity components: modeling this type of dark matter in totality provides cosmic structures shaped very differently than current observations. The ΛCDM model assumes the whole of dark matter is cold. Additional work has shown what dark matter *is not* [18]: first, given micro-lensing observations, it has been concluded that dark matter is unlikely to consist of massive compact halo objects (MACHOs); moreover, neutrinos are excluded given their small mass and relativistic speeds.

There are a plethora of dark candidates (e.g. sterile neutrinos, gravitinos) – we choose to review some of the leading ones:

- **WIMPs**: WIMPs (Weakly Interacting Massive Particles) are arguably the most compelling dark matter candidate, and are considered as thermal relics from the early Universe (when particles were in a state of thermal equilibrium). As the Universe expanded and subsequently cooled to a temperature T below the equivalent thermal level of the WIMP mass, m_χ, eventually the number of WIMPs within a given volume decreased to prevent annihilation, effectively fixing their number density (this is referred to as "freeze-out"). Such a freeze-out temperature T_f occurs when the annhilation rate approximately equals the Universe's expansion rate Γ. The corresponding mass level for WIMPs in order to reproduce an appropriate abundance of dark matter today is $O(10 - 1000\,\mathrm{GeV})$, a notable result in considering the gauge hierarchy problem

[19]. Moreover, if dark matter is such a relic particle, its annihilation cross-section ($\langle\sigma v\rangle \approx 3 \times 10^{-26}\,\mathrm{cm}^3/\mathrm{s}$) cannot exceed that of the weak interaction. The fact that a minimal supersymmetric extension to the SM with a weak-scale annhiliation cross section and aforementioned mass aligns with the dark matter abundance has been referred to as the WIMP "miracle".

The dark matter differential event rate for a single-target as a function of energy deposited is given by:

$$\frac{dR}{dE} = \frac{\rho_\chi}{m_\chi}\frac{d\sigma}{dE}\int_{v_{min}}^{\infty} d^3v\, v f(v) \tag{1.2}$$

where ρ_χ is the local WIMP density, $\int v f(v)$ is the averaged velocity, and σ is the interaction cross section [cm^2]; $f(v)$ is derived from treating dark matter as a self-gravitating, isothermal spherical distribution of an ideal gas, and expressed as a Maxwellian-Boltzman velocity distribution of the form:

$$f(v) = \frac{1}{v_0^3\pi^{3/2}}\exp(-\frac{|\tilde{v}|^2}{v_0^2}) \tag{1.3}$$

where $v_0 = \sqrt{\frac{2k_BT}{m_\chi}}$ and $\tilde{v} \sim v + v_E$ (v is the velocity of dark matter in the local galactic halo; v_E is the velocity of Earth with respect to the dark matter rest frame). To ensure that the particles would be confined to the galaxy, i.e. that the escape velocity v_{esc} is not exceeded, the condition $v < v_{esc}\,(\approx 544\,\mathrm{km/s})$ is met. The velocity distribution for a Standard Halo Model, outlined in Ref. [12], is given by:

$$f(v) = \begin{cases} \exp(-\frac{(v-v_E)^2}{v_0^2}) - \exp(-\frac{(v+v_E)^2}{v_0^2}) & v \le v_{esc} - v_E \\ \exp(-\frac{(v-v_E)^2}{v_0^2}) - \exp(-\frac{v_{esc}^2}{v_0^2}), & v_{esc} - v_E < v < v_{esc} + v_E \\ 0 & v > v_{esc} + v_E \end{cases} \tag{1.4}$$

where the Earth's velocity leads to an annual modulation signal.

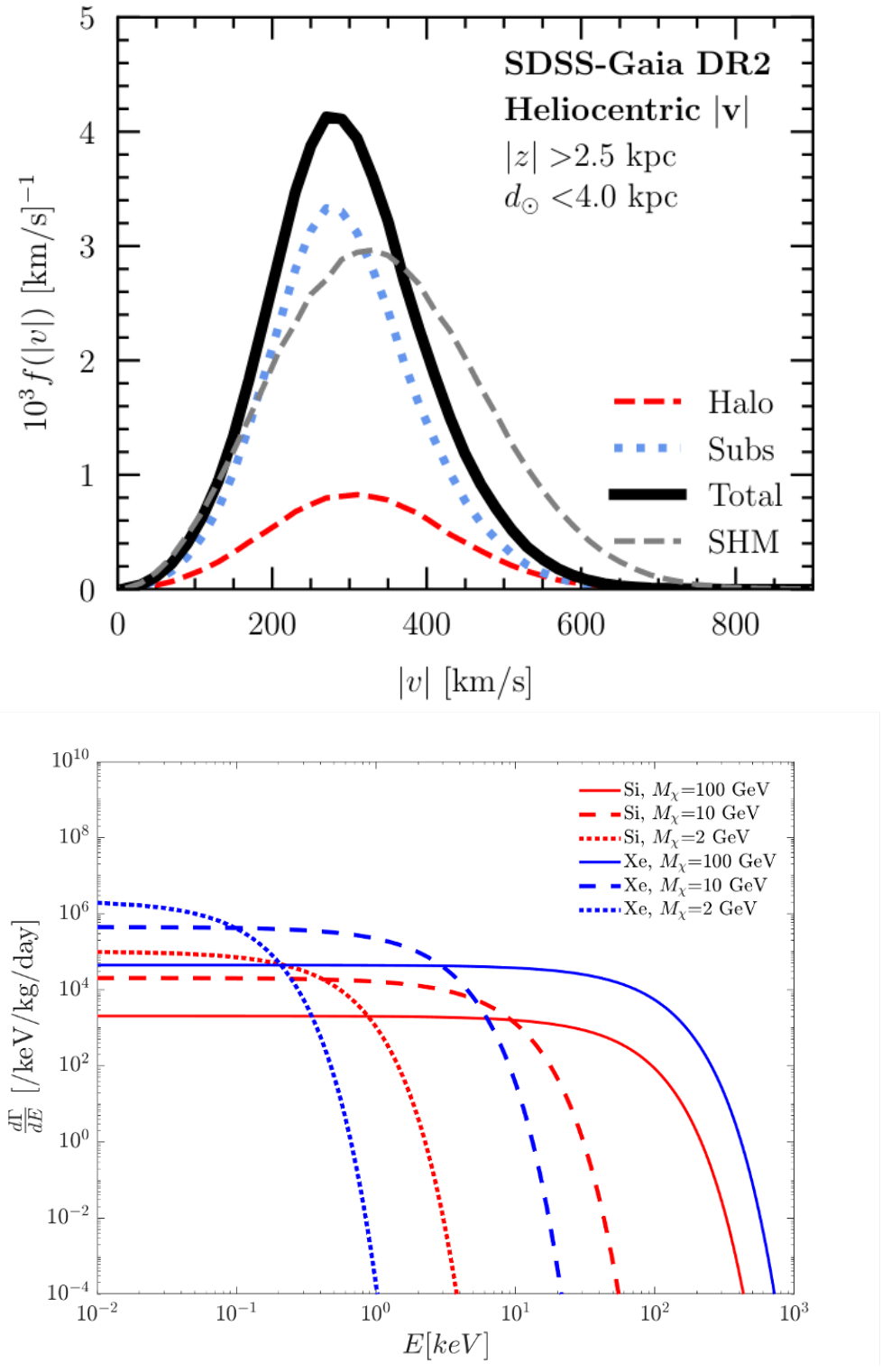

Figure 1.4: Top: WIMP velocity distribution (top) [14]. Bottom: calculated recoil spectrum for Si, Xe [53].

If we specifically consider dark matter scattering off of target nuclei, we can relate the differential rate as:

$$dR = \frac{1}{m_A}\sigma_A v dn \tag{1.5}$$

where m_A is the mass of the nucleus, σ_A is the nucleon cross-section. The recoil energy is therefore:

$$E_R = \frac{v^2 m_r^2 (1 - cos\theta)}{m_A} \tag{1.6}$$

where $m_r = \frac{m_A m_\chi}{m_A + m_\chi}$ is the effective reduced mass of the scattering system. The corresponding maximum recoil energy E_{max} by dark matter particles is:

$$E_{max} = \begin{cases} 400\text{keV}(\frac{m_A}{28\text{GeV}}) & m_\chi \gg m_A \\ 50\text{eV}(\frac{m_\chi}{1\text{GeV}})^2(\frac{28\text{GeV}}{m_A}) & m_\chi \ll m_A \end{cases} \tag{1.7}$$

where the detector mass has been scaled by that of silicon (the preferred detector target material for the purpose of this thesis). Note the relatively low imparted energy (50 eV) for a 1 GeV dark matter particle. We shall see in later chapters how challenging it is to reach such low thresholds. The final cross-sectional rate, assuming a spin-independent coupling, is:

$$\frac{dR}{dE_R} = N_T \frac{2 m_A \rho_\chi}{k\pi m_\chi} A^2 \sigma^2 F^2(q) \int_{v_{min}}^{v_{esc}} d^3 v \frac{f(v, v_E)}{v} \tag{1.8}$$

where A is the nucleus mass number, $N_T m_A$ is the total detector target mass, σ corresponds to the proton/neutron momentum cross section, and $F^2(q)$ is the nuclear form factor.

The local WIMP velocity distribution and the differential WIMP recoil spectrum for silicon and xenon can be seen in Fig. 1.4. For information on dark matter-electron scattering used to search for sub-GeV dark matter, the reader is guided to Ref. [15]. The default astrophysical parameters used to ensure like-for-like comparisons across experiments are: $v_0 = 220$ km/s, $v_E = 232$ km/s, $v_{esc} = 544$ km/s, $\rho_\chi = 0.3$ GeV/cm^3.

A more complete review of dark matter scattering and subsequent event rate calculations can be found in Ref. [10], [11], and [12]. The U.S. Cosmic Visions Community Report [13] states that while WIMP dark matter remains highly motivated, a broad program of small experiments can explore two attractive classes of candidates: hidden-sector dark matter and ultralight (axion) dark matter.

- **Hidden/Dark photons**: The dark photon is a hypothesized stable and massive hidden-sector particle [16]. Hidden-sector particles do not directly couple to normal matter, as there is a separate set of forces dictating their interactions. An interaction with SM particles is possible, however, via a kinetic mixing between a dark/ordinary photon. Given the increased efficiency in energy transfer for dark matter-electron interactions, this is the preferred technique used to search for this class of particles. Limits are also placed by non-observations of solar events, as hidden photons could realistically be generated in the Sun. The primary mass range targeted by searches for hidden-sector dark matter using direct-detection experiments and accelerators is keV-GeV; the former has better detection rates assuming the mediator of the scattering between dark matter and normal matter is much lighter than the dark matter itself.

- **Axions**: One frequent extension of the SM includes axion-like particles (ALPs), originally proposed to address the strong CP problem, but conveniently could be dark matter candidates if they fall within a specific low mass range. The techniques to search for axions are particularly unique; reading on the methodology for ADMX, a major axion experiment, can be found in Ref. [20].

1.3 Direct Detection Experiments

There are numerous techniques to search for the aforementioned candidates: indirect detection experiments look for products of dark matter self-annihilation or decay in outer space [21][22][23], while at colliders attempts are made to produce dark matter in the lab [24].

Our focus, however, rests on direct detection of dark matter, and the experiments that aim to identify the low-energy nuclear/electron recoils induced by interactions between dark matter and normal matter. These faint energy signatures can be measured via ionization, scintillation, and phonons. This thesis presents an extensive review of silicon CCDs as dark matter detectors aiming to measure ionization induced by dark matter. Both the DAMIC [31] and SENSEI [99] programs use this technology. Semiconductor detectors are popular and especially relevant for low-mass WIMP searches; typically silicon or germanium are used as target materials. The SuperCDMS experiment uses silicon and germanium crystals to try to detect both ionization and phonons [101]. The DAMA/LIBRA experiment uses NaI(Tl) with photomultiplier tubes (PMTs) to measure scintillation, and has famously claimed to have detected a dark matter annual modulation signal [25]. The PICO experiment [26] uses bubble chambers with superheated target fluids to search for spin-dependent dark matter interactions. Finally, time projection chambers (TPCs) filled with gaseous and liquid Xenon or Argon have been used by many experiments in order to measure scintillation and ionization signals [27]; the XENON program has been a consistent leader in the use of this technology, and is currently transitioning its ton-scale XENON1T experiment to XENONnT [28].

WIMP experiments are steadily approaching the neutrino floor (see Fig. 1.5), the point at which detectors will be sensitive to and flooded by neutrinos. This has motivated the need to dedicate more searches to low-mass WIMPs as well as hidden-sector dark matter, and Ref. [13] outlines a need for a multi-experiment program to pursue this effort. The report further stresses the value in being able to probe several candidates with high sensitivity simultaneously.

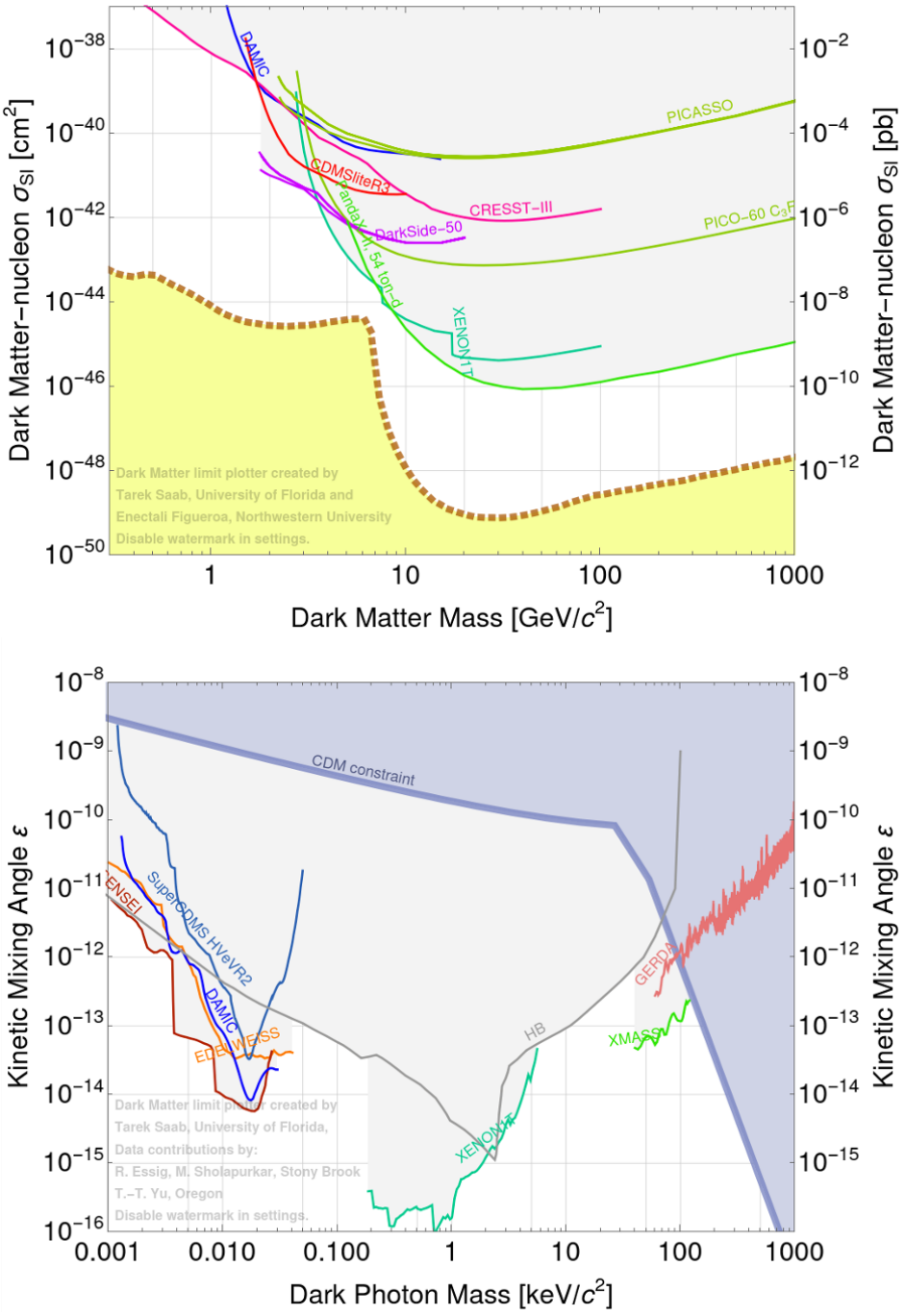

Figure 1.5: Current experimental limits for major dark matter searches [29].

The success of an experiment falls on two themes: energy threshold and backgrounds. Backgrounds from natural radioactivity, cosmogenic activation, and detector-specific processes such as dark counts pose a threat to direct-detection experiments. Radioactive backgrounds from beta decay and Compton scattering produce electron recoils with energies comparable to those of WIMP recoil kinematics. It is thus critical have the capability of identifying and rejecting such backgrounds.

We have already seen the main challenge in detecting cold, non-relativistic sub-GeV dark matter given the small size of its detectable signal, and we have touched on the kinematics of its recoil energy: the energy transfer from dark matter elastic scattering is simply an inefficient process. Below the GeV scale, this energy transfer falls below the threshold of even the most sensitive experiments today. For low-mass dark matter scattering off an electron, and the case of dark matter being heavier than the electron, the maximum energy transfer is the dark matter's kinetic energy: $E_{max} \leq \frac{1}{2} m_\chi v^2$, meaning bound electrons can give a signal with the condition $m_\chi \gtrsim 0.3\text{MeV} \times \frac{\Delta E_B}{1\text{eV}}$, where ΔE_B is the binding energy.

There are vast implications here: dark matter can induce ionization in drift chambers, cause ionized excitations or scintillation photons in semiconductors, or eject electrons from two-dimensional materials. An entire set of novel technologies corresponding to these detection principles is being built out. For semiconductor experiments that use single-crystal targets: larger recoil energies of electrons in a crystal are suppressed by a crystal form factor [15], meaning lower thresholds will lead to a substantial increase in the scattering rate of dark matter and electrons, and thus significantly improvement in sensitivity.

The DAMIC program is at the forefront of addressesing the aforementioned themes: its pioneering use of state-of-the-art CCD technologies continues to improve detector thresholds, and its unique detector capabilities allow it to directly measure problematic backgrounds. The program's search for nuclear and electron recoils induced by dark matter will continue to carve out parameter space for low-mass WIMPs and hidden-sector dark matter.

CHAPTER 2

INVESTIGATIONS INTO CCD MICROSTRUCTURE AND FABRICATION

The DAMIC (Dark Matter in CCDs) experiment at SNOLAB employs the bulk silicon of scientific CCDs to search for ionization signals produced by interactions of particle dark matter from the galactic halo of the Milky Way. Significant advances in CCD technology, partially driven by the ability to procure silicon of ultra-high purity [30], has enabled searches for dark matter using devices traditionally reserved for astronomical telescopes. By virtue of the low noise of DAMIC CCDs and the relatively low mass of the silicon nucleus, DAMIC is sensitive to small ionization signals from recoiling nuclei or electrons following the scattering of dark matter particles; it especially sensitive to low-mass WIMPs with m_χ in the $1-10$ Gev/c^2 range [31].

The DAMIC program has expanded for over a decade. It began with a team of seven collaborators executing preliminary R&D studies at Fermilab, and was extended by deploying three CCDs at the SNOLAB underground facility between 2012-2015. Following a successful run [32], DAMIC at SNOLAB, featuring a tower of seven CCDs, was deployed and operated between 2017-2019. DAMIC-M [100][102], a next-generation experiment that will utilize innovative "Skipper" CCD technology with sub-electron resolution, is currently under development. It will use a tower of 50 CCD modules, where each module will be over double the size of the conventional (non-Skipper) CCDs used for DAMIC at SNOLAB. In order for the reader to best understand and appreciate the distinctiveness of using CCDs to pursue dark matter direct detection, the first part of this chapter is dedicated to a review of CCDs: their structure, operation, and noise sources. A deep-dive into the nanofabrication work led by the author towards establishing a process flow for proof-of-concept detectors is then presented. DAMIC CCD fabrication is reviewed to preface key findings related to radioactive contamination and the effects on corresponding dark matter searches.

2.1 CCD Operation

In 2009, just as the DAMIC program was being launched, George E. Smith and Willard S. Boyle were jointly awarded half of the Nobel Prize in Physics "for the invention of an imaging semiconductor circuit – the CCD sensor" [33]. The CCD was invented at Bell Telephone Laboratories around four decades earlier, in October 1969. The idea originated from the desire to investigate creating a semiconductor device for memory storage analogous to magnetic bubble technology, but new uses for scientific CCDs related to light imaging were soon identified. Although it didn't generate as much excitement as the 1969 moon landing, the invention of the CCD was a major scientific and engineering achievement – it revolutionized astronomy and related imaging fields, pushing them to new boundaries.

2.1.1 Structure and Functionality

A practical first step to understanding the structure and functionality of CCDs is to start at the level of a metal oxide semiconductor (MOS) capacitor. A cross-section of a MOS capacitor can be seen in Fig. 2.1(a), featuring polysilicon-metal gates and an insulator oxide (SiO_2) layer above a thicker semiconductor bulk layer of n-type, phosphorous-doped silicon, forming a p-n junction; the figure also provides a rough sketch of the periodic diamond lattice structure of silicon. Keeping charge near the surface of a CCD has potential disadvantages, namely the possibility that mobile charge carriers will be captured within the Si-SiO_2 interface. In order to avoid this issue, a "buried channel" of boron-doped, p-type silicon approximately 1 μm-thick is fabricated just below the oxide layer to hold the charge.

Silicon is one of the most widely used materials for semiconductor fabrication; it has an electronic band structure, with a band gap energy corresponding to $E_g \sim 1.12$ eV, constricted by its valence and conduction bands. Charge is generated in a CCD when an incident particle interacts with the device's bulk silicon. An incident photon with energy E in the 1.1-3.1 eV range can generate a single electron-hole (e-h) pair: enough energy is imparted for the

electron to reach the conduction band, and the electron vacancy generates a hole that can flow in an electric field just as a physically charged particle does. At higher energies than this range, multiple (e-h) pairs are freed through further collisions by conduction band electrons with valence band electrons. The average energy (at a temperature of 300 K) required to generate an e-h pair is 3.65 eV for a photon with $E > 10$ eV [34]. Photons, however, are not the only particles that can deposit energy in the CCD bulk; other particles, such as cosmic ray muons, betas, alphas, and (hopefully) dark matter particles, can free e-h pairs by directly scattering off the nuclei or electrons of silicon atoms. As energetic particles traverse a CCD, they leave trails of ionized charge – this ionization is depicted in Fig. 2.1(d).

CCDs consist of large 2D arrays of coupled, ionization-sensitive MOS capacitors; each MOS capacitor is a fundamental element of a CCD pixel that can be operated by applying a substrate bias voltage, V_{sub}, to the CCD backside to collect and store charge. Fig. 2.1(b) shows several such pixels in close proximity, with each pixel featuring a common 3-phase gate structure: a trifecta of electrodes sit atop each MOS capacitor, and by applying appropriate modulated gate voltages (i.e. "clocking"), any stored charge within a pixel can be transferred and read out. Every third gate shares a clock driver, and the gates are parallel to each other. Their electrodes are connected to Phase 1, 2 and 3 clocks that form a single pixel register, with respective electrode potentials denoted by Φ_1, Φ_2, and Φ_3, as seen in Fig. 2.1(e)-(f).

Looking at Fig. 2.1(f): a pixel has charge under Φ_2. For clocking State 1, the values of Φ_1 and Φ_3 are high, with Φ_2 low. In State 2, Φ_3 is brought low: charge distributes between Φ_2-Φ_3. In State 3, Φ_3 is brought high again: charge moves fully from Φ_2 to Φ_3. Although States 4 and 5 are not explicitly shown, they are important to demonstrate the "charge-coupled" concept: State 4 requires bringing Φ_1 of the *neighboring* pixel from high to low, so that the charge moves fully to that pixel after Φ_3 of the original pixel is brought high. Charge is clocked in the $1 \rightarrow 2 \rightarrow 3$ direction, however Φ_1 and Φ_3 can be interchanged to clock as $3 \rightarrow 2 \rightarrow 1$. This convention is important to specify during CCD packaging.

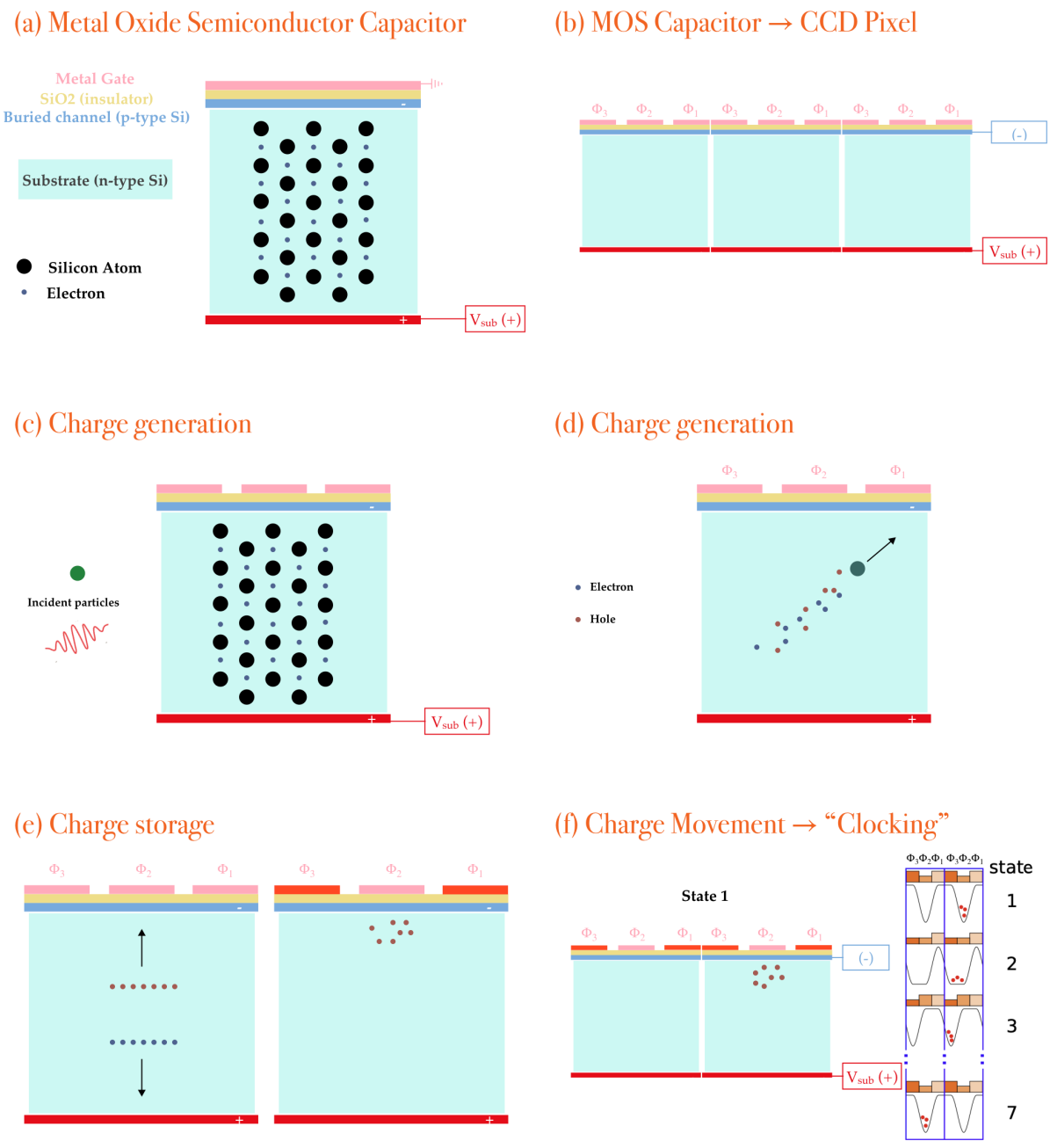

Figure 2.1: A CCD operation schematic, including: (a) the MOS capacitor building block, with a metal (gate) structure, silicon dioxide insulating layer, and p-type silicon buried channel fabricated over an n-type silicon substrate featuring a diamond lattice structure; (b) a coupled interlacing of three such CCD pixels with labeled 3-phase gates Φ_1, $\Phi 2$, and Φ_3; (c)/(d) incident particles (e.g. WIMPs, photons) moving through the CCD, creating ionization trails of freed electron-hole pairs; (e) holes being stored just below a pixel's gate; (f) clocking the charge towards the serial register in order to read it out.

The effective imaging area of a CCD pixel array is comprised of lines (columns in $\hat{y}$) of vertical, or parallel, registers separated by thermally-grown oxide barriers called "channel stops" that block the spread of charge between those columns. A CCD is read out by vertically shifting entire lines (rows in $\hat{x}$) of vertical pixels towards a horizontal, or serial, register. A row of pixel charge is transferred into the serial register, and the entire row is swiftly moved to and measured by the output amplifier, converting pixel charge to a voltage value, before a next row is shifted down. This clocking is shown in the schematic of Fig. 2.2 (right): clocking moves all the charge vertically within columns towards the serial register.

The clocking process for charge transfer is not full-proof: there is a small but quantifiable loss of charge in the CCD as charge is shifted from one pixel to another during readout due to a combination of potentially non-optimized clock voltage potentials and lattice traps and impurities. This loss of charge is called charge transfer inefficiency (CTI), and for scientific-grade devices with buried-channel technology is known to be $O(10^{-7})$ and thus negligible [35]. As a standard-size CCD is clocked out, millions of pixels need to be read and measured. A single, well-designed amplifier can read the charge of an entire CCD; modern CCDs can utilize four or more amplifiers together in order to streamline this process.

2.1.2 Readout, Images, and Noise Sources

A single-stage, source-follower amplifier such as that shown in Fig. 2.3 (top) is implemented to execute the readout and charge measurement of CCDs. Let us first focus on the final stages of clocking, and then on the implications of the amplifier architecture for charge measurement. Before the last row of pixels in a CCD moves into the serial register, it must pass the Transfer Gate (TG), which lets charge flow when its potential is held low. The serial register follows a similar 3-phase clocking scheme to that previously described for vertical clocks, but its horizontal clocks are significantly faster to ensure that, as mentioned, the entire row is emptied out before the next one flows through the TG.

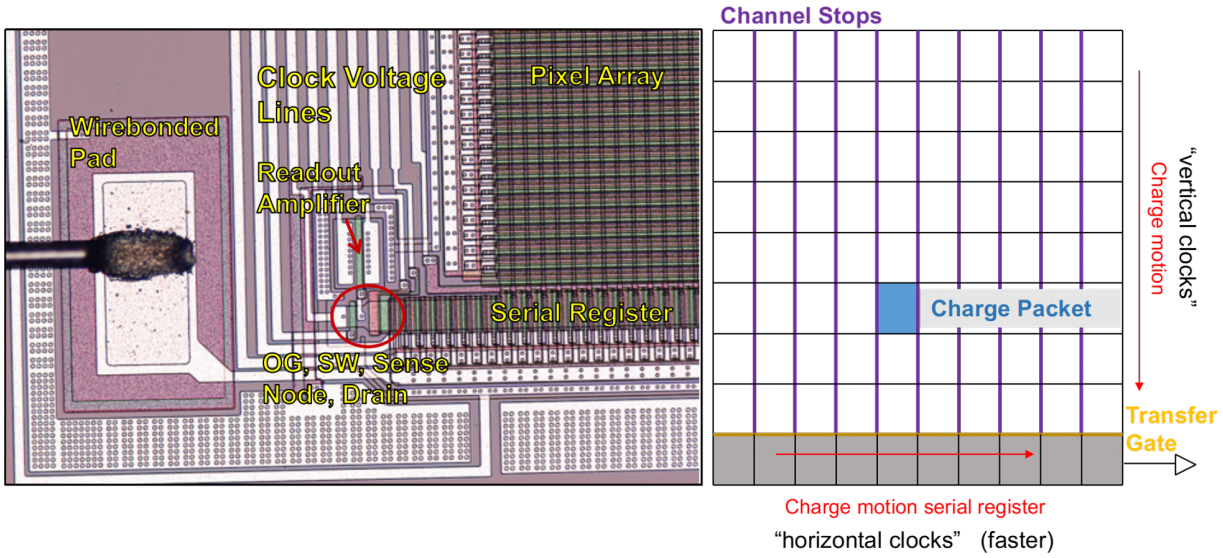

Figure 2.2: Left: Microscope image (20× magnification) of a CCD amplifier region, acquired at PNNL. Right: Clocking schematic, in which a charge packet is moved vertically into the transfer gate, faster-clocking serial register, and eventually the sense node for measurement.

The charge measurement for buried-channel CCDs is facilitated via a structure akin to a p-n junction with a gate and insulator exterior to the p-side. A depletion region forms by biasing a reference voltage (V_{REF}) connected via a reset switch to the amplifier Sense Node (SN). Charge passes through the serial register to a commonly implemented *destructive* readout amplifier via a sequence of gate transfers: first the Summing Well (SW), and then the Output Gate (OG), before finally reaching the SN, a capacitor of value C_s, for measurement. The injected charge changes the capacitor potential (V_c) proportionally to the charge magnitude as shown in Eq. 2.1. The key amplifier components include the charge transfer electrodes that move charge into the SN, the SN itself, the reset FET, and the output JFET; a microscope image of the readout section of a conventional CCD, acquired at Pacific Northwest National Laboratory (PNNL), can be seen in Fig. 2.2 (left). The voltage change across the SN is sensed by and passed through the output JFET; it is usually $O(\mu\text{V})$ per electron and is further amplified before passing through an Analog-to-Digital Converter (ADC), converting the signal into a digital number denoted as Analog-to-Digital

Units (ADU). A 16-bit ADC implemented in DAMIC's readout electronics has a dynamic range of 0 to 65535 ADU. The amplified voltage output is the CCD's "video" signal.

$$\Delta V_c = \frac{Q_c}{C_s} \tag{2.1}$$

Before a new charge packet can be injected and measured, a reset pulse is applied to clear the existing one. This reset, always seen within the CCD video output, as in Fig. 2.3 (bottom), introduces a significant noise component through spurious charge within the SN. This can be solved by taking two measurements for a given destructive charge read: a *pedestal*, and a *signal*. Once a charge packet is in the SW, the SN is measured over an integration period τ_{int}. The charge then moves through the SW, to the OG, and then SN as described before. It is measured for a period τ_{sig} (usually equal to τ_{int}) before the reset pulse is applied. A differential measurement between the signal and pedestal is then calculated. This technique, called *Correlated Double Sampling* (CDS), removes the reset noise. In addition to this, CDS can successfully attenuate high frequency noise sources, as demonstrated in Fig. 2.4; CDS is not effective in removing all low frequency noise components, though. The technique is performed analogically in standard CCD readout. Furthermore, in CCD readout, two MOSFET amplifiers at opposite ends of the serial register can be used: one to read transferred charge and the other to simultaneously read empty mirror pixels.

An example of a DAMIC-M prototype CCD and a pixel cross-section can be seen in Fig. 2.5. Once the CCD pixels' charge has been fully clocked and processed by the readout electronics, the pixel values are sent to a computer, where an image is constructed from the 2D stacked history of the pixels and stored as a FITS file [36]. Images are typically viewed using the SAOImageDS9 ("DS9") visualization tool. A section of a raw CCD image in DS9 can be seen in Fig. 2.6 (left); the image was taken at the LPNHE in Paris. There are ionization tracks visible; the image's bottom gray-scale shows pixel values in ADU, which depend on the magnitude of amplification, or *gain* (k), the system produces.

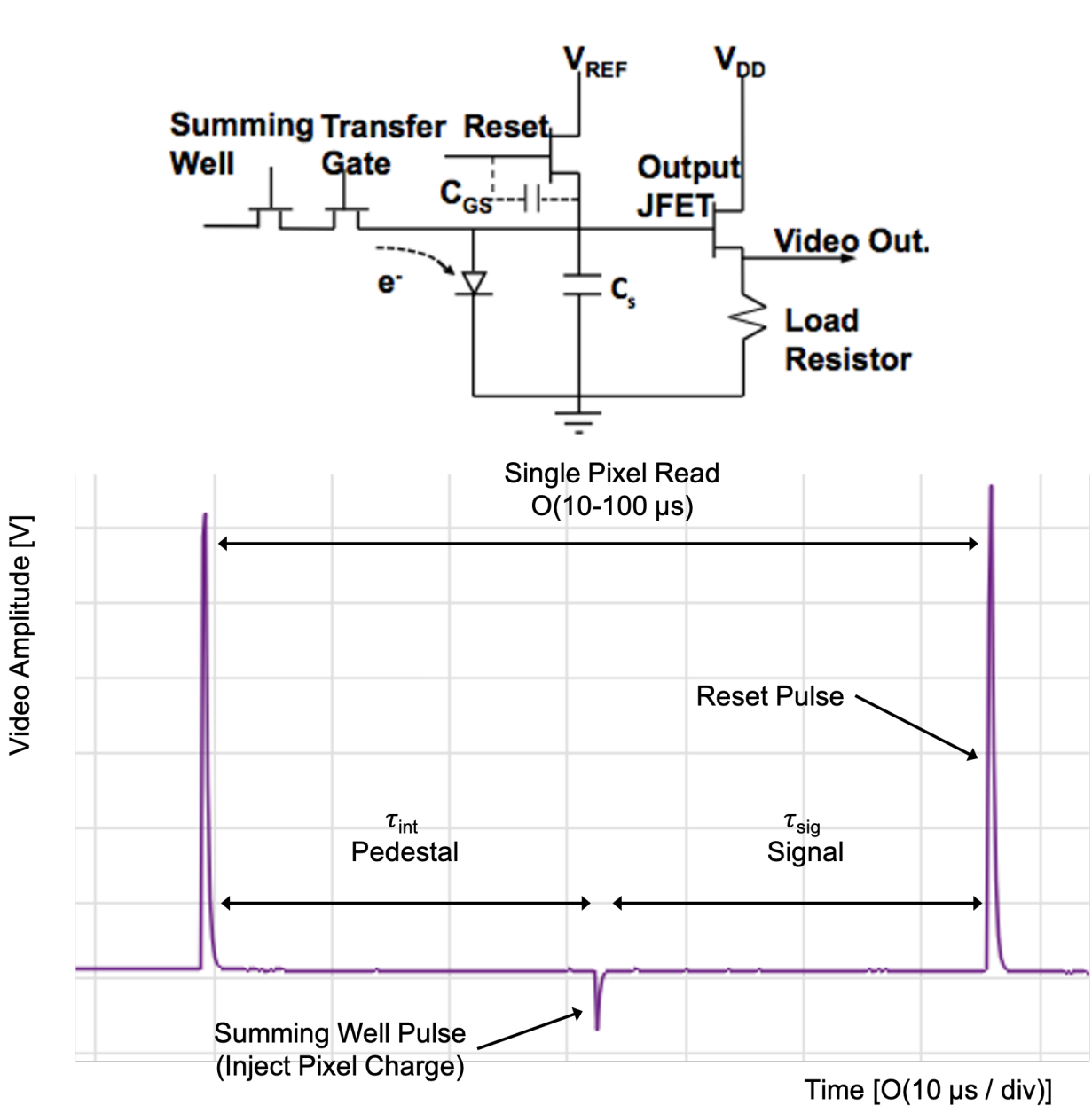

Figure 2.3: Top: Schematic a conventional CCD output amplifier. Bottom: Video waveform for a single pixel read with $\tau_{\text{int}} \approx O(10\mu\text{s})$, including labeled summing well and reset pulses.

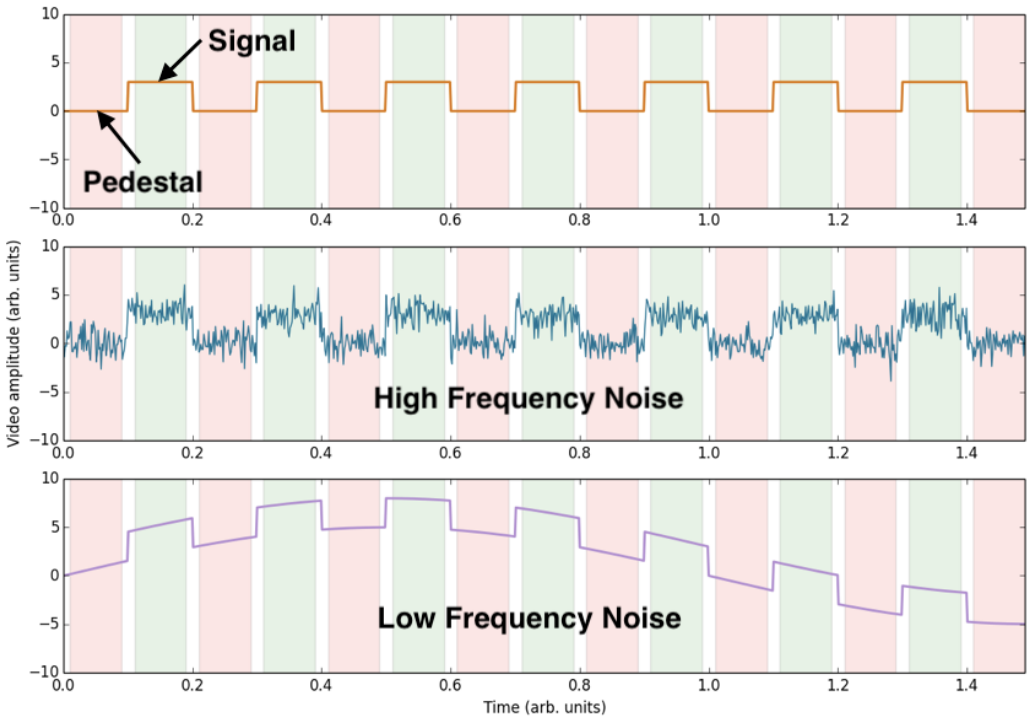

Figure 2.4: Examples of video signals featuring no noise (top), high frequency noise (middle), and low frequency noise (bottom); correlated double sampling removes CCD reset noise and attenuates low-frequency noise sources.

The convention for referring to a CCD is by the number of pixels in each dimension (e.g. 4k × 4k). While the final image stores values for physical pixels, it can also contain an *overscan*, where the amplifiers are read in x and y beyond the number of pixels available. The x-overscan is obtained by reading beyond the length of the serial register, the y-overscan by reading beyond the number of available rows in the CCD sensor. The overscan region, whose "pixels" are not exposed, gives a handle on the CCD *baseline*, or *image pedestal*, a constant added to pixel values to ensure none are negative (later subtracted during processing).

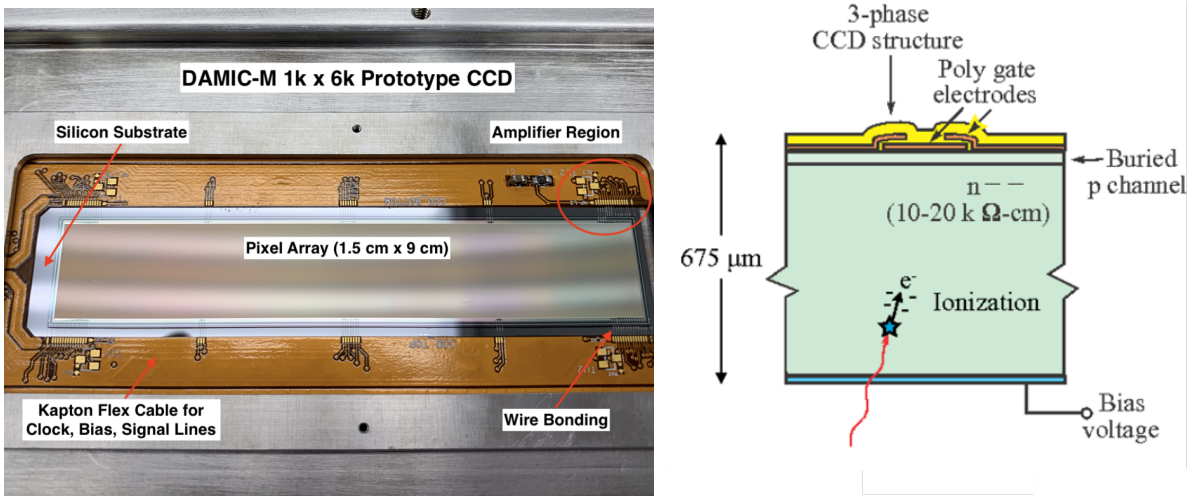

Figure 2.5: Left: DAMIC-M prototype 1k × 6k CCD; the kapton cable is wirebonded for delivery of clock, bias, and video lines. Right: schematic of a DAMIC CCD pixel (675 μm).

Moreover, pixels can be read out binned in $\hat{x}$ and/or $\hat{y}$: the former is done by moving multiple pixels' charge from the serial register into the readout stage together, and the latter is done by transferring multiple rows of the pixel array before the serial register is clocked. The binning trade-off is between improved *readout noise* due to fewer reads, and improved spatial resolution in an unbinned, 1×1 read mode. The readout noise can be obtained by the pixel charge distribution, a histogram of the CCD's pixel values. Even in the raw image section of Fig. 2.6 (left), it is evident that the majority of pixels don't contain charge. The analytical interpretation of this in the pixel distribution (following pedestal subtraction) is

a large Gaussian peak of $\mu = 0$ and σ_{pix} corresponding to the CCD readout noise.

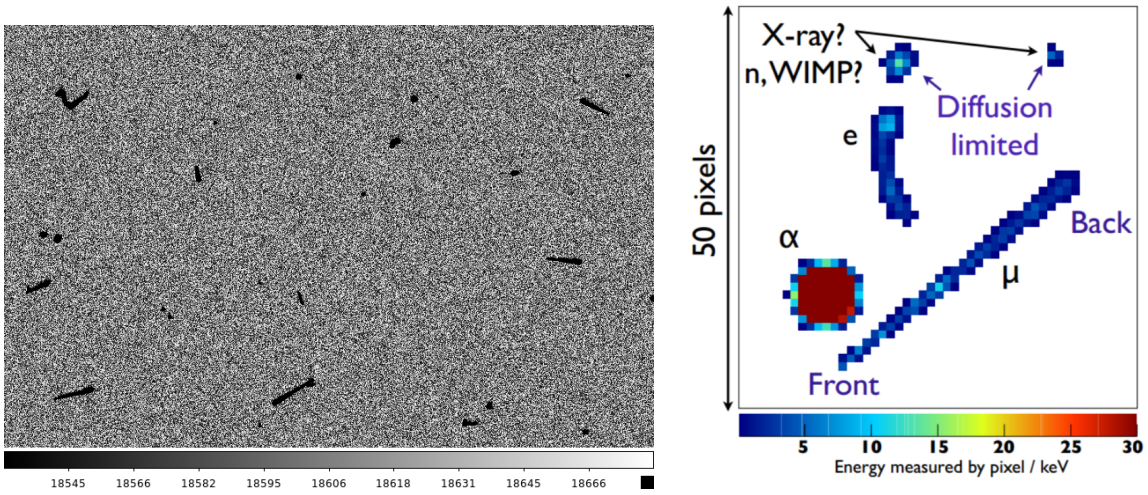

Figure 2.6: Left: A raw CCD image viewed in DS9. Right: Labeled, reconstructed particle tracks usually seen in CCD images, including electrons, muons, α particles, and diffusion-limited clusters.

While σ_{pix} (and the pixel distribution) may initially be in ADU, it is possible to directly obtain the energy calibration of the CCD. A *calibration constant* (k) converts the pixel ADU value to the energy measured by the pixel, usually in keV, incorporating the gain and energy required to produce an e-h pair. Fig. 2.6 (right) shows a sample segment of ionization tracks from various types of particles, with an energy scale included post-calibration. A value of $\sigma_{\text{pix}} \sim 1.6$ e$^-$ [32] has been achieved with conventional DAMIC CCDs. We will see later how the value of σ_{pix} can be further used in clustering algorithms used to identify and discriminate specific particle tracks, and how the zero-charge base-case for pixel charge distributions can be extended into full energy spectra from such tracks. Furthermore, the energy resolution of the device is obtained from σ_{pix} and the Fano factor F, which can guide analysis thresholds. The latter is the ratio between observed statistical fluctuations in the number of charge carriers and that predicted by Poisson statistics; recent measurements and low-energy modeling (for silicon detectors) of F are described in Ref. [37] and [38].

2.2 A Proof-of-Concept for CCD Production at the University of Chicago: Photodiode Fabrication at the Pritzker Nanofabrication Facility

2.2.1 A Review of Semiconductor Diode Detectors

Solid-state detectors have several key advantages in terms of radiation detection: superior energy resolution given a higher number of information carriers per incident event, compact size, fast timing characteristics, the ability to vary thickness, and relative ease of procurement of materials given related, large-scale commercial industries [39].

As mentioned, electrons within the valence band of silicon are part of tetra-covalent bonds: a silicon atom is grouped with four neighboring atoms around it. If such covalent bond is broken, as can happen through thermal excitation, an electron can leave an unsaturated bond. The resulting freed e and h partake in a random thermal walk, leading to some diffusion. Assuming a point-like origin, the broadening of charge is approximately Gaussian:

$$\sigma = \sqrt{2Dt} \tag{2.2}$$

where σ is the standard deviation, D is the diffusion coefficient, proportional to both charge carrier mobility (μ) and absolute temperature (T), and t is time. In a CCD, the correlation between charge spatial variance and carrier transit time enables the reconstruction of the depth of ionization events.

An *intrinsic* semiconductor corresponds to one that is completely pure. This implies the number of its electrons in the conduction band exactly equals the number of its holes in the valence band, i.e. its intrinsic carrier densities (n_i and p_i) are the same. These values are lowest in semiconductor materials operated at low temperatures, and with large bandgap energies. In semiconductors, both electrons and holes contribute to electrical conductivity

(or inversely, *resistivity*). The resistivity (ρ) of intrinsic silicon at room temperature could in principle exceed 200 kΩ-cm, but impurities are present even throughout purification processes; the best processes realistically can reach $\rho \approx 50$ kΩ-cm. The relation for resistivity, inversely proportional to charge carrier mobility (μ_e, μ_h), is:

$$\rho = \frac{1}{qn_i(\mu_e + \mu_h)} \tag{2.3}$$

Such impurities do not only come naturally, they may be added. Although intrinsic semiconductors can conduct a small current even at room temperature, they tend to not be practical for the production of different electronic devices, and therefore require an intentional and controlled introduction of suitable impurities to the material to tailor its properties as desired. For example, if an impurity is present, such as an atom that forms five covalent bonds (rather than four as in silicon), it occupies a lattice site and has an extra electron not bounded strongly to neighboring atoms. This type of impurity is called a donor impurity; it contributes to electrons in the conduction band without producing a partner hole. The donor impurity concentration is denoted by N_D. Furthermore, the condition $N_D \gg n_i$ is almost always met: the impurity concentration is large relative to intrinsic conduction-band electron concentration.

This description is analogous for an impurity that can accept charge from a neighboring atom; the donor impurity concentration of acceptors is denoted by N_A. In either case, the total number of charge carriers increases meaning the conductivity of a doped semiconductor is higher than its pure form. A material that is n-type (p-type) has electrons (holes) as majority carriers and holes (electrons) as minority carriers. Heavily doped layers are used to establish electrical contact in semiconductors due to their high majority carrier density.

The next step is to consider the details of the boundary, created by doping, between p-type and n-type material brought into contact. This p-n junction serves as the basis for numerous semiconductor detectors. As discussed, the p-type material contains an excess of

holes, while the n-type material contains an excess of electrons. These excess electrons can diffuse into the p-type material, filling holes; the excess holes can similarly diffuse and attract to n-type material electrons. Such cross-junction diffusion charges the originally neutral p-type and n-type layers, creating an electric field across the boundary, the influence of which gradually slows and ceases additional diffusion of charge across the boundary. At the point that diffusion stops, a steady-state charge distribution is established, and the electric field continues to work to repel mobile charge carriers from the junction. This region surrounding the junction is called a *depletion* region.

Depletion is key for the operation of semiconductor detectors. The scenario described above is for zero-bias equilibrium. However, unequal distributions of donor or acceptor atoms can extend the depletion region into one material's side. Furthermore, it is the ionized donor/acceptor sites that remain in the depletion region (but are not mobile). This implies a higher-resistivity in the depletion region relative to the original materials forming a junction: ionized *e*-*h* pairs flow out of the depletion region and can be measured.

The device need not be operated under a zero-bias condition: applying a voltage to the depletion region, for example within a p-n diode, has some key effects. The electric field increases with increasing applied voltage. For the p-type material connected to a negative terminal supply and n-type to a positive terminal, the respective carriers of those materials retract from the junction and the depletion region increases. The higher resistivity means less current flowing through the materials. This process is known as *reverse-biasing*. There is a limit to how much the electric field intensity can be increased, beyond which the depletion zone will break down and reverse current will drastically increase (often detrimental to the device). Semiconductor devices operating with a large enough reverse bias voltage can be fully-depleted, meaning the depletion region will extend across the entire wafer thickness. The converse, i.e. decreasing the electric field via an applied voltage, is forward biasing; it decreases the depletion region, allowing more current to flow between materials.

A silicon p-i-n diode is similar to a p-n diode, but has an additional intrinsic region between the highly-doped materials. An advantage to the p-i-n diode is the ability to vary the thickness of its depleted intrinsic region: if the silicon used is especially high-resistivity and care is taken in fabrication to avoid the introduction of impurities, then it is possible to achieve very low levels of *leakage current*. Leakage current is the small current that can flow through the depletion in reverse-bias mode, dependent on minority carriers and present even without ionization. In bulk it comes from thermally generated e-h pairs, and on surface from interfaces with large voltage gradients.

The 1-D form of Poisson's equation for calculating a potential is given by:

$$\frac{d^2\varphi}{dz^2} = -\frac{\varrho(z)}{\epsilon} \tag{2.4}$$

where ϱ is the space charge profile, $\varphi(z)$ is the electric potential, and ϵ is the medium's dielectric constant.

This can be applied to the case of a reverse-biased p-n junction, with electron diffusion in a uniform positive space charge region on the junction's n-side and a similar uniform negative space charge region from hole diffusion on the junction's p-side. Enforcing charge neutrality and boundary conditions, and assuming $N_D \gg N_A$, i.e. that the n-side doping level is significantly higher than that of the p-side (which is such for buried-channel CCDs), then a relation can be obtained for the depletion thickness, z_{dep}:

$$z_{dep} = \left[\frac{2\epsilon_{\mathrm{Si}}}{qN_A}(V_{REF})\right]^{1/2} \tag{2.5}$$

where ϵ_{Si} is the permittivity of silicon and V_{REF} is the previously mentioned reverse-biasing reference voltage.

A fully-depleted CCD is essentially a merging of p-i-n diode and conventional CCD technology: there is a similar n^+ ohmic contact, but the p^+ junction of the diode is replaced

with the p-type channel that has polysilicon electrodes over a gate insulator, as in Fig. 2.7 (left). The fully-depleted CCD's corresponding electric field is given by Ref. [40]:

$$\begin{aligned} E(z) &= E_{\max} + \frac{\rho_n}{\epsilon_{\mathrm{Si}}} z, \\ E_{\max} &= -\left(\frac{V_{\mathrm{sub}}}{z_{\mathrm{sub}}} + \frac{1}{2} \frac{\rho_n}{\epsilon_{\mathrm{Si}}} z_{\mathrm{sub}} \right), \\ E_J &= -\left(\frac{V_{\mathrm{sub}} - V_J}{z_{\mathrm{sub}}} + \frac{1}{2} \frac{\rho_n}{\epsilon_{\mathrm{Si}}} z_{\mathrm{sub}} \right) \end{aligned} \tag{2.6}$$

where z is depth, z_{sub} is the substrate thickness, $E_{\max}$ is the field at the junction of p^+ and the high-resistivity substrate, $\rho_n = qN_D$ is the donor volume charge density, and E_J is the 1-D solution for the electric field at the junction located at depth z_J. The shared fundamental structure across fully-depleted CCDs and p-i-n diodes is that thickness can be varied for application, while CCDs have the clear advantage in terms of noise. Technological developments over the last decades have enabled especially-thick CCDs motivated by a desire for improved near-infrared response of the cameras deployed in astronomical surveys [41]; these developments have simultaneously benefited the experimental community that uses CCDs to search for dark matter interactions, including DAMIC. Thick CCDs produced on high-resistivity silicon enable clock settings that optimize charge transfer efficiency (CTE) independent of the required V_{sub} to reach full depletion.

The cross section of a fully-depleted CCD from Ref. [42] is seen in Fig. 2.7 (left). Extracting the 1D solution for the potential at the junction of the buried channel and substrate (V_J) gives a value approximately equal to the potential minimum ($V_{\min}$), as in Eq. 2.7. The relation includes the applied gate voltage (V_G), the flat band voltage equal to the workfunction difference between the metal gate and semiconductor (V_{FB}), the gate insulator thickness (d), channel depth (z_J), and permitivitties of Si and SiO_2 (ϵ_{Si}, $\epsilon_{\mathrm{SiO_2}}$). This solution is for $N_A \gg N_D$, and for the n-type depletion thickness satisfying $z_n \gg z_J + (\epsilon_{\mathrm{Si}}/\epsilon_{\mathrm{SiO_2}})d$.

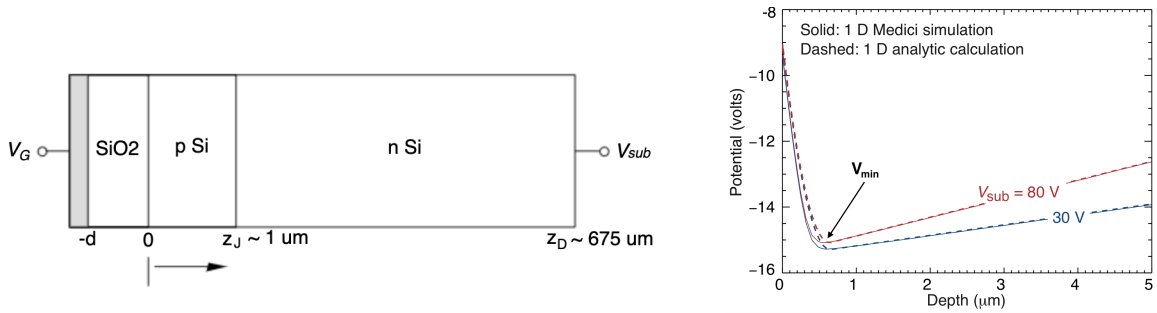

Figure 2.7: Left: Schematic of a CCD cross section. Right: Corresponding potential profile vs. depth for a CCD operated in an overdepleted mode, shown for analytic calculation and simulation. Figures taken from Ref. [42]

$$V_{\text{min}} \sim V_J \approx V_G - V_{FB} - \frac{qN_A}{2\epsilon_{\text{Si}}} z_J^2 \left(1 + \frac{2\epsilon_{\text{Si}} d}{\epsilon_{\text{SiO}_2} z_J}\right) \tag{2.7}$$

The electric field present will sweep electrons to the CCD backside at $z = z_D$ (675-μm) and move holes close to the front surface of the CCD $z \sim 0\,\mu$m. As with the p-i-n diode, V_{sub} is applied through a backside ohmic contact, a non-rectifying electrode junction that enables free flow of charge. Fig. 2.7 (right) shows the calculated and simulated potential profile for an overdepleted CCD and is taken directly from Ref. [42]. The overdepleted condition is for an applied voltage much larger than the depletion voltage so that the electric field is approximately uniform across the entire wafer thickness. It is worth stressing that V_{min} does not significantly change with different values of V_{sub}: the minimum potential is at an almost identical position for a V_{sub} of 30 V and 80 V, as in the cited study. This is due to the thick depletion region and large difference in doping between the channel and substrate.

Major advancements have been made in fabricating silicon junction detectors. Success depends on precision equipment and careful design in order to produce high-performance detectors with low leakage current. Planar fabrication is a common baseline processes used, it involves steps for oxide growth, photolithography to establish contacts and detector windows, ion implantation, and metallization. The similarity of p-i-n diodes and fully-depleted

CCDs make the former a good proof-of-concept in fabrication efforts of the latter. Such p-i-n diode structures were even included in early designs of the thick, fully-depleted CCDs developed by Lawrence Berkeley National Laboratory (LBNL) MicroSystems Lab and similar to those operated by DAMIC [44], motivating the author's fabrication efforts. Probing these structures gives device quality by measuring leakage current. With a foundation set for p-i-n diode, CCD microstructure and operation, the discussion can shift to their fabrication.

2.2.2 Key Fabrication Processes

A brief overview of fabrication materials, techniques, and tools are reviewed here in order to establish the necessary background to follow the subsequent process flows described.

Silicon: Procurement to Wafering

Silicon accounts for >90% of semiconductor wafer production: the steps towards wafer production can be seen in Fig. 2.8. Silicon is readily abundant in the form of silica sand, making up >25% of Earth's crust. Moreover, one can conveniently make chemically-stable insulator layers (SiO_2) from it. Such passivation layers act as diffusion barriers and can be easily etched, features important for ion implantation and photolithography. As discussed, thick or full depletion regions are feasible due to materials of high-resistivity and low impurity.

Metallurgical-grade polysilicon is necessary for crystal growth; it is produced in a high-temperature electric arc furnace, and purified through chlorosilane conversion in a fluid reactor: $Si + 3HCl \rightarrow SiHCl_3 + H_2$. There is an additional distillation step before it is re-deposited. Polysilicon in crystal growth has impurities in the parts per billion (ppb) or less. Monocrystalline silicon ingots are grown by the Czochralski method and floating zone (FZ) technique.

The Czochralski method is the industry standard, based on slight modifications to the process invented in 1950 [45]. To briefly summarize the process:

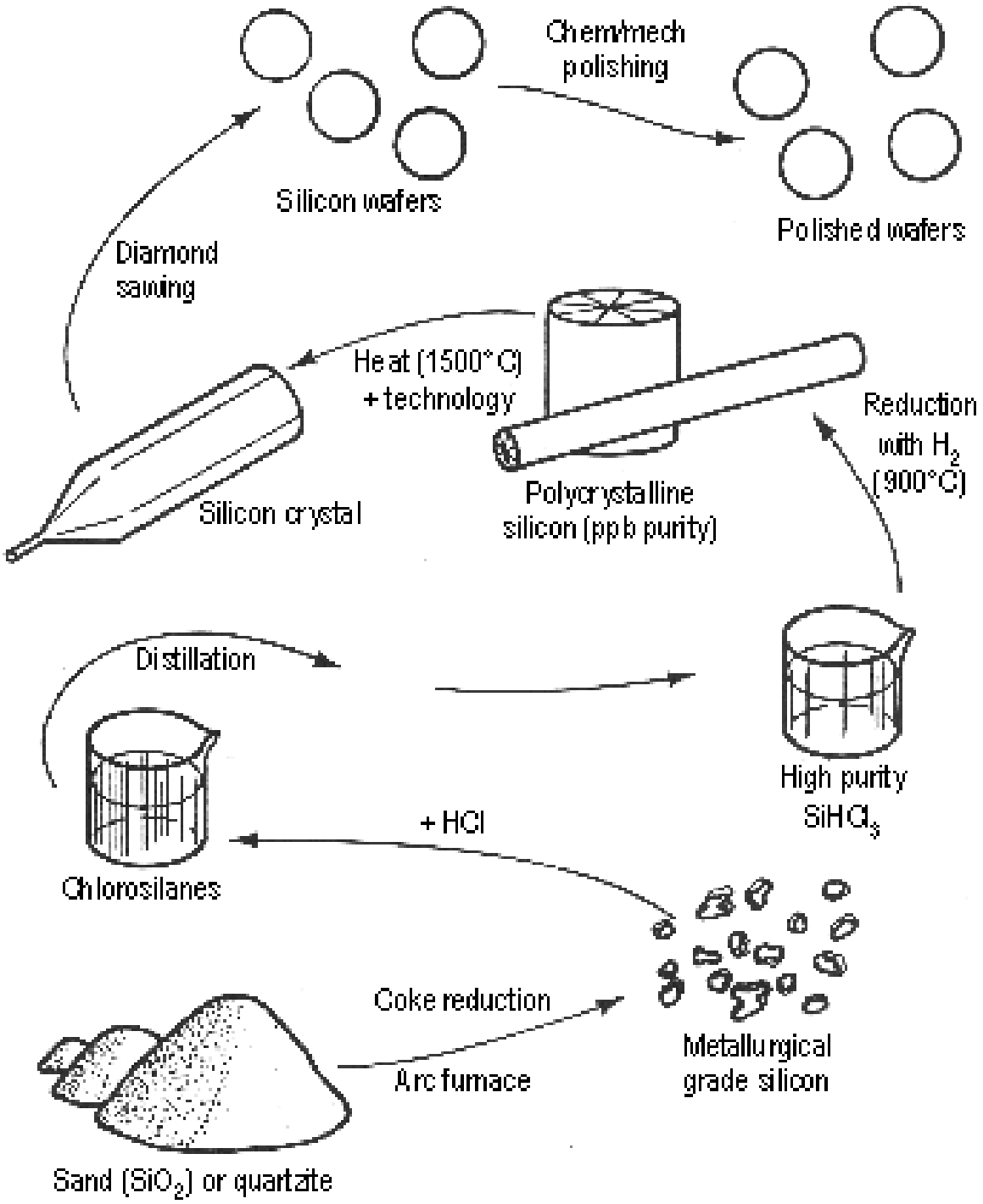

Figure 2.8: Chart showing steps to convert silica sand into detector-grade wafers.

- Electronic-grade polysilicon nuggets (and any desired dopants) are melted in a high-purity quartz crucible at a temperature slightly above the melting point ($\sim$1450°C).
- A silicon crystal seed is dipped into and withdrawn from the melt in a controlled way.
- A narrow "neck" is quickly pulled to make a dislocation-free lattice, since dislocations from thermal stress will terminate at the neck instead of the crystal body.
- Pull rate and temperature are lowered slightly; an ingot is grown to desired diameter.

FZ silicon crystal growth is done by high-purity zone melting. To summarize:

- A high-purity polysilicon rod is mounted in a high-vacuum chamber with inert gas.
- Doping is achieved by introducing dopants to the inert gas or pre-doping the polysilicon.
- A stable, targeted melting zone is formed at an end of the polysilicon using an RF coil.
- A monocrystalline silicon seed crystal is brought into contact with the molten polysilicon – this molten zone is maintained between the rotating rods via surface tension.
- A similar necking process (described before) creates a dislocation-free crystal lattice.
- The coil (and molten zone) moves along the polysilicon rod, carrying impurities along the way; coil parameters determine the final ingot's diameter and purity.

FZ crystals are the detector-choice for DAMIC given that: (1) they reach much higher resistivity; (2) although Czochralski silicon has more oxygen, which can remove metal impurities from the crystal (i.e. *gettering*), FZ silicon already starts with a lower metal impurity concentration, and gettering layers can be added during device fabrication [43]; (4) FZ silicon has higher bulk minority carrier lifetime (average time for recombination), $O(10\text{k}\,\mu\text{s})$ [30].

At this stage, full silicon ingots still need to be made into wafers. Ingots have standardized diameters: 100 mm (4 in), 150 mm (6 in), 200 mm (8 in), and so on. Wafers are sliced

using either a diamond saw or wire saw. The sliced wafer surfaces are aligned in specific orientations; an index (e.g. <100>) provides the directions of the silicon lattice's planes. Wafer edges are then ground; their surfaces are lapped and etched to ensure flattening, and then one side (or both) is polished to a mirror-like finish.

Wafer Cleaning and Surface Conditioning

Avoiding contamination of surfaces is critical to device fabrication. Leakage current across a surface can sometimes dominate the bulk current component. Cleaning and conditioning wafer surfaces can potentially reduce the formation of paths for such surface leakage current. This step is consistently repeated throughout processing. Standard RCA techniques are used for cleaning wafers before executing any high-temperature processing; the techniques rely on several solvents such as acetone and isopropyl alcohol (IPA) to remove any surface-level organic material. Additional conditioning, such as removal of thin oxide layers (e.g. $\sim 20\,\text{Å}$ native oxide layers), can be done using buffered hydrofluoric acid (BHF). Wafers are consistently rinsed in deionized (DI) water and dried carefully with nitrogen spray guns. An additional step may include briefly baking wafers on hot plates to ensure the removal of surface moisture in between processing steps. It is common practice to handle wafers with clean tweezers and transport them in specialized closed cassettes.

Film Growth and Deposition

Chemical vapor deposition (CVD) is a process used to develop high quality films on different substrates. A CVD setup features tanks with one or more monomers (reactant gases) that are vaporized by adjusting temperature and pressure so that they can form into polymers directly on the substrate surface. There are several types of CVD. In plasma-enhanced CVD (PECVD), chemical reactions occur after plasma is generated at RF frequency between two electrodes. An inductively coupled plasma (ICP) source can be used to generate high density

plasma so that deposition can be done at lower temperatures. Using similar ICP technology, one can also etch different films, depending on the chemistry of the gases used. In low pressure CVD (LPCVD), diffusion of gases decrease; the gas reactions occur more slowly across the substrate, generally leading to better film homogeneity. Any one of these CVD processes can be used to grow SiO_2 films on silicon wafers, however following absorption and reactions of gas on the surface of the wafer, the film growth comes with the release of volatile byproducts. In most CVD tools, the film is grown only on one side of the wafer.

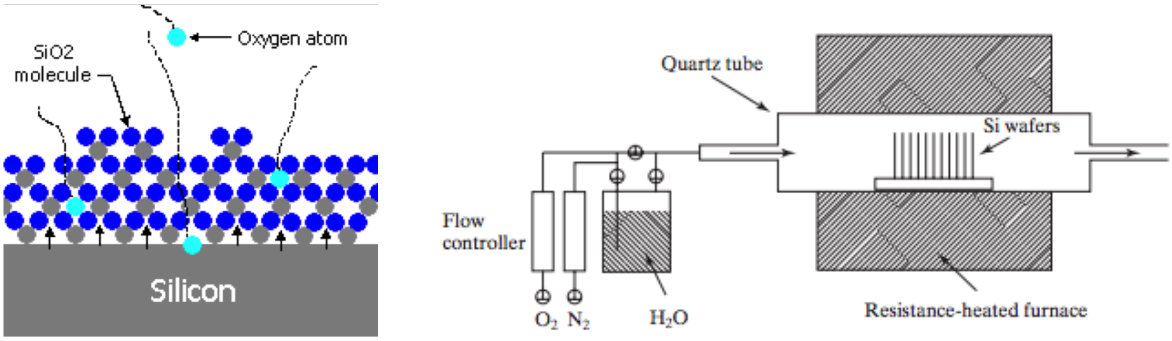

Figure 2.9: Left: Thermal oxidation for SiO_2 growth. Right: Schematic of a tube furnace.

An alternative to CVD for SiO_2 film growth is the use of thermal oxidation. This process involves a high temperature diffusion of an oxidizing agent to grow the film. For SiO_2 films, Si-Si bonds are broken and replaced with Si-O bonds, leading to volume expansion, as in Fig. 2.9 (left). Oxidation is typically performed in tube furnaces operated at temperatures $\approx 1000°C$. Multiple wafers may be loaded into a single run of a tube furnace, and oxide films are grown on both sides of wafers. There are two types of thermal oxidation: dry, which uses oxygen, and wet, which uses water vapor: $Si + O_2 \rightarrow SiO_2$, $Si + 2H_2O \rightarrow SiO_2 + 2H_2$. The former method is used for thin film growth, while the latter is used for thicker films due to a higher growth rate given the larger diffusion of water vapor.

Finally, physical vapor deposition (PVD) corresponds to processes in which a material in a condensed phase is vaporized and then condensed again onto the substrate. A commonly

used method is electron beam PVD, in which the desired material to be deposited is heated to high vapor pressure by striking it with an electron beam.

Photolithography

Photolithography is the process of patterning design masks onto films of a substrate. It utilizes photoresist (PR, or just "resist") – light sensitive material – to transfer the desired pattern. Once resist is uniformly spun and baked onto the substrate, it is exposed to (usually UV) light and chemically treated. There are two types of resist: positive and negative. Positive resist becomes soluble when exposed to UV, and is removed by a solvent developer. For negative resist, the unexposed regions become soluble to the developer. Fig. 2.10 (top) shows steps of photolithography for both types of resist.

Since photoresists are non-polar compounds and SiO_2 has polar bond characteristics (it is non-polar on the whole), there may be adhesion problems in applying photoresist. To deal with this issue, hexamethyldisilazane (HMDS), an organosilicon compound, is applied to the substrate before the resist. HMDS chemically bonds its silicon atom to the oxygen of oxidized surfaces, accompanied by the release of ammonia. Methyl groups of HMDS fragment and thus improve photoresist adhesion. HMDS is typically applied in a vapor prime oven.

After exposure, wafers are baked to solidify the resist profile. Wafers are then placed in developer, rinsed in DI water, and dried. Microscope inspection across the entire wafer is important to ensure there is no visible contamination. Following this, the wafer is etched – the photoresist can protect the layer that should not be etched. Wet etching utilizes BHF, and is isotropic – etching occurs vertically towards the substrate surface and laterally under the photoresist. In dry etching, the substrate is exposed to a plasma, whose action works with anisotropic vertical directional preference. Fig. 2.10 (bottom) outlines the different profiles obtained from isotropic and anisotropic etching. Once etching is complete, photoresist is stripped using 1-Methyl-2-pyrrolidon (NMP), and wafers are cleaned.

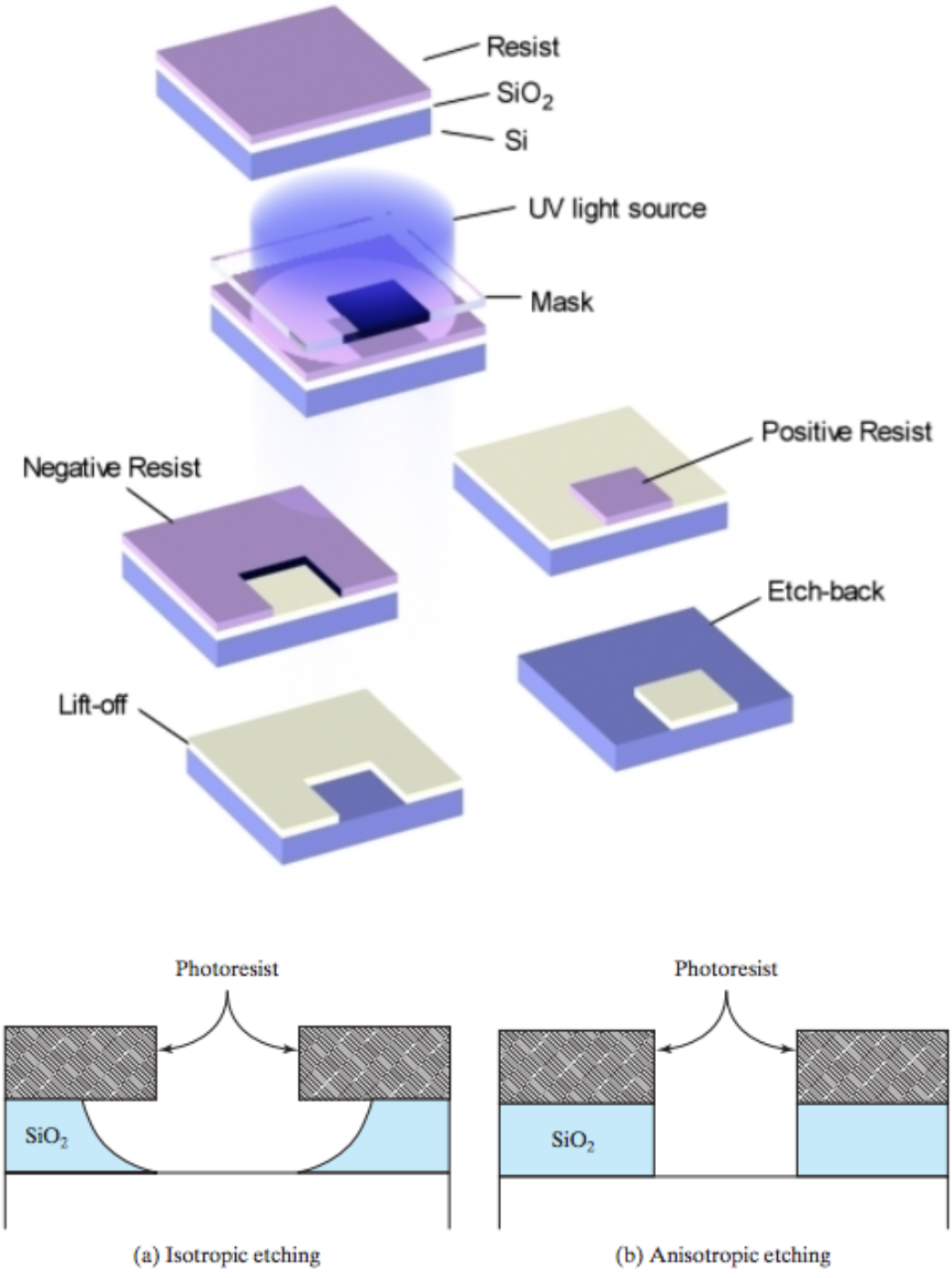

Figure 2.10: Top: Photolithography for positive and negative photoresist. Bottom: Isotropic vs. anisotropic etching of photoresist.

Ellipsometry Measurement

Device performance heavily depends on the interface between films, as well as achieving target film thicknesses. Ellipsometry is a non-invasive, non-destructive method for accurately obtaining the thickness and optical constants of different films as a function of wavelength by measuring the change in polarization state of light reflected off the sample. The polarization state is determined by the electric field: when two light waves are added in phase with one another, the result is linearly polarized light; when there is an arbitrary phase/amplitude shift between the waves, this gives elliptically polarized light. Obliquely reflected linearly polarized light also becomes elliptically polarized, and the incident and reflected beams define a plane. The components of the reflected beam are parallel (π) or perpendicular (σ) to this plane of incidence (see Fig. 2.11). Using a broadband light source and a monochromator, an ellipsometer measures two parameters as a function of wavelength: the amplitude ratio (Ψ) and phase difference between π and σ-components of the reflected light (Δ).

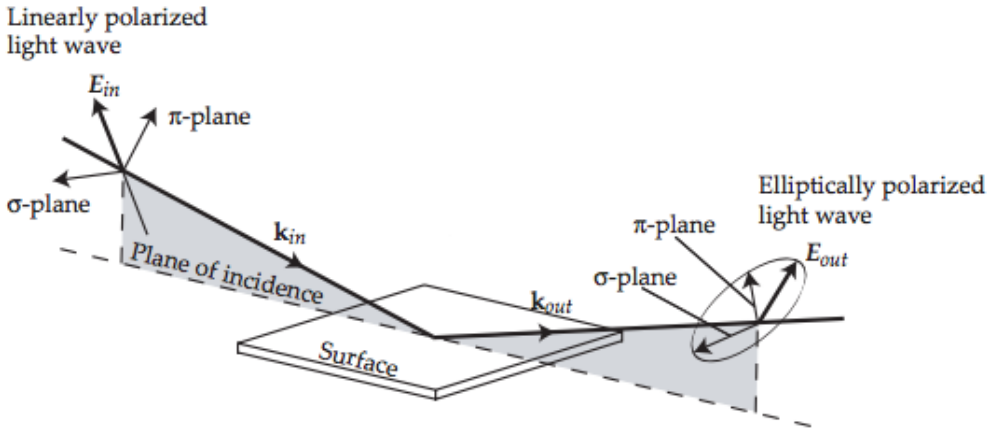

Figure 2.11: Standard optical system used for ellipsometry.

The relation between ellipsometry parameters and optical constants for a three phase optical system (e.g. air-SiO_2-Si) is:

$$P = \frac{P_\pi}{P_\sigma} = tan(\Psi)e^{i\Delta} \tag{2.8}$$

where P is the complex reflectance ratio, and P_π and P_σ can be further expanded in terms of Fresnel coefficients across different interfaces, the angle of incidence θ_0, as well as the complex refractive indexes (index of refraction and extinction coefficients). Ultimately the relation has 11 parameters: Ψ, Δ, d (film thickness), θ_0, λ, Re[$\tilde{n_0}$,$\tilde{n_1}$,$\tilde{n_2}$], Im[$\tilde{n_0}$,$\tilde{n_1}$,$\tilde{n_2}$]. The monochromator selects λ; the angle of incidence is fixed; the ellipsometry parameters are measured by the ellipsometer as a function of the wavelength; $\tilde{n_0}$ of air is known; $\tilde{n_2}$ of silicon has been measured precisely (see Fig. 2.12); $\tilde{n_2}$ will correspond to SiO_2 and is model-dependent. Once a model is chosen, the relation can extract the film thickness d as a function of wavelength. We expect this to be mostly uniform across the substrate; topographical uniformity can be checked with a profilometer.

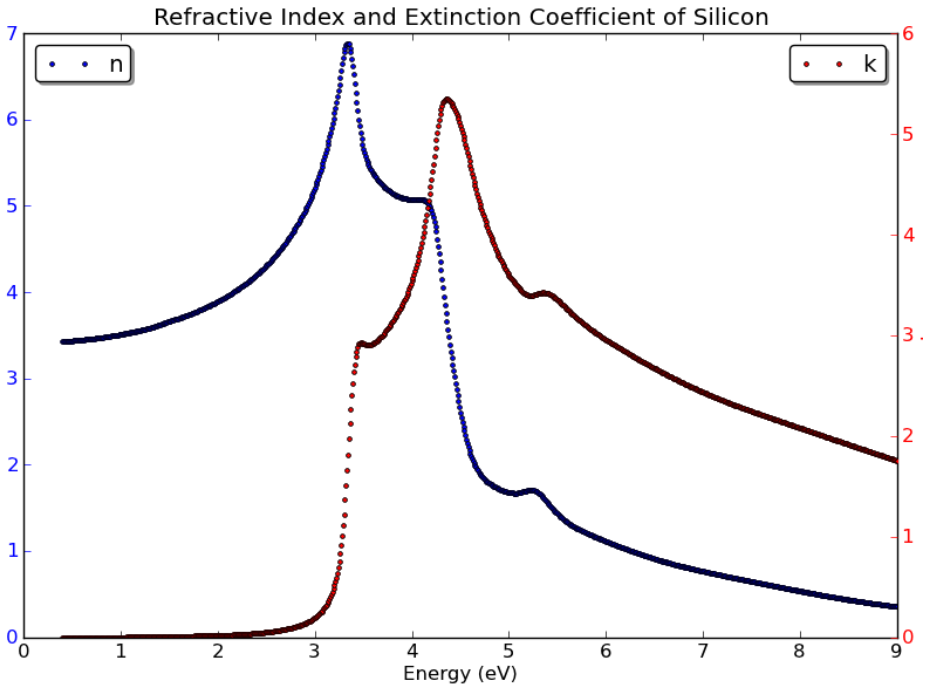

Figure 2.12: $n(\lambda), k(\lambda)$ for silicon, reconstructed from Ref. [46].

Ion Implanation

Ion implantation is a method in which doping impurities are introduced at the surface of the semiconductor by exposing it to a beam of accelerated ions. The implantation can form n^+ or p^+ layers, usually by accelerating phosphorous or boron ions, respectively. Ions are flowed through an accelerated field, and then pass through a strong magnetic field to separate unwanted impurities from dopants. Ions are then further accelerated and focused to strike the surface of the wafer. Ion impantation can be precisely controlled through known depth profiles of different dopants. Implantation requires a low annealing temperature ($< 500°$C) relative to the thermal diffusion of dopants. Since ions move in a narrowly directed beam, the doping area can be well-defined.

2.2.3 Photodiode Process Flow Development

Between 2016-2017, batches of thick silicon photodiodes arrays were fabricated at the Pritzker Nanofabrication Facility (PNF) located in the Eckhardt Research Center at the University of Chicago. The motivation for this work was three-fold to investigate: (1) design features of current-generation detectors that affect leakage current, (2) the feasibility of fabricating next-generation, record-thickness (mm-scale) fully-depleted detectors locally, and (3) potential sources of radioactive contamination during processing. The PNF is an ISO Class 5 cleanroom that specializes in advanced lithographic processing of hard and soft materials. It features six bays, each with specialized equipment for fabrication, packaging, and testing. The author completed general and tool-specific training at PNF between June and August 2016. Tab. 2.1 lists the main equipment used for the fabrication of p-i-n photodiode arrays.

Photodiodes were fabricated on 500 μm thick, 100-mm diameter, high resistivity ($>$ 10k Ωcm), double-sided polished FZ silicon wafers. The wafers were taken from the same lot, produced by Silicon Materials, Inc., and had <100> crystalline orientation. Fabrication was done based on slight modifications to work done by the LBNL Microsystems Lab [47].

Category	**Model**
Process Bench	WAFAB Solvent Bench (heated ultrasonic and H_2O baths)
Process Bench	WAFAB HF Bench
Process Bench	WAFAB Developer Bench
Film Deposition	Plasma-Therm Vision 310 PECVD
Film Deposition	Tystar Mini-Tytan 4600 Furnace System
Film Deposition	Angstrom EvoVac Electron Beam Evaporator
Photolithography	YES-58TA Vacuum Bake & HMDS Vapor Prime
Photolithography	Heidelberg MLA150 Direct Write Lithographer
Etching	Plasma-Therm ICP Chlorine Etch & Fluoride Etch
Characterization	Nikon Eclipse L200 Optical Microscope
Characterization	Horiba UVISEL 2 Spectroscopic Ellipsometer
Characterization	KLA-Tencor P-7 Surface Profilometer
Characterization	Signatone CheckMate Probe Station
Characterization	Keysight B1500A Semiconductor Device Analyzer
Packaging	Disco DAD3240 Dicing Saw

Table 2.1: PNF equipment used for photodiode fabrication. Process benches were all equipped with nitrogen spray guns, DI water sources, spin processors for wafers 10-150 mm in diameter, hot plates, and appropriate storage of chemicals.

The LBNL design was originally intended for 150 mm wafers. For easier handling, 100 mm wafers were used, while maintaining the original scale of features, namely the 3 mm dimension of each square photodiode; the design can be seen in Fig. 2.14. The steps for photodiode fabrication can be seen in Tab. 2.2. Three main masks were produced: diffusion barriers for ion implantation, contact masks to etch away oxide in specific areas, and metallization to enable electrical connections through ohmic contact.

In order to calibrate recipes of deposition/etch rates and to purge equipment, low resistivity (20 Ωcm) wafers were used in tandem with the high resistivity ones meant for final device production. The low resistivity wafers were 500 μm thick, with 100 mm diameter; they were front-side polished and caustic-etched for a backside finish, had <100> crystalline orientation, and made of Czochralski silicon produced by Silicon Quest International. All wafers featured a flat edge for easy handling – wafers were numbered on the underside of this edge using a diamond etch: W1,W2,W3,W4 denote the high resistivity wafers.

1. Implantation
a. RCA Clean, Nanostrip Bath, BHF Oxide Etch
b. Wet Thermal Oxidation: SiO_2, 7000 Å(both sides)
c. Backside SiO_2 Etch to 500 Å
d. Photolithography: Implant Mask
e. Frontside SiO_2 Etch, PR Strip
f. Implantation: $^{11}B^+$ Front, $^{31}P^+$ Back at 60 keV

2. Contacts
a. RCA Clean, Nanostrip Bath, BHF Oxide Etch
b. Wet Thermal Oxidation and Anneal: SiO_2, 1000 Å
c. Photolithography: Contact Mask
d. BHF Oxide Etch
e. PR strip
f. Aluminum Deposition: 5000 Å(frontside)

3. Metallization
a. Photolithography: Metal Mask
b. Aluminum Etch and PR strip
c. PR Coating (frontside, protect prior to deposition)
d. BHF Oxide Etch
e. Aluminum deposition, 1000 Å (backside)
f. PR strip, sintering (N_2H_2)

Table 2.2: Photodiode process flow, with corresponding visuals provided in Fig. 2.13.

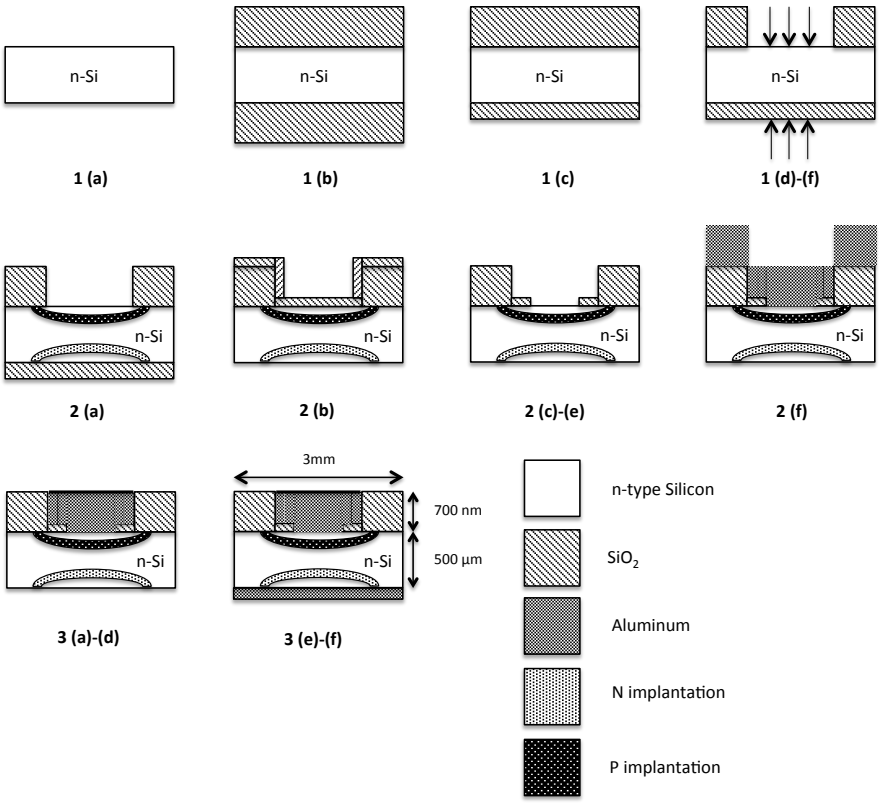

Figure 2.13: Photodiode fabrication steps shown across indididual detector cross-sections.

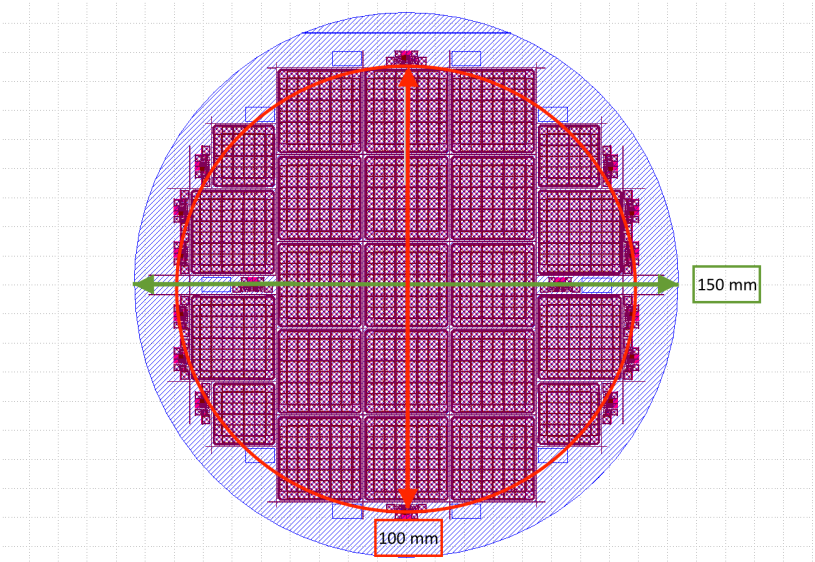

Figure 2.14: Mask layout for 8 × 8 arrays of p-i-n diodes (3 mm × 3 mm pixels); the red overlay is the effective area kept for a 100 mm wafer (maintaining original scales of features).

Wafers were cleaned thoroughly: this began with a 5 minute acetone soak and 5 minute IPA soak (both in ultrasonic baths of 104 kHz), followed by a DI water rinse. Wafers were then immersed in a 50°C nanostrip bath for 5 minutes, followed by a DI water rinse. They were transferred to BHF for 1 minute, removing their natural oxide layer, and rinsed in DI water once more. Fig. 2.16 (right) shows the garments worn when handling wafers in the PNF bay containing BHF.

Oxide films were initially grown on wafers using PECVD. However, several concerns were raised. The first was long lead-time, given that the PECVD tool has the capability to only load one wafer at a time and needs to be purged between runs. A second concern was the aforementioned use of reactants and release of volatile byproducts in CVD, leading to concerns about potential radiocontamination effects on devices (to be discussed further in later sections). Finally, given that the PNF is a shared facility, any breaks in using a specific tool could mean that other users could input substrates and run processes with different chemistries; even with purge procedures, the tool environment could be sufficiently different

to not guarantee reliable uniformity across wafers. It was therefore decided to grow SiO_2 films using wet thermal oxidation. The PNF tube furnace has cassettes that can hold up to twenty wafers in a single run. Low resistivity wafers were used to calibrate the film growth rate. To achieve the target thickness of 7000 Å, the resulting deposition time obtained was 90 minutes at a temperature of 1050°C (not including the long ramp time for the furnace to reach the target temperature).

Film thicknesses were measured using the ellipsometer with an incident angle $\theta_0 = 70°$. A sample spectrum of ellipsometry parameters can be seen in Fig. 2.15, and corresponding thickness results for the first oxide layers of W1-W4 can be seen in Tab. 2.3. Since the SiO_2 film is expected to be mostly transparent, this implies the exctinction coefficient approaches zero: $k \to 0$ (i.e. there is low or negligible absorption).

For ellipsometric measurement, a Lorentz dispersion model was implemented; the model describes a frequency-dependent polarization due to a bound charge system, essentially treating the electron and nucleus as a mass-spring system with a damped oscillator [48]. Solving the classical equations of motion and substituting the electric field for the driving force gives the relation for the complex dielectric function, from which the index of refraction and extinction coefficient can be obtained as functions of wavelength:

$$\tilde{\epsilon}(\omega) = \epsilon_\infty + \frac{(\epsilon_s - \epsilon_\infty)\omega_t^2}{\omega_t^2 - \omega^2 + i\Gamma_0\omega} \tag{2.9}$$

where $\epsilon_s = \tilde{\epsilon}(\omega \to 0)$ is the static dielectric constant, $\epsilon_\infty = \tilde{\epsilon}(\omega \to \infty)$ is the high frequency dielectric constant, ω_t is the resonant frequency, and Γ_0 is the damping factor. Expressing the dielectric constant in terms of real and imaginary components gives the relation: $\tilde{\epsilon} = \epsilon_r + i\epsilon_i$ where $n, k = \sqrt{\frac{|\tilde{\epsilon}| \pm \epsilon_r}{2}}$, respectively. The real part of the dielectric function physically corresponds to the slowing of light in the material, i.e. to the refractive index; the imaginary part of the function corresponds to the energy loss of light, i.e. to the extinction coefficient.

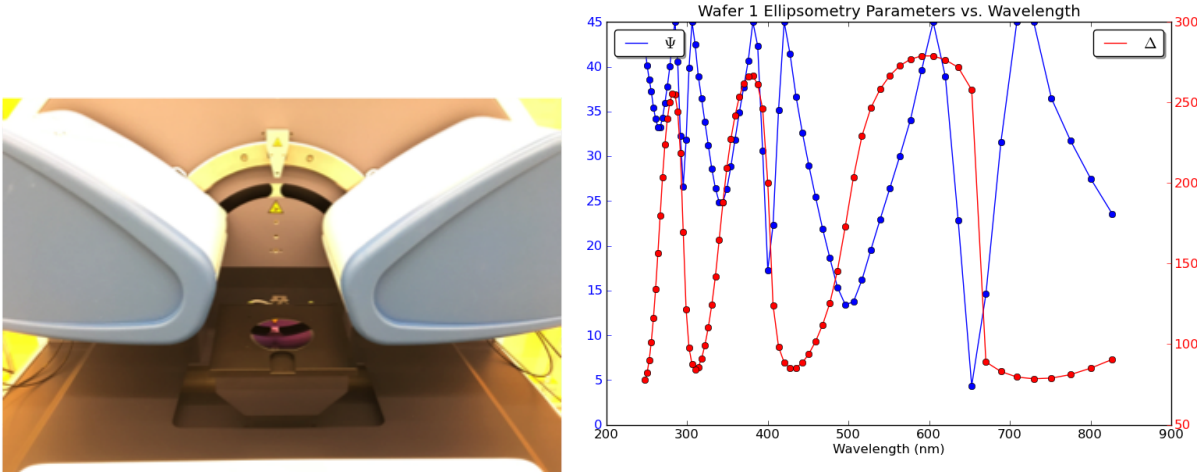

Figure 2.15: Left: W1 at the PNF ellipsometer; Right: Ellipsometer spectrum for W1.

Wafer	d, front side oxide (Å)	δ_{d} (Å)	χ^2	$n(\lambda = 632$ nm)
W1	6793	50	8.2	1.448
W2	6827	50	8.1	1.448
W3	6810	50	8.2	1.448
W4	6830	50	8.4	1.448

Wafer	d, back, post-etch (Å)	δ_{d} (Å)	χ^2	$n(\lambda = 632$ nm)
W1	692	1	0.6	1.476
W2	623	1	0.7	1.471
W3	578	1	0.7	1.471
W4	690	1	0.7	1.472

Table 2.3: Thickness of oxide layers grown in the PNF tube furnace (top); thickness of backside oxide layers following ICP Fluoride etching (bottom).

The thicknesses cited are from focusing the ellipsometer at the center of the substrate – additional measurements away from the center confirm film uniformity. To prepare for a backside oxide etch, the front side of the wafers were coated with AZ MiR 703 resist, spun at 3500 rpm for 45 seconds to obtain a coat approximately 1 μm thick. Wafers were then baked on a 95°C hot plate for 1 minute to solidify the resist. The PR coat served as protective layer for the front of each wafer during subsequent processing.

The ICP Fluoride etch tool (Fig. 2.16) was used to bring the backside SiO_2 thickness down to 500 Å. A clean and purge process was run on a dummy wafer prior to each etch, and then the etch was performed on the same dummy wafer. Low resistivity wafers were used to calibrate the etch rate. The final etch was performed by delivering 500 W ICP power, 50 W bias power, a CHF3 flow of 50 sccm, CF4 flow of 5 sccm, and Ar flow of 10 sccm. The average etch time to etch down close to 500 Å was about 9 minutes. The backside SiO_2 of two of the wafers (W1, W4) was kept for the backside implantation. To assess the difference in device performance related to effects of ion implantation, the backside layer was fully removed from the other two wafers (W2, W3). A fronstide PR strip was then performed.

Figure 2.16: Left: A wafer being loaded into an ICP Fluoride etch tool; Right: The author, pictured in Bay 6 of the PNF, wearing protective garments to etch wafers in BHF.

The impantation mask was patterned as follows: HMDS was applied to the wafers in the vapor prime oven at 150°C, and PR was coated once more for photolithography. The Heidelberg photolithography tool can handle up to 150 mm wafers; it has 405 nm and 375 nm light sources, alignment accuracy of 500 nm, and can write features to 1 μm resolution. The tool can take one wafer at a time. Wafers were exposed using the 405 nm source with a dose of 90 $\frac{\text{mJ}}{\text{cm}^2}$. Following exposure, wafers were baked on a 115°C hot plate to solidify the pattern profile, and then immersed and agitated in AZ 300 MIF developer for one minute. Wafers were rinsed and nitrogen-dried. The entire wafer surface was inspected carefully using a microscope to confirm the mask pattern and check for defects. An image of W1 post-development, and a microscope image (10× magnification) of W3's patterned guard rings surrounding a diode array, can be seen in Fig. 2.17.

The imprinted pattern was etched onto the front side of wafers. There was concern surrounding the relative etch rate of the protective PR and SiO_2 under the same operating parameters used for the previously mentioned backside oxide etch. If too much of the PR were to be etched away, it could risk cutting into the profile of the SiO_2. To confirm both rates, a combination of ellipsometer and profilometer stylus measurements were used, giving $R_{\text{PR}} \approx 50$ nm/min, $R_{SiO_2} \approx 75$ nm/min. For the given etch time, this implies less than one third of the PR is etched away, so the relevant film structure is properly protected.

The wafers were sent out to an external company, CuttingEdge Ions, for ion implantation. On the front side, wafers were implanted with $^{11}B^+$ at a 7° tilt angle, with an implant dose and energy equal to $2 \times 10^{15} \frac{\text{ions}}{\text{cm}^2}$ and 60 keV, respectively. Backside implantation of $^{31}P^+$ used the same tilt angle and implant energy, with an implant dose of $1 \times 10^{16} \frac{\text{ions}}{\text{cm}^2}$.

Upon return from implantation, wafers were cleaned in nanostrip and BHF, and an additional 1000 Å SiO_2 was grown in the tube furnace for the contact mask. The photolithography parameters were identical, with contact and implantation mask overlay done via wafer alignment marks. Oxide etch was performed via immersion in BHF for 90 seconds.

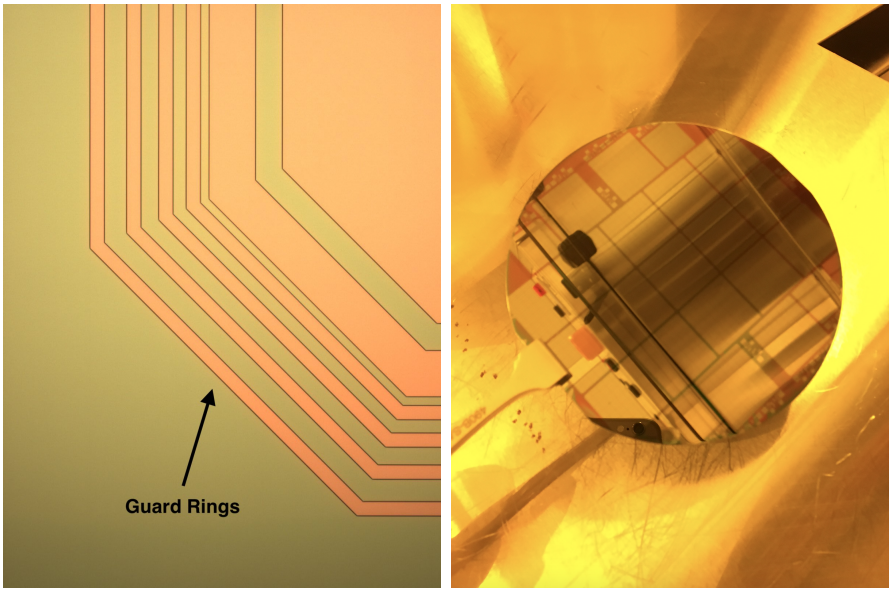

Figure 2.17: Left: Microscope image of W3 (10× magnification) guard rings following implantation mask patterning – the guard rings surround a diode array, and help lower device leakage current. Right: implantation mask of W1 – image taken after developer agitation.

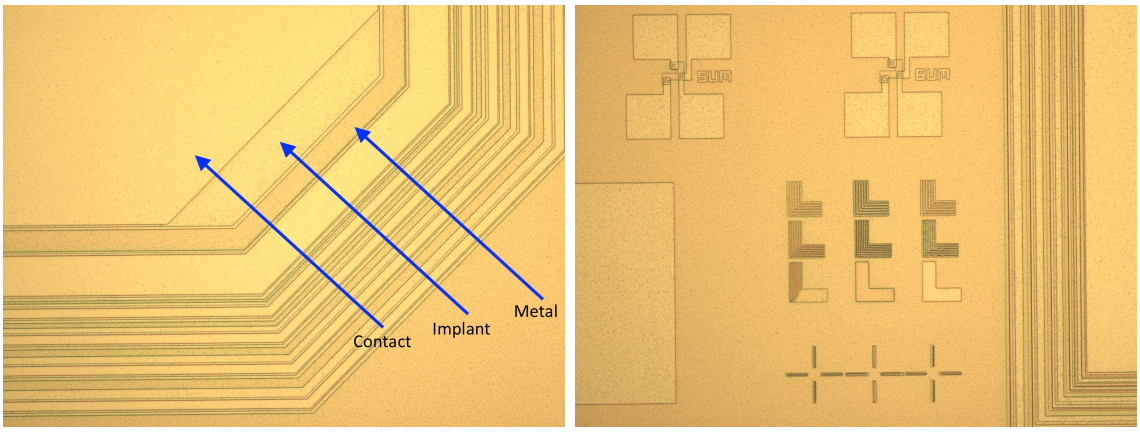

Figure 2.18: Microscope images (10× magnification) of W1: all 3 masks are visible, as well as guard rings and alignment marks used as reference points during patterning.

The final steps in the process flow were for metallization, in order to give appropriate ohmic contact across the devices. 5000 Å of aluminum was deposited on wafers' frontsides at a rate of 2 Å/s using the electron beam evaporator. Wafers were again coated in PR, and metal mask alignment and photolithography were completed. Aluminum was etched in the ICP Chlorine tool under the following operating procedure and parameters: clean/purge process on a dummy wafer, etch with 400 W ICP power, 50 W bias power, BCl3 flow of 30 sccm, Cl2 flow of 30 sccm, Ar flow of 10 sccm, 5 mTorr pressure. The etch time used for each wafer was 1 minute. Mask photoresist was then stripped, and a new PR coat applied for front side protection. A BHF oxide etch was done, followed by a backside aluminum deposition of 1000 Å. PR was stripped and wafers were cleaned once more. The final step was sintering in an N_2H_2 environment at 400°C for the purpose of dispersion-strengthening the aluminum.

2.2.4 Results

Fabrication and Packaging

The process flow was successfully calibrated using low resistivity wafers, and then carried out for wafers W1-W4 with high yield: the central-most photodiode arrays passed quality checks; exterior arrays were cut off given the aforementioned scaling-down to 100 mm wafers. Given the specifications of PNF tools, it would be feasible to execute the process flow on the originally-intended 150 mm wafers. Following checks, entire diode arrays were separated from the wafer using the facility's dicing saw and placed in gel boxes. Further capability exists to bag and nitrogen-flush such device storage packs.

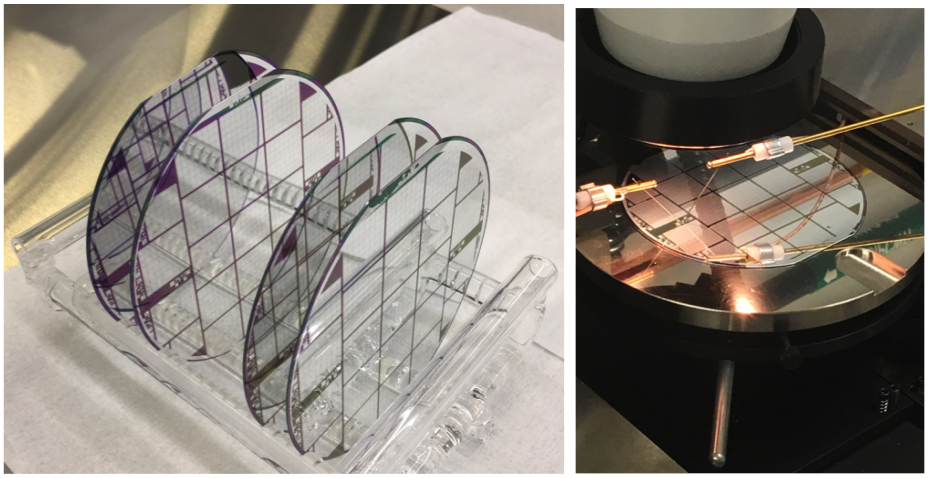

Figure 2.19: Left: Photodiode arrays on W1-W4; Right: Wafer W1 being reverse-biased at the probe station, with probes positioned at a single test diode along the wafer edge.

Depletion

The diode junction was formed through the previously-described ion implantation. There was careful selection for ion type and implant energy to minimize dislocation loops (traps). The preference for phosphorous over arsenic as a donor impurity among Group V of the periodic table came from LBNL's findings, which outlined improved leakage current levels with the former. Boron is the industry-standard among Group III acceptor impurity options. Given the implant specifications for this process flow, the zero-bias equilibrium depletion region width was calculated to be $z_{dep} \sim O(0.3\ \mu\text{m})$. Depletion was observed at $\approx$ 40 V, given the plateau position of the diode potential profile seen in Fig. 2.20.

Leakage Current

I-V curves were obtained at the PNF probe station by reverse-biasing wafers across a 15 V sweep. Fig. 2.21 (right) shows curves for W1's central most photodiode arrays, with data acquired by probing one of the 4 central diodes within each 8×8 array. The diodes measured had leakage current values of $O(1\ \mu\text{A/cm}^2)$. W1 and W4 had significantly lower

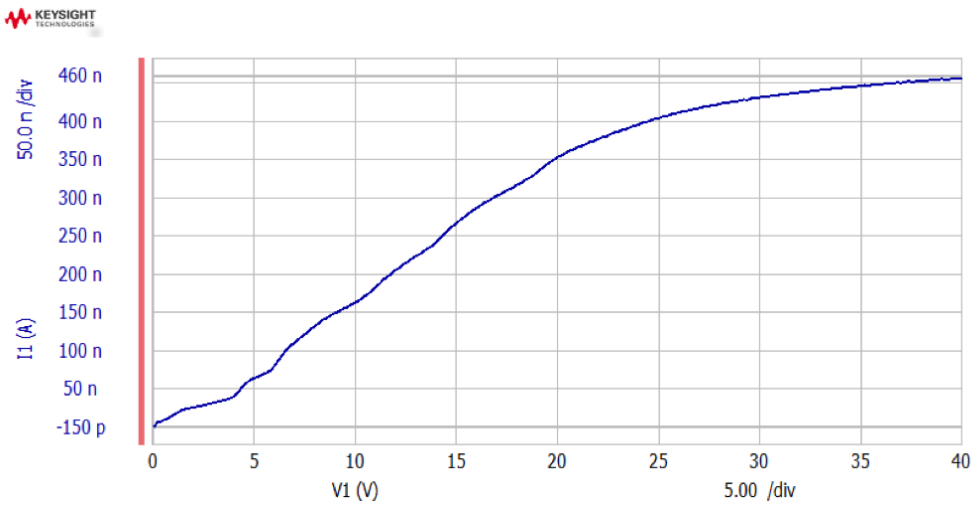

Figure 2.20: I-V scan of a photodiode, with a depletion voltage of $\approx$ 40 V.

($\times$10 decrease) values of leakage current compared to W2 and W3, which can be attributed to the backside SiO_2 layers of the former being kept prior to ion implantation. The process flow was modified to keep this backside layer for future batches. Furthermore, the leakage current measured across a given array was observed to be mostly uniform, with a maximum 20% spread in values (increasing radially) seen in W1.

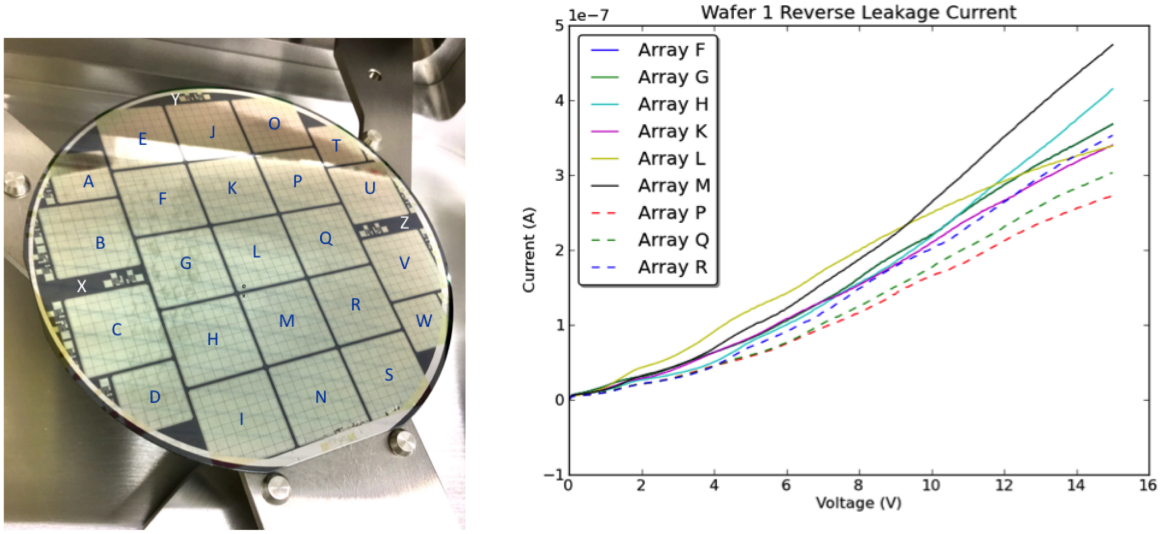

Figure 2.21: Left: labeled arrays of wafer W1; Right: corresponding leakage current profiles.

Finally, it was observed that test diodes with individual guard rings consistently had lower leakage current values: as low as 500 pA per 3 mm square element, in good agreement with values observed at LBNL [47]. Depending on the application requirements, a design was envisioned for fabricating each diode with individual guard rings, a step that would decrease the number of devices per production batch but improve the noise of the final devices. The production time for a batch of 20 wafers with photodiode arrays is estimated to be approximately 200 working hours, with an additional 2-4 weeks turnaround time for ion implantation. This estimate's main constraint comes from photolithography and ICP etch tools that can only handle one wafer. Fabricating record-thickness detectors externally could prove to be difficult given that most manufacturers don't operate machinery for wafers thicker than 1 mm. This triple-photomask, proof-of-concept project successfully demonstrates that thick, scientific-grade detectors can be produced locally at PNF.

2.3 CCD Fabrication and DAMIC CCDs

In order to fabricate a conventional 3-phase CCD, at least 6 photomasks are required [34]:

1. **Poly-1:** defines phase-1 for horizontal and vertical clocks, TG, RG to reset the SN to V_{REF}, and the output of the SW gate. The latter features increased charge storage capacity to allow for proper binning.

2. **Poly-2:** defines phase-2 for horizontal and vertical clocks, forms the TG output that injects charge into the serial register.

3. **Poly-3:** defines phase-3 for horizontal and vertical clocks and forms the gate for the output MOSFET amplifier.

4. **Contact:** defines oxidation patterns to electrically isolate each poly layer and to enable appropriate electrical connections and diffusion in specific regions (e.g. between the SN and output amplifier).

5. **Metal:** interconnects the 3-phases of horizontal and vertical clocks, connects the amplifier source and drains, and connects the SN to the amplifier gate.

6. **Pad:** etches the oxide over the metal bond pads that can later be wire-bonded to pads, as previously shown in Fig. 2.2 (left).

7. **Light Shield (optional):** allows for an additional metal light shield to define a smaller active detector area.

The obvious distinction between the required masks in the photodiode fabrication and PNF and the fabrication of conventional CCD is in the development of the 3-phase gate structure of the CCD registers. There are additional, optional masks that can be fabricated depending on the CCD's application, such as a notch mask to define a buried channel and provide proper isolation from channel stops, or a split-frame transfer mask for the name-sake operation mode. CCDs can be fabricated on thick, high-purity silicon substrates that are good electrical ground planes.

DAMIC CCDs were developed by the LBNL MicroSystems Lab [42] and consist of a $\sim$675 μm-thick substrate of n-type high-resistivity (>10 kΩ cm) silicon with a buried p-channel and an array of 4116 $\times$ 4128 pixels on the front surface for charge collection and transfer. Each pixel is 15 $\times$ 15 μm^2 in size and consists of a 3-phase polysilicon gate structure. The CCDs feature a 1 μm thick in-situ doped polysilicon (ISDP) backside gettering layer that acts as the backside contact to fully-deplete the device during operation. The overall thickness of a CCD is estimated to be 674 $\pm$ 3 μm, with an active thickness of 669 $\pm$ 3 μm and $\sim$2 μm-thick dead layers on the front and back surfaces. Considering the pixel array area of 6 $\times$ 6 cm^2, the total active mass of each CCD is 6.0 g. The high resistivity implies a low donor density of $O(10^{11}$ cm$^{-3})$, which means that the device can be fully depleted with a relatively low bias potential of $\sim$40 V applied to its backside, although it is nominally operated over-depleted with 70 V applied.

Some additional noteworthy features of the CCDs and their processing include:

- Gate insulators formed by thermally-grown SiO_2 and LPCVD Si_3N_4 layers; triple polysilicon gate structures formed by ICP Cl etching to the silicon nitride layer.
- A notch implant that enables binning by increasing the width of the serial register relative to the vertical channels.
- A split serial register to allow faster readout rates (leads to images split left/right).
- Growth of the ISDP backside gettering layer using LPCVD at 650°C, with 1.5% PH_3 in SiH_4 (silane) as a source gas. Ref. [42] shows the phosphorous concentration depth profile of this layer, obtained through Secondary ion mass-spectrometry (SIMS).
- Conventional floating diffusion amplifiers with p-channel MOSFETs; the single stage, source-follower amplifiers have 47/6 (W/L) transistor geometry [49].
- A $\sim$10 μm spatial resolution at the full-depletion operating voltage.

This chapter introduced key concepts of CCD operation, microstructure and fabrication. The features outlined set the foundation for the reader to follow the deployment of these unique devices as dark matter detectors. In subsequent chapters, connections will be highlighted between the processes and specifications described and their effects on corresponding analyses. For example (1) the electric field and donor charge density profiles of CCDs guide diffusion studies and event depth reconstruction; (2) knowledge of specific layers within the CCD provide input for `GEANT4` simulations of the DAMIC detector; (3) measurements of elemental composition across such layers inform the interpretation of the radioactive background model constructed for DAMIC at SNOLAB; (4) wafer treatment and processing history give insight into several concerning radiocontaminants, including ^{3}H and ^{210}Pb. The discussion will be driven around such insights and the results of these analyses, and how the design of next-generation detectors can be optimized.

CHAPTER 3

DAMIC AT SNOLAB: CCDS AS DARK MATTER DETECTORS

3.1 DAMIC at SNOLAB Setup: Detector and Commissioning

The CCDs used in R&D studies from 2012-2015 and the current-generation DAMIC experiment were deployed at the SNOLAB Underground Laboratory in Sudbury, Ontario, Canada [50]. The SNOLAB laboratory is located below the surface in the active Vale Creighton Mine. The facility features a 2 km rock overburden (6000 m.w.e.) contributing to a low muon flux of 0.27 $m^{-2}d^{-1}$, and a clean lab (Class 2000) 5000 m^2 in area. [51]. The DAMIC at SNOLAB detector consists of an array of eight CCDs in a vertical tower configuration. The CCDs are denoted by *extension numbers* (EXT #): for example, we refer to the topmost CCD in the stack as CCD 1 or EXT 1. The DAMIC at SNOLAB setup can be seen in Fig. 3.1.

The crystalline silicon ingots used for DAMIC CCD production were grown at the TOPSIL facility in Denmark. The ingots were then sliced and polished in November 2009. The ISDP backside layer processing step was executed by Teledyne DALSA in Canada; front-side polishing was done by OMNISIL in the United States in 2010, and wafers were then stored at DALSA until their 11-step fabrication was completed in 2014. They were then diced into 4k $\times$ 4k and 4k $\times$ 2k CCDs at LBNL. CCD packaging was subsequently completed at Fermilab.

CCD packages feature the CCD device itself, a Kapton flex cable wire-bonded to the CCD and glued onto a silicon support frame diced from the same batch of high-resistivity silicon wafers used for CCD fabrication. Sensors were glued to support frames with Epotek 301-2 epoxy; Kapton flex cables, produced by Cordova Printed Cirtuits, Inc., were glued with pressure-sensitive adhesive ARclad IS-7876. An automatic wedge-bonder and fine aluminum wires were used to make contact to the CCD pads (electrical contacts). Copper bars above

the Kapton cables' narrow end further secured each module. The Kapton cables feature an Airborn connector on one end; the cables carry clocking and bias voltages, and the CCD video signals.

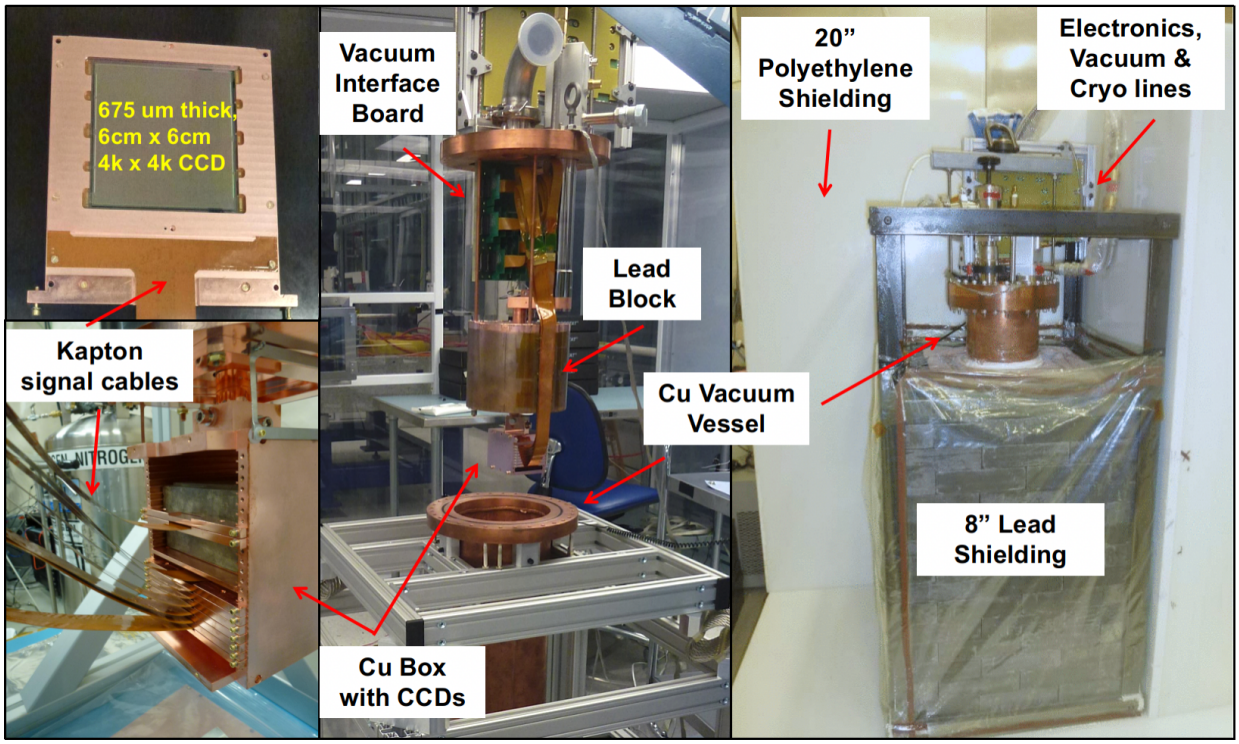

Figure 3.1: The DAMIC at SNOLAB setup. The left-most column shows a 4k × 4k CCD in its copper module, and the entire set of modules installed in the detector's copper box at SNOLAB. CCD 1 is seen sandwiched between lead bricks. Kapton signal cables can be seen extending from all CCDs. The middle column shows the Vacuum Interface Board that Kapton cables feed into, and the copper vacuum vessel. The right-most column shows detector shielding: 20" of polyethylene used to shield neutrons, surrounding 8" (20 cm) of lead used to shield gammas. Image taken from Ref. [53].

CCD packages were installed in copper modules that slide into a copper box that provides mechanical support and acts as a cold infrared shield. Additional copper trays were slotted in to hold the archaeological lead bricks (each 2.5 cm thick) that surround CCD 1. These bricks were obtained from sunken Spanish galleon and a Roman ship [52], implying high radiopurity given the long time for isotopes such as ^{210}Pb to decay away. The module of CCD 1 is made of low background copper that was electroformed at PNNL, while all remaining copper parts

of the copper modules and box were machined at the University of Chicago from Copper-101 procured from the South Copper & Supply Company; the machining used propylene glycol as a lubricant. Machined copper was cleaned in an acidified peroxide solution and passivated with nitric acid. Assembly was done using brass fasteners.

The copper box is maintained beneath 18 cm of cylindrical lead shielding inside a cylindrical copper cryostat – a HiCube 80 Eco turbomolecular pump maintains a pressure of $\approx 10^{-6}$ mbar. Thermal contact is made with the copper box using a copper cold finger that is concentric and fed through the cylindrical shielding to make additional contact with a Cryomech AL63 cold head located above the shield. A temperature sensor and heater were mounted along the cold head and cold finger contact point, feeding into a LakeShore 335 unit temperature controller. Kapton flex cables extend along the lead shielding before connecting to a "second-stage" Kapton extension featuring an amplifier for the CCD video signal. The extensions run to the electronics feedthrough, the Vacuum Interface Board (VIB).

The copper cryostat is surrounded by a rectangular lead castle to shield gamma rays; the cryostat flange remains above the shielding for proper access to necessary feedthrough ports. The CCDs have 20 cm of lead shielding in all directions, and the innermost part (5 cm) of this lead shielding is ancient, archaeological lead. A hermetically sealed box surrounds the lead castle and cryostat neck and has a nitrogen flow rate of 2 L/min in order to purge the inner volume and cryostat-exterior of radon. This N_2 gas reduces the radon level from ≈ 135 Bq/m^3 [54] to < 1 Bq/m^3. As a final shielding element, 42 cm of polyethylene surrounds the detector to block external neutrons; this shielding features a feedthrough for the compressor, nitrogen dewar, and electrical lines. The electrical lines are co-axial cables on the air-side of the setup, and connect to the Monsoon CCD controller, a system developed for the Dark Energy Survey Camera [55]. The controller sends clock and bias signals to the CCDs and digitizes their analog signals; it is programmed by a DAQ computer that receives image data via fiber optic cables. A slow control system enables remote operation and monitoring.

3.2 Data Sets and Image Processing: A Tale of Two Readouts

As mentioned, the DAMIC detector at SNOLAB has eight CCDs installed within a tower configuration. The initial intention was to operate 18 CCDs in order to achieve an active mass of ≈ 100 g. Seven CCDs (CCDs 1-7, corresponding to EXT 1, 2, 3, 4, 6, 11, 12) were fully functional from first deployment. One CCD (EXT 5) was disconnected because it was glowing from the corner during the first cool-down of the detector. From the commissioning onset, EXT 2 was not initially operational, but was resurrected after the first power outage at SNOLAB on April 29, 2017. All CCDs described are 4116 pixels in x by 4128 pixels in y. The nominal value of V_{sub} was 70 V.

Different formats of data were acquired at different periods. In Chapter 2, the concept of binning was introduced. Unbinned, or 1×1 readout mode, data optimizes spatial resolution. A significant portion of DAMIC data, however, was acquired in a 1×100 readout mode: 100 rows of the CCD pixel array were transferred into the serial register before the serial register was clocked and the pixel charge measured, implying an image pixel size of 15×1500 μm^2. While there is a loss in the position resolution in the $\hat{y}$-direction, this method allows the charge from an ionization event to be read out in a fewer measurements, reducing the uncertainty in the total ionization charge (and energy) from an interaction. Background data was taken in the 1×1 readout mode during most of 2017 – the author's work in analyzing this data can be seen in Chapter 4. Acquisition of WIMP search data with 7 CCDs ran between September 2017 and December 2018. Exposure times of images were initially 100 ks; a decision was later made to switch exposure times to 30 ks so as to reduce the effective leakage current per image.

DAMIC images were processed and with a reconstruction code and clustering algorithm developed at the University of Chicago, the procedures of which are outlined in Ref. [32].

To summarize:

- **Pedestal subtraction**: each image column was divided into four equal segments – a pedestal, estimated as the median of the pixel values within a column segment, was subtracted from each pixel value. Each row was then divided into eight equal segments, and any residual pedestal was subtracted from each pixel value by a Gaussian fit to the pixel distribution (subtracting the mean accordingly). The typical pedestal of DAMIC images is roughly 10^4 ADU, giving a maximum pixel value of ≈ 4000 e^-.

- **Correlated noise removal**: Pixels at given (x, y) coordinates and their mirror pixels were read out simultaneously across all CCD extensions. For each pixel on the right-hand side of images, we subtract a weighted sum of the mirrored pixel values, with the corresponding coefficients of the sum computed as to minimize the variance of pixel values.

- **Masks**: Masks exclude regions of spatially-localized, high-leakage-current pixels due to lattice defects that may lead to charge mimicing ionization. An "iron mask" was constructed for DAMIC at SNOLAB, combining masks from multiple data sets. The general mask procedure is to calculate the median and median absolute deviation (MAD) of all pixels within an image set: pixels are masked if they deviate more than 3 times the MAD from the median value in at least half of the images in a set, or have a median or MAD that is an outlier ($> 5\sigma$ from the mean of the MAD distribution). The number of pixels masked across CCDs varies, but the iron mask removes $\sim$7% of pixels per CCD, implying a reduction in effective target mass of ~ 0.42 g per sensor.

- **Clustering**: clustering algorithms were run to identify charge over multiple pixels from the same ionizing particle event. Two methods were applied: "fast clustering" and "likelihood clustering." The former identifies contiguous groups of pixels with signal larger than $4\sigma_{pix}$. The algorithm effectively clusters all types of ionization events, but its efficiency decreases rapidly for clusters with energies <1 keV [31]. The

latter algorithm scans over images and calculates the likelihood of an energy deposition present square moving window of 11×11 pixels. This algorithm only works for energies below 10 keV, where energy deposition are reasonably assumed to be point-like before any diffusion. The algorithm calculates for each image row the likelihood that the pixel values can be described by white noise $\mathcal{L}_n$, or white noise plus a Gaussian distribution of charge $\mathcal{L}_G$. When the log-likelihood of their ratio, $\Delta LL \equiv -\ln \frac{\mathcal{L}_G}{\mathcal{L}_n}$, is sufficiently negative, a cluster is identified. The likelihood clustering plateaus at 90% above 120 $\mathrm{eV_{ee}}$ [31]. Once clustering is performed, key parameters (pixel coordinates and charge, number of pixels in a cluster, etc.) of images were stored in `ROOT` Tree structures for analysis.

3.2.1 CCD Characterization: Diffusion, Energy Calibration, Dark Current

Diffusion and Depth Calibration

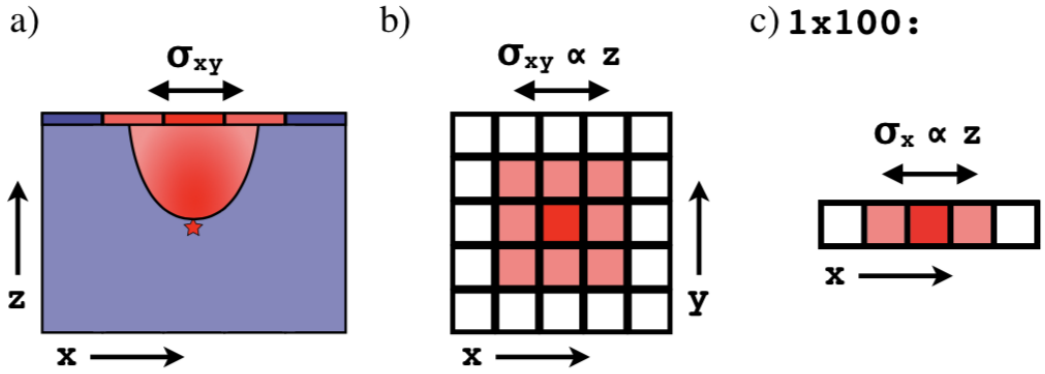

Figure 3.2: (a) Cross-sectional representation of the charge produced by a point-like ionization event (star) in the CCD bulk as it is drifted to the pixel array. (b) The x-y distribution of charge on the pixel array following the ionization event. (c) By reading the CCD in column segments 100 pixels tall, the pixel contents are collapsed along the y axis. The one-dimensional lateral spread (σ_x) is positively correlated to the depth of the interaction.

As mentioned in Sec. 2.2.1, for a point-like interaction in the active region of the CCD, diffusion leads to a Gaussian distribution of charge with spatial variance $\sigma_{xy}^2 = \sigma_y^2 = \sigma_x^2$ that is proportional to the carrier transit time and thus positively correlated with the depth of the interaction. In cases where the 1×100 readout mode is used, clusters are collapsed along y and only the lateral spread in x can be measured, meaning σ_x is directly used to reconstruct the depth z of an event (see Fig. 3.2).

In general, diffusion can be modeled as:

$$\sigma_{xy}^2(z) = \sigma_x^2(z) = -A\ln(1 - bz), \tag{3.1}$$

where the two parameters A and b are defined as

$$\begin{aligned} A^{(\text{theory})} &= \frac{2\epsilon_{\text{Si}} k_B T}{\rho_n e} \approx 150\ \mu\text{m}^2 \\ b^{(\text{theory})} &= \left(\frac{\epsilon_{\text{Si}} V_b}{\rho_n z_D} + \frac{z_D}{2}\right)^{-1} \approx 10^{-3}\ \mu\text{m}^{-1}. \end{aligned} \tag{3.2}$$

In the diffusion parameter relations, ϵ_{Si} is the permittivity of silicon at the operating temperature $T \approx 140$ K, $\rho_n \approx 10^{11}\ e\ \text{cm}^{-3}$ is the nominal donor charge density, k_B is Boltzmann's constant, e is the charge of an electron, $V_b \approx 85$ V is the potential difference between the charge-collection well and the CCD backside, and $z_D \approx 669\ \mu$m is the thickness of the CCD active region.

By using 1x1 data taken above-ground (at Fermilab), diffusion parameters were extracted directly. Images taken on surface have numerous tracks induced by cosmic ray muons, which deposit their energy in straight trajectories $[\vec{M}]$ through the bulk of CCDs. Given diffusion properties, we are able to identify the point where the muon crosses the front ($z = 0$) and back ($z = z_D$) of the CCD active region, meaning the depth z can be reconstructed along entire tracks. We perform a fit to the charge distribution of the observed muon tracks by maximizing:

$$\log \mathcal{L}_{\text{muon}} = \sum_{i=0}^{N} \log(f_q(q_i|A, b, [\vec{M}])), \tag{3.3}$$

where $f_q(q_i)$ is the probability of measuring charge q_i for the i^{th} pixel out of N from a muon track constructed from trajectory $[\vec{M}]$ convolved with a Gaussian charge spread as a function of depth using Eq. (3.1). By fitting to a series of muon tracks, we obtain diffusion parameter values $A = 285 \pm 24\ \mu\text{m}^2$ and $b = (8.2 \pm 0.3) \times 10^{-4}\ \mu\text{m}^{-1}$, which agree with the theoretical calculations in Eq. (3.2) assuming a donor charge density ρ_n equal to $0.8 \times 10^{11}\ e\ \text{cm}^{-3}$. This value is further consistent with Ref. [42]. For additional information on depth calibration, the reader can turn to Ref. [56].

Energy Calibration

The detector was commissioned with a red LED installed inside the cryostat. A series of images were acquired with the LED turned on. Since all pixels in the y overscan of each column should be effectively exposed to the same fluence assuming constant LED intensity over image read time (a few minutes), then the number of charge carriers detected should follow a Poisson distribution. The mean (μ_l) and variance (σ_l) of pixel values above the pedestal induced by LED exposure are related to the calibration constant by $k = \frac{1}{3.77\ \text{eV}_{\text{ee}}} \frac{\sigma_l^2}{\mu_l}$ (where an average of 3.77 eV is needed to generate an e-h pair). Calibration constants from LED data and further in-situ calibration done by fits to Cu K_α (from copper parts) and ^{210}Pb X-ray lines, are shown in Tab. 3.1. The in-situ energy calibration relied on the fluorescence Cu lines from surrounding detector material, and the X-ray lines coming from ^{210}Pb contamination. A binned log-likelihood fit across individual extensions was performed over parameters including a multiplicative factor correcting k, a flat background level, and the amplitudes of the aforementioned lines – the resulting calibration energy spectrum can be seen in Fig. 3.3.

CCD Extension	1	2	3	4	6	11	12
k [2.6×10^{-4} keV/ADU]	1.009	0.956	0.979	0.984	1.010	0.969	0.999
Gain [ADU/e$^-$]	14.30	15.15	14.81	14.71	14.37	14.87	14.53

Table 3.1: Energy calibration constants for DAMIC at SNOLAB CCDs, obtained from LED data and additional fits to Cu K_α and ^{210}Pb X-ray lines.

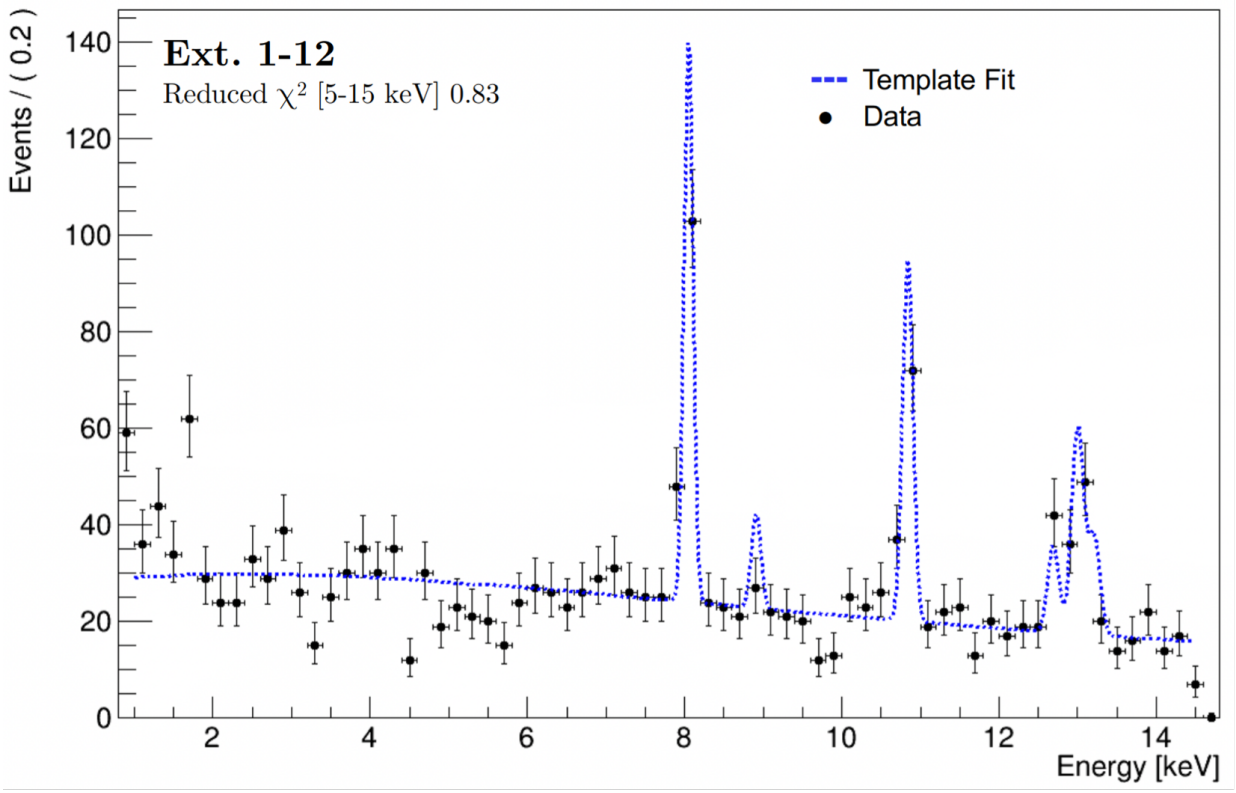

Figure 3.3: In-situ energy calibration of DAMIC CCDs: the energy spectrum is shown for 0-15 keV. There are visible peaks from Cu fluorescence lines (Cu K$_\alpha$ at 8.05 keV, Cu K$_\beta$ at 8.91 keV) and from ^{210}Pb X-ray lines (Bi L$_\alpha$ at 10.84 keV, Bi L$_{\beta_4}$ at 12.69 keV, Bi L$_{\beta_2}$ at 12.97 keV, Bi L$_{\beta_1}$ at 13.02 keV, Bi L$_{\beta_3}$ at 13.21 keV). The relevant emission energies are taken from Ref. [57].

Accurately characterizing the energy response of CCDs to ionization induced by electrons or nuclear recoils within the silicon lattice is critical in the context of a low-energy experiment such as DAMIC. The current generation experiment uses an analysis threshold of 50 eV, chosen to exceed $5\sigma_{\text{pix}}$, where σ_{pix} is $< 2\text{e}^-$ (as shown in Fig. 3.4). The optimal way to extract such energy characterization is by deploying radioactive or optical sources of fixed energies (see X-ray calibration in Fig. 3.5). Other experiments also pursue extensive calibration campaigns: XENON1T homogeneously distributes ^{220}Rn and $^{83\text{m}}$Kr via a gas purification loop to calibrate detector response to low-energy electron recoil events [58].

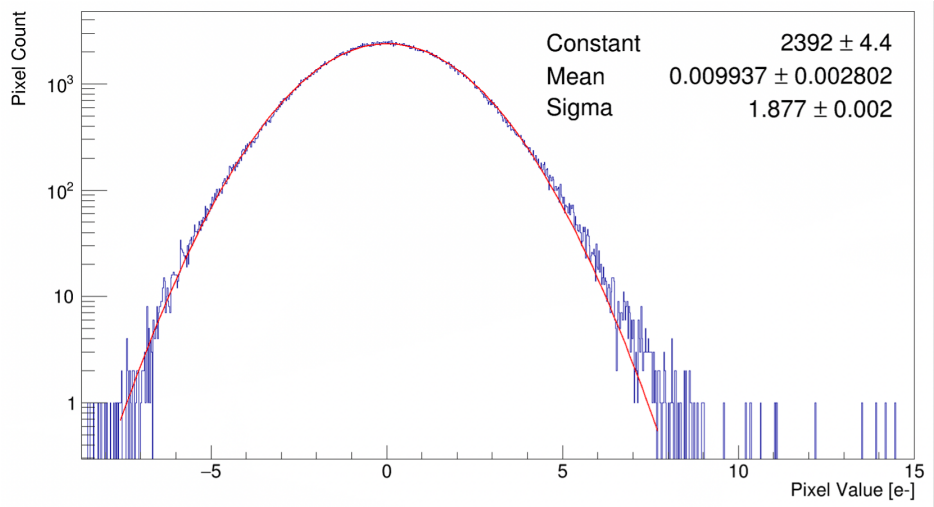

Figure 3.4: Pixel charge distribution for a DAMIC CCD image following steps for pedestal subtraction and calibration. The Gaussian fit shows the distribution is reasonably described as white noise with $\sigma_{\text{pix}} \sim 1.9\text{e}^-$.

While we were able to successfully execute the aforementioned in-situ energy calibration, a more forward-looking strategy has been explored for the next-generation DAMIC-M experiment that will feature a stack of 50 large-format CCD modules. In particular, a CCD was calibrated at the University of Chicago using a gaseous ^{127}Xe source. Ref. [53] outlines the details of this campaign, in which several X-ray peaks were clearly identified, indicating a successful attempt for a gaseous source to be used for solid-state detectors. The author has helped commission a similar test chamber at the University of Zurich.

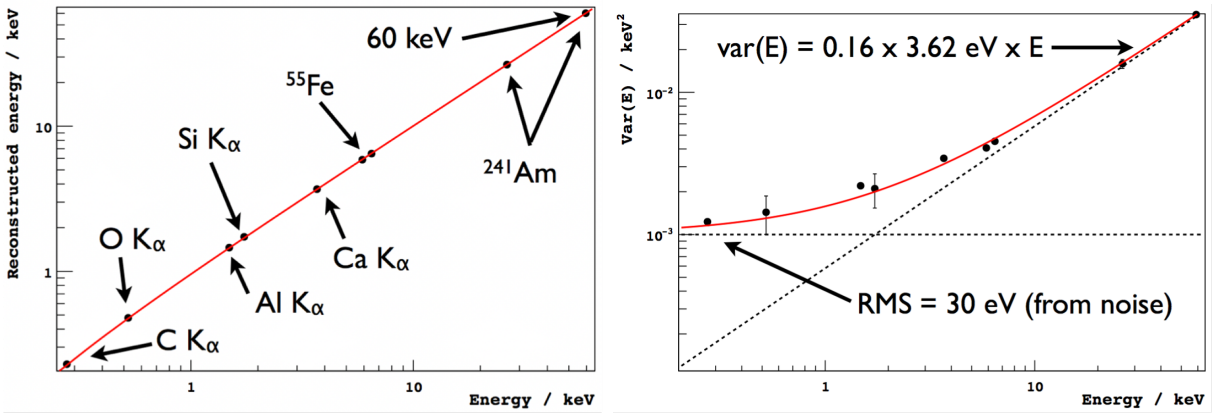

Figure 3.5: Left: linearity of the energy response of a DAMIC CCD. The reconstructed energy of an X-ray line compared to its true energy is shown. Labels corresponding to ^{55}Fe and ^{241}Am emission energies are shown; additional labeled markers correspond to fluorescence lines from elements in the Kapton and other materials in the CCD setup previously described. Linearity in the measurement of ionization energy is demonstrated from 0.3 keV$_{\rm ee}$ to 60 keV$_{\rm ee}$. Right: energy resolution – variance of energy as a function of X-ray energy, with a Fano factor of 0.16, consistent with the value expected for a CCD [34]. Figures taken from Ref. [59].

Moreover, electron recoils produced by γ rays from ^{57}Co and ^{241}Am radioactive sources were measured between 60 eV and 4 keV using a setup at the University of Chicago [60], enabling the study of ionization signals down to a 15 e^- equivalent. The low-energy spectra obtained by a DAMIC-style 4k×2k CCD from Compton scattering of γ rays in bulk silicon agreed with theoretical predictions: in particular, the features agreed down to the level of the binding energies of different atomic shells within the silicon lattice (see Fig. 3.6).

Regarding ionization induced by nuclear recoils: at low energies, the ionization energy produced through silicon recoils mostly disperses through atomic collisions; at high recoil energies, we approach a case where the ionization energies closely resembles that of an electron with the same energy. Investigations by the DAMIC collaboration explored nuclear recoil ionization efficiency, key in determining the sensitivity of dark matter experiments [62]. By studying CCD response to ionization generated by nuclear recoils between 0.7 and 2.3 keV$_{\rm nr}$ (a range previously unexplored), the measured efficiency was noted to significantly

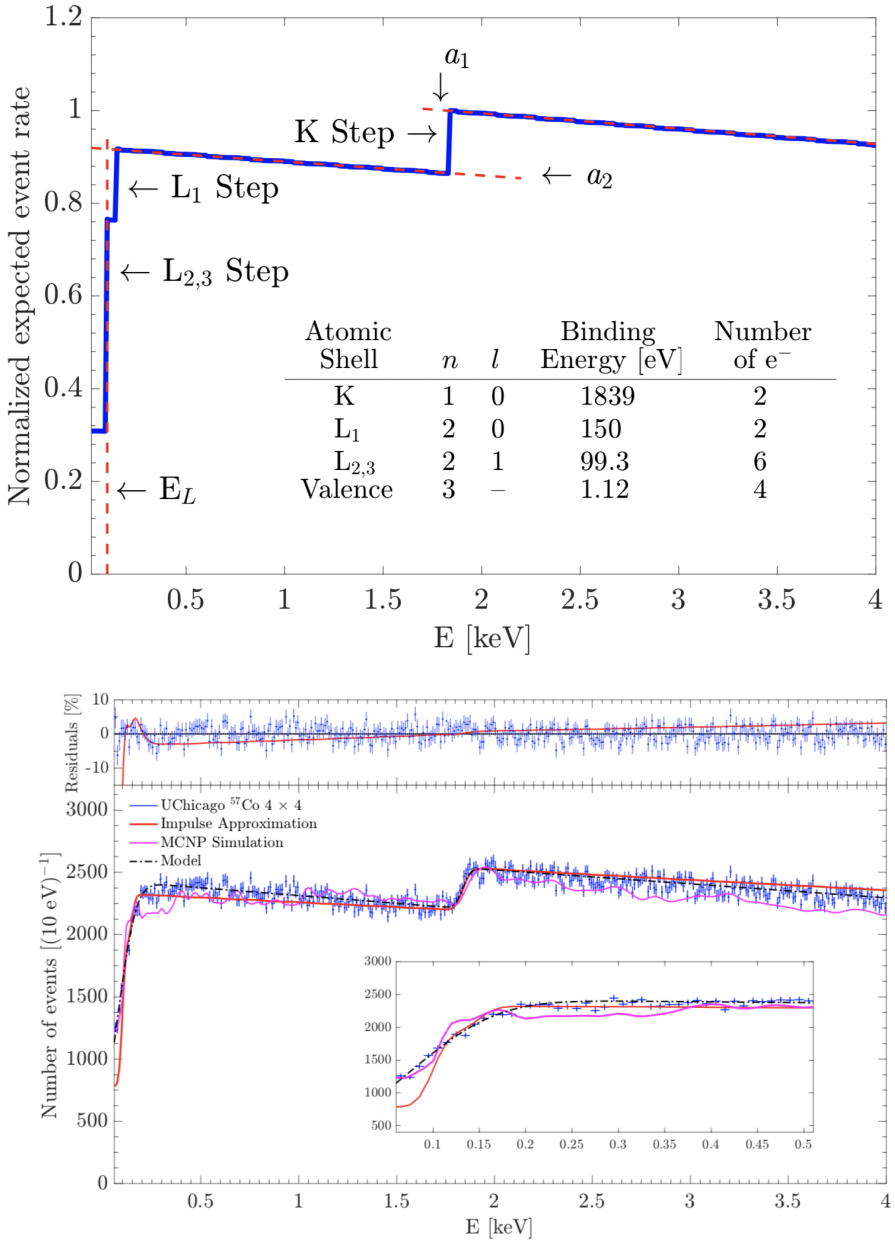

Atomic Shell	n	l	Binding Energy [eV]	Number of e$^-$
K	1	0	1839	2
L_1	2	0	150	2
$L_{2,3}$	2	1	99.3	6
Valence	3	–	1.12	4

Figure 3.6: Top: Computed low-energy spectrum from Compton scattering of 122 keV γ rays in silicon (a_1, a_2, and E_L are defined in Ref. [60] and used to parametrize the model of the Compton spectra at low energies). The steps seen in the spectra are at the binding energies of the different atomic shells. Bottom: Measured low-energy Compton spectra acquired by a 4k×2k CCD using 4×4 binning – the source used to produced this spectrum was ^{57}Co, which has a 122.0607 keV highest-intensity decay [61]. Spectra from MCNP simulations and analytic approximations are also shown. Figures taken from Ref. [60].

deviate from values expected after extrapolation of the Lindhard model [63] (usually used in sensitivity projections) to low energies. This study demonstrated that by using the Lindhard model in this way, the sensitivity at the lowest WIMP masses is overstated. This work and that of the Compton measurement can be expanded by deploying the Skipper CCDs described in later chapters: at the time of writing, first results on the measurement of Compton scattering on silicon atomic shell electrons with Skipper CCDs have been presented [64].

Leakage (Dark) Current

Leakage current was introduced in Chapter 2 as the small current that flows intrinsically in semiconductors through thermal generation of minority carriers. It is broadly the shot noise produced from spurious charge, and can come from numerous sources including light leaks, mechanical stress on CCDs due to packaging or thermal cycling leading to expansion/contraction of silicon, and CCD clocking. In the context of the DAMIC and DAMIC-M experiment, where the CCDs are operated in a non-optical way, leakage current can be used interchangeably with *dark current*. As previously discussed, quantifying and reaching low levels of dark current is critical to achieving the highest performance of detectors.

Quantifying the depletion bulk dark current can be done after images are processed through pedestal subtraction, masking high energy clusters, and computing the median image scaled by calibration constants (this image processing follows the procedure previously summarized). The mean of a Gaussian fit to the pixel charge distribution then corresponds to the leakage current per image, which can be converted into units of e^-/pix/d since the exposure and readout time of the images are known. For 1×100 binning, we expect an offset in the mean pixel values between the first 42 rows (active region of DAMIC at SNOLAB CCDs) and subsequent rows (y-overscan). The charge drop-off at the y-overscan corresponds to the leakage current. This can be seen in Fig. 3.7, taken from Ref. [65]. The non-linear

behavior observed in CCD 2 (EXT 2) and CCD 7 (EXT 12) could be due to a small amount of light, since these CCDs are at the edges of the tower and would be more prone to a leak. Moreover, this approach to analyzing leakage current was executed across all CCD extensions for a full temperature sweep, giving an approximately log-linear relationship between the two [53].

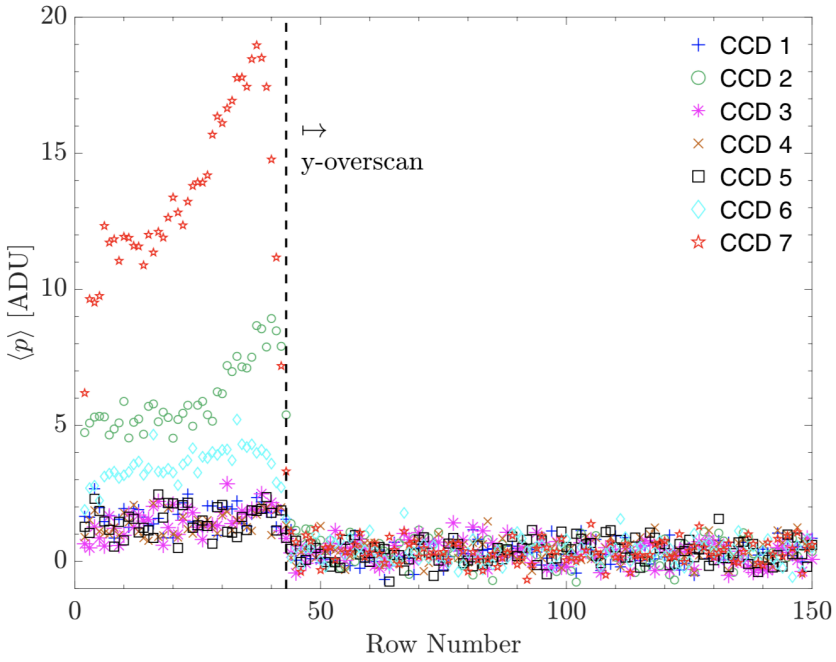

Figure 3.7: Mean pixel values ($\langle p \rangle$) as a function of CCD row. The start of the y-overscan is marked by the dashed line. Taken from Ref. [65].

Lattice imperfections and impurities within the bulk silicon or oxide interface of the CCD generate dark current carriers by introducing energy steps that are otherwise forbidden within the bandgap. These steps enable *hopping conduction* [34], or additional generation and recombination processes that lead to dark charge. The processes of generation and recombination are described by the Shockley/Hall/Read equation [34]:

$$U = \frac{\sigma_h \sigma_p v_{th} (pn - n_i^2) N_T}{\sigma_h \left[h + n_i exp(\frac{E_t - E_i}{kT}) \right] \left[p + n_i exp(\frac{E_i - E_t}{kT}) \right]} \tag{3.4}$$

where U is the net carrier generation/recombination, N_T is the concentration of traps at the energy level E_t, $E_t - E_i$ is the energy of the defect level relative to the intrinsic Fermi level (E_i), n, p are the number of free electrons, holes, respectively, $\sigma_{h,p}$ are electron and hole cross sections, and k is the Boltzmann constant.

As outlined in Chapter 2, there is not thermal equilibrium under the condition of depletion of majority carriers, and the corresponding electric field in this condition separates dark current electrons and holes. This state corresponds to $p = n = 0$, and has a carrier-generation rate in the depletion region U_{DEP} given by:

$$U_{DEP} = \frac{\sigma v_{th} n_i N_B}{2cosh\left[\frac{E_i - E_t}{kT}\right]} \tag{3.5}$$

$$U_{DEP} = \frac{n_i}{2\tau_{DEP}} \tag{3.6}$$

Here, N_B is the bulk state density.

The relation of Eq. 3.5 can be integrated over energy for a given N_B, and for energies over 1.2 eV (i.e. for silicon) we arrive at a value approaching $\pi/2$. This reduces our relation to that of Eq. 3.6, allowing us to define the *carrier lifetime* (τ_{DEP}), or the average time it takes to thermally generate an electron-hole pair. We use Eq. 3.6 to extract the overall expected dark current in a single pixel volume (λ), multiplying by the depletion depth and pixel area. Ref. [34] further demonstrates that this pixel-volume dark current rate is $\propto T^{3/2}$. DAMIC CCDs have the lowest dark current ever measured in a semiconductor detector: 2-6 $\times 10^{-22}$ A/cm^2 at an operating temperature of 105 K [65].

The study of leakage (dark) current will be revisited in later chapters discussing the characterization of Skipper CCDs. The following sections and chapter will outline key analysis results from DAMIC at SNOLAB, which leverage unique features of these CCDs, including the aforementioned extremely low level of leakage current.

3.3 Light Dark Matter Searches: Results from the DAMIC at SNOLAB Experiment

3.3.1 Constraints on Light Dark Matter Particles Interacting with Electrons

By exploiting the extremely low levels of leakage current of the DAMIC at SNOLAB detector and interpreting dark current as induced by LDM, we are able to place significant constraints on LDM (sub-GeV) interacting with electrons as well as limits on hidden-sector particles ("dark," or "hidden"-photons) [65]. As mentioned in Chapter 1, hidden-sector particles – ones that couple weakly with ordinary matter through (for example) a mixing of a hidden-photon with an ordinary photon – are promising candidates beyond the WIMP paradigm.

The work in Ref. [66] provides the differential event rate for dark matter of mass m_χ for a detector in which the crystalline band structure and bound nature of electrons are accounted for:

$$\frac{dR}{dE_e} \propto \bar{\sigma_e} \int \frac{dq}{q^2} \eta(m_\chi, q, E_e) |F_{DM}(q)|^2 |f_c(q, E_e)|^2 \tag{3.7}$$

where $\bar{\sigma_e}$ is the reference cross section for free electron scattering, η describes astrophysical parameters for the incident flux of galactic dark matter particles, F_{DM} is the dark matter form factor, and $f_c(q, E_e)$ quantifies the atomic transitions of bound-state electrons.

The following parameters were used for the calculation of η: a dark matter density $\rho_{DM} = 0.3$ GeV/c^2, an isothermal Maxwellian velocity distribution with escape velocity $v_{esc} = 544$ km/s and mean velocity $v_0 = 220$ km/s, and periodic Earth motion of mean velocity $v_E = 232$ km/s. The dark matter form factor expresses the momentum-transfer dependence of the interaction and is described as $F_{DM} = (\alpha m_e/q)^n$ $\{n = 0, 1, 2\}$, where $n = 0$ corresponds to point-like interactions with heavy mediators or a magnetic coupling,

$n = 1$ to electric dipole coupling, and $n = 2$ to massless or ultra-light mediators. The crystal form factor contains target material properties specficially for silicon and is numerically derived using a density functional theory approach in Ref. [66]. The ionization rate of Eq. 3.7 was discretized into $\frac{dR}{dn_e}$, where n_e is the number of ionization charges.

A 2017 data set was used for this analysis, consisting of 38 images with 100 ks exposure time, 1×100 binning, and noise $\sigma_{\text{pix}} \approx 1.6\text{e}^-$. Hot pixels and clusters with signals above $8\sigma_{\text{pix}}$ were masked: since this analysis relies on assuming LDM interactions produce dark current in order to place limits below DAMIC's effective clustering threshold, then it becomes necessary to mask the aforementioned clusters. The image processing leakage current extraction was done using the methodology previously described in Sec. 3.2; in fact, Fig. 3.7 shows the mean pixel values and y-overscan for the exact data set of this analysis. The CCDs mentioned to have higher leakage current (CCDs 2, 6, and 7) were excluded from this search, giving a total equivalent exposure of 200 g d.

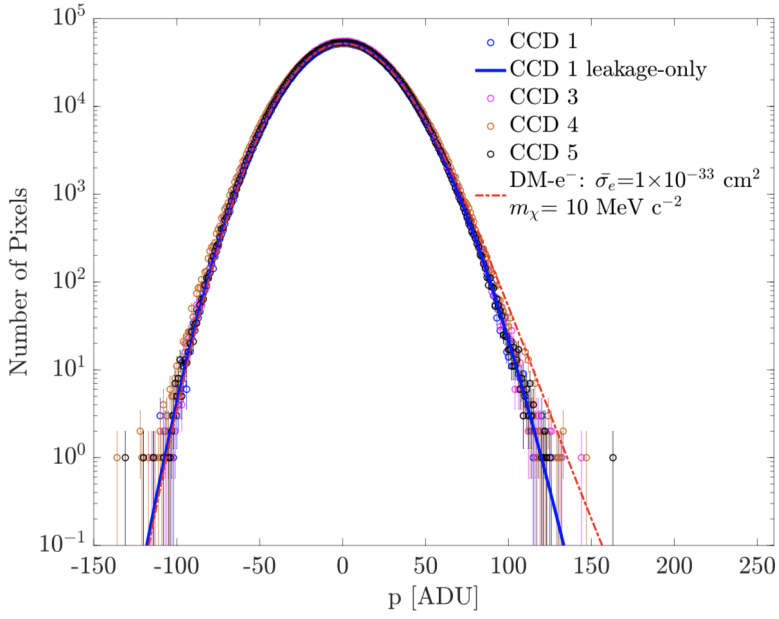

Figure 3.8: Pixel value distributions for DAMIC CCDs used to search for light dark matter interacting with electrons. Models for CCD 1 leakage-only and DM-e$^-$ are also shown.

The pixel value distributions for the four remaining CCDs used can be seen in Fig. 3.8 with a calibration constant of ≈ 14.5 ADU/e$^-$, and including the best fit result for the leakage-only model of CCD 1 as well as the expectation for a DM-e$^-$ model with $\bar{\sigma_e} = 1 \times 10^{-33}$ cm^2, $m_\chi = 10$ MeV/c^2, and $F_{DM} = 1$. These distributions are modeled by a function that convolves the pixel charge distribution with the pixel readout noise:

$$\Pi(p) = N \sum_{n_{tot}=0}^{\infty} \Big(\Big[\sum_{j=0}^{n_{tot}} S(j|\bar{\sigma_e}, m_\chi) \mathrm{Pois}(n_{tot} - j|\lambda_{tot}) \Big] \mathrm{Pois}(n_l|\lambda_d) \mathrm{Gaus}(p|\Omega[n_{tot}+\mu_0], \Omega\sigma_{\mathrm{pix}}) \Big) \tag{3.8}$$

The pixel charge distribution is the sum of spatially-uniform, Poission-distributed leakage current λ collected during image exposure and the DM signal $S \equiv S(j|\bar{\sigma_e}, m_\chi)$, which is the probability to produce j charges in a pixel from DM interactions. The pixel readout noise is described by the convolution of a Poisson (λ_d mean) and Gaussian (σ_{pix} standard deviation) across distributions of overscans and blanks (images of ≤ 30 s exposure data images).

N is the number of pixels in the data set, $n_{tot} = n_c + n_l$ (n_c is the number of charges in a pixel from a DM signal, n_l is the number of charges in a pixel from readout shot noise), Ω is the previously cited calibration constant, $\lambda_{tot} = \lambda + \lambda_d$, and μ_0 is the offset from pedestal subtraction. The DM signal is computed from Eq. 3.7, and the effect of diffusion in CCDs is included as described by Ref. [65]. The DM signal is constrained by using a likelihood in the $(\bar{\sigma_e}, m_\chi)$ space: namely, for every CCD i the negative log-likelihood $\mathcal{LL}_i$ of $\Pi(p)$ is minimized while leaving λ_{tot} as a free parameter. Non-zero values of $\bar{\sigma_e}$ are preferred for DM masses above a few MeV/c^2, potentially due to imperfect modeling of extreme tails of the noise distribution. Conservative limits are placed when the minimum log-likelihood ($\mathcal{LL}_{min}$) is found at a non-zero value of $\bar{\sigma_e}$: 90% C.L. constraints are obtained on $\bar{\sigma_e}$ for each m_χ using the statistic $2(\mathcal{LL} - \mathcal{LL}_{min})$. Moreover, limits on hidden-photon dark matter were extracted using analogous methodology to that described here. The previous limits in

Ref. [67] were improved using the lower leakage current λ of this data set. We obtained the 90% C.L. upper limits on the kinetic mixing parameter k as a function of hidden-photon mass m_ν. DAMIC has established the best direct-detection limits on DM-e$^-$ scattering in the mass range 0.6-6 MeV/c^2, and the best direct-detection constraints on hidden-photon dark matter in the mass range 1.2-9 eV/c^2 (Fig. 3.9).

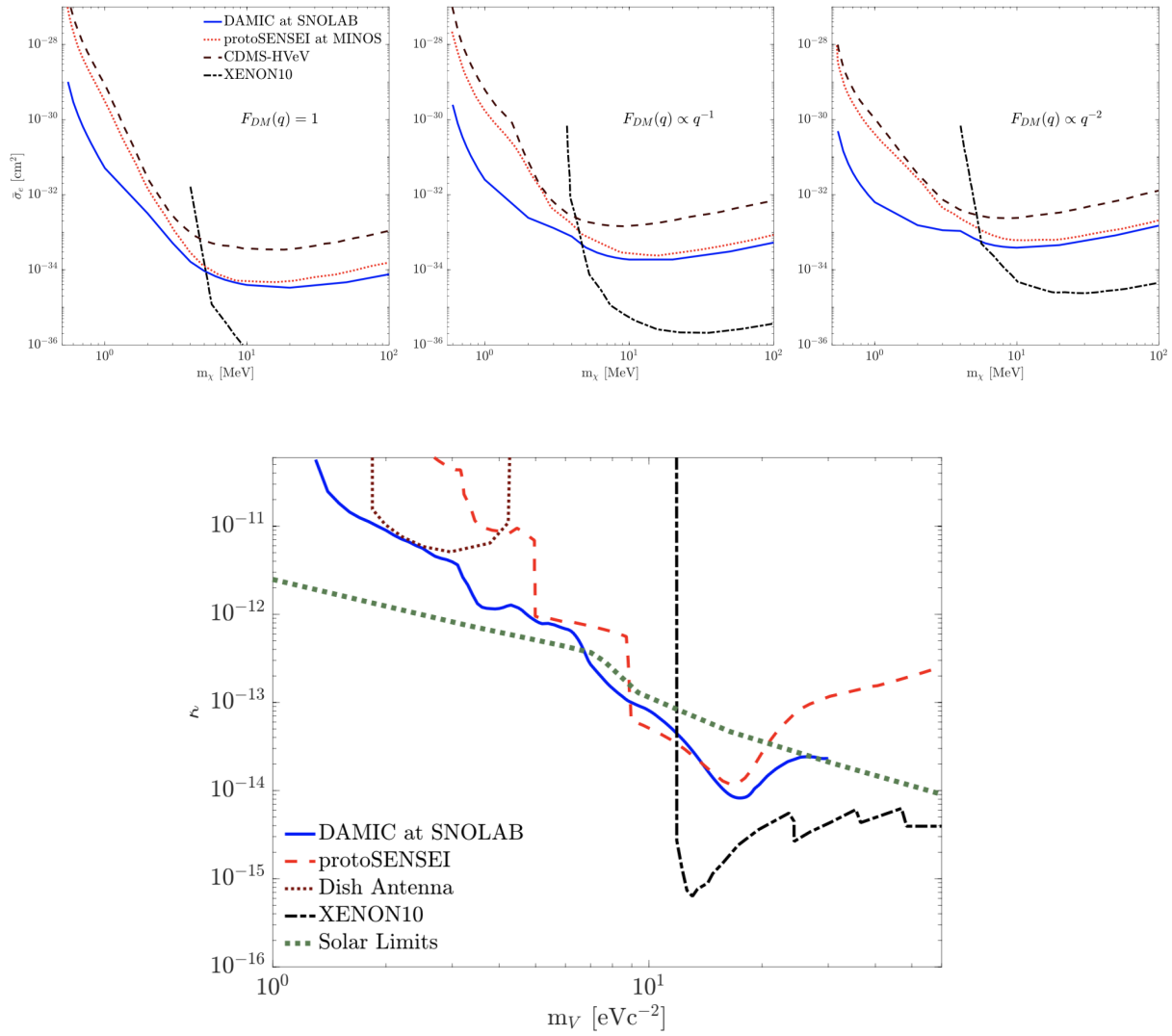

Figure 3.9: Top: 90% C.L. upper limits on the DM-e$^-$ free scattering cross section $\bar{\sigma}_e$ vs. DM mass m_χ. Bottom: 90% C.L. upper limits on the hidden-photon DM kinetic mixing parameter k vs. hidden-photon mass m_ν. Comparison limits [68]-[74] are also shown.

3.3.2 WIMP Search from an 11 kg-day Target Exposure

WIMPs were introduced in Chapter 1: the paradigm of WIMPs remains one of the most compelling explanations for the existence of of dark matter. Such WIMPs would scatter elastically with nuclei to produce nuclear recoils, and the DAMIC experiment at SNOLAB has executed extensive campaigns to search for such dark matter candidates [32][31]. The low noise of CCDs and low mass of the silicon nucleus imply that DAMIC is especially sensitive to WIMPs with masses m_χ in the range 1-10 GeV/c^2. It also enabled the exploration of the same parameter space with the same target material as the CDMS collaboration, who observed an event excess corresponding to $m_\chi \sim 9$ GeV/c^2 [75].

As previously mentioned, DAMIC WIMP search data was acquired between 2017-2018 using 7 CCDs read out in the 1×100 mode, initially with 100 ks exposures, later changed to 30 ks for reduced leakage current. Any images with poor quality due to visible transients from leakage current or visible noise patterns, as well as images taken with cryostat radon levels > 5 Bq/m^3, were discarded. The final data set consisted of 5607 images together with corresponding blanks (in this analysis defined as zero-exposure-time images that only have their effective exposure come from a 130 s readout), equivalent to 308.1 d. Image processing followed steps summarized in Sec 3.2 and detailed further in Ref. [32].

For low-energy events, the ionization range of particles is smaller than the DAMIC CCD pixel size, meaning diffusion dominates the charge distribution. Given the readout mode, the subsequent pattern is well-described by a Gaussian along a row with amplitude proportional to energy E, with μ_x corresponding to the x position of the interaction, and σ_x denoting the spatial width in $\hat{x}$. Clustering was done using the fast and likelihood algorithms, and σ_x and the z coordinate of interactions were related by the diffusion model outlined earlier in this chapter. A radioactive background model was constructed using `GEANT4` simulations [76], with fast clustering applied and outputs grouped into 49 templates based on decay type or material. More details of this background model will be discussed in the next section.

A 2-D binned Poisson likelihood fit was performed between 6-20 keV_{ee} (excluding the 7.5-8.5 keV_{ee} range due to the K-shell line from copper fluorescence) on data from CCDs 2-7 with simulated (E, σ_x) templates, maintaining CCD 1 as a cross-check. The fit results for all CCDs combined and projected onto E and σ_x dimensions are shown in Fig. 3.10.

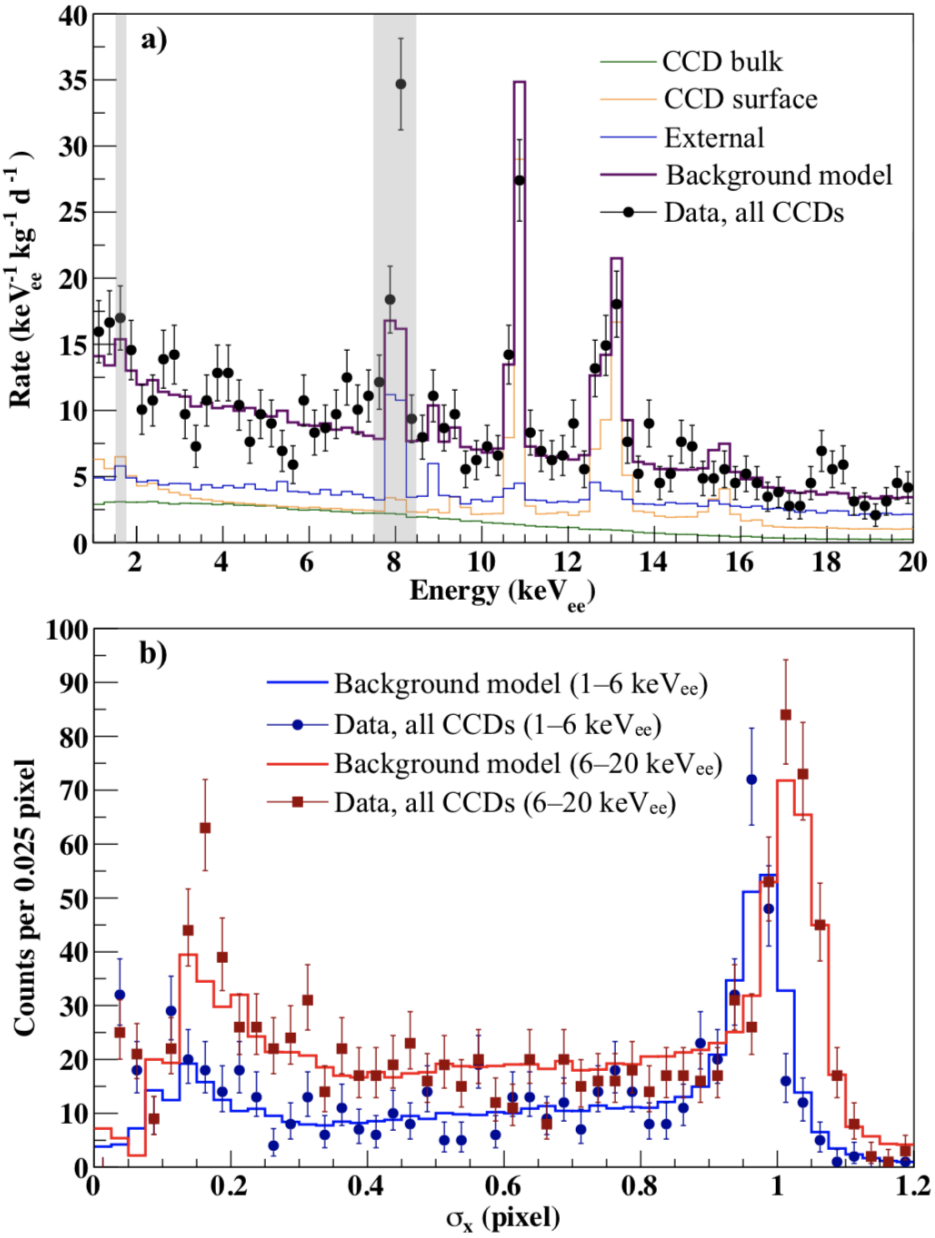

Figure 3.10: Projections in E, σ_x of the best-fit background model (solid lines) compared to fast-clustered data (markers); fit shown for 6-20 keV_{ee} and extrapolated to 1-6 keV_{ee} [31].

The background model was consistent with the observed spectra in CCDs 2-7 and correctly predicted the expected lower background of CCD 1. It extracted components of interest, including surface ^{210}Pb due to radon exposure, a bulk component driven by ^{3}H and ^{22}Na from cosmogenic activation and ^{32}Si from intrinsic decays, and energetic photons/electrons external to the CCD. A major systematic uncertainty in this analysis came from a $\sim 5\,\mu$m partial charge collection (PCC) region in the back of the CCDs.

The likelihood clustering output was used to search for event excess beyond predictions by the background model for 0.05-6 keV$_{\rm ee}$; the final target exposure was 10.93 kg d. Detection efficiency of ionization events as a function of energy was obtained via Monte Carlo simulations and validated with γ-ray calibration data: the acceptance plateaus at 90% above 120 eV$_{\rm ee}$. Probability density functions in (E, σ_x) were generated from images with simulated events sampled from templates of the background model and an additive correction for the PCC region. Clusters from CCD 1 and 2-7 were considered as independent data sets with independent background PDFs, and processed separately using a 2D (E, σ_x) unbinned extended likelihood function:

$$\begin{aligned} \log\mathcal{L}_{s+b}(s,b,M|\vec{E}) &= -(s+b) + \sum_{i=1}^{N} log(s\, f_s((E_i|M) + b\, f_b(E_i)) \\ \log\mathcal{L}_{s+b}(s,b,M|\vec{E},\vec{\sigma_{xy}}) &= -(s+b) + \sum_{i=1}^{N} log(s\, f_s((E_i,\vec{\sigma_{xyi}}|M) + b\, f_b(E_i,\vec{\sigma_{xyi}})) \end{aligned} \tag{3.9}$$

where the top line is the likelihood function predicated on the energy spectra data, and the bottom is the 2D likelihood using the joint PDFs of energy and spatial spread; s and b are the expected number of signal and background events, M is the WIMP mass, $f_s((E_i,\vec{\sigma_{xyi}}|M)$ is the probability that the given energy (E_i) and spread of an event (σ_{xyi}) being a WIMP of mass M, and and f_b is the probability an event is background. Both f_s and f_b capture spectra and location information (e.g. of surface vs. bulk background decays) of WIMP and background distributions. Distributions were scaled by the expected WIMP spectrum.

We estimate the detection of a WIMP signal by defining a test statistic $q = \max\{\mathcal{L}_{\text{free}}\} - \{\mathcal{L}_{\text{restricted}}\}$ [32], where the free log likelihood has no constraints on s or b, and the restricted case requires $s = 0$ (i.e. the null hypothesis). The extent of the difference between the two indicates the likelihood of measuring a WIMP signal. To set the limit, we iterate through WIMP masses and values of s in the restricted likelihood until a signal would be seen with 90% C.L., and set the WIMP-nucleon cross section, $\sigma_{\chi-n}$, based on how many signal events were required. Our best fit exhibited a preference for an exponential bulk component with $s = 17.7 \pm 7.6$ events. Limited statistics and possible unidentified inaccuracies in the detector background model prevent a definite interpretation of this event excess. Fig. 3.11 shows the 90% C.L. upper limit obtained for spin-independent coherent WIMP-nucleus elastic scattering, with a $\pm 1\sigma$ expectation band extracted from running the limit-setting procedure on Monte Carlo data sets drawn from the best-fit background model. The exclusion limit is the most stringent from a silicon DM experiment for WIMPs with $m_\chi < 9$ GeV/c^2.

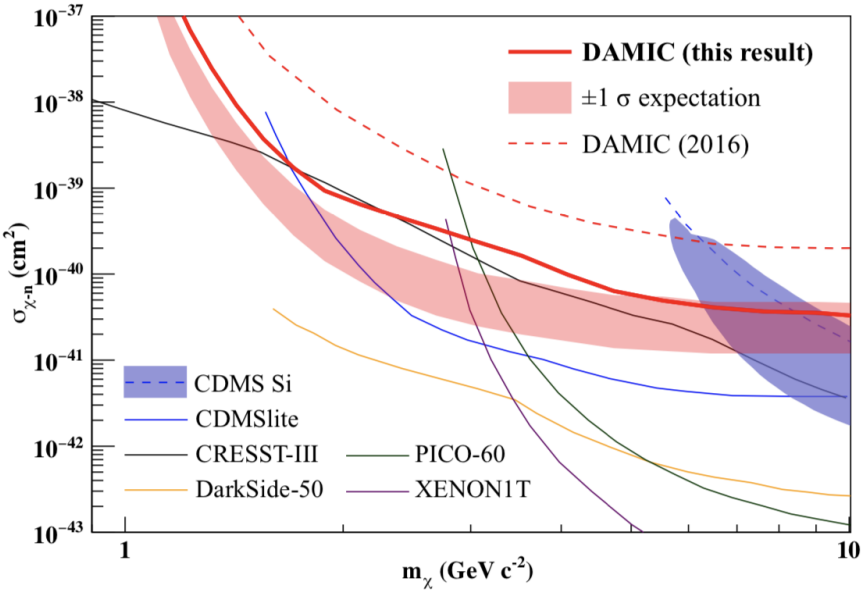

Figure 3.11: DAMIC upper limit (90% C.L.) on $\sigma_{\chi-n}$ ($\pm 1\sigma$ band shown for only known backgrounds). Previous DAMIC [32] and other experiments' limits [77] are shown.

3.3.3 A Radioactive Background Model for DAMIC at SNOLAB

Note: the following section is based on a paper of which I am a contributing author; it is being prepared for journal submission at the time of writing.

The previous section eluded to the necessity for a more detailed background model in order to better describe our detector. This section provides detail on the construction of the first comprehensive radioactive background model for a dark matter search with CCDs. By using the well-characterized position and energy resolution of the DAMIC at SNOLAB detector in tandem with extensive `GEANT4` simulations, we model bulk and surface backgrounds from natural radioactivity down to 50 eV_{ee}, and fit energy and space distributions of ionization events to differentiate and constrain background sources. The fiducial background rate and numerous individual background rates will be cited following standard practice of normalizing to units of dru, or counts/day/keV_{ee}/kg.

In this section, we will summarize DAMIC's detector material radiopurity, `GEANT4` simulations, handling the systematic uncertainty due to a partial charge collection (PCC) region in the back of DAMIC CCDs, template fitting of reconstructed simulation outputs, and discussion on the best-fit template and connection to the event excess over the background model mentioned in the previous section. The insights from this work have major implications for strategic improvements of next-generation experiments.

Material Radiopurity

DAMIC at SNOLAB materials were carefully catalogued and assayed for long-lived radioactivity, focusing primarily on the primordial ^{238}U and ^{232}Th chains, but also measuring long-lived ^{40}K in the detector materials. For the ^{238}U chain, we consider the possibility that three different segments of this chain may be out of secular equilibrium on the time-scale of the casting of our detector materials, from ^{226}Ra ($\tau_{1/2} = 1.6$ kyr) and ^{210}Pb ($\tau_{1/2} = 22$ yr). A full list of the assay results of the materials used in the detector can be found in Table 3.2.

	^{238}U	^{226}Ra	^{210}Pb	^{232}Th	^{40}K	^{32}Si
CCD / Si frame	<11 [79]	<5.3 [79]	<160 [79]	<7.3 [79]	<0.5 $^{[M]}$	140 ± 30 [79]
Epotek 301-2						
Kapton Cable	58000 ± 5000 $^{[M]}$	4900 ± 5700 $^{[G]}$	...	3200 ± 500 $^{[M]}$	29000 ± 2000 $^{[M]}$	...
OFHC Copper	<120 $^{[M]}$	<130 $^{[G]}$	27000 ± 8000 [81]	<41 $^{[M]}$	<31 $^{[M]}$	...
Module Screws	16000 ± 44000 $^{[G]}$	<138 $^{[G]}$	27000 ± 8000	2300 ± 1600 $^{[G]}$	28000 ± 15000 $^{[G]}$	...
Box Screws						
Ancient Lead	<23 [52]	<260 $^{[G]}$	33000[52]	2.3[52]	<5.8 $^{[M]}$	...
Outer Lead	<13 [80]	<200 $^{[G]}$	$(19 \pm 5)\times10^{6}$ [80]	<4.6 [80]	<220 [80]	...

Table 3.2: Activities [μBq/kg] used to constrain the radioactivity in each simulated detector part. A superscript M (G) indicates a value measured with mass spectrometry (γ counting).

Many assays were performed using either Inductively-Coupled Mass Spectrometry (ICP-MS) or Glow Discharge Mass Spectrometry (GDMS), techniques that measure the elemental composition of a sample and estimate the activity of a specific isotope from its elemental abundance. Materials constrained by mass spectrometry are indicated as such in Table 3.2 with a superscript$^{[M]}$. Many materials were screened by Germanium γ-ray spectrometry at the SNOLAB γ-ray counting facility [84]. This method non-destructively measures the isotopic abundance from the intensity of specific γ lines from radioactive decays in the sample; materials best-constrained by γ-ray counting are indicated in Table 3.2 with a superscript$^{[G]}$.

Furthermore, some materials are best constrained by measurements published elsewhere. For example, the archaeological lead used in the inner shield and around CCD 1 is from the same batch cited in Ref. [52]. We thus use this measurement to constrain the bulk ^{210}Pb content of our ancient lead sample. Similarly, the XMASS collaboration has presented a robust analysis of the variation of bulk ^{210}Pb content in commercially available OFHC copper [81]. The values used for the low-activity lead of the outer DAMIC shield are described in Ref. [80].

Importantly, for CCD silicon, only the ^{40}K estimate from Secondary Ion Mass Spectrometry (SIMS) is better than the constraints that we can place with the CCDs themselves. Chapter 4 is dedicated to an updated analysis [79] that provides better numbers for many of the long-lived isotopes in our detector and was key constructing the background model.

Parent Chain	Isoptope	Q value
^{238}U	^{234}Th	274 keV
	^{234m}Pa	2.27 MeV
^{226}Ra	^{214}Pb	1.02 MeV
	^{214}Bi	3.27 MeV
^{210}Pb	^{210}Pb	63.5 keV
	^{210}Bi	1.16 MeV
^{232}Th	^{228}Ra	45.5 keV
	^{228}Ac	2.12 MeV
	^{212}Pb	569 keV
	^{212}Bi	2.25 MeV
	^{208}Tl	5.00 MeV
^{40}K	^{40}K	1.31 MeV
Copper	^{60}Co	2.82 MeV
Activation	^{59}Fe	1.56 MeV
	^{58}Co	2.31 MeV
	^{57}Co	836 keV
	^{56}Co	4.57 MeV
	^{54}Mn	1.38 MeV
	^{46}Sc	2.37 MeV
^{32}Si	^{32}Si	227 keV
	^{32}P	1.71 MeV
Silicon	^{22}Na	2.84 MeV
Activation	^{3}H	18.6 keV

Table 3.3: Isotopes (with Q values) considered in this work, grouped by parent decay chain.

Cosmogenic activation also plays a role in detector materials' radiopurity before they were transported underground at SNOLAB. This activation occurs when high-energy cosmogenic neutrons undergo spallation interactions with material nuclei. We considered activation of the silicon CCDs and copper parts (Kapton cables were treated as 50% copper). The activity A of copper parts is described by:

$$A = \frac{S}{\lambda T_{run}}(1 - e^{-\lambda T_{act}})(e^{-\lambda T_{cool}})(1 - e^{-\lambda T_{run}}) \tag{3.10}$$

where λ is the isotope decay constant (see major isotopes considered in Tab. 3.3), S is the saturation activity at sea level, and T_{act}, T_{cool}, and T_{run} are the activation, cooldown, and run times, respectively. The activation (cooldown) times of the DAMIC copper modules, box, and vessel are 8 months, 16 months, and an over-estimate equilibrium assumption of 1000 yrs (540 d, 300 d, and 6.6 yrs), respectively; the run time is 441 d. For cosmogenic activation of silicon: we assume an initial guess for bulk ^{3}H in CCDs of 0.3 mBq/kg but keep that value as a free parameter. Activity of ^{22}Na was constrained at 0.32 ± 0.06 mBq/kg by measuring the 850 $\mathrm{eV_{ee}}$ K-shell peak its daughter ^{22}Ne produces 8.7% of the time when it is in an excited state. Additional material radiopurity components come from surface contamination and neutron backgrounds. The former refers to ^{210}Pb from radon plate-out on detector surfaces. We leave discussion of this to the dedicated work the author led in Chapter 4. The latter were shown to have negligible contributions by dedicated simulations. In particular, the neutron-induced events expected across the entire WIMP search exposure (332.5 d) is an estimated 5.64 ± 0.53 neutrons crossing sensors (3% probability of having had more than 2 recoils), and an estimated 0.1 neutron-induced nuclear recoils expected from reactions in the VIB board.

`GEANT4` Simulations

The `GEANT4` Livermore physics list [76] was used to simulate radioactive background sources, accurate down to 10 eV for electron depositions and 100 eV for photon cross sections. Fig. 3.12 shows a cross-section of the `GEANT4` geometry for the DAMIC at SNOLAB detector, as well as a cross section of a CCD module. The CCD geometry was split for accuracy into simulated sub-regions, guided by the detailed fabrication knowledge reviewed in Chapter 2:

- Bulk: the 669 μm thick active bulk was simulated between two "dead" layers. The z position increases from front ($z < 0\mu$m) to back ($z > 669\mu$m). The total simulated thickness was 674.2 μm,

- Frontside dead layer: the frontside dead layer includes 2.0 μm total of insulator (1.6 μm SiO_2), polysilicon gate electrodes (0.3 μm Si), and gate dielectric (0.1 μm Si_3N_4).

- Backside dead layer: the backside dead layer consists of the ISDP gettering layer (1.0 μm Si), a dielectric layer (0.1 μm Si_3N_4), and three sets of alternating polysilicon (0.4 μm Si each) and silicon dioxide (0.3 μm SiO_2 each) layers, for a total simulated backside thickness of 3.2 μm

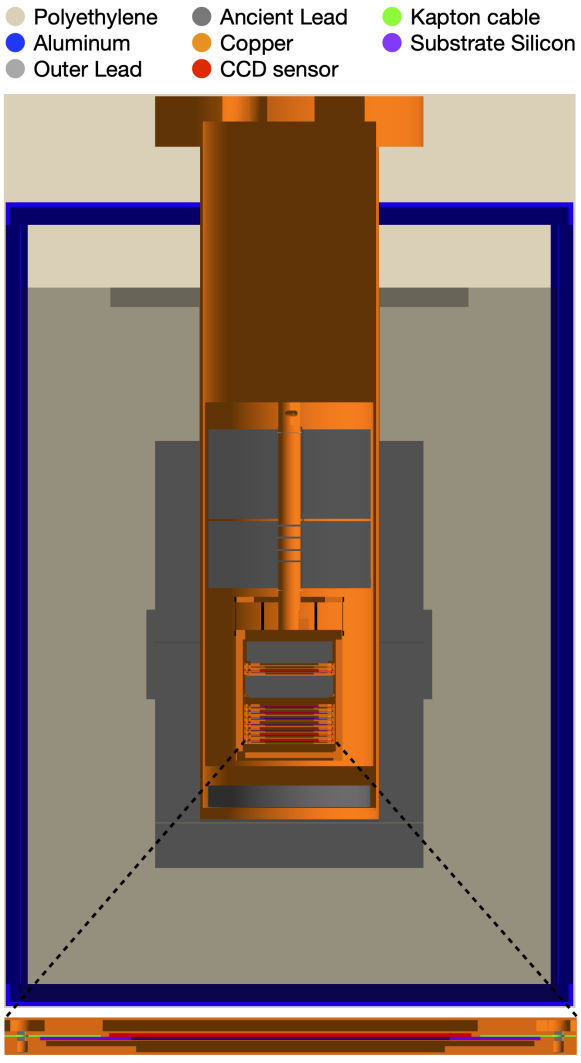

Figure 3.12: Cross-section of `GEANT4` geometry for the DAMIC at SNOLAB detector parts (see legend). A zoomed-in cross-sectional view of a CCD module is also show.

The detector geometry was divided into 64 volumes and grouped into eight detector parts by material origin, summarized in Tab. 3.2, where the OHFC copper is actually sub-divided into the vacuum vessel, copper box, and CCD modules given distinct histories. For each volume, up to 5×10^8 unique β/γ decays were simulated from isotopes that contribute low-energy backgrounds. `GEANT4` outputs the energy and position of each interaction in the CCD detectors. These outputs were processed to match data reconstruction: energy depositions were converted into electron values (assuming 3.77 eV/e$^-$ and a Fano factor $F = 0.129$), fed through the DAMIC diffusion model, projected onto pixel arrays, converted into analogous output from CCD images, rebinned to a 1×100 format with added Gaussian readout noise, and clustered with our fast algorithm. This enabled turning terabytes of simulated data into values including E, σ_x, and x and y positions. Finally, for energy depositions within the PCC region, we assigned a probability based on the depth of interaction that simulated whether an electron would be collected. Let us shift the discussion to detail this PCC region.

Partial Charge Collection

The dominant uncertainty in the response of the DAMIC CCDs is the loss of ionization charge by recombination in the CCD backside. In Chapter 2, we introduced the 1 μm thick ISDP layer that acts as the backside contact: it is heavily doped with phosphorous (P) during fabrication, leading to a transition in concentration from 10^{20} cm^{-3} in the backside contact, where all free charge immediately recombines, to 10^{11} cm^{-3} in the fully-depleted CCD active region, where there is negligible recombination over the free carrier transit time. A fraction of the charge carriers produced by ionization events in this transition region may recombine before they reach the fully-depleted region and are drifted across the substrate to the CCD gates. This partial charge collection causes a distortion in the observed energy spectrum because events occurring on the backside have a smaller ionization signal than they would if they were to occur in the fully-depleted region.

To construct an accurate model of the CCD backside, we performed two measurements (one ~ 2.5 μm deep, the second ~ 7 μm deep) by secondary ion mass-spectrometry (SIMS) of the concentration of different elements (silicon, hydrogen, oxygen, and phosophorous) from the backside of some wafer scraps from the same batch as the DAMIC at SNOLAB CCDs, with results shown in Figure 3.13. Both of these measurements clearly resolve the outermost 1.5 μm polysilicon and silicon-dioxide layers, as well as an unexpectedly high concentration of hydrogen in the 1 μm thick ISDP region. The origin of the hydrogen is unknown, but given the relevant fabircation processes it likely is captured during the deposition of the ISDP in an environment of SiH_4 and PH_3 gasses. The hydrogen may contains trace levels of radioactive tritium, expected to have activities in the ISDP on the order of 0.1–3.1 mBq/kg.

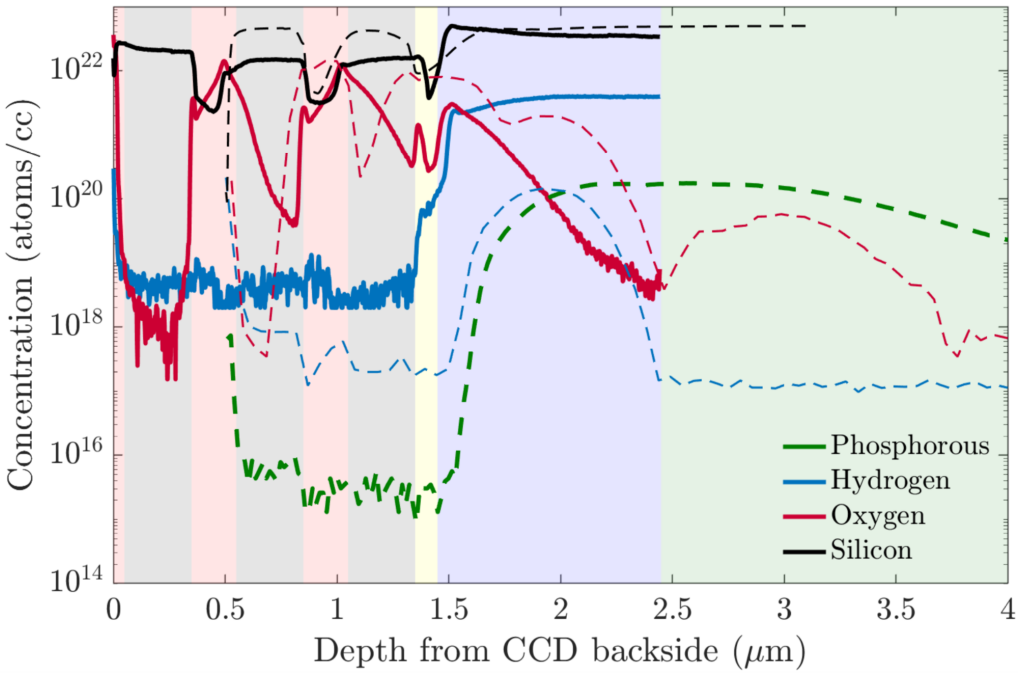

Figure 3.13: SIMS results of the CCD backside: elemental concentrations of oxygen (red), phosphorous (green), and hydrogen (blue) as a function of depth, with silicon (black) for reference. Two different measurements using fine (solid) and coarse (dashed) beam widths are shown, which probe different depths into the CCD. The backside layer structure is clearly visible. Shaded areas from left to right: alternating SiO_2 (red) and polysilicon (grey) layers, Si_3N_4 (yellow), ISDP gettering layer (blue), and high-resistivity n-type crystalline silicon (green).

The SIMS results show that the transition in P concentration occurs over a distance of ≈ 8 μm. The P concentration determines the transport properties of the free charge carriers and the electric field profile, which control the fraction of charge carriers that survive recombination. The location and profile of the PCC region has as significant impact on the spectral shape of radioactive decays originating on the backside of the CCDs, specifically ^{210}Pb decays. Work is ongoing to quantify the systematic uncertainty that the PCC introduces in our background model, but current efforts to parametrize the PCC describe the spectral differences between nominal and varied cases well, worsening above ~ 1 keV, negligible given the statistical uncertainty of the WIMP search measured spectrum.

The DAMIC Background Model

The simulations for each isotope-volume were transformed for template fitting against data in (E, σ_x) space, with 49 templates constructed after grouping by material. A sub-component of the data not used for the WIMP search was dedicated to this analysis. We implemented a custom binned log-likelihood fit: for each 0.25 keV energy bin i and 0.025 pixels bin j, the observed events k_{ij} is compared against the expected number of events from simulation ν_{ij}. We assume the probability of observing k_{ij} events in a bin given an expectation of ν_{ij} is a Poissonian process. The 2D log likelihood is calculated to be the sum over all energy and sigma bins for this probability distribution:

$$LL_{2D} = \sum_i \sum_j \left(k_{ij} \log(\nu_{ij}) - \nu_{ij} - \log(k_{ij}!) \right). \tag{3.11}$$

In cases where $k > 100$, we apply Sterling's approximation such that $\log(k!) \approx k \log(k) - k$. We minimize the total negative log-likelihood including some number n of nuisance

parameters according to:

$$LL_{total} = LL_{2D} - \sum_n \frac{(N_n^0 - N_n)^2}{2\sigma_n^2}, \tag{3.12}$$

where N_n^0 is the expected value of the n^{th} nuisance parameter with uncertainty σ_n, and N_n is the best fit value. The number of expected events ν_{ijl} in bin (i, j) from template l was found by summing over each binned simulation output multiplied by the corresponding activity, the mass of the material simulated, the efficiency-corrected exposure of the data, and divided by the efficiency-corrected number of decays simulated. The normalization of each template l is handled as a fit parameter with a scaling factor C_l: $\nu_{ij} = \sum_l C_l \nu_{ijl}$. Each simulated decay chain in each detector part gets its own scaling factor which simultaneously applies to all (E, σ_x) bins in that template. We fit the combined 2D spectra for CCDs 2–7 and compare the result against CCD 1 as a check. We provide a list of best fit scaling factors C_l for each template in Table 3.4, along with calculated differential rates in different energy ranges. Furthermore, the previously mentioned bulk event excess was found to reasonably match an exponential profile in decaying energies described by systematic uncertainties.

The background model showed dominant contributions from bulk ^{3}H and surface ^{210}Pb, including the original wafer surface embedded $\sim 2.5\,\mu$m beneath the backside layer. The ^{3}H contribution can be cross-checked based on the exposure history of the CCDs, and adjusted for the diffusion of ^{3}H during high-temperature fabrication processes [78]. It was determined that it will be essential to remove the $\sim 8\,\mu$m PCC region for future low-background experiments, which could also help remove the ISDP layer that was found to contain levels of hydrogen (and corresponding ^{3}H). For ^{210}Pb: this work provided an independent check of its activity relative to the methodology of Chapter 4. It confirmed the need for novel methods of handling CCDs and detector materials, by employing extensive shielding or growing certain materials underground. There is a need for low-background facilities with new, stringent protocols. We will revisit this in discussing DAMIC-M and its prototype in Chapter 7.

	Detector Part	Chain	C_l	Best Fit Activity	Rate (dru): CCDs 2–7 1–6 keV	6–20 keV	Rate (dru): CCD 1 1–6 keV	6–20 keV
1	CCD	^{238}U	0.897	$\lesssim 9.86$ μBq/kg	0.01	0.01	< 0.01	0.01
2	CCD	^{226}Ra	0.900	$\lesssim 4.79$ μBq/kg	0.01	0.01	< 0.01	< 0.01
3	CCD	^{232}Th	0.900	$\lesssim 6.56$ μBq/kg	0.01	0.03	0.01	0.02
4	CCD	^{40}K	0.910	$\lesssim 0.42$ μBq/kg	< 0.01	< 0.01	< 0.01	< 0.01
5	CCD	^{22}Na	1.066	340 ± 60 μBq/kg	0.17	0.16	0.10	0.09
6	CCD	^{32}Si	1.042	150 ± 30 μBq/kg	0.20	0.17	0.15	0.13
7	CCD	^{3}H	1.131	330 ± 90 μBq/kg	2.87	0.87	2.39	0.74
8	CCD (front surf.)	^{210}Pb	1.658	69 ± 12 nBq/cm^2	1.51	1.63	0.53	0.91
9	CCD (back surf.)	^{210}Pb	$< 10^{-4}$	< 0.1 nBq/cm^2	< 0.01	< 0.01	< 0.01	< 0.01
10	CCD (wafer surf.)	^{210}Pb	1.343	56 ± 8 nBq/cm^2	2.52	1.83	2.03	1.23
11	Copper Box	^{238}U	0.900	$\lesssim 110$ μBq/kg	0.01	0.01	< 0.01	< 0.01
12	Copper Box	^{226}Ra	0.900	$\lesssim 120$ μBq/kg	0.19	0.16	0.03	0.03
13	Copper Box	^{210}Pb	0.380	10 ± 6 mBq/kg	0.33	0.25	0.01	0.01
14	Copper Box	^{232}Th	0.900	$\lesssim 36$ μBq/kg	0.08	0.07	0.01	0.01
15	Copper Box	^{40}K	0.900	$\lesssim 28$ μBq/kg	< 0.01	< 0.01	< 0.01	< 0.01
16	Copper Box	Act.	1.015	various	0.63	0.51	0.10	0.09
17	Copper Modules	^{238}U	0.900	$\lesssim 110$ μBq/kg	0.05	0.04	< 0.01	< 0.01
18	Copper Modules	^{226}Ra	0.900	$\lesssim 120$ μBq/kg	0.21	0.17	< 0.01	< 0.01
19	Copper Modules	^{210}Pb	0.557	15 ± 4 mBq/kg	1.22	0.89	< 0.01	< 0.01
20	Copper Modules	^{232}Th	0.900	$\lesssim 36$ μBq/kg	0.10	0.08	< 0.01	< 0.01
21	Copper Modules	^{40}K	0.900	$\lesssim 28$ μBq/kg	< 0.01	< 0.01	< 0.01	< 0.01
22	Copper Modules	Act.	1.006	various	0.30	0.24	0.01	0.01
23	Kapton Cable	^{238}U	1.016	59 ± 5 mBq/kg	0.52	0.32	0.24	0.13
24	Kapton Cable	^{226}Ra	1.362	7 ± 5 mBq/kg	0.24	0.19	0.05	0.04
25	Kapton Cable	^{232}Th	1.010	32 ± 0.5 mBq/kg	0.17	0.13	0.04	0.03
26	Kapton Cable	^{40}K	1.003	29 ± 2 mBq/kg	0.09	0.06	0.04	0.02
27	Kapton Cable	Act.	1.000	various	0.01	0.01	< 0.01	< 0.01
28	Ancient Lead	^{238}U	0.911	$\lesssim 21$ μBq/kg	< 0.01	< 0.01	< 0.01	< 0.01
29	Ancient Lead	^{226}Ra	0.900	$\lesssim 230$ μBq/kg	0.45	0.36	0.21	0.21
30	Ancient Lead	^{210}Pb	1.000	~ 33 mBq/kg	0.04	0.03	0.24	0.19
31	Ancient Lead	^{232}Th	1.000	~ 2.3 μBq/kg	< 0.01	< 0.01	< 0.01	< 0.01
32	Ancient Lead	^{40}K	0.916	$\lesssim 5.3$ μBq/kg	< 0.01	< 0.01	< 0.01	< 0.01
33	Outer Lead	^{238}U	0.916	$\lesssim 12$ μBq/kg	< 0.01	< 0.01	< 0.01	< 0.01
34	Outer Lead	^{226}Ra	0.909	$\lesssim 190$ μBq/kg	< 0.01	< 0.01	< 0.01	< 0.01
35	Outer Lead	^{210}Pb	1.000	18 ± 5 Bq/kg	< 0.01	< 0.01	< 0.01	< 0.01
36	Outer Lead	^{232}Th	0.907	$\lesssim 4.2$ μBq/kg	< 0.01	< 0.01	< 0.01	< 0.01
37	Outer Lead	^{40}K	0.906	$\lesssim 200$ μBq/kg	< 0.01	< 0.01	< 0.01	< 0.01
38	Module Screws	^{238}U	1.000	20 ± 40 mBq/kg	< 0.01	< 0.01	< 0.01	< 0.01
39	Module Screws	^{226}Ra	0.900	$\lesssim 1.4$ mBq/kg	0.01	0.01	< 0.01	< 0.01
40	Module Screws	^{210}Pb	1.000	27 ± 8 mBq/kg	< 0.01	< 0.01	< 0.01	< 0.01
41	Module Screws	^{232}Th	1.024	2.4 ± 1.6 mBq/kg	0.02	0.01	< 0.01	< 0.01
42	Module Screws	^{40}K	1.000	28 ± 15 mBq/kg	< 0.01	< 0.01	< 0.01	< 0.01
43	Module Screws	Act.	1.000	various	< 0.01	< 0.01	< 0.01	< 0.01
44	Copper Vessel	^{238}U	0.903	$\lesssim 110$ μBq/kg	< 0.01	< 0.01	< 0.01	< 0.01
45	Copper Vessel	^{226}Ra	0.900	$\lesssim 120$ μBq/kg	0.10	0.09	0.01	0.01
46	Copper Vessel	^{210}Pb	0.731	20 ± 8 mBq/kg	0.06	0.03	< 0.01	< 0.01
47	Copper Vessel	^{232}Th	0.900	$\lesssim 36$ μBq/kg	0.04	0.03	< 0.01	< 0.01
48	Copper Vessel	^{40}K	0.901	$\lesssim 28$ μBq/kg	< 0.01	< 0.01	< 0.01	< 0.01
49	Copper Vessel	Act.	0.486	various	0.33	0.27	0.05	0.04
	Total				12.51	8.67	6.27	3.96

Table 3.4: Fit results for the 49 simulated templates used to construct the background model, each corresponding to a unique detector part and decay chain. The final fit parameter C_l indicates the fractional deviation from the initial guess of each template's activity. The mean differential rate in counts dru is calculated separately for CCDs 2–7 and CCD 1 in the energy ranges of 1–6 keV and 6–20 keV.

3.3.4 DAMIC CCD Irradiation: Cosmogenic Activation of Silicon

Note: the following section is based on Ref. [85], of which I am a co-author. Copyright rests with the Physical Review D journal.

As we discussed in the last section, cosmogenic activation via spallation plays an important role in the overall radiopurity of detector materials used for dark matter experiments, including for those that employ high-purity, single-crystal silicon detectors such as DAMIC [31], SENSEI [68], and SuperCDMS [101]. Despite the best mitigation strategies, a residual background is unavoidable; this is partially driven by beta-emitting radiocontaminants whose decay products have energy signals that can mimic the desired expected dark matter signal. We have already highlighted tritium ^{3}H, ^{32}Si, and ^{210}Pb as leading background sources. DAMIC has the capability to directly measure ^{32}Si contamination of CCDs, and the work in this section addresses a previous deficiency in measurements, namely a direct experimental measurement of the cosmogenic activation rate of ^{3}H in silicon. This is key given that the background level from cosmogenic isotopes is determined via above-ground exposure, cosmic ray flux, and production cross-sections.

Isotope	Half-Life [yrs]	Decay Mode	Q-value [keV]
^{3}H	12.32 ± 0.02	β-	18.591 ± 0.003
^{7}Be	0.1457 ± 0.0020	EC	861.82 ± 0.02
^{10}Be	$(1.51 \pm 0.06) \times 10^{6}$	β-	556.0 ± 0.6
^{14}C	5700 ± 30	β-	156.475 ± 0.004
^{22}Na	2.6018 ± 0.0022	β+	2842.2 ± 0.2
^{26}Al	$(7.17 \pm 0.24) \times 10^{5}$	EC	4004.14 ± 6.00

Table 3.5: List of all radioisotopes with half-lives > 30 days that can be produced by cosmogenic interactions with natural silicon (data from Ref. [86]).

A list of relevant cosmogenic isotopes can be found in Tab. 3.5, including ^{3}H, ^{7}Be, and ^{22}Na. Tritium decays by pure beta emission with a low Q-value of 18.6 keV, a major concern for dark matter searches, whereas ^{7}Be is not as much a concern given its relatively short half-life of 53.22 d. For ^{22}Na, its higher β^{+} endpoint of 546 keV implies a smaller number of

decays within the energy range of interest for dark matter searches. Also noteworthy is that none of these isotopes have radioactive daughters that may contribute further backgrounds.

Measurements of production rates were obtained by irradiating CCDs and silicon wafers (and one germanium wafer) with a neutron beam at the Los Alamos Neutron Science Center (LANSCE) facility [88] (Target 4 Flight Path 30 Right, 4FP30R). The beam has a similar energy spectrum to that of cosmic-ray neutrons at sea level (see Fig. 3.15), enabling extrapolation from measured beam rates; above 10 MeV, it also has $> \times 10^8$ the cosmic-ray flux (nominal fluence: 2.4×10^{12} neutrons), implying measurements can be done on reasonable time scales. CCDs were used to measure the subsequent β activity within their active regions, and wafers' γ activity was measured with a low-background γ-ray spectroscopy counter at PNNL [87].

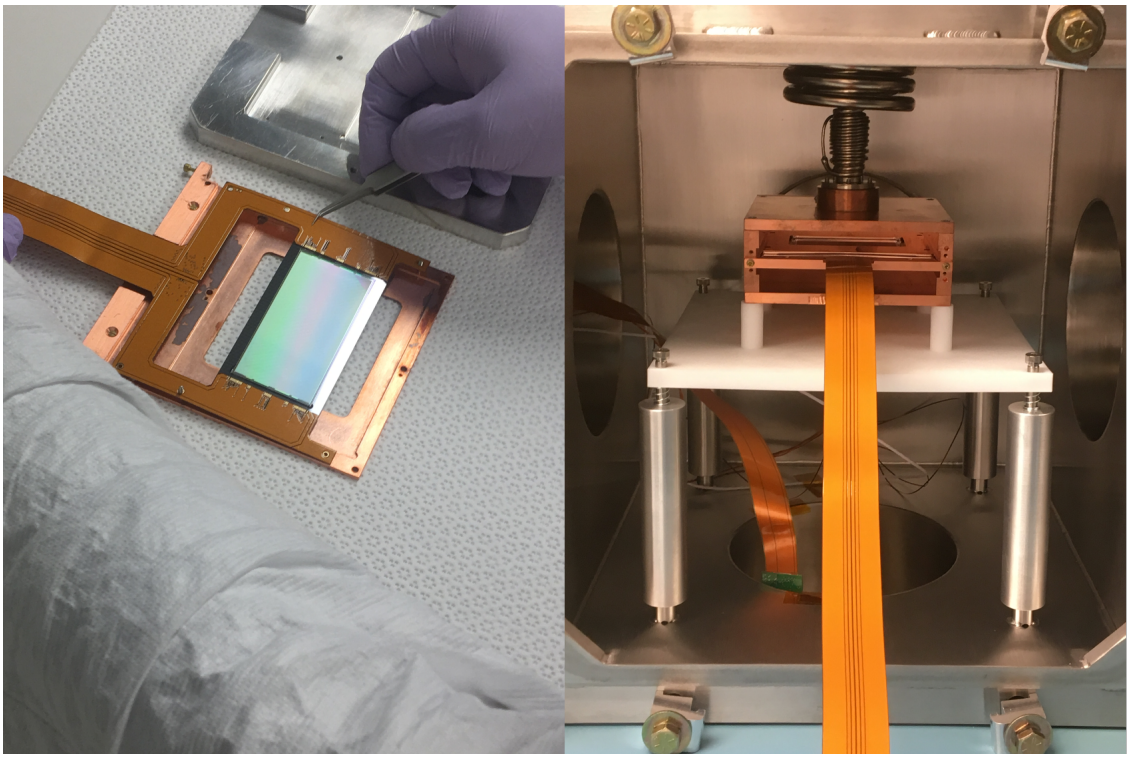

Figure 3.14: Left: transferring a DAMIC CCD from its aluminum shipping/storage container to a copper module used for testing. Right: collecting background data with a pre-irradiation DAMIC CCD installed in a test chamber at the University of Chicago.

Three DAMIC 4k×2k (4098 × 2046 pixels) CCDs were deployed for the measurement. The CCDs were packaged at the University of Washington with the standard DAMIC procedure, and placed in aluminum storage/shipping containers. Prior to irradiation, the CCDs' CTI was $< 10^{-6}$, dark current $< 1\,\mathrm{e}^-/\mathrm{pix/h}$, and $\sigma_{\mathrm{pix}} \sim 2\,\mathrm{e}^-$. Background data was collected at the University of Chicago before shipment to LANSCE. CCDs were transferred from their aluminum storage containers to copper modules for installation in a dedicated test chamber (see Fig. 3.14). A total of 1236 images were acquired with 913 s exposure (13.06 d total counting time). The background data reflects the laboratory and vacuum chamber environments, intrinsic CCD contamination, and cosmic rays.

The CCDs were irradiated at the neutron beam in September 2018 with varying exposure: 2.4×10^{12}, 1.6×10^{12}, and 0.8×10^{12} neutrons, respectively. A 1" (2.54 cm) collimator was used to suppress irradiation of the CCDs' serial registers; we simulated the beam profile and setup geometry with `GEANT4`. The beam spectrum (Fig. 3.15) falls off faster at higher energies than that of cosmic rays. Although irradiation generates silicon defects, fully-depleted CCDs are resilient because ionization is collected over a short time, minimizing trapped charge. CCDs still resolved the ^{3}H β-spectrum: the least irradiated CCD (CCD 3) was selected since it had enough activity above background and the best post-irradiation response.

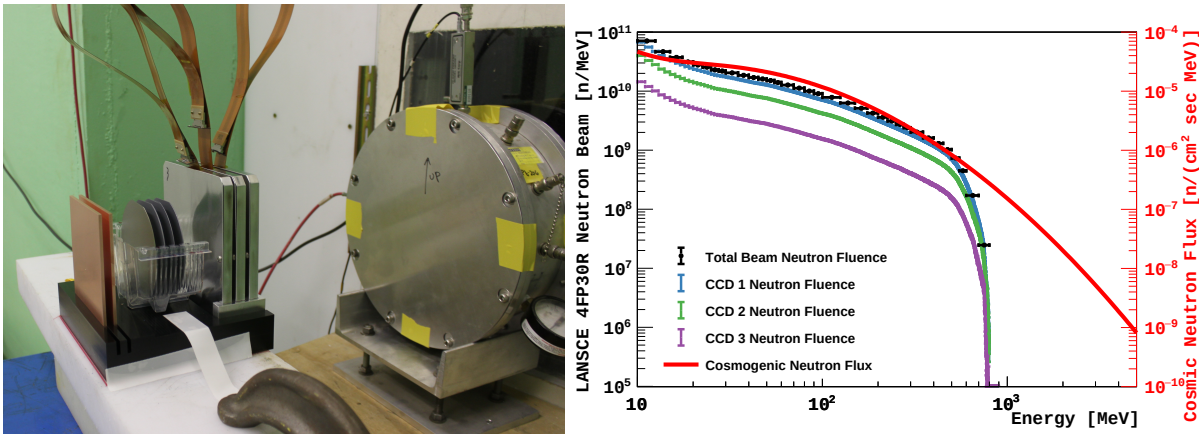

Figure 3.15: Left: Layout of CCDs and wafers irradiated at the LANSCE neutron beam. Right: Comparison of LANSCE beam fluences with sea-level cosmic-ray neutrons [89].

Following irradiation, 8030 images (417 s exposure), or 38.76 d-equivalent, were acquired at the University of Chicago with CCD 3 using the same readout settings as for the previously acquired background data. The irradiated CCDs were functional but had worsened CTI of $\sim 10^{-4}$ and dark current of $\sim$ 100 e^-/pix/h. The higher CCD dark current, as in Fig. 3.16 (top), necessitated modifications to standard image processing described earlier. In particular, masking and pedestal subtraction accounted for non-uniformity of average pixel values across the CCD by splitting images into 20-column segments, each treated separately.

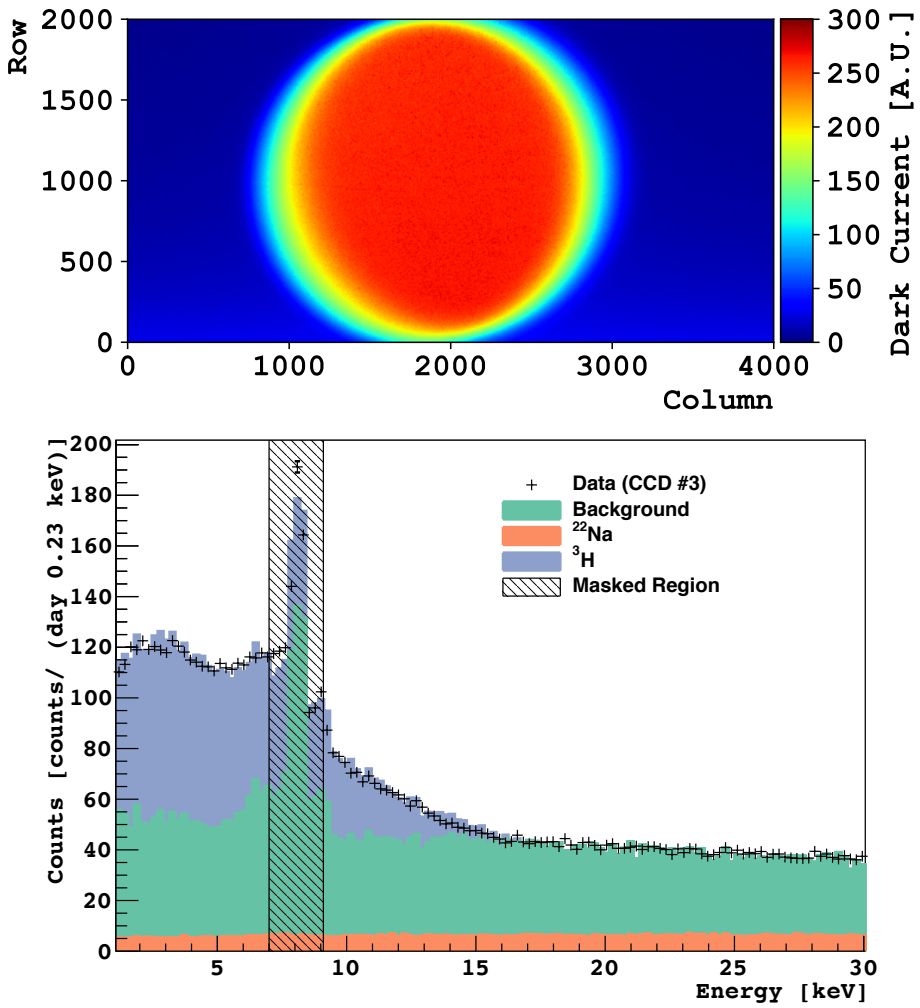

Figure 3.16: Top: Post-irradiation dark current profile of CCD 3. Bottom: Data spectrum and best-fit model in the 2-25 keV range, excluding the ∼8 keV copper K-fluorescence line. The rise in the spectrum below 18 keV due to ^{3}H is visible above the approximately flat ^{22}Na contribution.

Blank images were generated with the same dark current profile as post-irradiation data. To obtain isotope-specific detection efficiencies in the energy region of interest, events of ^{3}H, ^{22}Na, and ^{7}Be simulated using `GEANT4` with a simplified geometry of the CCD and surrounding box were pasted onto these blanks and processed in the same way as data. The identified clusters from the aforementioned pre-irradiation background data were also introduced on simulated blank images to model the effects of dark current, defects, and CTI on the background spectrum in the activated region of the CCD. The post-irradiated energy spectrum was fit with components of the CCD background, ^{22}Na decays, and ^{3}H decays. ^{7}Be was excluded because its decay does not contribute significantly to the final spectrum.

To find the best-fit parameters, a binned Poisson log-likelihood test statistic was minimized, described in detail in Ref. [85]. The final energy spectrum and best-fit result are shown in Fig. 3.16 (bottom). The predicted activity P for a given model of isotope cross-section $\sigma(E)$ is given by:

$$P = \frac{n_a}{\tau} \int S(E) \cdot \sigma(E) dE \tag{3.13}$$

where n_a is the areal number density of the target silicon atoms, τ is the mean life of isotope decay, and $S(E)$ is the neutron energy spectrum.

The final extracted estimates of the radioisotope production rates in silicon exposed to sea-level cosmogenic particles are shown in Tab. 3.6, including activation by cosmic neutrons and other particles described in Ref. [85]. These rates can be scaled by knowing aspects of the geomagnetic field, variations in particle flux with altitude/depth, etc. in order to obtain the total expected activity in silicon-based detectors. At sea level, the production rate is dominated by neutron-induced interactions.

Tritium is the main cosmogenic background concern for silicon-based dark matter searches. In particular, at low energies of 0-5 keV, the estimated production rate implies an activity of roughly 0.002 dru per day of exposure. This means that if an experiment (for example, DAMIC-M) were to aim to operate a 1 kg silicon detector and conduct a search in the

Source	^{3}H production rate [atoms/(kg d)]	^{7}Be production rate [atoms/(kg d)]	^{22}Na production rate [atoms/(kg d)]
Neutrons	112(24)	8.1(19)	43.0(72)
Protons	10.0(45)	1.14(14)	3.96(89)
Gamma Rays	0.73(51)	0.118(83)	2.2(15)
Muon Capture	1.57(92)	0.09(9)	0.48(11)
Total	124(25)	9.4(20)	49.6(74)

Table 3.6: Final estimates of the radioisotope production rates in silicon exposed to cosmogenic particles at sea level.

cited energy range, while aiming for a ^{3}H "budget" of 0.3 dru (approximately a $\times$10 decrease relative to DAMIC at SNOLAB), then the corresponding exposure budget at sea level would be 150 d. This analysis shows how such calculations can guide stringent protocols during detector material fabrication, transportation, and storage, a theme we shall continue to revisit.

CHAPTER 4

RADIOACTIVE CONTAMINATION OF DETECTOR-GRADE SILICON

Note: the following chapter is based on Ref. [79] (of which I am first author), but provides more detail into the analysis. Copyright rests with the Journal of Instrumentation.

One of the largest challenges in constructing a direct-detection experiment is that dark matter is not the only source of energy depositions in the detector. Other sources, predominantly radiogenic backgrounds, can mimic a dark matter signal and fundamentally limit the sensitivity of a direct-detection experiment to dark matter models. The primary means of addressing such backgrounds are mitigation and rejection. Mitigation includes material selection and shielding. Detector materials are carefully selected and measured to ensure low levels of long-lived radioactive isotopes, such as primordial ^{238}U and ^{232}Th (Fig. 4.1). Rejection is the process by which radioactive backgrounds are eliminated using analysis techniques to distinguish standard model decays from a potential dark matter signal. This chapter will show how the capabilities of silicon CCDs can identify radioactive background events to enable and guide both techniques.

We present improved measurements of bulk radioactive backgrounds in high-resistivity silicon CCDs from the DArk Matter In CCDs (DAMIC) experiment at SNOLAB. We build on a method to distinguish and reject background events coming from the same radioactive decay chain, initially presented in Ref. [90]. By utilizing the precise spatial resolution of CCDs and discrimination between α and β particles, we identify spatially-correlated radioactive decay sequences over periods of up to several weeks. In addition to constraining ^{238}U and ^{232}Th activities with comparable sensitivity to mass-spectroscopy techniques [91], we employ this method to measure, with unprecedented sensitivity, shorter-lived isotopes in the bulk silicon, such as ^{32}Si and ^{210}Pb.

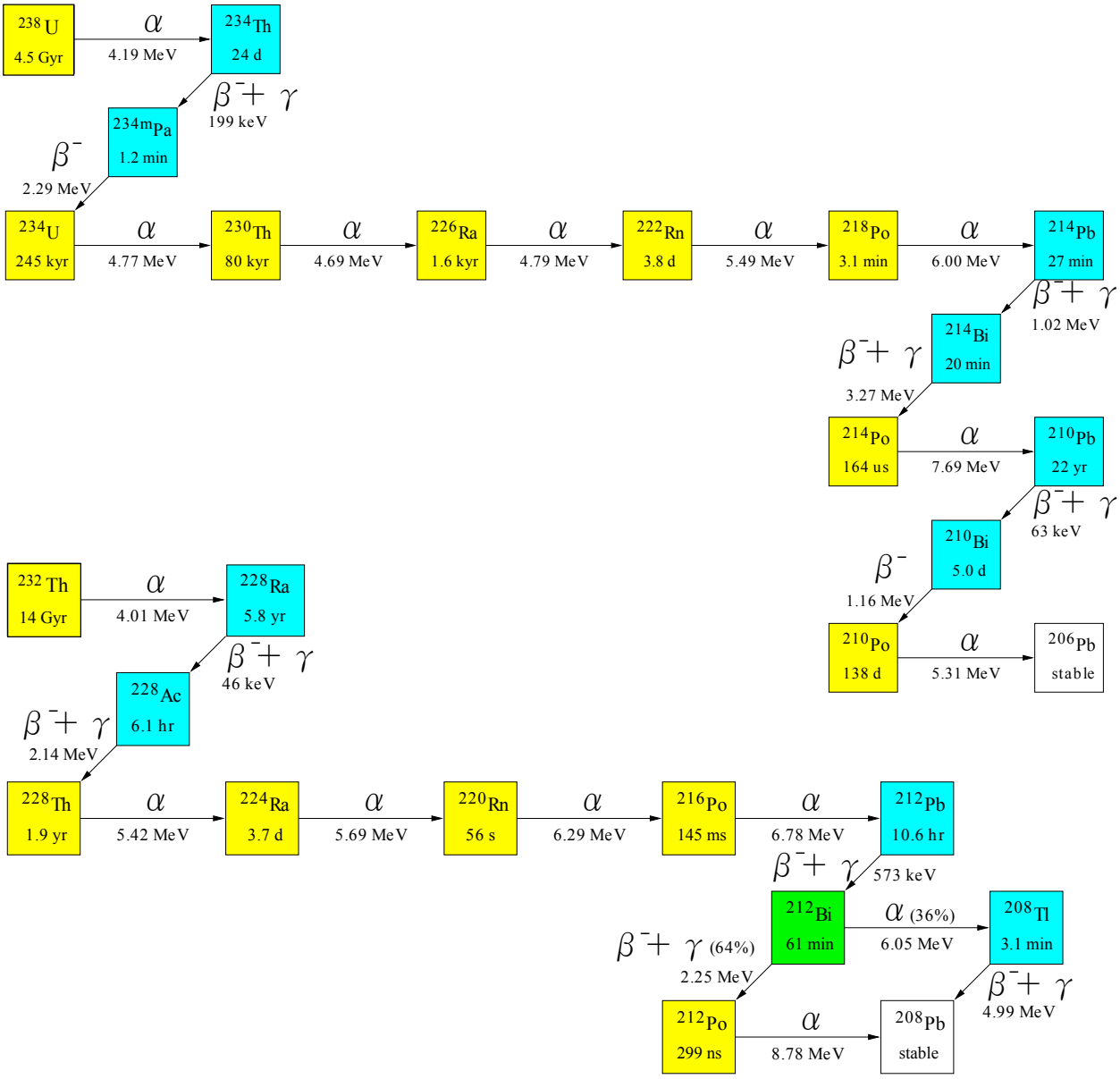

Figure 4.1: ^{238}U and ^{232}Th decay chains.

4.1 Methodology: Searching for Spatially-Correlated Decays

Background data used in this analysis was acquired between February and September 2017 with six CCDs (total exposure time $t = 181.3$ d; total mass $M = 36$ g). A seventh CCD began taking data partway through the time period of this analysis, and is thus excluded. The energy response of each CCD was obtained during the commissioning phase at SNOLAB, similar to the procedure in Ref. [32]. Images in this dataset had $t_{\rm exp} = 3 \times 10^4$ s (0.35 d) exposure and pixels were read out individually (1×1 mode) to improve spatial resolution. Images are processed using the same procedure described in Ref. [32] and summarized before, including steps for pedestal subtraction, correlated noise subtraction, and masking regions with high leakage current or defects. After image processing is completed, clustering reconstruction is performed: contiguous pixels not excluded by masked regions are grouped together if they exceed a threshold value of $4\sigma_{\rm pix}$.

4.1.1 Discriminating between α and β Decays

In DAMIC CCDs, low-energy electrons and nuclear recoils produce clusters whose spatial extent is due primarily to charge diffusion. The spatial characteristics of reconstructed α and high-energy β clusters enable efficient event-by-event discrimination. In particular, β's have long, "worm"-like tracks compared to α's, which appear as spatially concentrated "blobs", as shown in Fig. 4.2. To differentiate α and β events, we calculate $f_{\rm pix}$, the fraction of a cluster's number of pixels over the total pixel area of the the smallest rectangle drawn around the entire cluster. The value of $f_{\rm pix}$ is larger for α's than high-energy β's since α's tend to fill more of the space inside this rectangle. We define α's as clusters having $f_{\rm pix} > 0.75$ for $E > 550$ keV, $f_{\rm pix} > 0.45$ for $E > 900$ keV, or $E > 5$ MeV with linear interpolation between these points, as shown in Fig. 4.3 (top). This cut is chosen to accept >99.9% of simulated β decays and categorizes all reconstructed events in data with energy greater than 2 MeV as α's.

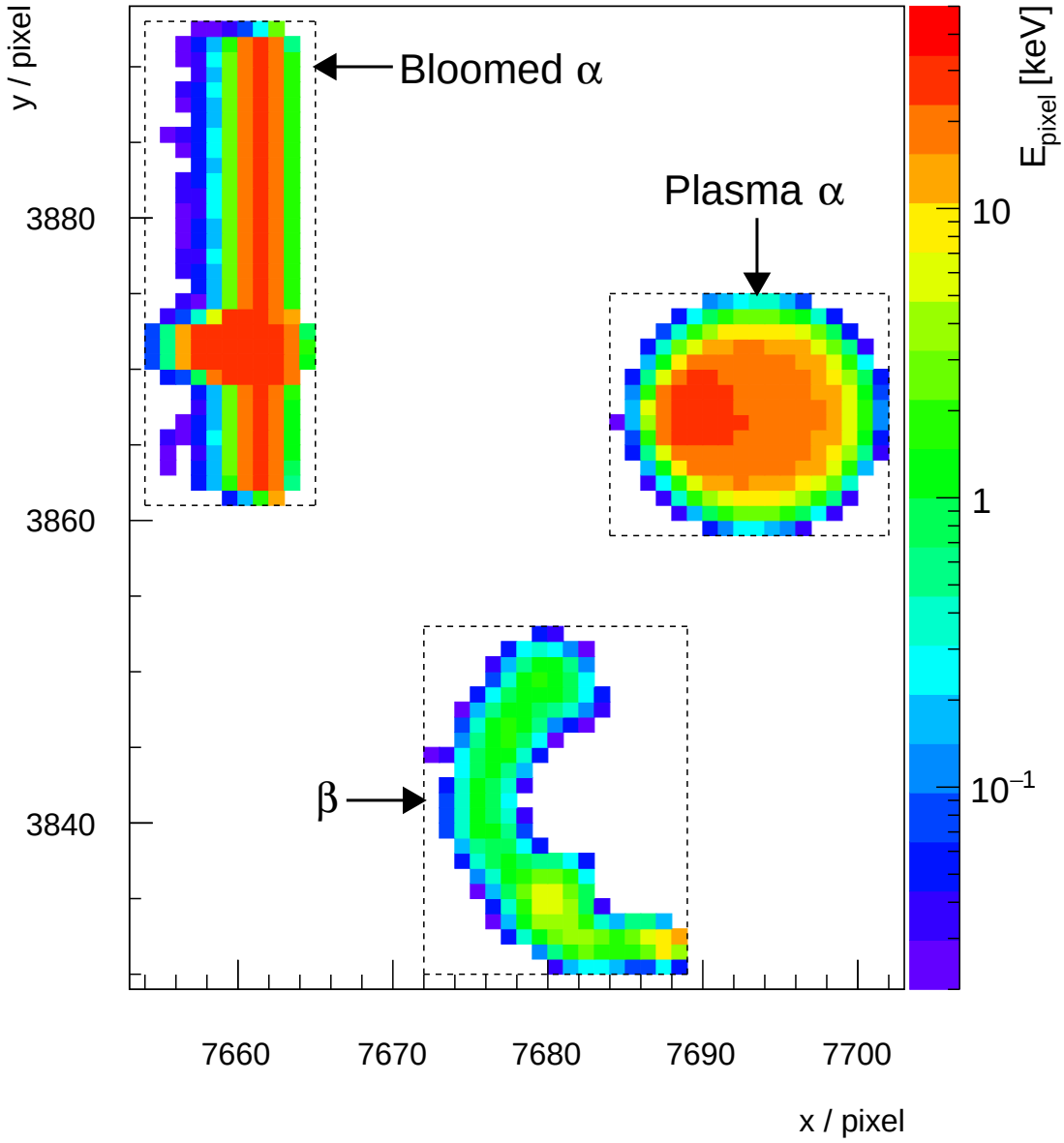

Figure 4.2: Example of α and β clusters reconstructed in data. We note the bloomed α's higher spatial variance in $\hat{y}$ compared to that of the plasma α (see text). The "worm"-like track of the β takes up little space inside the rectangle drawn around it.

Furthermore, α's can be separated into two types by the diffusion of charges: "plasma" and "bloomed". Plasma α's correspond to highly-diffuse and round clusters as a result of

the plasma effect [94] and originate in the bulk or close to the back of the CCD. Bloomed α's, by contrast, originate near the front of the CCD and produce elongated tracks in $\hat{y}$ due to charge spilling between pixels along a column. More information on both types of α's can be found in Refs. [90, 94]. To differentiate plasma and bloomed α's, we determine the spatial RMS spread of a cluster's x and y pixel distributions, σ_x and σ_y. The ratio σ_x/σ_y successfully separates α's into the two categories, as shown in Fig. 4.3 (bottom). Plasma α's are defined to have $\sigma_x/\sigma_y > 0.9$; bloomed α's are defined to have $\sigma_x/\sigma_y \leq 0.9$.

Fig. 4.3 shows two distinct populations of bloomed and plasma α's with energies clustered around 5.3 MeV with a tail toward lower energies. These events are consistent with ^{210}Po decays on the front and back surfaces of the CCDs, which deposit a fraction of their energy in the inactive, few-μm thick CCD dead layers. This background arises from long-lived ^{210}Pb surface contamination due to exposure of the CCDs to environmental ^{222}Rn during fabrication, packaging, and handling. We set upper limits on bulk ^{210}Pb contamination, and separately present a detailed analysis of surface ^{210}Pb. Higher energy α's ($E_\alpha \gtrsim 5.3$ MeV) must originate from the ^{238}U and ^{232}Th chains. However, the absence of any definitive bulk ^{238}U and ^{232}Th coincidences in the data suggests that these events are likely from dust particulates in the CCD surfaces or radon decays in the volume around the CCDs.

4.1.2 Search Design and Criteria

The decay characteristics, specifically the half-life ($t_{1/2}$) and Q values of isotope decays, listed in Tab. 4.1, guide the searches. For a decay sequence to be considered a candidate: events must occur in the same CCD, isotope daughter clusters have to occur in later images than their parents, clusters must match appropriate α, β classification and be spatially-coincident (minimum one-pixel overlap) in unmasked regions of the CCD, and sequences have to fall within energy (E) and separation time (Δt) selection, as defined in Tab. 4.1. We constrain the separation time of most searches to be within $\approx 5t_{1/2}$.

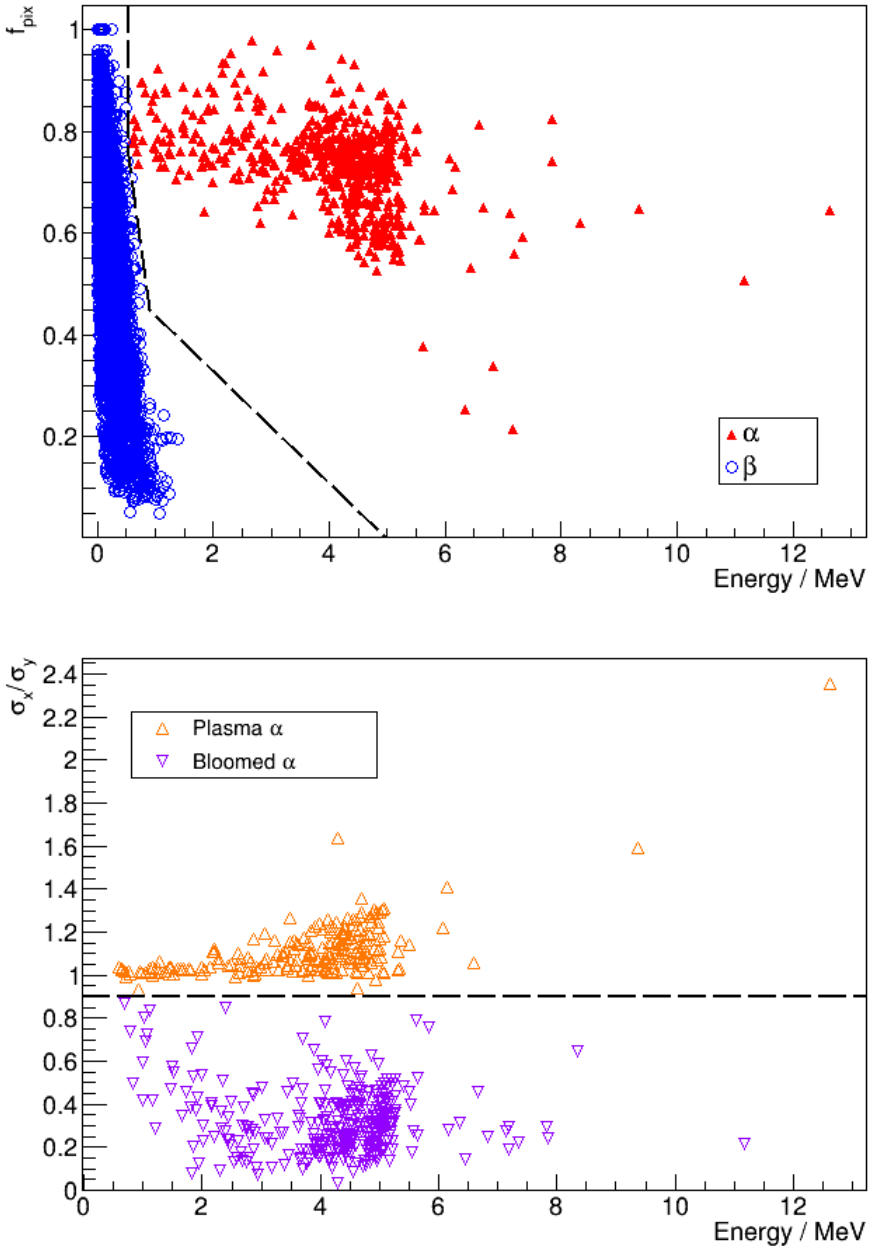

Figure 4.3: Top: discrimination of α's (triangles) and β's (circles) in the 2017 background dataset using f_{pix}, the fraction of a cluster's pixel number over the smallest rectangle covering its area. Bottom: discrimination of bulk or back surface (plasma) α's from front surface (bloomed) α's using the ratio σ_x/σ_y, which leverages bloomed α's higher spatial variance in $\hat{y}$.

Table 4.1: Constraints on the activities A of the ^{32}Si, ^{238}U, and ^{232}Th decay chains according to the background-subtracted number of events $n_{\rm ev}$ found in each search with efficiency ϵ from DAMIC data. Events must meet the correct α or β classification for each search (according to Fig. 4.3) and pass all relevant energy and time cuts defined here (where Δt is defined as the difference between image end times). Note that rapid, subsequent α decays will be reconstructed as a single α-like event of higher energy. Additional details on the numbered $\beta \to \beta$ searches can be found in Tab. 4.2. The weighted-average result of the ^{32}Si searches is given in this table for simplicity, but the individual searches determine A of 120 ± 30 μBq/kg (1a) and 260 ± 80 μBq/kg (1b). Any isotope with $t_{1/2} < 30$ days is assumed to have the activity of its long-lived parent. We truncate the ^{232}Th chain at ^{212}Pb as the remaining decays to stable ^{208}Pb are short-lived ($t_{1/2} \leq 1$ hr), in secular equilibrium (s.e.) with ^{228}Th, and not used for this analysis. Decay information is taken from Refs. [95, 96, 97].

	Decay	$t_{1/2}$	Q value	Search	Energy cut [keV]	Time cut [d]	ϵ	$n_{\rm ev}$	A [μBq/kg]
^{32}Si Chain									
^{32}Si	β	153 yr	227 keV	$\beta \to \beta$ (1a)	$70 < E_{\beta 1} < 230$	$\Delta t < 70$	0.279	19.5	140 ± 30
^{32}P	β	14.3 d	1.71 MeV	$\beta \to \beta$ (1b)	$0.5 < E_{\beta 1} < 70$	$25 < \Delta t < 70$	0.088	12.7	
^{238}U Chain									
^{238}U	α	4.47 Gyr	4.27 MeV						
^{234}Th	β	24.1 d	274 keV	$\alpha \to \beta$	$3800 < E_{\alpha 1} < 4600$, $E_{\beta 2} > 0.5$	$\Delta t < 120$	0.650	-0.2	< 11
^{234m}Pa	β	1.16 min	2.27 MeV						
^{234}U	α	246 kyr	4.86 MeV	^{238}U (s.e.)					
^{230}Th	α	75.4 kyr	4.77 MeV						no limit
^{226}Ra	α	1.60 kyr	4.87 MeV						
^{222}Rn	α	3.82 d	5.59 MeV						
^{218}Po	α	3.10 min	6.11 MeV	$(\alpha + \alpha + \alpha)$	$E_\alpha > 15000$	$\Delta t = 0$			
^{214}Pb	β	27.1 min	1.02 MeV	OR			~ 1	0	< 5.3
^{214}Bi	β	19.9 min	3.27 MeV	$(\alpha + \alpha) \to \beta/\alpha$	$E_{\alpha 1} > 10000$	$\Delta t = t_{\rm exp}$			
^{214}Po	α	164 μs	7.83 MeV						
^{210}Pb	β	22.2 yr	63.5 keV	$\beta \to \beta$ (2)	$0.5 < E_{\beta 1} < 70$	$\Delta t < 25$	0.734	47.1	< 160
^{210}Bi	β	5.01 d	1.16 MeV						
^{210}Po	α	138 d	5.41 MeV						
^{232}Th Chain									
^{232}Th	α	14.0 Gyr	4.08 MeV	^{228}Th (s.e.)					< 7.3
^{228}Ra	β	5.75 yr	45.5 keV	$\beta \to \beta$ (3)	$0.5 < E_{\beta 1} < 55$	$\Delta t < 1.3$	0.440	2.6	< 40
^{228}Th	α	1.91 yr	5.52 MeV						
^{224}Ra	α	3.63 d	5.79 MeV	$\alpha \to (\alpha + \alpha)$	$E_{\alpha 2} > 10000$	$\Delta t = t_{\rm exp}$	0.727	0	< 7.3
^{220}Rn	α	55.6 s	6.40 MeV						
^{216}Po	α	145 ms	6.91 MeV						
^{212}Pb	β	10.6 hr	569 keV						
...									

4.2 Intrinsic ^{32}Si Measurement

We leverage the unique spatial resolution of DAMIC CCDs to search for decays coming from the same decay chain at the same location over long times. We conduct searches to identify spatially-correlated decay sequences in order to directly measure bulk radioactive contamination in the CCDs. The isotope ^{32}Si is produced by spallation, or nuclear fragmentation, of atmospheric ^{40}Ar by impact of cosmic rays; it falls to the surface with precipitation and is present when silicon is eventually gathered to fabricate ingots for semiconductor production [98]. The isotope ^{32}Si and its daughter, ^{32}P, are of particular concern for DAMIC and other silicon-based direct-detection experiments, because they are intrinsic to the bulk of the detector with β electrons that span the low energies of interest for DM searches. The sensitivity of next-generation, large-exposure, solid state silicon experiments [99, 100, 101] depends greatly on how much intrinsic radioactive contamination can be reduced. Improving understanding of such contamination aides in establishing mitigation protocols for the material selection and fabrication of future detectors.

The analysis of ^{32}Si-^{32}P spatially-coincident $\beta \rightarrow \beta$ events is split into two searches according to Table 4.1, to disentangle any event overlap with spatially-coincident ^{210}Pb-^{210}Bi decays. The first ^{32}Si search (1a) is at an energy range above the Q value of ^{210}Pb, and thus includes no potential event overlap. The second ^{32}Si search (1b) includes a lower separation time bound of 25 d ($\approx 5t_{1/2}$ of ^{210}Pb but only $1.75t_{1/2}$ of ^{32}Si). Fig. 4.4 shows an example of a spatially-correlated candidate decay from the ^{32}Si search. We additionally construct a ^{210}Pb-^{210}Bi $\beta \rightarrow \beta$ search (2) to extract an upper limit on the isotopic contamination of the bulk silicon, which is expected to be out of secular equilibrium with its parent ^{238}U. Finally, we construct a ^{228}Ra-^{228}Ac $\beta \rightarrow \beta$ search (3) to constrain the part of the ^{232}Th chain which may be out of secular equilibrium. Searches (2) and (3) will be discussed below along with the rest of the ^{238}U and ^{232}Th decay chains.

We adjust the number of identified candidate sequences (N_{pair}) to account for accidental

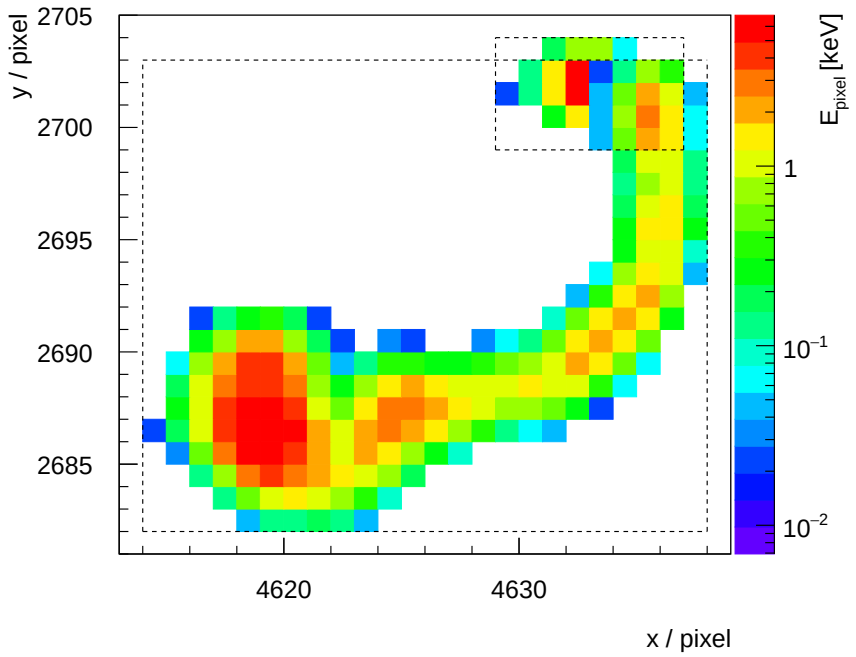

Figure 4.4: A spatially-correlated $\beta \rightarrow \beta$ candidate decay in the reconstructed data from the ^{32}Si-^{32}P search. The first decay has an energy of $E_{\beta_1} = 77$ keV and the second decay has an energy of $E_{\beta_2} = 399$ keV with a time separation of $\Delta t = 13.7$ d.

spatial coincidences of clusters (N_{acc}) and overlapping events from searches of other decay chains (N_{overlap}). The number of accidental spatial coincidences is simulated by randomizing cluster positions from data over many iterations, and reapplying the search criteria for each iteration. One thousand iterations are performed to obtain the mean value of accidental coincidences, as reported for $\beta \rightarrow \beta$ searches in Tab. 4.2. The number of events listed in Tab. 4.1 reflect the number of identified sequences adjusted for accidentals and overlap ($n_{\text{ev}} = N_{\text{pair}} - N_{\text{acc}} - N_{\text{overlap}}$).

Pair selection efficiencies (ϵ_{sel})—efficiencies of matching spatially-correlated parent-daughter sequences passing energy cuts—are calculated using `GEANT4` [76], with 10,000 decays individually simulated for each isotope of interest. Steps of image processing and clustering

Table 4.2: Details for the $\beta \rightarrow \beta$ coincidence searches, including pair selection and time efficiencies ($\epsilon_{\rm sel}$ and ϵ_t, respectively), number of coincident pairs found ($N_{\rm pair}$), number of accidental pairs expected ($N_{\rm acc}$), and number of pairs expected from overlap with other decay searches ($N_{\rm overlap}$), which are used to calculate the adjusted number events ($n_{\rm ev}$) attributed to coincident decays for a given search.

Isotope	$\epsilon_{\rm sel}$	ϵ_t	$N_{\rm pair}$	$N_{\rm acc}$	$N_{\rm overlap}$	$n_{\rm ev}$
^{32}Si (1a)	0.398	0.701	26	6.5 ± 0.1	0	19.5 ± 5.1
^{32}Si (1b)	0.521	0.169	17	3.0 ± 0.1	1.3 ± 0.3	12.7 ± 4.1
^{210}Pb (2)	0.981	0.748	69	2.5 ± 0.1	19.4 ± 5.1	27.1 ± 9.7
^{228}Ra (3)	1	0.440	8	0.08 ± 0.01	5.28 ± 1.15	2.6 ± 3.0

reconstruction are applied to each simulation output file, to ensure that the same set of clustering parameters as extracted for DAMIC images are present. There were breaks in data acquisition due to image readout (< 9 min per image) and power outages at the underground site. As such, the time efficiency (ϵ_t) of each search is obtained by analytically solving for probabilities of seeing subsequent decays within the time cuts given these periods of down-time, following identification of initial, first-decay candidates (see the Appendix at the end of this chapter for explicit derivations). Time efficiency values are cross-checked with Monte Carlo simulations, which agree with analytical calculations to within $< 1\%$. The time and pair selection efficiencies of ^{32}Si and ^{210}Pb searches can be found in Tab. 4.2. The overall efficiency of a search is equal to the product of the individual efficiencies ($\epsilon = \epsilon_{\rm sel} \times \epsilon_t$), and is used to calculate the isotopic activity A, reported in Tab. 4.1, such that

$$A = \frac{n_{\rm ev}}{\epsilon M t}, \tag{4.1}$$

where Mt is the total exposure considered in the search, 6.5 kg-d for this analysis.

We measure a bulk ^{32}Si activity of 140 ± 30 μBq/kg ($\pm 1\sigma$ statistical uncertainty) by taking the weighted average of the split searches in Tab. 4.1 ($A_{\rm 1a} = 120 \pm 30$ μBq/kg; $A_{\rm 1b} = 260 \pm 80$ μBq/kg). When calculating the activity for search (1b) according to Eq. 4.1,

the 1.3 ± 0.3 overlapping coincident events in Tab. 4.2 come from ^{210}Pb-^{210}Bi coincident decays. The ($\times 6$) smaller central value of ^{32}Si contamination compared to DAMIC's previous R&D measurement of 926^{+1273}_{-752} μBq/kg (95% CI) [90] suggests that intrinsic contamination levels may vary depending on the silicon sample [98], as the CCDs in the previous study were fabricated from a different silicon ingot.

4.3 Uranium and Thorium Chains

We construct similar searches to look for the activities of ^{238}U and ^{232}Th chains in the bulk silicon using both α and β decays. Parts of the ^{238}U and ^{232}Th chains include multiple subsequent decays with half-lives much less than an image exposure time and should result in spatially-coincident events within the same image. For such sequences of short-lived bulk isotopes, we can assume a selection efficiency $\epsilon_{\text{sel}} \approx 1$ to reconstruct the rapid decays as a single cluster. In certain cases, we can use the searches for these short-lived isotopes to place limits on parent isotopes or any longer-lived isotopes immediately preceding them.

4.3.1 ^{238}U

We begin with the ^{238}U decay chain, for which we perform a number of searches. We constrain the activity of ^{238}U by performing an $\alpha \rightarrow \beta$ search. If an α parent candidate corresponding to the ^{238}U-^{234}Th decay were observed, we would then expect a β decay from ^{234}Th ($t_{1/2} = 24$ d), and an additional β from the rapid decay of ^{234m}Pa ($t_{1/2} = 1.2$ min). As before, we calculate the time efficiency for this search analytically and through a Monte Carlo simulation; we obtain a value of $\epsilon_t = 0.650$. Observation of a single $\alpha \rightarrow \beta$ sequence in our data is consistent with $N_{\text{acc}} = 1.18 \pm 0.03$ and allows us to set an upper limit (95% CL) on ^{238}U contamination of < 11 μBq/kg (0.9 ppt).

4.3.2 ^{222}Rn

Further down the ^{238}U decay chain is ^{222}Rn ($t_{1/2}$ = 3.8 d), a noble element with high mobility produced from the decay of ^{226}Ra. Following the primary ^{222}Rn α , we would expect an α from ^{218}Po within minutes and energy pile-up from further short-lived isotopes (the decays of ^{214}Pb-Bi-Po) within hours. As such, we construct a search for pile-up events within a single image with total cluster energy $E > 15$ MeV, or a first pile-up of events with $E > 10$ MeV followed by a spatially-coinciding α (or $\alpha + \beta$) in the next image. While two parent candidates with 10 MeV $< E <$ 15 MeV are found, there are no spatially-coinciding daughter decays in the following images. No clusters with $E > 15$ MeV are observed. Thus, we place a limit of < 5.3 μBq/kg (95% CL) for ^{222}Rn in the bulk of the CCDs. The diffusion coefficient of elemental gases in crystalline silicon at cryogenic temperatures is expected to be $\ll 10^{-2}$ μm^2 d^{-1}, based on measurements of xenon at 700°C [103, 104]. Thus, we do not expect ^{222}Rn to readily escape the CCDs, and the ^{222}Rn measurement can be considered an upper limit on the ^{226}Ra activity in the CCDs.

4.3.3 ^{210}Pb *(Bulk)*

At the bottom of the ^{238}U decay chain is ^{210}Pb ($t_{1/2}$ = 22.2 yr), which is expected to be out of secular equilibrium with the rest of the ^{238}U decay chain, and whose β spectrum is a major concern for DM searches. We implement a $\beta \rightarrow \beta$ search similar to ^{32}Si to find coincident ^{210}Pb-^{210}Bi decays. Unlike the case of ^{32}Si, which is expected to be intrinsic to the CCD bulk, the location of ^{210}Pb contamination is unknown. The selection efficiency of the ^{210}Pb search is highly dependent on the location of the ^{210}Pb contamination, whether it is in the bulk silicon or distributed on the CCD surfaces. In this analysis, we make the overly-conservative assumption that all identified ^{210}Pb coincidences are in the bulk of the silicon in order to place a strong upper limit on such contributions of < 160 μBq/kg (95% CL). This upper limit is orders of magnitude better than the mBq/kg sensitivity obtained by

direct assay techniques that measure bulk ^{210}Pb in materials [91, 81]. When calculating this activity according to Eq. 4.1, the 19.4 ± 5.1 overlapping coincident events in Tab. 4.2 come from ^{32}Si-^{32}P coincident decays with intersecting energy ranges, calculated using the activity from the ^{32}Si search (1a). We expect the majority of the 69 coincident $\beta \rightarrow \beta$ candidates in this search to be from surface ^{210}Pb, as suggested by the two distinct α populations observed in Fig. 4.3.

4.3.4 ^{210}Pb (Surface)

The location and activity of surface ^{210}Pb from radon plate-out on detector surfaces is the source of a dominant background and major uncertainty. Radon plate-out occurs when ^{222}Rn ($\tau_{1/2} = 3.8$ days) from the primordial ^{238}U chain is produced near the detector materials during fabrication. This ^{222}Rn will then diffuse into the air around the materials until it decays into a ^{218}Po daughter ion, which will be attracted to nearby surfaces. The subsequent alpha decays will then embed the long-lived ^{210}Pb daughter ion up to 100 nm into a surface, where it will otherwise remain until it undergoes low energy beta-decay. We can leverage the same powerful and unique spatial-correlation analysis technique to constrain the activity of surface ^{210}Pb deposits in our detector.

The activity of ^{210}Pb is notoriously difficult to measure via standard assay techniques, as it is too short-lived for mass spectrometry and too low energy of a decay (with too small of a branching fraction to produce a photon) for most gamma counters. Therefore, we have no a priori knowledge which detector surfaces have experienced radon plate-out, or to what degree. In the construction of the radioactive background model for DAMIC at SNOLAB, an initial guess for a surface activity of 0.7 decays day^{-1} m^{-2} for ^{210}Pb deposited on all surfaces was used, but then left as a free parameter – different surface activities of ^{210}Pb on the front and back of the CCDs were also allowed, but it was required that each CCD have the same contamination history. The amount of deposition depends on the air volume above

a surface [105]. Throughout handling, CCDs are almost never placed face down to avoid the risk of damaging front-side electronics. It is thus likely that more ^{210}Pb will be on the front surface.

The original silicon wafers used to manufacture DAMIC CCDs were stored for several years in a warehouse, exposed to air in a vertical position. This implies approximately equal ^{210}Pb activity on the front and back of those original silicon wafers; a few microns of silicon is later removed from the front of wafers during fabrication, effectively eliminating the front wafer component. No analogous backside treatment is performed, so the back-side wafer ^{210}Pb is expected to be a dominant background contributor. In a CCD, the back wafer component corresponds to a layer of ^{210}Pb contamination ~ 3 μm below the backside outer surface. The assumed profile of ^{210}Pb deposited on a surface follows a complementary error function [82] with characteristic maximum depth $z_M = 50$ nm [83] such that:

$$\mathrm{erfc}\left(\frac{z'}{z_M}\right) = \frac{2}{\sqrt{\pi}} \int_{z'/z_M}^{\infty} e^{-t^2} dt. \tag{4.2}$$

We apply the same framework of the spatial-correlation analysis to the study of surface ^{210}Pb. For two events to qualify as a coincident ^{210}Pb candidate, they must both be classified as β's, occur within the same CCD in images less than 25 days apart ($\approx 5t_{1/2}$ of ^{210}Bi), include a minimum of one pixel overlap, and have $E_{\beta 1}$ reconstructed between 0.5–70 keV. In total, 69 event pairs are found passing these cuts in an exposure of 6.5 kg-days.

The background model produced a best fit activity of 69 ± 12 (56 ± 8) nBq/cm^2 for the front (wafer back) surface, as shown in Tab. 3.4. We determine the selection efficiencies for front (wafer back) surface coincidences from 50,000 `GEANT4` simulated decay sequences to be $\epsilon_{sel} = 0.138$ (0.315). The wafer back surface has a higher selection efficiency because it is closer to the active bulk, meaning that, despite the PCC region, it has a higher probability for both decays in a sequence to be reconstructed and identified. As in Ref. [79], this search has a time efficiency of $\epsilon_t = 0.748$ to take into account the readout time between images and

detector downtime. Given a surface area of 38 cm^2 for each of the 6 CCDs used in this search, 25.6 ± 4.5 (47.4 ± 6.8) coincident events are expected in this search from front (wafer back) surface ^{210}Pb. Additionally, 2.5 ± 0.1 accidental coincidences are expected from random events overlapping spatially and 19.4 ± 5.1 coincident events are expected within the cuts from ^{32}Si-^{32}P decays. The resulting 94.9 ± 9.6 expected pairs is slightly larger than the 69 coincident event pairs observed; this difference could be accounted for by an over-estimation of the wafer back surface selection efficiency due to imprecision of the PCC depth relative to the back wafer surface ^{210}Pb. A close compatibility with the independent measurement of this analysis and the aforementioned fit result is a good confirmation of the magnitude of surface activities.

4.3.5 $^{232}Th/^{228}Th$

Because ^{232}Th and ^{228}Th are two long-lived isotopes of the same element, we assume that they remain in secular equilibrium throughout the production of high-purity detector-grade silicon. We perform an $\alpha \rightarrow \alpha$ spatial coincidence search across different images. We search first for the α decay of ^{228}Th followed by (in a separate image) the rapid sequence of α decays from ^{224}Ra ($t_{1/2}$ = 3.7 d), ^{220}Rn ($t_{1/2}$ = 56 s), and ^{216}Po ($t_{1/2}$ = 145 ms). We assume that thoron (^{220}Rn) does not diffuse significantly in its minute-long lifetime. For the second cluster of this search, we thus expect a triple-α pileup with an energy exceeding 18 MeV within a single image. We construct an $\alpha \rightarrow \alpha$ search in which the energy of the second cluster $E > 10$ MeV. The time efficiency of the search, dominated by the 3.7 d half-life of ^{224}Ra, is $\epsilon_t = 0.727$. Non-observation of appropriate α sequences allows us to place an upper limit (95% CL) on ^{228}Th, and by extension ^{232}Th, contamination: < 7.3 μBq/kg (1.8 ppt).

4.3.6 ^{228}Ra

Another long-lived decay in the ^{232}Th chain is ^{228}Ra, which can be identified with a $\beta \rightarrow \beta$ search. We place an energy cut on the initial β of $E_{\beta 1} < 55$ keV. Given the 0.254 d half-life of ^{228}Ac, we obtain $\epsilon_t = 0.440$ that the two β's occur in different images. Eight candidate events are identified, all of which also appear in the $\beta \rightarrow \beta$ search of ^{210}Pb. Applying the time and energy bounds of the ^{228}Ra search to bulk ^{210}Pb decay gives overlap efficiencies of $\epsilon_{\rm sel} = 0.802$ and $\epsilon_t = 0.11$, resulting in an expectation of 5.28 ± 1.15 overlapping events. We note that spatial accidentals are very small (0.08 events) for this search given the small value of $t_{1/2}$. We use the observation of $n_{\rm ev} = 2.6 \pm 3.1$ events to place an upper limit on ^{228}Ra: < 40 μBq/kg (95% CL).

4.4 Identification of Spatially-Correlated Triple Decay Sequences

The impressive capability of DAMIC CCDs to identify and reject spatially-correlated events over long periods extends even to triple decay sequences, and in particular ^{210}Pb nuclei undergoing $\beta \rightarrow \beta \rightarrow \alpha$ decay. Given the best fit activity for ^{210}Pb surface rates, we can calculate the number of such triple decay events in our data. The efficiencies for this process are $\epsilon_{{\rm sel}_{\beta_1-\beta_2}} = 0.075$, $\epsilon_{{\rm sel}_{\beta_2-\alpha}} = 0.164$, and $\epsilon_t = 0.248$, giving a total efficiency $\epsilon = 0.003$. We therefore expect 2.7 ± 0.4 events. Three candidates were observed in data, in good agreement with the aforementioned value. One such candidate can be seen in Fig. 4.5, where the overall separation time between the first beta decay and the final alpha decay in the sequence is almost two weeks. A red star in each of the clusters indicates the same pixel position for reference, and is centrally located in the plasma alpha – this is a good example of the type of diffusion from plasma α's following an approximately point-like origin in the CCD.

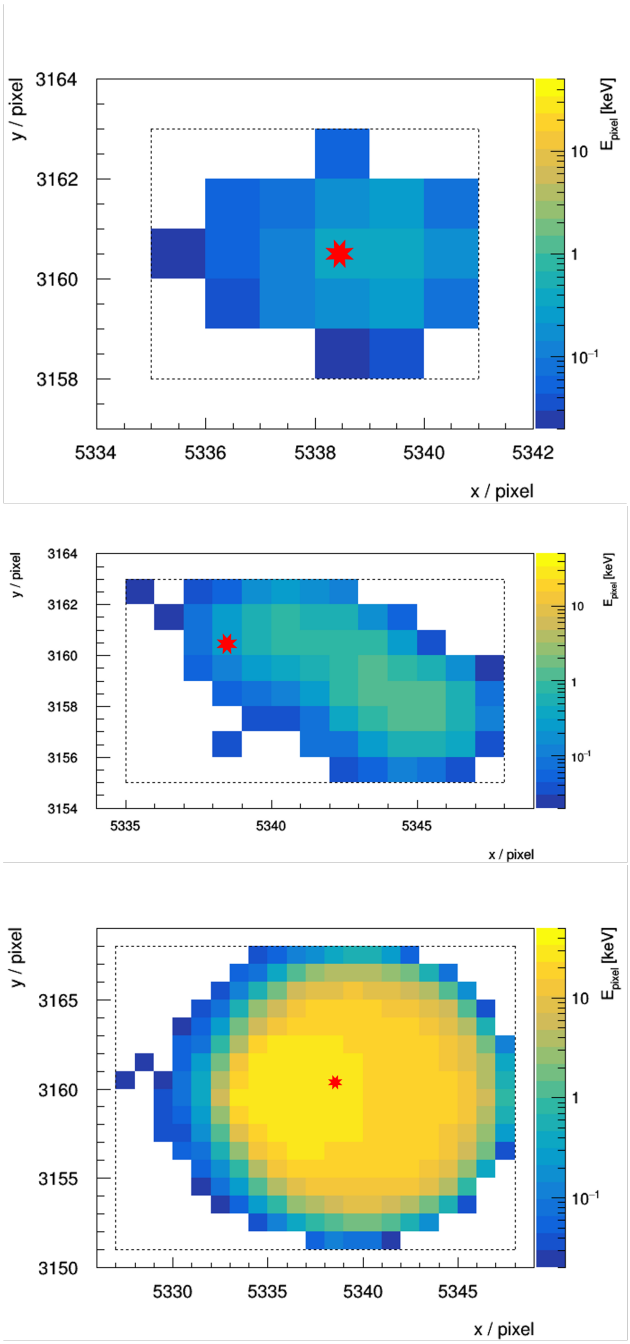

Figure 4.5: A spatially-correlated $\beta \rightarrow \beta \rightarrow \alpha$ candidate decay in the reconstructed data from a ^{210}Pb-^{210}Bi-^{210}Po search. The first decay has an energy of $E_{\beta_1} = 4.4$ keV; the second decay occurs after a time separation of $\Delta t = 3.9$ d and has an energy of $E_{\beta_2} = 41.4$ keV; the third decay occurs after a time separation of $\Delta t = 9.6$ d and has an energy of $E_\alpha = 4.3$ MeV. The red star is positioned at the same pixel in each of the three sub-figures.

4.5 Implications for Next-Generation Silicon-Based Dark Matter Experiments

We demonstrate an analysis technique that utilizes spatial-coincidence searches to directly measure the radioactive contamination within DAMIC CCDs. We determine the activity of ^{32}Si in our CCDs, and set limits on bulk contamination from the ^{238}U and ^{232}Th chains, including the activities of all β emitters, problematic backgrounds for DM searches. The ^{32}Si result, together with ICP-MS, germanium γ-counting, `GEANT4` simulations, and detector component activation analysis, plays a critical role in constraining the background model for DAMIC's WIMP search analysis [92]. It provides the first comparison of the ^{32}Si contamination level in different science-grade silicon detectors, and suggests that ^{32}Si levels may vary geographically, as suggested in Ref. [98]. CCDs will be critical in the effort to scale up silicon-based detectors as a feasible technology to screen detector-grade silicon for the desired background levels of next-generation experiments. This may allow for low background silicon ingot selection via multiple production cycles across several ingots. Both the future CCD program [100, 102] and other leading silicon-based experiments [101] benefit from such measurements of intrinsic contamination.

CHAPTER 5

DEVELOPMENT OF CCD TEST CHAMBERS FOR DAMIC-M

The DAMIC-M collaboration is currently developing a kg-size dark matter detector, which will be located in the south of France at Laboratoire Souterrain de Modane (LSM). There are ongoing discussions on the final design and requirements of DAMIC-M. Collaborators at the University Washington are advancing packaging protocol [106]; collaborators at the University of Chicago, with expertise in CCD characterization, are developing standard testing sequences; collaborators at the University of Zurich are mobilizing efforts for equipment slow-control and gaseous calibration of CCDs. The LPNHE group has historically been involved in the design and engineering of DAMIC's electronics [107], simulations [108], and analysis efforts. The group is actively designing novel electronics to control CCDs including the Clocks and Biases ASIC for CCDs (CABAC), CCD ReadOut Chip (CROC), and Online Digital Interface for Low-noise Electronics (ODILE), which will be revisited in later chapters.

Given DAMIC-M's goal of a large-scale operation with CCDs of sub-electron resolution, there is a high level of coordination required across different groups. The development of electronics must be done in tandem with the deployment of novel Skipper CCD readout, a technology that uses multiple, non-destructive measurements of charge for improved resolution (detailed in Chapter 6). To facilitate such synergy across work streams, the author, in the context of an international dual-PhD between the University of Chicago and Sorbonne Université, has bridged the expertise across multiple groups to develop an automated test system/chamber for the study of Skipper CCDs and integration of novel electronics. This chamber is effectively a scaled-down, DAMIC-style experiment at surface level that enables CCD testing in a comparable environment to the expected final installation at LSM.

5.1 Construction of Automated CCD Test Systems

5.1.1 Setup at LPNHE, Paris

The construction of the first CCD test system at LPNHE was completed in 2018. The schematic of the setup can be seen in Fig. 5.1, with relevant equipment listed in Tab. 5.1. All equipment (except the cryocooler) was hooked up to an uninterruptible power supply that supplies power during outages and can remotely shut down the DAQ computer. Since optimal operation of CCDs requires a clean environment, a modular, ISO Class 7 (<10,000 particles/ft^3, particle size $> 0.5\,\mu$m) cleanroom was built at LPNHE. It features an aluminum base structure, vinyl curtains, a gowning area, an effective detector room surface area of 12 m^2, and two Fanjet fan filter Units with HEPA filters. The cleanroom is operated in a self-regulated mode to maintain ≈ 0.5 m/s airflow speed. All tools and materials entering the cleanroom are thoroughly cleaned with IPA and ethanol solutions. The cleanroom is also equipped with a dry-nitrogen supply. Given concerns of electrostatic-discharge (ESD) around CCDs, ESD matting and wrist straps were installed throughout.

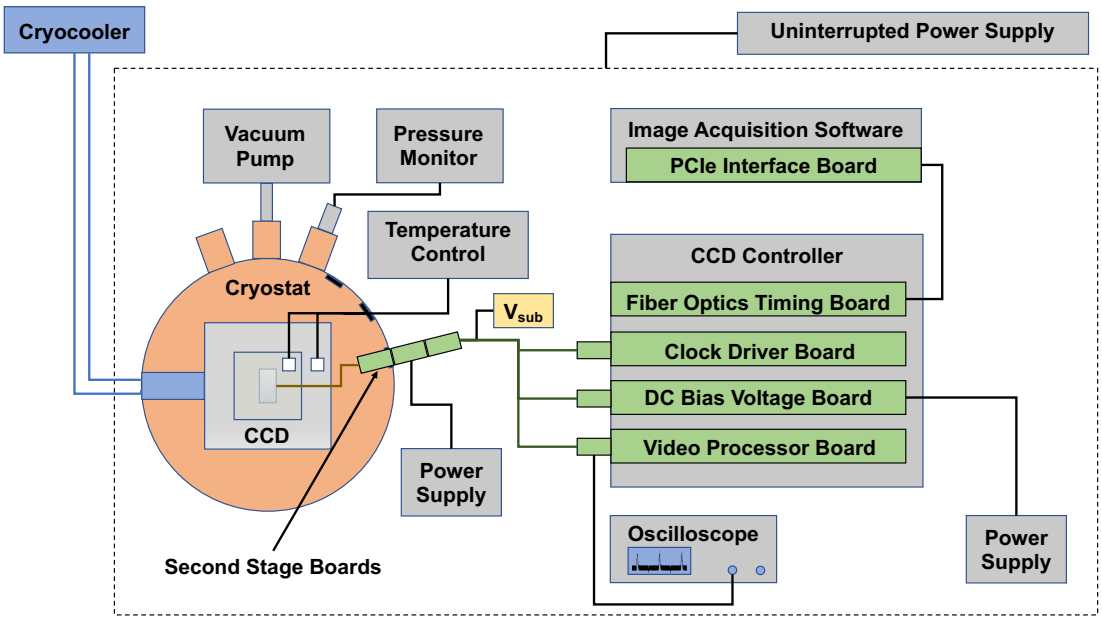

Figure 5.1: Schematic of an automated CCD test chamber at LPNHE, Paris.

Equipment	**Model**
Cryocooler	Advanced Research Systems – HW DE-MRCM-150-2
Vacuum pump	Pfeiffer TSH 071E; HiCube 80 Eco Turbo Pump
Power supply for V_{sub} to CCD	Custom Battery Pack
Power supplies for controller	Tektronix PS280 DC Power Supply
Temperature controller	Lakeshore Model 325
Pressure gauge and controller	Alcatel ACS 1000; Pfeiffer Pirani PTR 91
Oscilloscope	Rohde & Schwarz RTB2004 (4-Channel Digital Scope)
Uninterrupted Power Supply	APC Smart-UPS 1000VA LCD 230V

Table 5.1: Equipment list for the LPNHE CCD test chamber.

Cryogenics

Cryogenic equipment is a critical technical element of CCD test chambers. To maintain the right cryogenic conditions (nominally a pressure P of $O(10^{-6}\,\mathrm{mbar})$ and temperature $T \approx$ 145 K), a closed-cycle cryostat and cryocooler were implemented. Such cryostats consist of a primary machined structure, typically made of aluminum, stainless steel, or copper. The cryostat is attached to a cryocooler (compressor), cold finger (expander), and vacuum pump. Cold fingers are connected to a cryocoolers by a pair of lines that provide and return high and low pressure gas in a controlled manner to achieve desired cooling.

The cryostat used for the LPNHE test chamber was initially designed for the Large Synoptic Survey Telescope [109] and manufactured in the United States. It features an aluminum cylindrical structure (33 cm diameter). The cyrostat was installed in a vertical orientation above a rectangular aluminum base, for a total system height of 1 m.

The cryostat is equipped with several flanges of standard industry sizes (KF16, KF25, KF40) to enable attaching equipment such as the pump and pressure gauges; it also features custom flanges for the cryocooler gas lines, and six 50-pin electrical feedthroughs. Connections are made with o-rings in grooved slots, aluminum or plastic centering rings, and aluminum or plastic clamps. These components are thoroughly cleaned with alcohol solutions any time the cryostat is opened. The cryostat top and bottom plates were secure using

8 CHC M4 25-mm screws. This cryostat also featured a small quartz window within its top cover, which was covered using an aluminum plate and black tape to prevent light leaks.

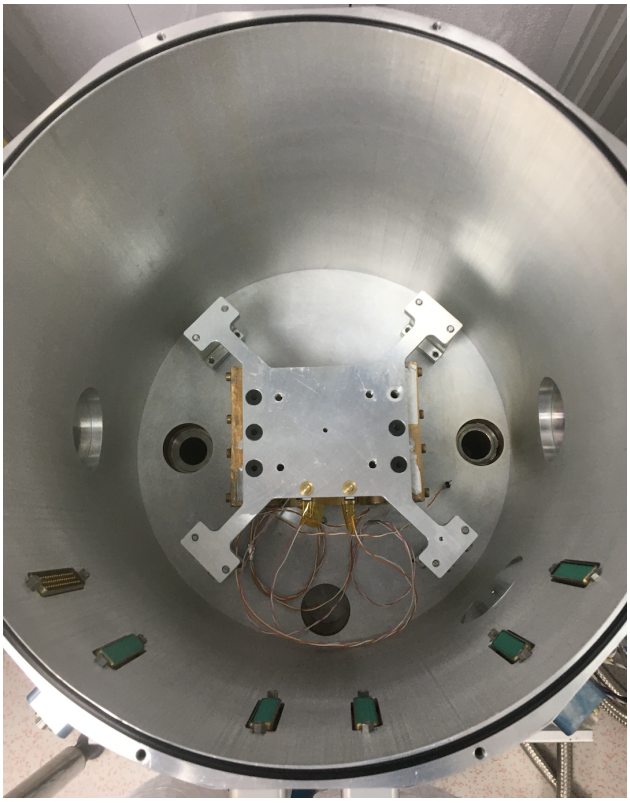

Figure 5.2: The LPNHE cryostat: an aluminum plate in thermal contact with the cryocooler cold head, six 50-pin electrical feedthroughs, and two heat resistor lines can be seen.

A widening copper piece was machined and screwed to the cryocooler copper cold head, and an aluminum plate was attached to this copper piece (see Fig. 5.2). This plate has threaded holes that enable directly securing CCDs to the cold contact, keeping them inside their storage containers. The advantage to this is that the CCDs do not have to be transferred to copper modules, preventing handling errors that could damage wire bonds and cabling. Given different materials in this installation sequence, we expect a temperature gradient due to varying thermal conductivity values. Thermal simulations can provide a reliable modeling of this gradient, but require extensive detail. Instead, we rely on a hardware solution with sufficient monitoring.

Temperature monitoring is done on the DAQ computer to protect the CCD, namely to maintain the cold temperatures at which DAMIC CCDs are operated. A Lakeshore 325 temperature controller and Pfeiffer Pirani pressure gauge are utilized. Two temperature sensors are secured in the setup using RUAG B-R50 cryogenic adhesive aluminum tape, one on the copper piece attached to the cryocooler cold head, and the other directly onto the top plate of the CCD storage container. The time to cool down or warm up the system is about 12 hours.

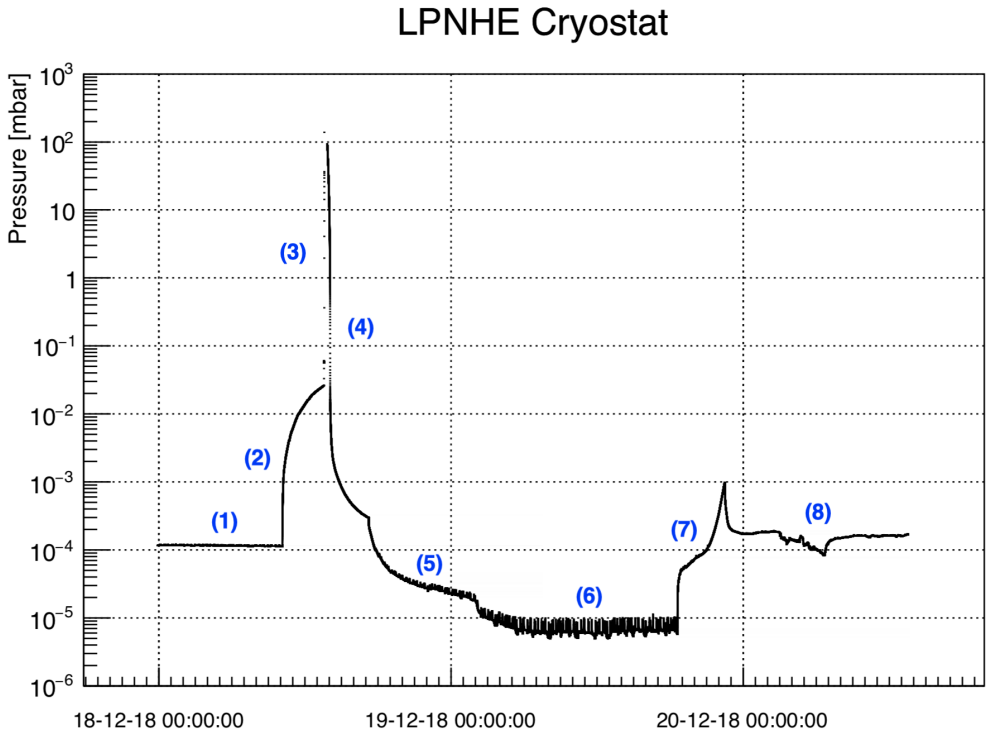

Figure 5.3: Pressure profile of the LPNHE CCD test system, with various temporal steps described in the text.

Pressure monitoring is done to ensure a vacuum level for the removal of water vapor that could otherwise collect on CCD surfaces, freeze, and potentially short-circuit the sensors. The gauges used in the setup rely on the collection of ions to give an indirect measurement of gas density and pressure. The vacuum pump is fed in to the cryostat using a 70 cm tube with a KF40 flange; its turbo's maximum operating frequency is 1500 Hz.

A pressure profile for the cryostat can be seen in Fig. 5.3 with labeled features:

1. The cryostat is at a stable pressure of $O(10^{-4}\,\text{mbar})$ with the vacuum pump operating at its maximum frequency. This level of pressure implies a sufficiently low level of water vapor or similar molecules to enable switching on the cryocooler.

2. This slow increase of pressure occurs when the pump is switched off, but the valve of the cryostat is maintained closed. The pressure begins to plateau around 10^{-2} mbar.

3. The rapid increase all the way to atmospheric pressure corresponds to when the release valve of the cryostat is opened in a controlled manner. All o-rings are inspected, cleaned, and potentially replaced when vacuum is broken.

4. This feature reflects sealing the cryostat and pumping it back down, quickly (<30 m) reaching $O(10^{-3}\,\text{mbar})$, and eventually ($\approx$ 2 hr) reaching $O(10^{-4}\,\text{mbar})$ again.

5. The cryocooler is turned on at this point, further reducing the pressure since the lower temperature causes a deceleration of gas molecules, which are also attracted to the cryostat walls [110].

6. The pressure level reaches levels as low as $O(10^{-6}\,\text{mbar})$ once the system temperature stabilizes. The visible fluctuations comes from degassing of materials within the cryostat, but the pressure doesn't exceed $O(10^{-5}\,\text{mbar})$.

7. At this point, the cryocooler is switched off and the system begins to warm. A notable outgassing spike is observed, due to the acceleration of gas molecules.

8. Following the outgassing spike, the continuously operating pump helps to stabilize the pressure back to $O(10^{-4}\,\text{mbar})$.

When the system is idle and requires being at atmospheric pressure, the cryostat is filled with dry nitrogen using a balloon of comparable volume fed into the release valve. To ensure optimal vacuum, gas ballasting is used to purge the pump of vapor condensation.

CCD Controller, Cabling, and Electronics

Proper delivery of the CCD's bias voltages and clocks, as well as the reading and processing of its video signal, is necessary for effective operation. Given the ongoing development of custom electronics, the DAMIC-M collaboration has met this requirement by implementing a commercial CCD controller produced by Astronomical Research Cameras (ARC), Inc. [111]. We will assign the namesake of this controller based on ARC's founder, Robert Leach, and refer to this controller interchangeably as the "Leach" from this point on.

Controller Component	**Description**
ARC-22	250 MHz Fiber Optic Timing Board
ARC-32	CCD Clock Driver Board
ARC-33	LBNL Bias Board
ARC-45	2-Channel CCD Video Board
ARC-66	PCIe Interface Board
ARC-70	6-Slot Closed Housing Crate
ARC-74	15 m fiber optic cable
ARC-80, ARC-82	Power supply and cable

Table 5.2: CCD controller components produced by Astronomical Research Cameras, Inc.

The Leach (Tab. 5.2) was configured with the host computer, a Dell OptiPlex 7060 machine operating CENTOS8. The timing board (ARC-22) communicates between the Leach and host computer via a 15 m fiber optic cable fed into a PCIe card (ARC-66), providing necessary timing waveforms and transfering data at 12.5 Mpix/s. Two LEDs on Leach crate (ARC-70) indicate when communication is established. The clock board (ARC-32) converts digital input signals into analog output to provide CCDs with programmable, high and low (H/L) voltages within $\pm$13 V. The control of clock rise and fall times of this board is limited, requiring insertion of additional resistors and capacitors in output circuit. The bias board (ARC-33) was developed at LBNL; it provides the CCD all necessary DC bias voltages, and is powered by a -30 V source (either external or from the Leach crate). The dual readout video board (ARC-45) processes and digitizes CCD video outputs.

Recall that DAMIC-style CCDs are packaged with Kapton flex cables and have an Air-

born connector on one end. To interface this connector with the electrical feedthrough, and provide additional control over CCD lines, dedicated printed circuit boards were fabricated at the University of Washington. We refer to these as the first-generation "second stage" amplifier board and "crossover" board. The second stage board is installed in the cryostat (Fig. 5.4 (left)), has arrays of resistors and capacitors to provide additional shaping to clock and bias lines, and its ends feature Airborn and 50-pin DSub connectors. The crossover board is installed at the cryostat exterior; it has a port to externally power the CCD amplifiers with ±15 V, and enables inverting the CCD video signal (often desirable for noise and pixel saturation reasons).

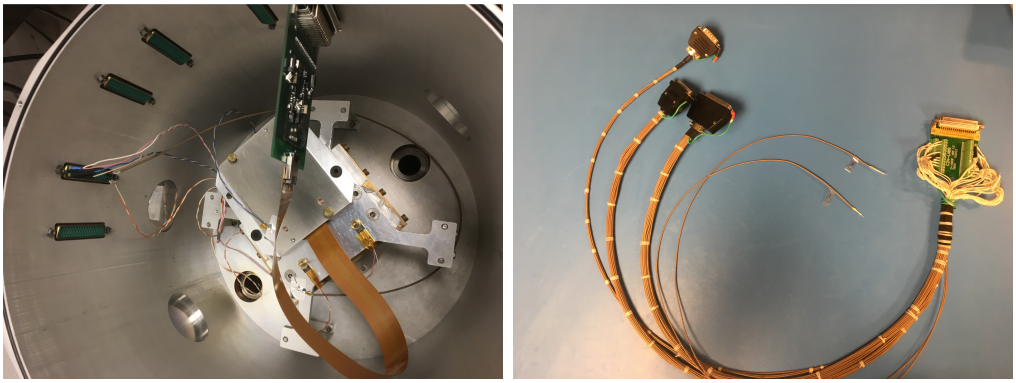

Figure 5.4: Left: A 4k×2k CCD installed in the LPNHE setup and secured to a UW second stage board. Right: The Medusa cable used to deliver clock, bias, and video lines.

A 1 m Medusa cable (Fig. 5.4 (right)) was fabricated to connect the Leach output to the crossover board at the cryostat's exterior. The cable has a split end with 37-pin, 25-pin, and 15-pin DSub connectors to connect to the Leach clock, bias, and video boards, respectively. These lead to a single 50-pin Dsub right angle breakout connector. Thin, 50 Ω coaxial cables were used for fabrication. Video lines were isolated from the connector case, and all shields were connected to their respective cases. Cable pin contacts were tested at opposite ends to check for shorts. Additional lines were put in for the two CCD video outputs then displayed on the oscilloscope, and for external V_{sub} supply.

Commissioning with a DAMIC CCD

The test system was commissioned in 2019 using a DAMIC R&D-era 4k×2k CCD (labeled D3500) of 500 μm thickness. It was packaged at Fermilab with a C-shaped Kapton cable (see Fig. 5.5), and wire bonding done on the CCD's narrow sides (compared to the standard U-shaped Kapton cable that has wire bonding done on the CCD's longer sides).

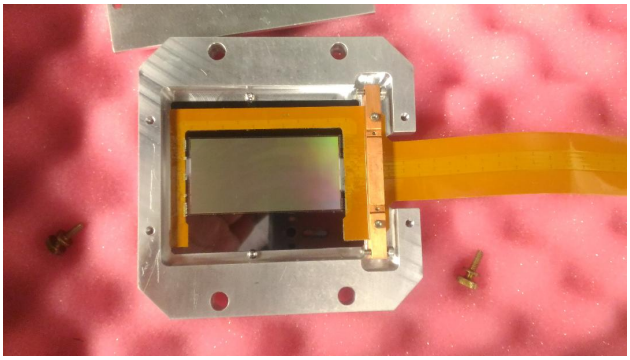

Figure 5.5: CCD D3500, packaged with a C-shaped flex cable, in its aluminum storage container. The CCD was mounted in the LPNHE test system for its commissioning phase. The pink foam is for mechanical protection and is ESD-safe.

Before proceeding with commissioning details, a brief review of CCD naming conventions and signal descriptions is in order. For a 4k×4k CCD, the sensor is divided into quadrants, first by two halves (1 and 2) along pixel columns, and then by sets of separate serial registers and readout amplifiers (*L and U amplifiers*). Final quadrants are labeled U1, U2, L1, L2. The serial and parallel clock phases are labeled with $p = 1, 2, 3$ subscripts as denoted in Chapter 2, and can be further labeled with $a = \mathrm{U}, \mathrm{L}$ subscripts denoting amplifier side. For this 4k×2k CCD, it suffices to just label lines based on the U and L amplifiers, and in particular only the L amplifier was operational. A summary of the various clocks and biases, first introduced in Chapter 2, can be found in Tab. 5.3.

The CCD was mounted onto the cryostat's aluminum plate and its cabling secured to the second stage board. A 50-pin shorting plug was inserted on the external feedthrough for ESD protection. The system was pumped and the CCD cooled down to $T \approx 145$ K.

Signal	Category	Description
V_p	Parallel clocks	Vertical/parallel clocks
TG_a	Parallel clocks	Transfer gate
H_p	Serial clocks	Horizontal/serial clocks
SW_a	Serial clocks	Summing well transfer clock
RG_a	Serial clocks	Floating diffusion capacitor reset gate clock
OG_a	Bias voltages	Summing well / floating diffusion isolation gate (DC)
V_{r_a}	Bias voltages	Floating diffusion capacitor reset reference voltage
V_{dd_a}	Bias voltages	Readout source follower transistor drain voltage (DC)
V_{og_a}	Bias voltages	Readout source follower transistors sources – output signal
p+	Bias voltages	p+ guard ring contact
n+	Bias voltages	n+ channel stop implant contacts
V_{sub}	Bias voltages	substrate depletion voltage

Table 5.3: DAMIC CCD signal naming conventions (p subscripts correspond to phase and a subscripts correspond to amplifier U/L).

The CCD was supplied with V_{sub} from a pack consisting of twelve 9 V batteries soldered in series and connected individually to incremental switches and overall to a master switch. The LBNL literature for DAMIC CCDs [112] specifies a linear ramp rate of 75 V/s, and recommends not significantly exceeding this rate. To control the V_{sub} ramp, an RC circuit (see Fig. 5.6) was formed with a 10 kΩ resistor and 50 μF capacitor (time constant τ = RC = 0.5). A relay was also installed in order to control the master switch remotely.

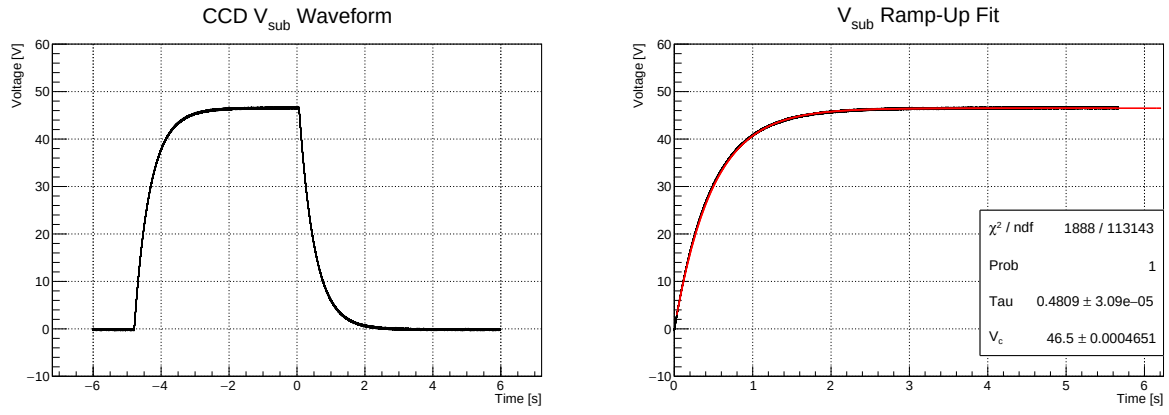

Figure 5.6: Left: The V_{sub} waveform generated from a custom battery pack with an RC circuit and relay. Right: A fit to the ramp-up waveform, with extracted time constant and voltage of 46.5 V produced from five of the twelve batteries in the pack switched on.

For commissioning, image acquisition was done with `Owl`, the default software that comes with the Leach controller. `Owl` has a graphic user interface that facilitates loading and running the CCD's sequencer, which encodes the timing and waveform generation that must be executed. It also has options to edit exposure time, gain parameters, and selecting amplifiers for readout. While clocks and bias values can be manually edited, CCD scripts were written and loaded for relevant procedures:

- Setting Bias and Clock Voltages: this procedure stores tables with the default parameters for when the CCD is idly clocking (charge is not actually read out).

- Erase Procedure: CCDs are initially subjected to strong illumination when they are first turned on, due to high dark current caused partially by the emptying of electron traps at Si-SiO_2 interface. The erase procedure clocks off excess charge by ramping V_{sub} to 0 V in a controlled manner, then creating an equipotential of all parallel clocks by setting them to 9 V (leading to inversion and flooding the CCD surface with charge), and finally re-ramping V_{sub} back to its nominal value. It is then necessary to wait the equivalent time for all of the CCD's pixels to be clocked off in its idle mode. For example, a sufficient wait time for a 8 Mpix CCD with pixel integration time of 10 μs would be 2 m.

- Purge Procedure: if CCD channel stops are left in different charged states following initial power-up (leading to images with irregular baselines), then a purge by setting all parallel clocks to -9 V for a fraction of a second can rectify the situation.

- Exposure: acquire an image for a specified exposure time.

Prior to connecting and operating the CCD, bias voltages were confirmed by running the system and probing corresponding lines with a multimeter. These values are summarized in Tab. 5.4. Clock waveforms were checked using the oscilloscope; their 10-90 rise times ($t_{10\text{-}90}$) and signal widths (t_w) were extracted, and can be seen in Tab. 5.5 and Fig. 5.7.

Signal	LPNHE Value	LBNL Value
V_{r_U}	-12.47 V	-12.5 V
V_{r_L}	-12.44 V	-12.5 V
V_{dd_U}	-21.89 V	-22.0 V
V_{dd_L}	-21.89 V	-22.0 V
V_{og_U}	2.21 V	2.16 V
V_{og_L}	2.21 V	2.16 V

Table 5.4: Multimeter measurements of Leach-generated CCD bias voltages.

Signal	V_L	V_H	t_{10-90} [ns]	t_w [μs]
$V1$	3.3	7.9	52.8	69.3
$V2$	3.3	7.9	48.0	69.3
$V3$	3.4	7.9	40.8	69.3
TG	3.2	8.1	43.2	115.0
$H1$	1.2	6.6	44.0	0.864
$H2$	1.4	6.5	38.4	0.885
$H3$	1.2	6.6	39.2	0.862
SW	-2.5	5.2	37.6	0.557
RG	-4.0	0.1	56.0	0.4

Table 5.5: Clock voltages used to operate a DAMIC 4k×2k CCD in the LPNHE test chamber. Rise times and signal widths are provided, consistent with values listed in Ref. [112].

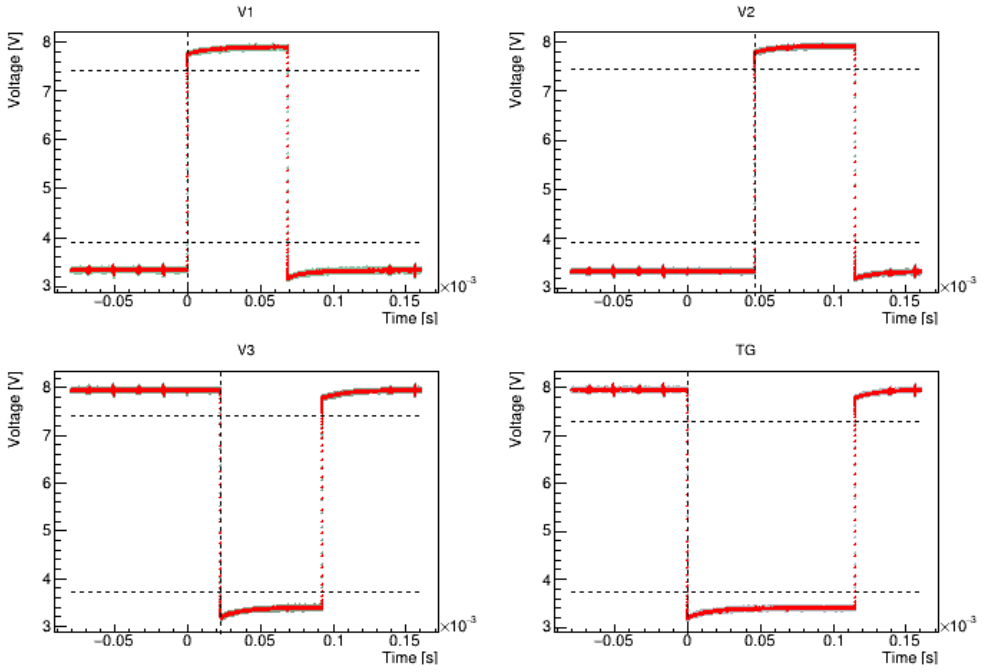

Figure 5.7: Sample waveforms for CCD vertical clocks.

Revisiting the discussion on energy calibration of CCDs, recall that optimal approach requires the use of radioactive or optical sources. A 1 μC (37k decays/s) ^{241}Am source was made available for initial image acquisition. ^{241}Am decays by alpha transitions; most decays (84%) populate the excited level of ^{237}Np with an energy of 59.54 keV [113] that can be used to obtain the CCD's calibration constant. To do so, we must account for photon conversion and CCD collection probability. Namely, we must consider the attenuation by material between the source and the CCD, the solid angle subtended by the sensor active area, the absorption processes in the CCD, and the activity of the source. Using information from the `NIST XCOM` database [114], we can proceed with a rough estimate of expected statistics.

$$I_x = I_o e^{-\mu x} \tag{5.1}$$

We start with the material thicknesses within the setup: the aluminum plate covering the cryostat (atop which the source rests) is $x_{plate} \approx 0.8$ cm; the quartz window of the cryostat is $x_{quartz} \approx 0.8$ cm; the aluminum cover of the CCD shipping container is $x_{cover} \approx 0.5$ cm; the aforementioned CCD thickness is $x_{CCD} = 500$ μm. The corresponding material densities are: $\rho_{Al} = 2.7$ g/cm^3, $\rho_{Quartz} = 2.648$ g/cm^3, and $\rho_{Si} = 2.324$ g/cm^3.

Attenuation is calculated using Eq. 5.1, where I_o is the initial intensity of an assumed narrow beam of mono-energetic photons, I_x is the intensity of photons transmitted across some distance x, and μ is the energy-dependent linear attenuation coefficient of the material. We define three attenuation factors, corresponding to the aluminum plate $f_1 = e^{-\mu_{Al} x_{plate}} \approx 0.55$, the quartz window $f_2 = e^{-\mu_{quartz} x_{quartz}} \approx 0.63$, and the aluminum storage container cover $f_3 = e^{-\mu_{Al} x_{cover}} \approx 0.69$, and one solid angle factor $f_4 = \frac{A_{CCD}}{4\pi r^2} \approx 0.0036$. Here, $A_{CCD} = 18$ cm^2 and $r \approx 20$ cm is the distance from the source to the CCD. The photo-electric absorption at 60 keV for silicon is 0.1288 cm^2/g. Multiplying this by ρ_{Si} and x_{CCD} gives a factor $f_5 \approx 0.015$. The net reduction factor is thus $f \approx 1.3 \times 10^{-5}$, meaning a 1 μC source would require a 1 d exposure for 40k detected events.

First Image Acquisition and Results

An example of an oscilloscope-acquired CCD video waveform during idle clocking can be seen in Fig. 5.8, with $\approx$ 20 μs pixel integration time, and both reset and summing well pulses visible (as first shown in Fig. 2.3). In 2019, we completed a first data run. Images (4200×2100) including overscan were taken with $T_{CCD} = 145$ K, 40 μs integration time, $V_{sub} = 47.0$ V, and 224 s exposure time. The bias board and amplifiers were powered with external power supplies. Image processing followed the standard DAMIC procedure.

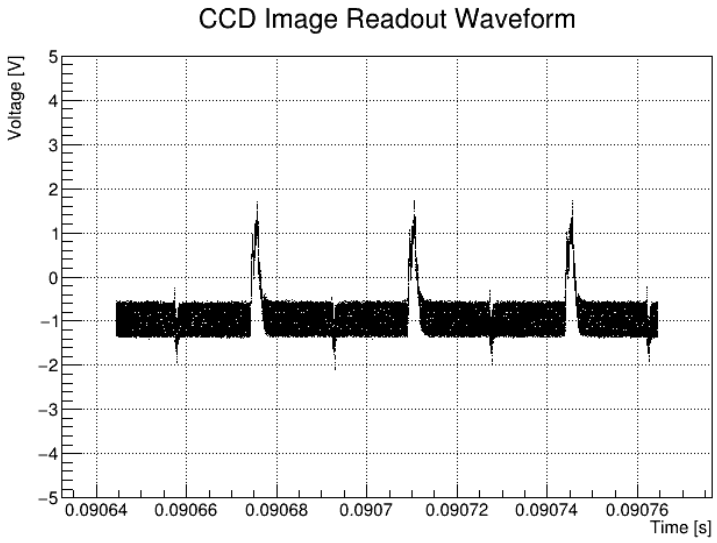

Figure 5.8: Oscilloscope waveform of the CCD video signal during idle clocking.

We initially acquired 15 h of background data (no source), followed by 30 h of ^{241}Am data. The resulting energy spectrum between 0-500 keV can be seen in Fig. 5.9, with the background data scaled to reflect the same equivalent exposure as the ^{241}Am run. Background data acquired with the same CCD under near-identical operating parameters at the University of Chicago is also shown. The discrepancy between the background spectra is primarily due to the system orientation at the University of Chicago, requiring CCD installation with the sensor's area perpendicular to the surface (as in Ref. [60]), leading to a decrease in cosmic rays traversing the device. The background-subtracted spectrum between

0-100 keV can be seen in Fig. 5.10. The calibration constant is $C = 5.57 \times 10^{-4}$ keV/ADU.

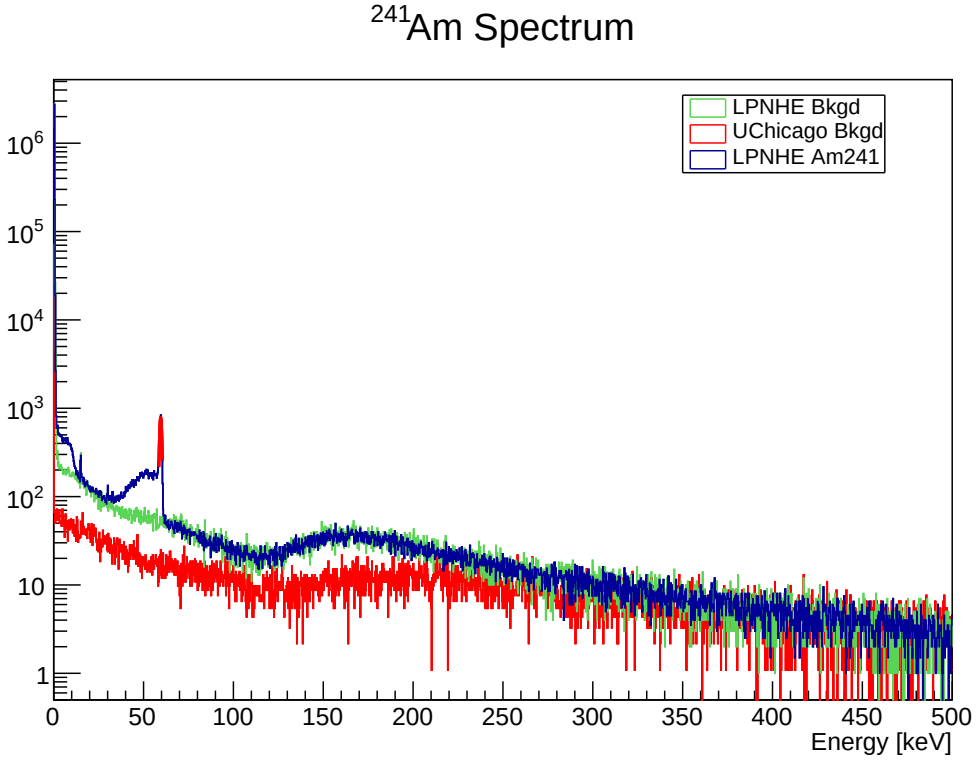

Figure 5.9: CCD energy spectrum of ^{241}Am data, with background data acquired at LPNHE and the University of Chicago (discrepancy in background spectra described in the text). A cosmic ray muon peak is visible between 150-200 keV.

Optimizing Readout Noise

As we have seen, the readout noise determines the effective energy threshold of a CCD dark matter experiment. Optimizing the readout noise of CCD test systems is therefore a critical task. Some noise patterns can be seen by eye within images. For example, there were recurring noise patterns (Fig. 5.11) that were successfully removed following several modifications to the setup. To summarize efforts to reduce the system noise:

- The preamp video lines were removed and terminated during acquisition.
- The pressure gauge was switched off.

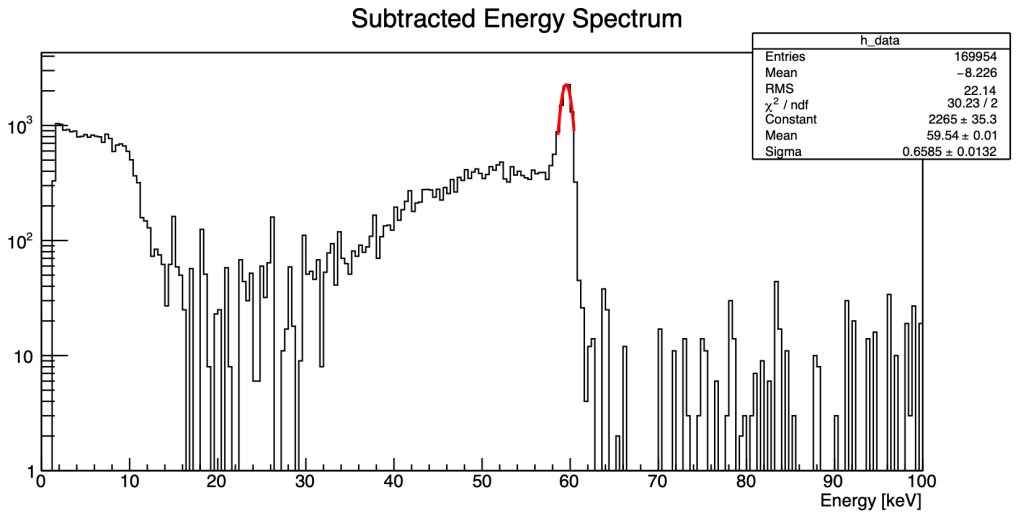

Figure 5.10: Subtracted energy spectrum for ^{241}Am data, with the fit to its 59.54 keV peak used to extract the CCD calibration constant.

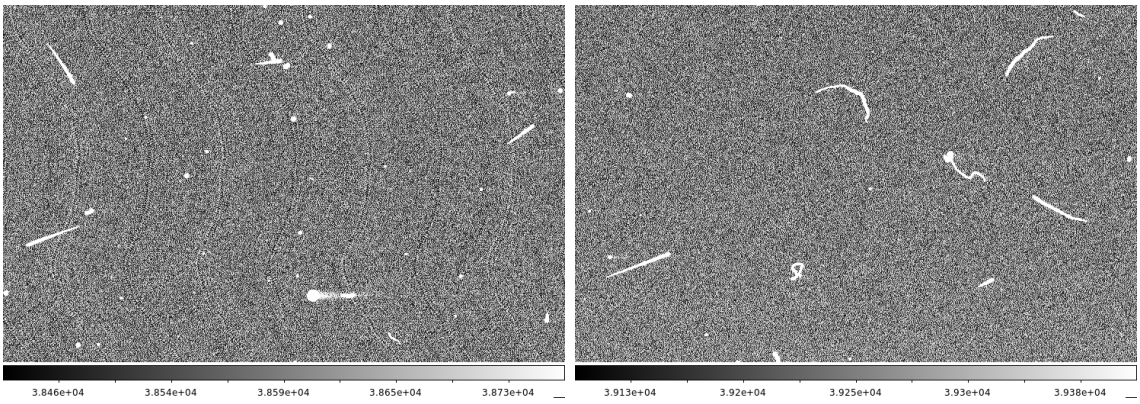

Figure 5.11: Sample images viewed in DS9: the recurring, "wavy" noise bands on the left image are removed in the right image after the described hardware intervention to optimize the noise of the setup.

- The pump was electrically isolated with a plastic KF40 centering ring and clamp.
- A jumper was put in to connect the analog and digital ground planes of the bias board.
- The Medusa cable video lines were soldered directly to the 50-pin breakout connector.
- External, low-noise power supplies (in a floating ground configuration) were used to power the bias board and CCD amplifiers instead of the noisier Leach back plane.
- A grounding strap was installed between the crossover board and Leach housing crate.

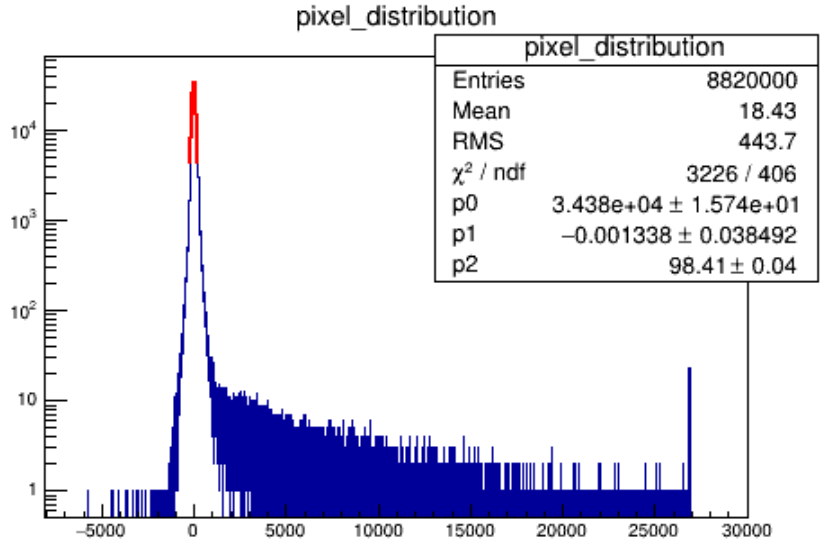

Figure 5.12: Pixel charge distribution of CCD D3500 prior to any work on noise optimization.

To quantify this noise reduction work, let's revisit CCD pixel charge distributions. Fig. 5.12 shows such a pedestal-subtracted distribution for CCD D3500, prior to the execution of processing steps. The fit gives $\sigma_{\text{pix}} = 98.41$ ADU. Given the calibration constant, we can convert this to units of eV, and then using 3.77 eV per electron, we obtain a value of σ_{pix} in standardized units [e^-] that can be used to compare performance across different systems. The system initially had a noise of 15 e^-; we were able to reduce this to 6 e^-.

An optimal integration time is also important to minimizing the system noise. For longer integration, which would decrease white noise, the $1/f$ noise of the CCD amplifier becomes

dominant. We investigated the noise across a sweep of integration times and with varying gain, as seen in Fig. 5.13. The noise plateaued at 6 e^- starting at 25 μs; the University of Chicago reference point at a 4 e^- level can be explained by an electrically-isolated cryocooler in that system. We note that acquisition with the lowest possible integration time (that still optimizes noise) saves on readout time necessary per image, and can thus enable a larger overall exposure. Reaching low noise at short integration times thus becomes an important challenge to address.

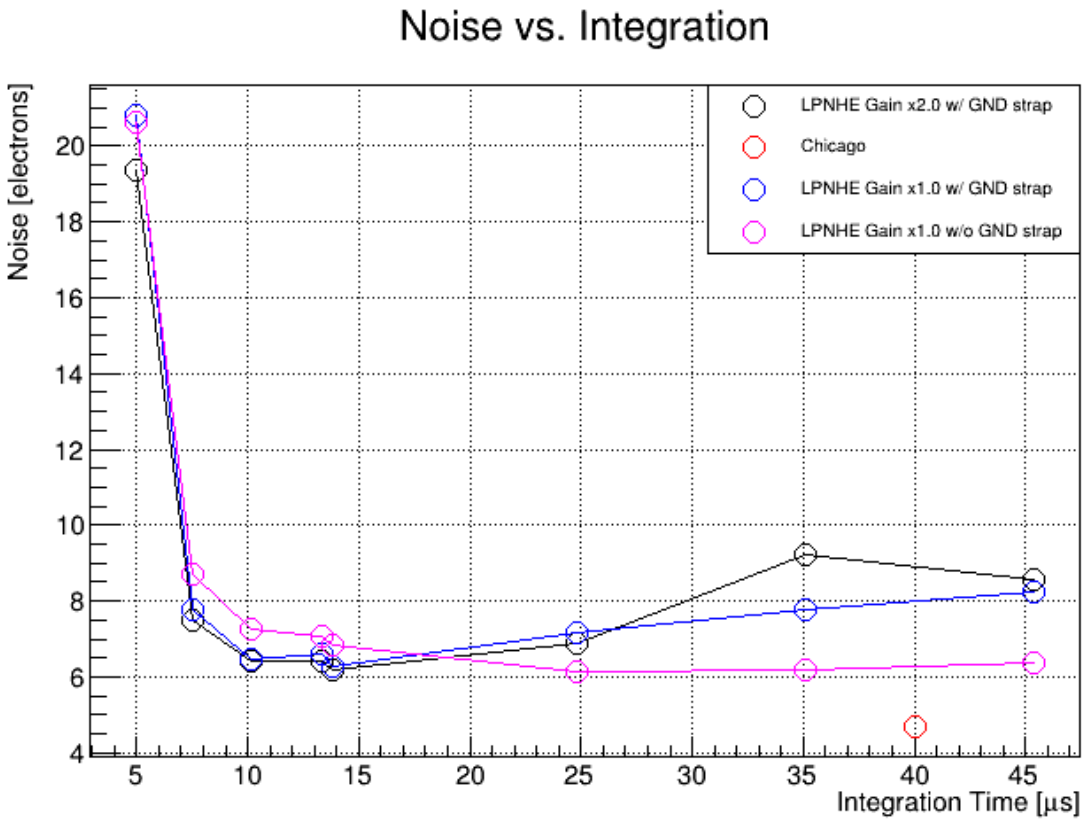

Figure 5.13: Readout noise vs. integration time, obtained for CCD D3500.

CHAPTER 6

SKIPPER CCDS: THE FUTURE OF CCD DARK MATTER SEARCHES

In earlier chapters, we introduced the microstructure and operation of conventional CCDs, demonstrated the capabilities of CCDs as dark matter detectors, and discussed the noise levels of operating such conventional CCDs. The ultimate limitations on improving these noise levels are due to $1/f$ noise, and the future of CCD dark matter searches rely on breaking the sub-electron noise barrier. To that end, in this chapter we turn our discussion to Skipper CCD technology, first proposed by Janesick et al. [115]. We provide a review of Skipper CCD operation, and then discuss DAMIC-M Skipper CCD characterization efforts.

6.1 Skipper CCD Operating Principles

The core concept of Skipper CCDs is to reach sub-electron resolution by performing a non-destructive, multiple measurement of pixel charge. We refer to these non-destructive charge measurements (NDCMs) interchangeably as "skips" and note that by averaging several samples of charge from the same pixel, we are able to reduce noise by the square root of the number N of NDCMs: $\sigma_{\rm pix} \rightarrow \frac{\sigma_{\rm pix}}{\sqrt{N}}$. This is due to modeling pixel charge as the actual induced ionization, with an additional Gaussian white noise component from readout.

An important outcome of Skipper readout is a reduction in low-frequency noise, driven by the shorter integration time of each measurement relative to conventional readout, shown Fig. 6.1. But there is a trade-off between noise reduction image acquisition time. For example, let's say we want to take our noise level from a noise of 6 e^- (that of the LPNHE test system) down to 0.1 e^-. This would require 3600 skips; assuming we are able to operate with a pixel integration time of 5 μs and that we are reading a 6 Mpix CCD, a single image would take 1.25 d to read. For reference, recall that the typical read time for DAMIC at

SNOLAB images is on the order of 10 m. Reducing the starting noise continues to be crucial: for the scenario above, it would take only 400 skips to reach 0.1 e^- if the starting noise were 2 e^- (and thus 3.33 h read time for the cited image size).

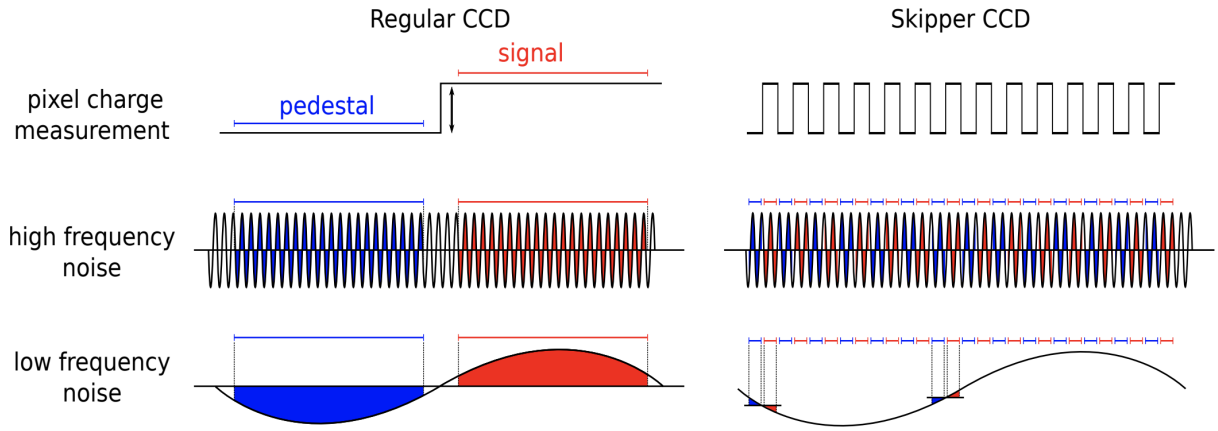

Figure 6.1: Conventional vs. Skipper CCD readout: the effect of low-frequency noise is visibly smaller for the Skipper case. Figure taken from Ref. [116].

The Skipper read procedure relies on some key modifications to the output stage. Conventional CCDs utilize floating diffusion gates, and Skipper CCDs instead use floating gates [117]. The former creates ohmic contact between the heavily-doped diffusion region and the reset transistor / amplifier MOSFET. This contact means the charge is read via a voltage change of the SN (Eq. 2.1) and that the readout is destructive – the subsequent SN reset to V_R flushes out the charge. Replacing the readout node with a floating gate is an elegant solution, since the SN operates equivalently to a gate: the charge still induces a voltage measured by the output amplifier, but there's no ohmic contact that forces the charge to be flushed when RG sets the floating gate potential back to V_R. Modulation of the SW and OG (where OG is a clock in Skipper CCDs) can flow the charge back to the SN for an additional number of desired measurements, before a dump gate (DG) and drain potential V_{drain} discard the charge. Fig. 6.2 shows a schematic of this process, and Fig. 6.3 shows a microscope image of a Skipper output stage area, which can be contrasted to that of a conventional CCD's in Fig. 2.2 (left).

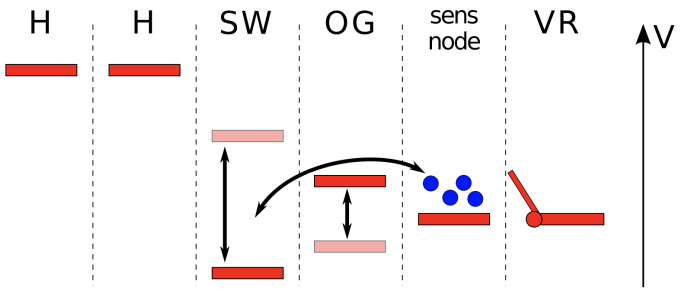

Figure 6.2: Schematic of a Skipper read: instead of throwing away the charge after one measurement, the OG and SW voltages can be lowered to move the charge from the SN back to the SW again for additional NDCMs. Figure taken from Ref. [116].

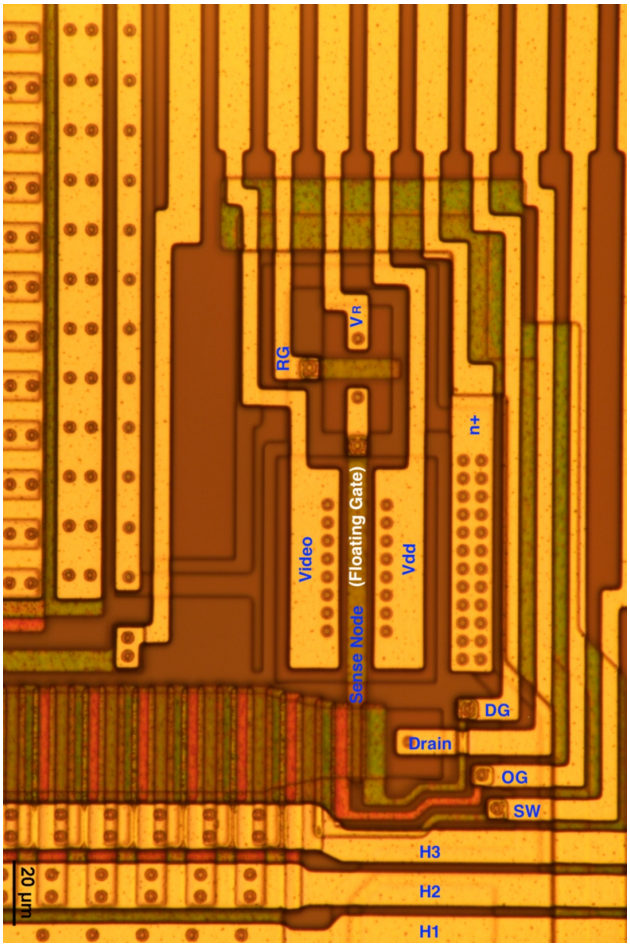

Figure 6.3: Microscope image (50× magnification) of a DAMIC-M Skipper CCD output stage, featuring the 47/6 output amplifier described in the text.

6.2 DAMIC-M Skipper CCD Characterization

In order to guide the design of the final CCDs to be deployed for the DAMIC-M experiment, the DAMIC-M collaboration organized for multiple cycles of pre-production batches. These CCDs enable R&D studies of Skipper design features and performance, namely single electron resolution, dark current, and amplifier characteristics. The first batch of such Skipper devices were 1k×6k CCDs (1024×6176 pixels) diced from a wafer with an effective area of 6k×6k (see Fig. 6.4) and packaged at the University of Washington. A labeled prototype 1k×6k CCD was first shown in Fig. 2.5.

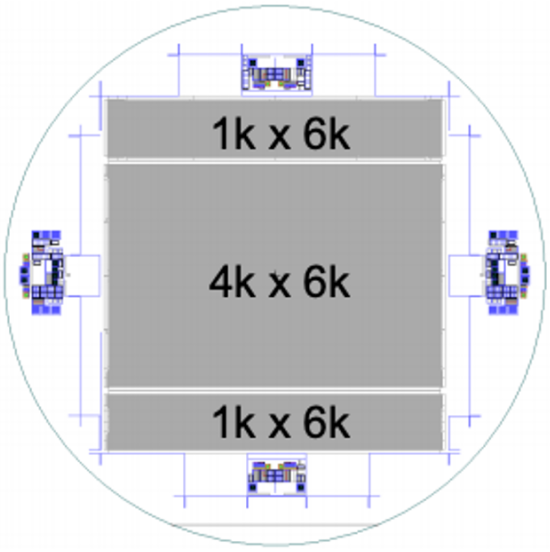

Figure 6.4: Schematic of a large wafer from which DAMIC-M CCDs are diced.

The convention of these CCDs follows that previously outlined for conventional LBNL CCDs. However, following the work presented by S. Haque et al. in Ref. [49] on the design of low-noise CCD output amplifiers, two pairs of different output amplifiers were deployed in DAMIC-M 1k×6k CCDs. The 47/6 (W/L) "standard" amplifier used in DAMIC at SNOLAB CCDs has an n^+ polysilicon gate and metal connection to the SN; the "new" amplifier aims to reduce noise and minimize the capacitance C_s at the SN by featuring

buried contact technology with a p^+ polysilicon gate that directly connects to the SN. The pairs of amplifiers were used on different *Registers* (sides) of the CCD: Register 1's U1 and L1 amplifiers incorporated the 20/6 output amplifier, whereas Register 2's U2 and L2 amplifiers incorporated the standard 47/6 one. The CCDs also feature JFETs to ensure 50 Ω impedance and to better drive the output signal across nearly 2 m of cabling.

6.2.1 Modifications to CCD Test Chambers

A DAMIC-M prototype CCD (UW1603S) was deployed in the LPNHE chamber (Fig. 6.5) in 2019; its flex cable uses a 50-pin connector instead of an Airborn one. In order to improve system performance and operate Skipper CCDs, several modifications/tests were made/run:

- A different cryocooler was used, enabling a lower CCD temperature $T_{CCD} \approx 120$ K
- The previous vacuum-side amplifier board was replaced with an updated air-side board. The advantage of an air-side board is being able to more easily change RC components to test various clock timing parameters without having the break system vacuum.
- The Medusa cable 50-pin DSub connector was replaced with a breakout board, standardizing cabling assembly. This board features direct SMA connection for the CCD's V_{sub} line. It also has two separate video outputs for each CCD Register.
- Custom image acquisition tools, `CCDDrone` and `CCDSequencer` [118], were developed at the University of Washington to facilitate easier interfacing with and control of the Leach, execution of CCD image procedures (e.g. exposure, erase), and testing of CCD parameters via the use of user-friendly configuration files.
- Checks on bias voltages and clocks were performed as before. A test of the full electronics chain was done (Fig. 6.6). A dual-channel function generator was used to mimic a CCD video signal by generating two sine waves. The subsequent output from the Leach video board was measured on a scope, with a measured system gain of ×32.

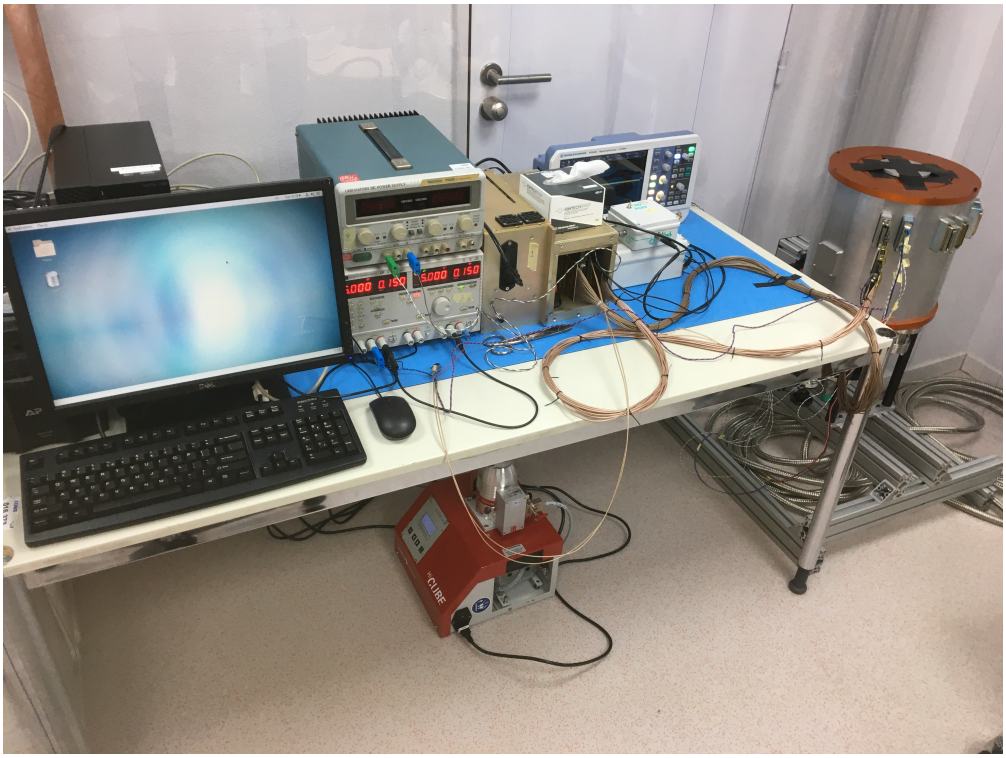

Figure 6.5: The LPNHE Skipper CCD test system.

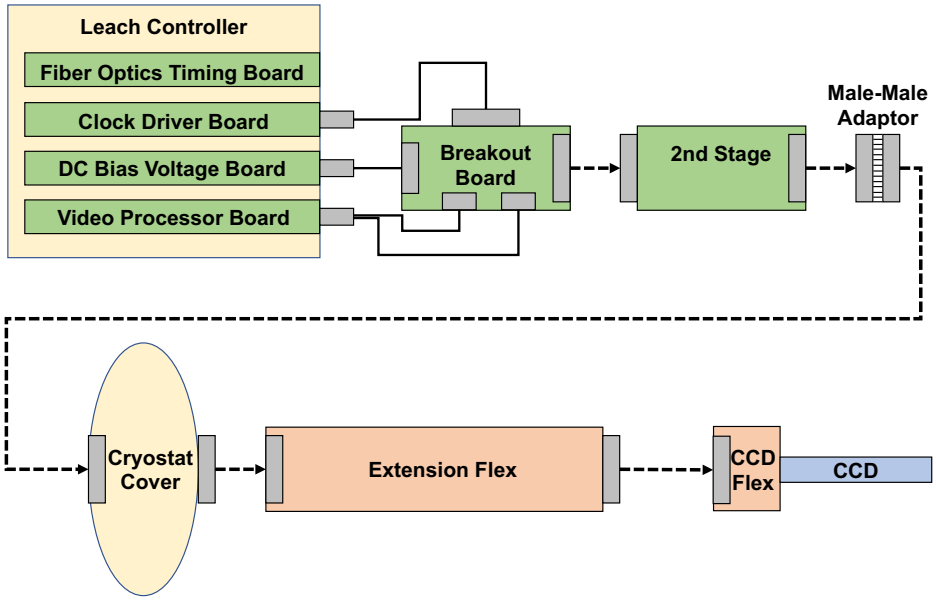

Figure 6.6: Schematic showing the electronics chain of the LPNHE test system.

6.2.2 Achieving Single-Electron Resolution

The R&D studies of Ref. [119] set the ground-work to achieve reliable single-electron sensitivity in a large-format CCD (3.6 Mpix), addressing the spurious charge generation concerns of Ref. [120] by deploying the floating gate design described above. DAMIC-M, however, aims to implement the largest-ever Skipper CCDs in order to maximize its exposure. Achieving single-electron sensitivity in DAMIC-M CCDs has therefore been a core focus.

Our efforts to characterize the UW1603S Skipper CCD at LPNHE were guided by those of conventional LBNL CCDs [112] as a starting point, in addition to the work of Ref. [49], which indicates an effect of bias voltages V_R and V_{dd} on noise. We aim to optimize readout noise and charge loss between skips (note that charge loss here refers to a possible loss due to non-optimal clock settings in executing NDCMs, not CTI by traps or clocking charge across the sensor's active area). There are many factors at play in this process. An automated image acquisition/analysis procedure was established to efficiently test across this vast parameter space and identify optimal parameters. We will touch on this shortly.

To review the steps for a skipper measurement: by modulating horizontal clocks, charge is moved within the serial register to the summing well, which sits low, shown in a sample timing waveform in Fig. 6.7 (top). At this point, we can refer to Fig. 6.7 (bottom) as a visual reference. The RG is triggered in order to prepare the SN for charge measurement. As in a conventional CCD, the SN is then read for integration time τ_{int} to obtain a pedestal value. The SW is sent to its high value, pushing charge into the OG and then into the SN, which is integrated for a time τ_{sig} to get a signal value. This describes the continued use of correlated double sampling. The OG is briefly set low, enabling charge to move back into the SW; it is then set back high. Then the RG is triggered once more to prepare the SN for measurement. It is optional to do this after every skip, and can be done after every complete pixel read or even after every row. Once the desired NDCMs is reached, the DG is triggered low while the SW is high so that the charge can move to the drain.

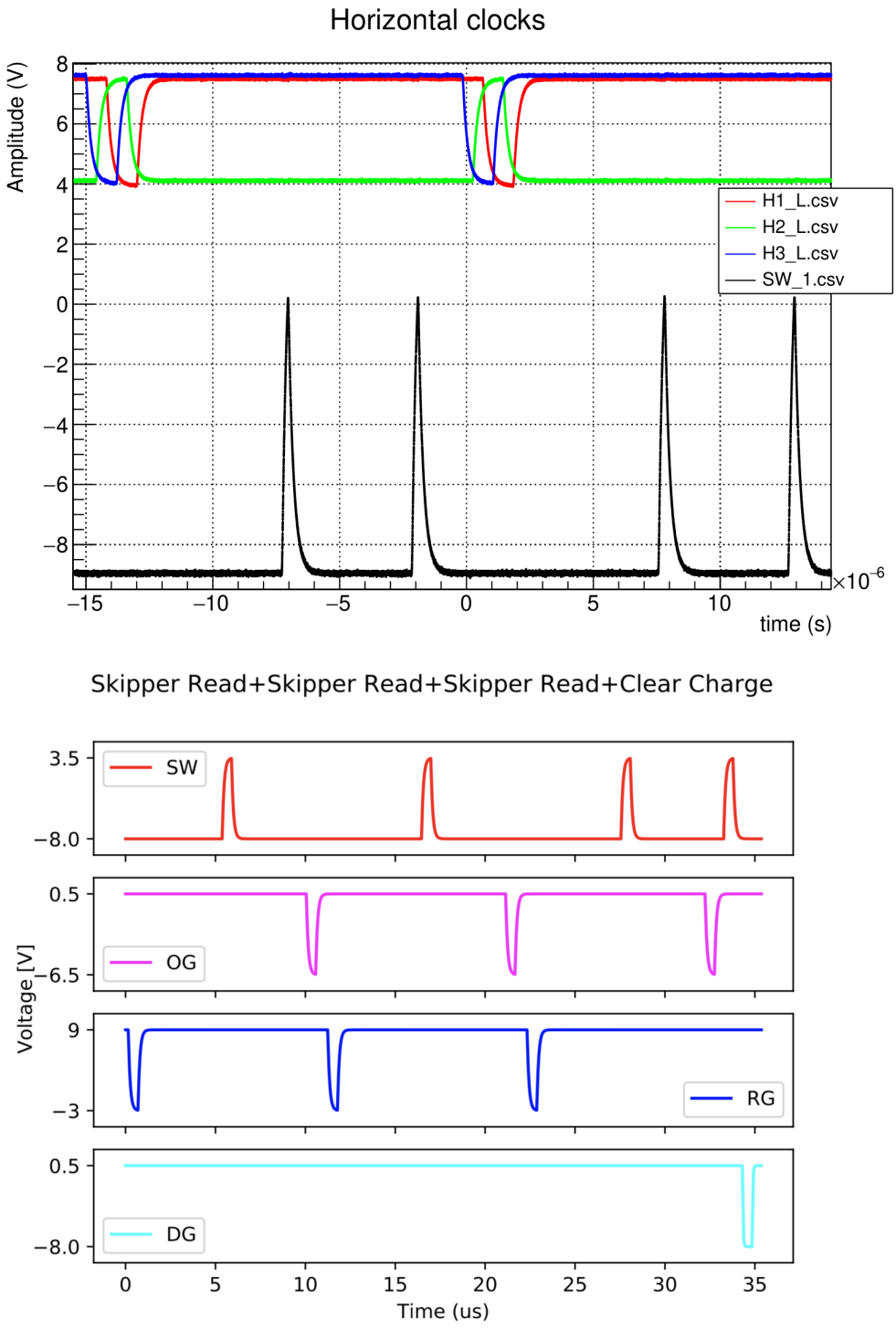

Figure 6.7: Top: Timing diagram for horizontal clocking to move charge into the SW. Bottom: Timing diagram demonstrating 3 NDCMs of charge.

As mentioned, a standardized procedure was implemented to scan across the parameter space of principal bias voltages, clock voltages, and timing parameters. For a given configuration of parameters, images were initially evaluated for readout noise, Skipper charge loss, an appropriate $\frac{1}{\sqrt{N}}$ reduction of noise, gain (calibration) extracted from the single-electron peak of the pixel charge distribution. We have already motivated the need for a low starting readout noise: the nominal value from commissioning the LPNHE system was about 6 e^-.

In Fig. 6.9, we see an example of a visual inspection that can be done to quickly verify charge loss. The same section of the CCD is shown, but the left side corresponds to the averaged-out image across all skips, whereas the right side shows the difference in pixel values for this section of the image between the first and last skips. The visible residual presence of charge tracks after taking the skip difference indicates charge loss: this is shown in the bottom of Fig. 6.9, where we see that the pixel charge difference distribution isn't centered at zero (the value expected for no charge loss). We can subsequently quantify this loss using Eq. 6.1:

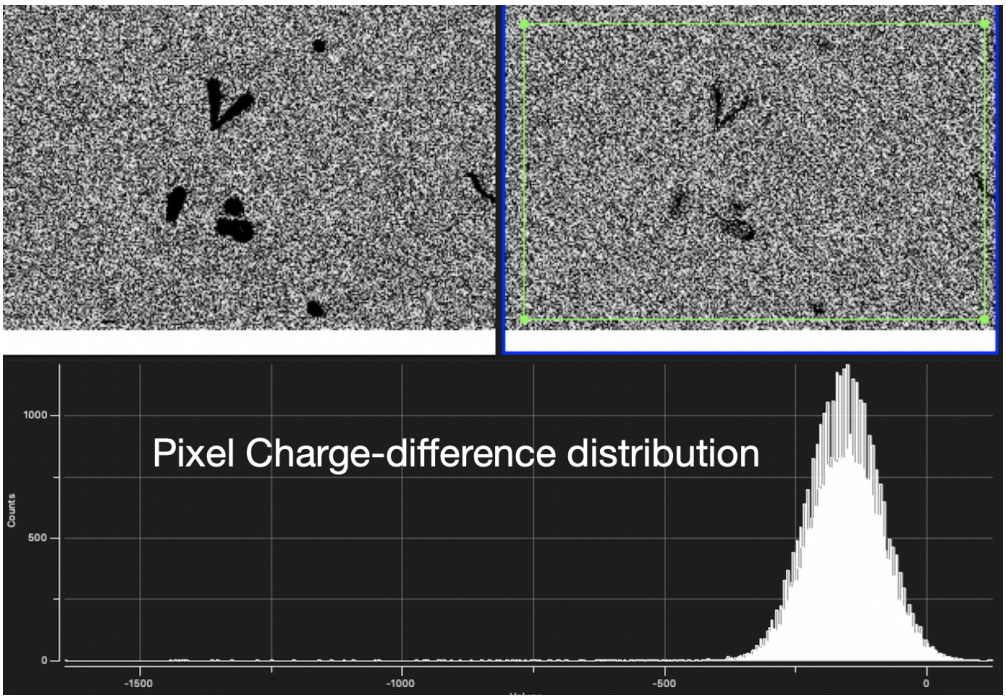

Figure 6.8: Example of charge loss between first and last NDCMs of a Skipper CCD image.

$$k_{cl}(3.5\sigma_{\text{diff}}) = \frac{N_{>} - N_{<}}{N_{>} + N_{<}} \tag{6.1}$$

where k_{cl} quantifies the number of outliers greater than ($N_{>}$) or less than ($N_{<}$) a nominal 3.5σ of the pixel charge difference distribution. During parameter scans, most high-skip images were taken with only 10 rows of the CCD (recall the large readout times required when reading an entire CCD with many skips). A limiting factor in using k_{cl} is therefore low statistics of outliers in some cases; as a solution, we introduced $S(k_{cl})$, which simply weights k_{cl} by its uncertainty. Both k_{cl} and $S(k_{cl})$ should be ≈ 0 for cases of no charge loss; a value < 0 indicates charge loss, while > 0 indicates potential charge injection in the system.

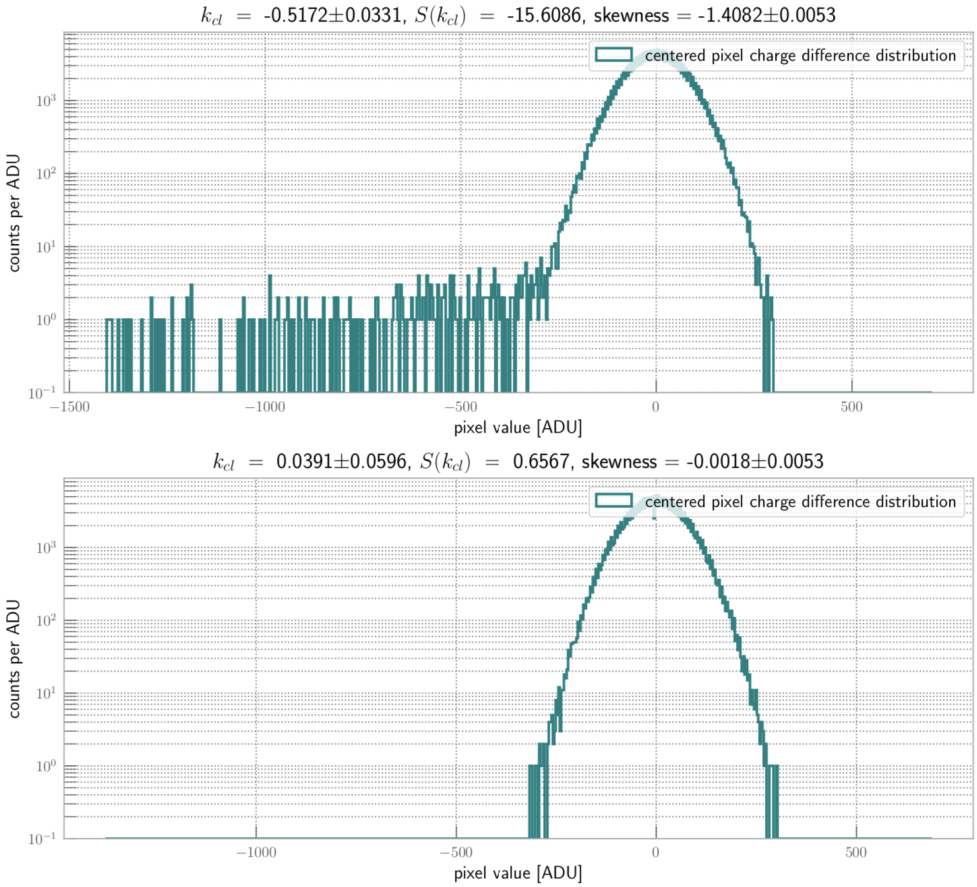

Figure 6.9: Quantifying charge loss in the pixel charge difference spectra of two Skipper images. Charge loss is observed in the top spectrum, but not the bottom.

Following a full-parameter scan, a standard configuration of values (summarized in Tab. 6.1) was obtained to operate the LPNHE Skipper CCD. The table summarizes values for Register 1; the values for Register 2 were identical, with the exception of V_R (set to -4.4 V), summing well voltages (set to 1.0 V high, -8 V low), and the output gate low voltage (set to -6.5 V). This enabled the first single-electron resolution obtained at LPNHE: the corresponding spectrum and expected decreasing noise trend can be seen in Fig. 6.10. This work guided parameter scans for other DAMIC-M CCDs, enabling a resolution of $\sigma_{\text{pix}} \sim 0.07$ e^- after 1000 skips for the best-performing CCD tested so far (see Fig. 6.12). Calibration constants are conveniently obtained by fitting the single-electron peak (a constant $k \sim 10$ ADU/e^- was typically observed in the LPNHE setup under nominal operating parameters). This result reflects a major achievement towards the development of DAMIC-M.

Parameter	**Value**
Horizontal Clocks	4.5 V (High), 1.0 V (Low)
Vertical Clocks	5.5 V (High), 1.5 V (Low)
Transfer Gate	5.0 V (High), 1.5 V (Low)
Summing Well	2.5 V (High), -9.0 V (Low)
Output Gate	-3.0 V (High), -8.0 V (Low)
Reset Gate	7.3 V (High), -4.0 V (Low)
Dump Gate	2.0 V (High), -8.0 V (Low)
Pedestal Wait Time	4.0 μs
Signal Wait Time	4.0 μs
Integration Time	10.0 μs
Summing Well Pulse Width	0.2 μs
Output Gate Pulse Width	0.2 μs
Skipping Reset Gate Pulse Width	0.28 μs
Dump Gate Pulse Width	0.28 μs
V_R	-4.5 V
V_{dd}	-17.0 V
V_{drain}	-17.0 V
V_{sub}	47.0 V

Table 6.1: Voltage and timing parameters used to operate CCD UW1603S at LPNHE.

Several noteworthy observations were made during testing of 1k×6k Skipper CCDs across multiple institutions. In particular:

- There seems to be greater charge loss between the first and second skips compared to the second and Nth skips. This is potentially due the different underlying transfer processes at play. The charge is in the floating gate during first measurement, and then has to be brought back to the SW for the second measurement. While the process of modulating the SW and OG for later skips seems fine, ensuring the SW is sufficiently low and that there is enough time to transfer the charge for the first measurement seems to be important. Another culprit could be the DG, which must be set sufficiently high to fully remove charge.

- The ideal separation between high/low voltage levels of H and V clocks was found to be 2-5 V. The SW requires the largest span in high/low values since the high value has to ensure proper transfer of charge for measurement by the SN, while the low must ensure proper, complete storage of charge prior to any SN measurement. The OG, a clock in Skipper operation, is balanced around the value of V_R to ensure charge can proceed to measurement or move back to the SW (this also means that in shifting V_R, one must shift other clock levels accordingly).

- In a Skipper CCD V_R sets the potential of the floating gate SN, while V_{drain} sets the minimum potential and (together with the gate voltages) defines the extent of the depletion region at the p-n junction; it acts as the reverse biasing reference voltage we previously outlined in Eq. 2.5. We have found that V_{drain} cannot be too low for risk of overdepleting the Si-SiO_2 interface.

- Despite the results outlined in Ref. [49], no significant different in gain was observed between the 47/6 and 20/6 amplifiers of the 1k×6k CCDs. Moreover, scans across V_{dd} did not produce the cited decrease in readout noise. Given the experience using the 47/6 amplifiers at DAMIC at SNOLAB, this continued as the default design choice for DAMIC-M CCD amplifiers.

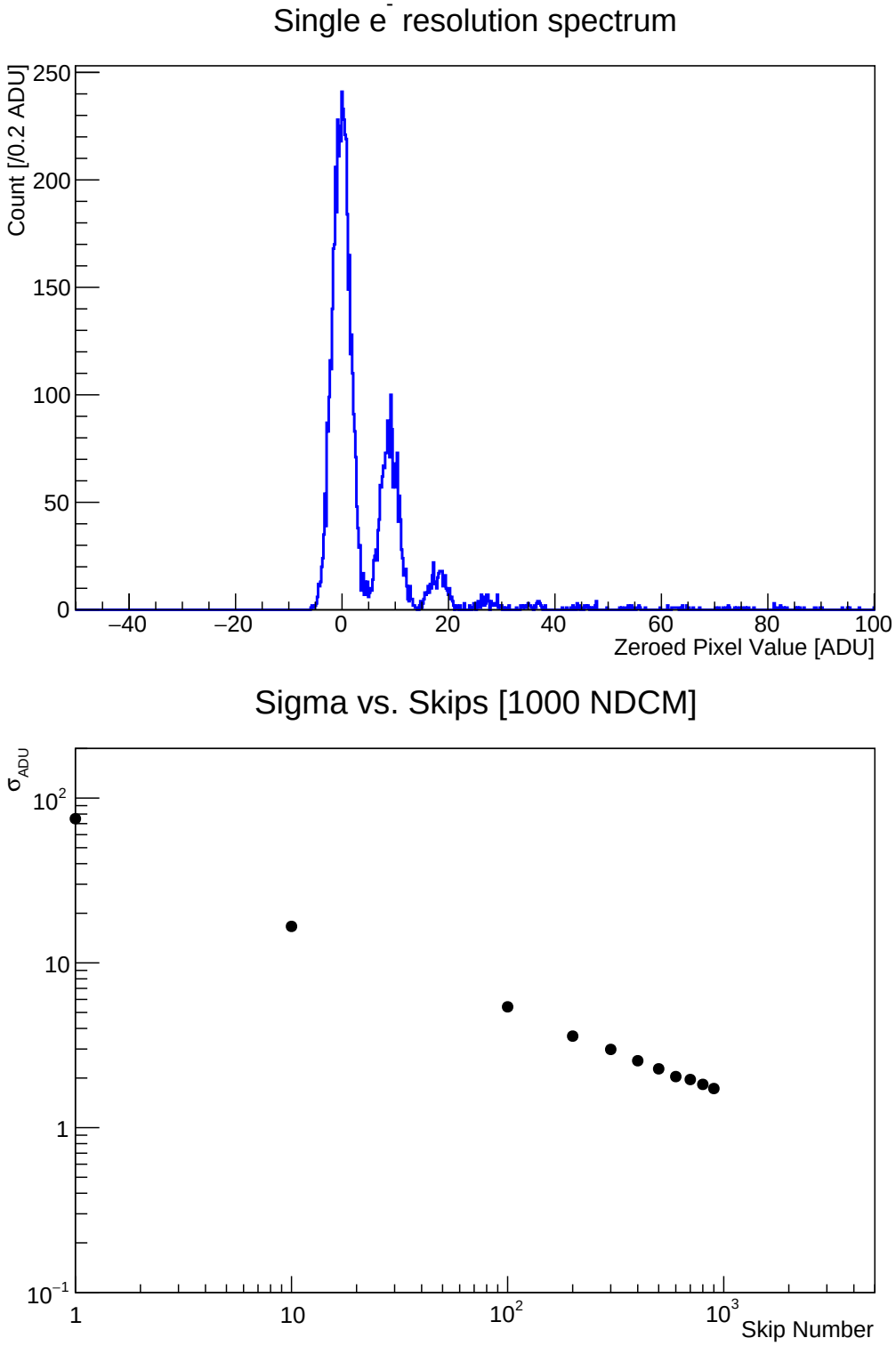

Figure 6.10: The first successful singe-electron distribution and corresponding $1/\sqrt{N}$ decrease in noise (1000 skips) observed at LPNHE.

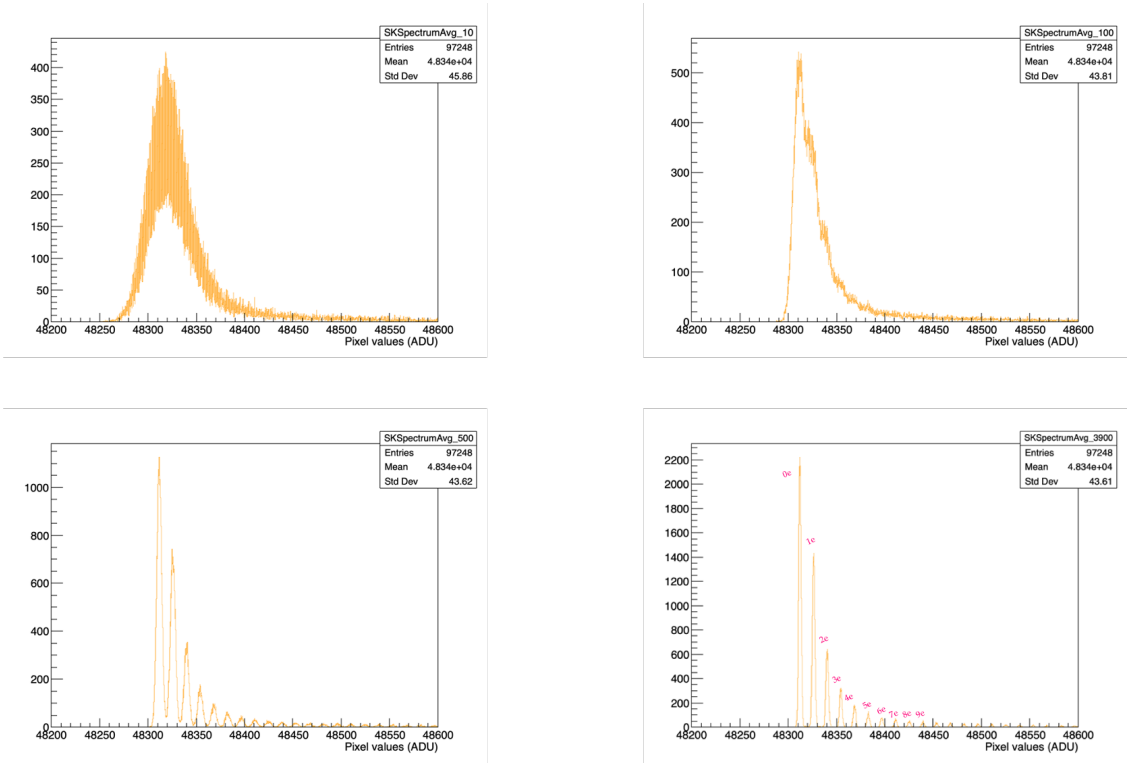

Figure 6.11: Evolution of a CCD's pixel charge distribution for 10, 100, 500, and 3900 skips. Individual electron peaks are resolved at 500 skips, with clear separation at 1000+ skips

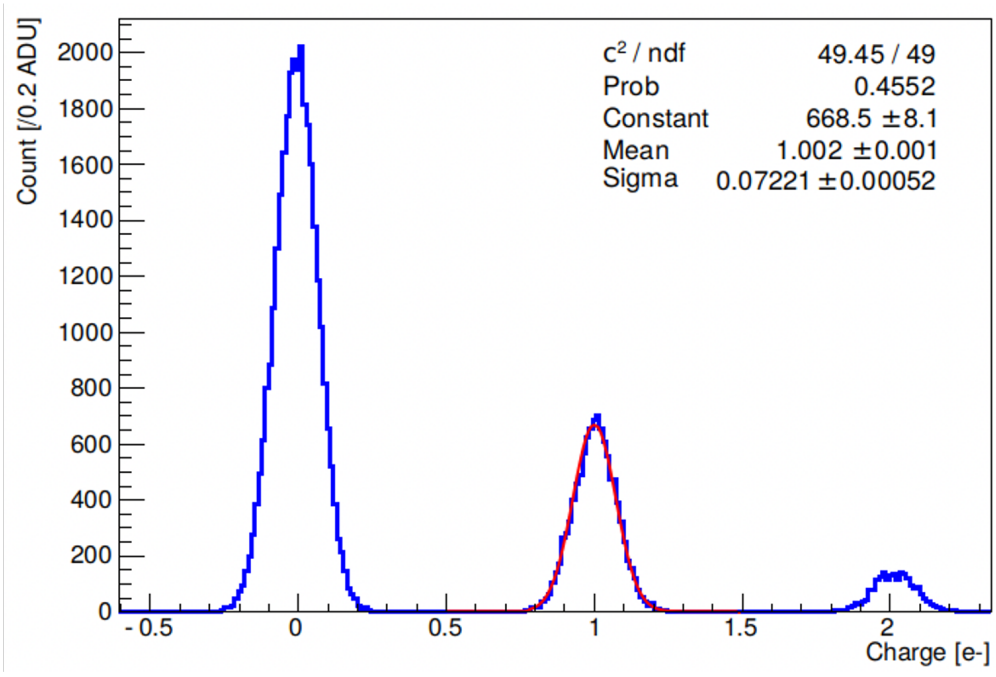

Figure 6.12: Best resolution ($\sigma_{\text{pix}} \sim 0.07$ e$^-$ at 1000 skips) yet achieved in a DAMIC-M prototype CCD.

6.2.3 Studies of Dark Current

The very low levels of dark current in DAMIC CCDs enabled several successful analyses, including those presented in Chapter 3. It is absolutely critical that dark current levels be minimized: for a Skipper CCD, as the readout noise becomes negligible, it is the dark current that may become a limiting factor. The previously cited value of dark current for DAMIC at SNOLAB was 2-6 $\times$ 10^{-22} A/cm^2, or $\approx 10^{-3}$ e$^-$/pixel/d (we will use the latter's units for the results described in this section).

Note that Skipper images are split into vertical bands that reflect a collection of NDCMs, and we obtain an average image by averaging across column values across these bands. The subsequent single-electron, multiple-peak distribution is similar to that shown in the previous section. We re-orient the distribution, equalizing by the mean value of the 0-electron peak, μ_0 (extracted by a Gaussian fit). As mentioned, any calibration is done using by fitting the 1-electron peak. Clustering is done for contiguous pixels above a seed exceeding a 5 e$^-$ threshold; the algorithm to identify and remove clusters is important to accurately measure the CCD dark current. In order to quantify dark current, a Gaussian-Poisson convolution fit, described by Eq. 6.2, was used across individual electron peaks (see Fig. 6.13).

$$f(p) = N_{\text{pix}} \sum_{n=0}^{n=\infty} Pois(n|\lambda)\, Gaus(x - nk|\mu_0, \sigma_{\text{pix}}) \tag{6.2}$$

In this relation, λ is the calculated dark current rate, $f(p)$ is the pixel distribution value for a binned pixel value p, N_{pix} is the number of pixels, and k is the calibration constant. We have performed a cross-institutional study of dark current, investigating residual image origins, clock-induced charge, scans of V_{dd}, V_{sub}, V_R, V_{drain}, exposure time, and temperature. All studies were executed using similar test chambers at surface level: we allowed time for the Leach controller to stabilize and ran initial erase procedures, and ran "clean" images (full-size, NDCM = 1) between dark current image sets to clear track accumulation.

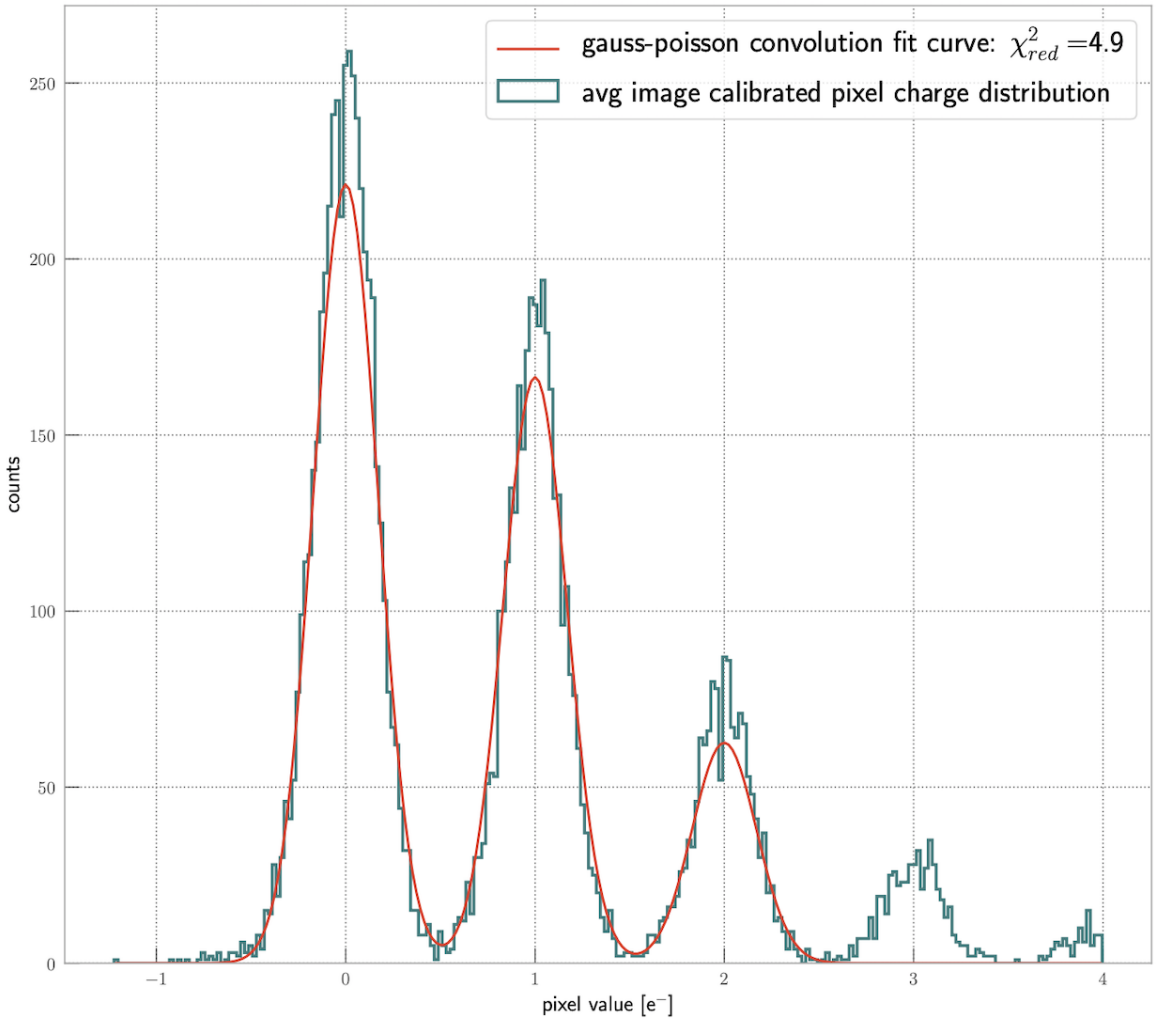

Figure 6.13: Sample calibrated pixel charge distribution of a Skipper CCD's average image. The calibration constant, measured from the 1-electron peak, is $k = 9.607 ADU/\mathrm{e}^-$. The dark current is computed using a convolution fit described in the text.

- **Residual Images**: One origin of dark current could be a "residual image" induced by tracks that leave charge at the CCD interfaces (e.g. front Si-SiO_2, back Si-gettering layer) where they can get trapped. We expect such charges to be released from traps over a period of hours or longer. We tested for this effect by running the CCD continuously with 500 skips for a $\sim$ 0.5 d exposure, followed by an image clean and then immediately taking another 500-skip image. No residual image was observed: the dark current level at the latter stage was the equivalent to restarting from zero exposure.

- **Clock-Induced Charge**: This effect is caused when a CCD is clocked into inversion [34] and some carriers become trapped at the Si-SiO_2 interface. Upon returning to a non-inversion state, trapped carriers are freed, accelerated, and generate additional spurious e-h pairs. This spurious charge is generated on the rising edge of a clock's phase, decreases exponentially with clock rise time, and increases with clock pulse width. We were able to verify the presence of such spurious charge by looking at the charge distribution of the image overscan where, as previously mentioned, we expect no charge. This source of dark current further motivates the capability to easily control the CCD's clocking parameters, an underlying goal of custom electronics being developed for DAMIC-M. In considering dark current generated by clocking, we also studied the effect of the serial register on dark current. In particular, in assessing Register 1, we extracted the noise and dark current on one amplifier by reading that amplifier while clocking the actual charge to a second amplifier on the opposite side. The corresponding distribution did not show actual single-electron events, but did feature a small tail that could be attributed to cross-talk.

- V_{sub}: A scan of V_{sub} between 20-120 V ($\sim$9 V steps) showed dark current values plateauing from $\sim$ 38 V. At the lowest voltage, spatial features of tracks were lost due to heavy diffusion from underdepletion. While DAMIC at SNOLAB CCDs were operated overdepleted, it may be favorable to operate these CCDs at full-depletion.

- V_{dd}: Recall that the single-stage output amplifiers of the CCDs are powered by V_{dd}. The amplifiers are known to "glow" at high V_{dd} voltage magnitudes – they warm up and begin to emit photons in the infrared, which causes an increase in dark current that can be observed along the edge / near the corner of the sensor. We scanned through values of V_{dd} to test for glowing: Fig. 6.14 shows the same area of the CCD during operation at V_{dd} = -20 V and V_{dd} = -24 V. The latter value leads to a significant increase in dark current around the top-left corner.

- V_R, V_{drain}: By scanning across V_{drain}, we observed that moving from a value of -24.5 V to -17 V lowered the dark current. The current parameter space that can be tested for V_{drain}, V_R, and the voltages that are correspondingly affected by the set-points, is limited by dynamic ranges of the Leach controller and yet again requires custom electronics to be designed for DAMIC-M goals.

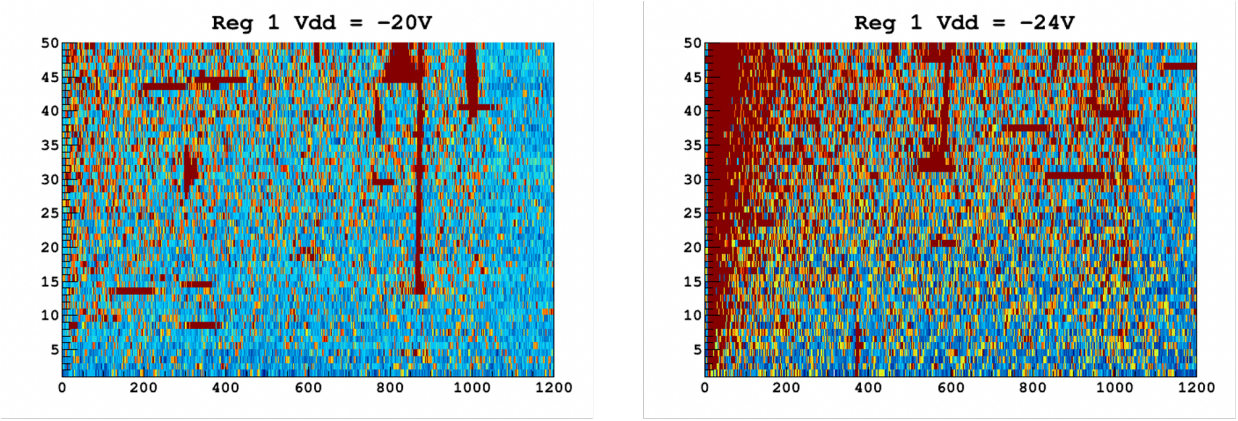

Figure 6.14: Increased dark current by operating V_{dd} at a higher magnitude, seemingly causing localized glowing of the CCD amplifier.

- **Temperature**: Leakage current decreases by operating CCDs at lower temperatures. Ref. [53] outlines a temperature scan run at the University of Chicago. As of June 2021, LPNHE has commissioned at second test system with capable of LN_2 cooling. This will

enable temperature scans down to ∼80 K, approaching CCD freeze-out temperature (at which point CTE begins to degrade).

- **Exposure Time**: We ran tests to confirm the linearity of dark current with increasing exposure time, the results of which can be seen in Fig. 6.15. Due to the continuous (and often long) reading of Skipper CCDs, parts of the CCD will effectively see a longer exposure than those already read out. At a certain point ($\lesssim$1 d), the entire CCD is read, meaning every row has seen the same exposure. At this steady state of readout, we expect (and observe) a plateau in dark current.

At present, the best dark current level achieved by a DAMIC-M prototype CCD has been that deployed in the LPNHE test system. However, its level of ≈ 0.03 e^-/pix/d rests roughly an order-of-magnitude above the levels achieved at DAMIC at SNOLAB. Our current leading hypothesis for this difference in performance is related to the work presented in Ref. [121], describing the particle tracks from cosmic rays and β's from radioactive decays producing Cherenkov photons inside the silicon of the CCDs. Some of these Cherenkov photons may travel sufficiently far from their originating track in order to induce single-electron events and contribute to higher dark current at ground level. Ref. [121] also discusses possibilities for low-energy events due to transition radiation and luminescence from $e^- - h$ recombination.

The characterization and understanding of Skipper CCDs has rapidly evolved thanks to the efforts of DAMIC-M's development. DAMIC-M will profit greatly from the Skipper cutting-edge design features presented in this chapter. The current limitations to ongoing studies of dark current cannot be address at surface-level. The LPNHE test chamber has background levels of ∼300,000 dru for an energy range <10 keV; the University of Chicago's usual surface rate in the same range was ∼225,000 dru, and was reduced to ∼30,000 dru after deploying a 4-cm-thick copper box that acts as an infrared shield. While this level may be enough to enable certain science runs [64], ultimately testing and operation will have to move underground to the Laboratoire Souterrain de Modane (see Chapter 7).

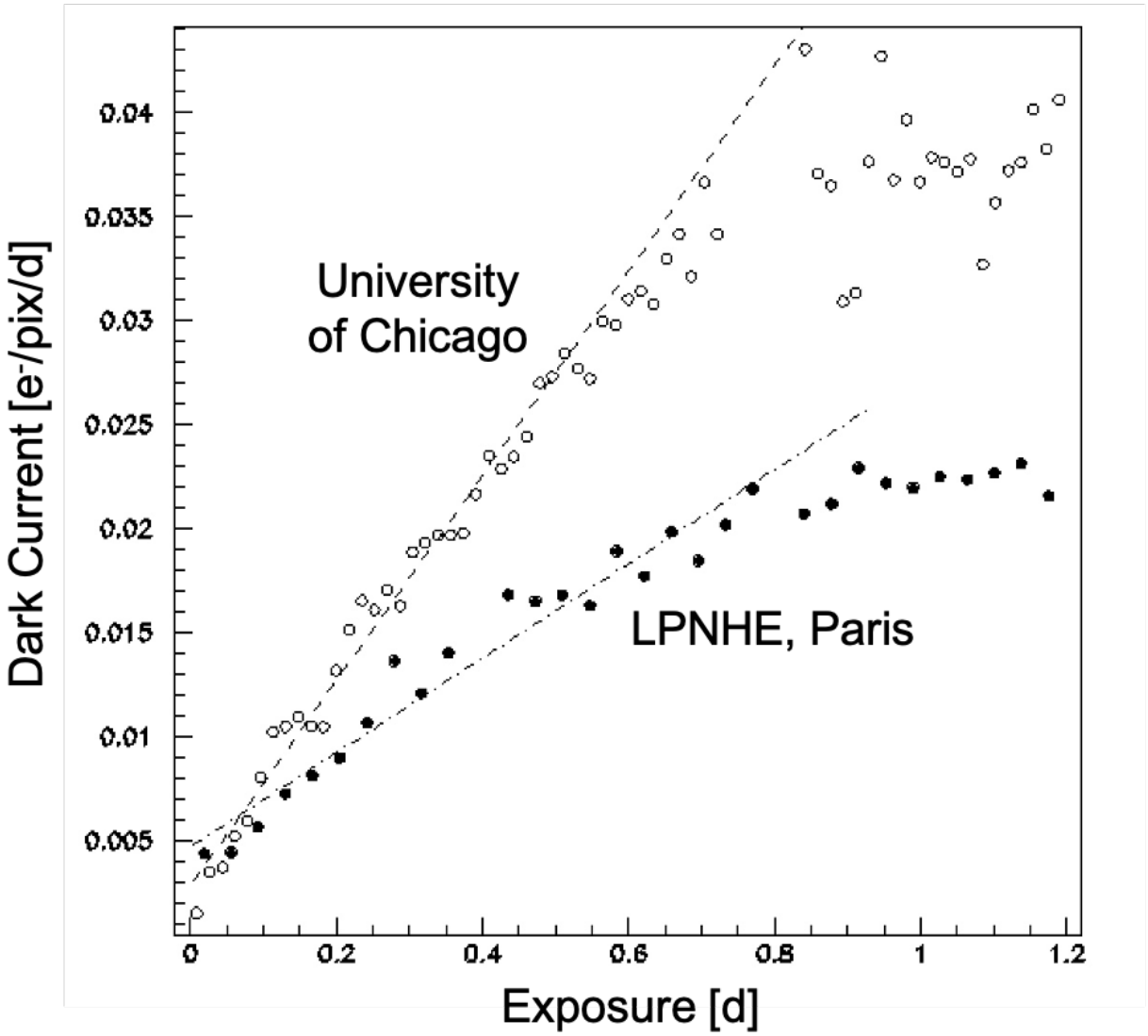

Figure 6.15: Dark current profiles for two 1k×6k Skipper CCDs operated in similar test chambers at the University of Chicago and LPNHE, Paris. An linear increase of dark current with overall exposure time is observed, followed by a plateau due to each system reaching a steady-state in which the CCD has been fully read out. The dark current observed (≈ 0.03 e^-/pix/d) is the lowest yet achieved during DAMIC-M R&D studies.

6.2.4 Integration of Novel Readout Electronics

There are limitations to the use of commercial CCD controllers (including the Leach system currently deployed). For optimal CCD performance, it is desirable to be able to independently adjust clock and bias parameters. We will aim for each DAMIC-M CCD module to be read out and controlled by an independent electronics module. At the start of Chapter 5, we briefly introduced the custom electronics module for DAMIC-M. It includes the ODILE, which features a primary motherboard card with a field programmable gate array (FPGA) for overall control, an ADC, CABAC, and CROC. The LPNHE group has led the design and testing of the latter two. Demonstrating successful integration with current CCD test systems is a necessary step in advancing the development of such novel electronics. To that end, preliminary versions of the CABAC (CABAC3) and CROC (CROC v1) were deployed in the LPNHE test system, the former used to control a 4k×2k CCD, and the latter used to read out the UW1603S Skipper CCD. Details of efforts surrounding development and integration of the remaining electronics components led by the University of Chicago group can be found in Ref. [122].

The CABAC3 setup featured an FPGA evaluation card with a serial peripheral interface [107]. The clock triggers passed through a low-voltage differential signal translators and external supplies were used to provide power. Three sections on the board delivered different sets of clocks and biases: Section 1 provided horizontal/vertical clocks, and the TG, Section 2 provided the OG, V_{dd}, and V_R, and Section 3 provided the SW, RG, and V_{sub}. Voltage values, rise times, and signal widths were programmed to exactly match those in Tab. 5.4 and 5.5. An "ASPIC" ASIC chip and "BEB" 18-bit ADC developed and tested for the Large Synoptic Survey Telescope [123] were used for video processing and readout. First successful image acquisition was completed in July 2019.

The CROC is a 4-channel chip with single-ended input to differential output. It can operate in two modes: *transparent mode*, operating as a simple amplifier with programmable

gain and CDS capability, and *dual slope integrator (DSI) mode*, in which the integration of pedestal and signal is done via a hardware mechanism that introduces a programmable RC time constant (the input still has programmable gain just as in transparent mode).

Figure 6.16: CROC chip integration using the LPNHE test system.

A custom board was designed to operate CROC with a CCD at low temperature, with the chip controlled by an FPGA programmed at LPNHE. This board was operated in tandem with the Leach controller: a custom cable was fabricated to connect the two, synchronization was done by programming additional timing triggers on the Leach back-end, and the CCD video signal was passed through the CROC (in transparent mode) to then be processed for DSI and CDS by the Leach video board. The board was secured directly to the flex cable output of the CCD (see Fig. 6.16) – the final goal is to mount CROC chips on CCD modules in order to keep them as close as possible to the sensors for improved signal-to-noise. All clocks and biases were provided by the Leach. While image acquisition was successful, the noise was measured to be ∼50% higher using this configuration. For this test, the CROC had an absolute gain of 140. The board housing the chip did not have good thermal contact within the cryostat: its measured temperature was 278 K, with $T_{CCD} \approx 160$ K. Future testing will aim to optimize the chip's noise performance and test the CROC at desired cryogenic conditions of DAMIC-M.

6.2.5 Packaging and Testing Record-Mass Skipper CCDs

Turning back to Fig. 6.4, we can see that the pre-production 1k×6k CCDs are not the only ones diced out of fabricated wafers. From each wafer, a 6k×4k CCD (of record-mass) is extracted. By dicing, packaging, and testing different geometries of CCDs, we have an avenue to estimate the yield of progressively larger devices. This is an important intermediate step given that the effective goal of DAMIC-M is to produce 6k×6k CCD modules. We leave additional discussion on yield and the design selection of DAMIC-M CCDs to Chapter 7.

One of the core elements of the entire process is packaging. Having already identified ^{210}Pb (and thus radon) as a serious background concern, it was clear from the beginning of the DAMIC-M program that packaging protocol would have to be improved relative to what was done at Fermilab for DAMIC at SNOLAB CCDs (specifically, long cure times of up to a day, with CCDs left uncovered in a high-level clean environment). The University of Washington has led efforts to develop a single, repeatable process for all CCD package types in order to address this need and prepare for production stages of DAMIC-M. A dedicated cleanroom was constructed there, with careful measures adopted: the use of ESD equipment, control/monitoring systems to ensure all packaging is done above 35% relative humidity, and selection of high-purity silicon for the 200 μm-thick shims that provide mechanical support for packaged CCDs.

The CCD packages were designed to minimize material around the sensor: one such package for a 6k×4k CCD can be seen in Fig. 6.17 (right). The packaging process involves: (1) cable preparation, including cleaning with acetone and IPA, and plasma etching of one side for improved adhesion to the CCDs, (2) a controlled application of EpoTek 301-2 epoxy to the substrate, with automatic curing (4 hr) at 80°C and positional constraint via copper t-bar supports at CCD edges, and (3) wirebonding (30 m). This shorter packaging time and cleaner environment is expected to significantly reduce radon exposure. The eventual goal of DAMIC-M is perform this packaging underground at the Modane lab.

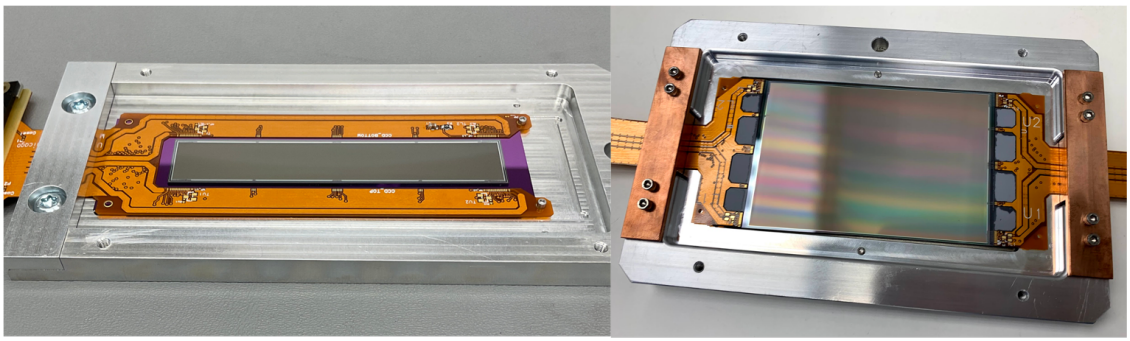

Figure 6.17: 1k×6k and 6k×4k DAMIC-M pre-production CCDs packaged at the University of Washington.

A total of six 6k×4k CCDs have been packaged and tested with the aforementioned procedures. Note that 6k×4k CCDs have a pair of flex cables in their packaging from either end of the CCD – this required the fabrication of a 2-1 board to later recombine lines. The board was introduced to the electronics chain between the breakout board and amplifier board. Of the six mentioned CCDs, two were deemed to be engineering-grade, meaning that single-electron resolution was attained but there were also defects present that lowered charge transfer efficiency. Two CCDs were deemed to be "toy"-grade, meaning they could be used for commissioning new systems, but had significant performance issues.

The remaining two CCDs were deemed to be science-grade, and we plan to deploy them at a modified setup at SNOLAB for additional studies of backside calibration. This stems from the $\approx 8\,\mu$m partial charge collection region found after SIMS measurements of DAMIC at SNOLAB CCDs. The high phosphorous concentration we observed affects carrier transport parameters (e.g. lifetime, mobility, E field). The varied collection efficiency in this region impacts the corresponding energy spectrum produced by ionization events, such as those from ^{210}Pb. Importantly, the pre-production CCDs for DAMIC-M were fabricated with the same backside layer. There is therefore motivation to characterize the position and shape of the PCC region by calibrating the CCD through backside illumination. We will do this with an ^{241}Am source, whose internal electrons of fixed energies are projected to travel only 10s of microns into the CCD backside.

CHAPTER 7

THE STATUS OF THE DAMIC-M PROGRAM

DAMIC-M will feature a large-scale, kg-scale deployment of innovative Skipper CCDs to search for dark matter. The experiment is in the third year of a five-year program and has seen significant progress, partially by the results presented in Chapter 6. Given the need to measure CCD dark current and intrinsic background levels underground, prepare necessary infrastructure, and establish cleaning, packaging, shielding, and testing protocols, a prototype detector, the Low Background Chamber (LBC), was conceived for DAMIC-M. In this chapter, we will review the ongoing development of both the LBC and DAMIC-M.

Both DAMIC-M and the LBC will be hosted in the Laboratoire Souterrain de Modane. LSM is one of the deepest underground laboratories in the world; the facility is located beneath the French Alps, and is easily accessible via the tunnel of Frejus (significantly improving infrastructure logistics relative to SNOLAB). It features a 1.7 km rock overburden (4800 m.w.e.) contributing to a low muon flux of 5.4 $m^{-2}d^{-1}$ [124]. The neutron flux of the facility was measured to be 9.6×10^{-6} $cm^{-2}s^{-1}$ [125], and the radon concentration ranges between 5-15 Bqm^{-3} [126]. An ISO Class 5 cleanroom by ADS Laminaire was constructed in January 2021 for the DAMIC-M program, with dedicated packaging, testing, and detector spaces, as well as a retractable roof opening for convenient transport of heavier materials.

LSM's low level of radon is due to a radon-trapping facility with activated charcoal columns, and will lead to a major background reduction. DAMIC-M CCDs will be stored in a nitrogen atmosphere until arrival at LSM, and packaging and testing will use the lab's radon-free air supply to further minimize exposure to radon and any airborne dust deposits that may contain ^{238}U and ^{232}Th. Shielding protocols will be put in place to minimize cosmogenic activation of detector materials. These approaches will help address radioactive backgrounds presented in Sec. 3.3 and Chapter 4. There is a 10 dru background-level goal for the LBC (comparable to DAMIC at SNOLAB levels), and 0.1 dru for DAMIC-M.

7.1 A DAMIC-M Prototype: The Low Background Chamber

The LBC will feature two 6k×4k Skipper CCDs. To reiterate the collaboration's goal for the detector – we aim to: (1) measure the dark current of Skipper CCDs underground in a low-background environment to ascertain their best possible performance, (2) measure the backgrounds (bulk ^{32}Si, surface ^{210}Pb, and ^{3}H from activation or in the gettering layer) in DAMIC-M pre-production CCDs, and (3) validate component designs regarding packaging, electronics integration, and slow control operation. Regarding the science goals of the prototype detector: the 10 dru target corresponds to 0.4 events between 2-10 e^- in a 1 kg-d of exposure (assuming a flat background).

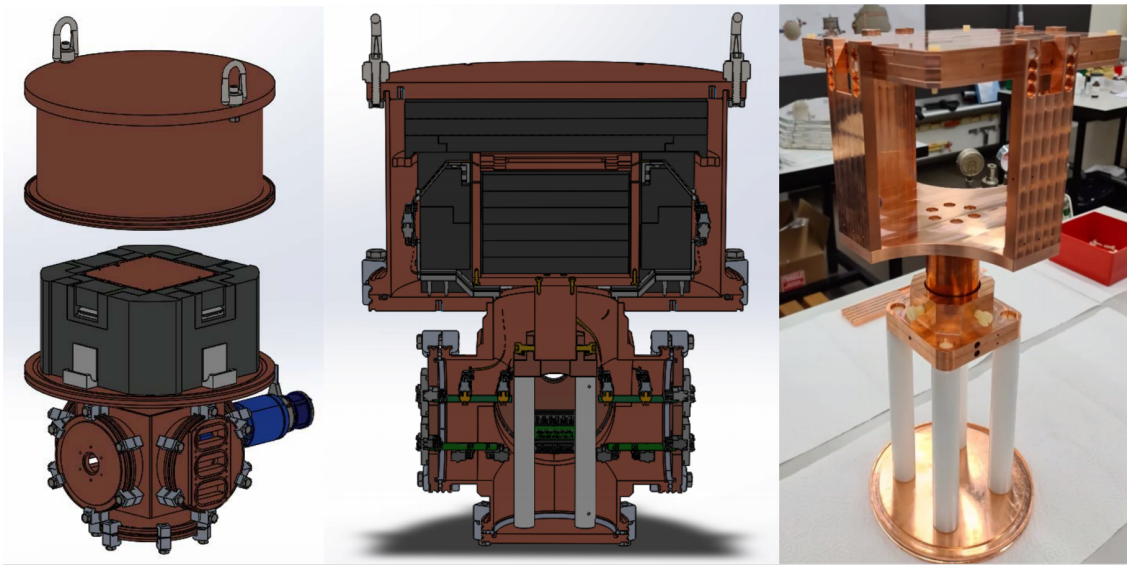

Figure 7.1: Left: Conceptual drawing of the LBC detector, with an easily removable cryostat top hat to enable access to the CCD box and cabling. Middle: Cross-section of the detector, with the copper CCD box surrounded by ancient lead shielding. Right: Fabricated and cleaned CCD box and copper arm, hand, and fingers for thermal contact with the cryocooler cold head. The Teflon stands for thermal isolation from the cryostat base.

The LBC cryostat (see Fig. 7.1), fabricated out of copper by Luvata Wolverhampton Ltd., is designed in two halves: a "bottom cross" that contains all permanent-installation components (e.g. the cryocooler cold head), and a "top hat" component that can be pulled off by bolts via the use of a crane. The top hat enables access to the upper half of the

LBC detector, namely to the CCD box from above and to the amplifier boards and CCD cabling from the sides. The CCDs will be shielded by 6+ cm of ancient lead on all sides. In DAMIC at SNOLAB, higher levels of copper activation and tritium prevented a direct screening of radioactive background levels of this lead. We hope that by minimizing the the aforementioned sources, we will be able to directly characterize the background levels of isotopes (i.e. ^{226}Ra, ^{214}Bi, ^{214}Pb) in ancient lead that are otherwise difficult to assay.

The CCD box acts as an infrared shield: it is made of an electroformed copper base and OHFC copper lids machined and cleaned at the University of Zurich. A cold copper "hand" with four "fingers" will elevate the CCD box to make space for lead shielding from below; the base of this hand will make contact with a cold copper "arm" from a Cryotel GT cryocooler. This copper arm is separated from the bottom flange of the cryostat's bottom cross using four Teflon posts. The amplifier board will be positioned 15 cm from the CCD, and PCTFE cable guides will be used to pass the cold flex cables through the warmer surrounding lead. External cylindrical lead and polyethelyne shielding will surround the entire detector.

The CCDs of the LBC will initially be controlled by a Leach, with the intention of eventually swapping the controller out for DAMIC-M electronics. The goal is to acquire 4 months (1 kg-d) of data, and the Skipper CCDs will be read out either in a binned format to optimize noise, or continuously. For operation of a 24 Mpix CCD, at $\sim$2 byte/skip we expect 48 MB (48 GB) for an image with 1 (1000) skips. Assuming a 30 ks exposure time and 10 μs integration time, a 1000 skip image would take almost 4 d to acquire and read, which is unreasonable. We thus plan to operate this read mode only for single-skip images. If instead we operate with a 1$\times$4000 readout mode (through simultaneous transfer of pixels into the serial register), it would take 1 minute to read out the entire CCD with 1000 skips, and generate 36 MB/d. If we opt for a continuous readout with 1000 skips per pixel (i.e. 10 ms readout time per pixel), the target data set would correspond to 2 TB of storage. All data will have a remote back-up on the French CC-IN2P3 server.

The second test system at LPNHE features several components that will be used in the LBC, including the Leach, DAQ computer, cryocooler, V_{sub} linear power supply, and slow control interface hardware. All air-side electronics of the LBC will be tested at LPNHE prior to underground installation. As of June 2021, the cryostat and inner lead shielding have been delivered to the LSM. Cleaning of detector parts is scheduled to commence at Grenoble (near LSM) in July 2021, and there is a large-scale assay campaign to measure and simulate background levels of detector materials. LBC commissioning is set for September 2021, with final assembly and first acquisition projected for the end of 2021.

The projected physics reach of the DAMIC-M LBC can be seen in Fig. 7.2, along with other Skipper CCD experiments that are active or planned. With just 1 kg-d of exposure, we plan to have $\sim$ 4 orders-of-magnitude improvement relative to the protoSENSEI detector running at Fermilab [68]. The LBC will produce competitive scientific results and help to bridge the phase-space of existing limits with those targeted for the DAMIC-M experiment.

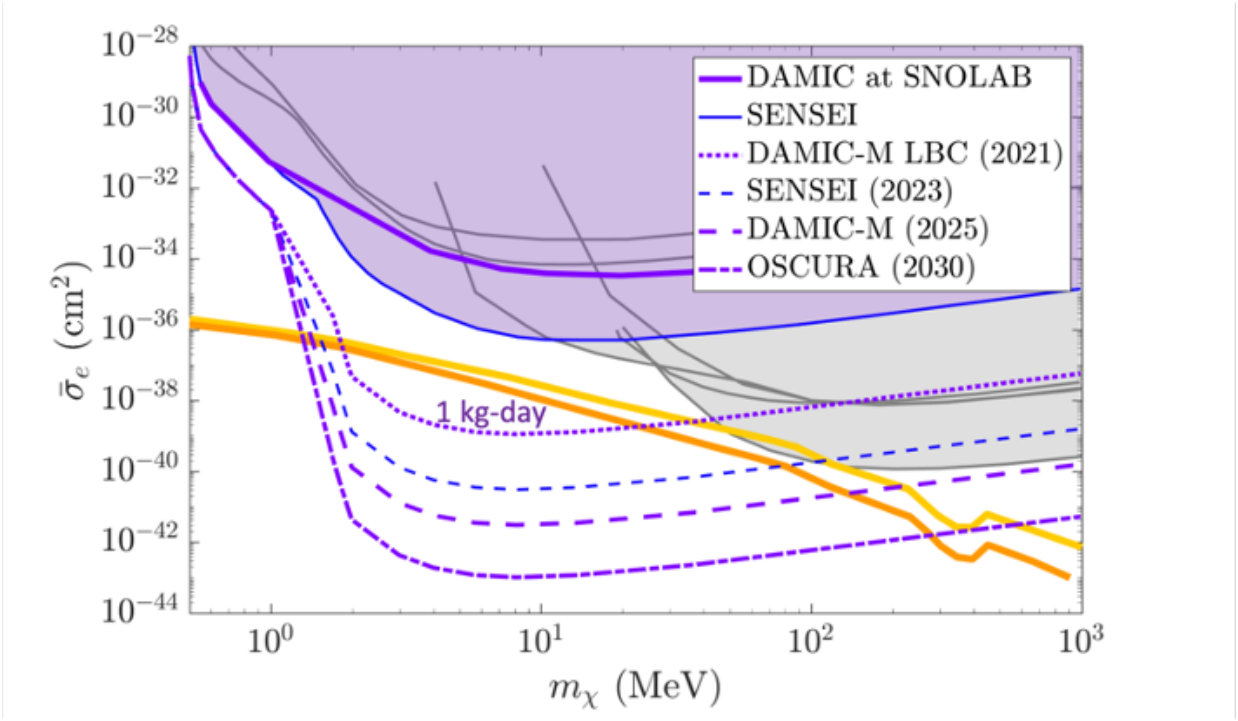

Figure 7.2: Projected DAMIC-M LBC constraints on the dark matter-electron scattering cross-section, $\bar{\sigma_e}$, as a function of dark matter mass, m_χ, for a 1 kg-d exposure.

7.2 The DAMIC-M Experiment: Design and Scientific Goals

The DAMIC-M experiment has aggressive but achievable goals for size (1 kg), resolution (0.1 e^-), and background levels (0.1 dru). We have already touched on achievements of Skipper CCDs towards the resolution goal, and work to minimize backgrounds by host site selection featuring radon-free air, expedited packaging procedures, careful detector material selection, and potential to measure ^{32}Si. In this section, we will extend this discussion towards additional strategic protocol for mitigating backgrounds, especially from cosmogenic activation. Additionally, we will outline the back-end of what it really takes to construct this type of next-generation dark matter experiment.

7.2.1 DAMIC-M CCD Design Choice

In testing DAMIC-M pre-production CCDs, we were able to gauge the performance of progressively larger devices. While sub-electron resolution has been demonstrated in 6k×4k CCDs, there are concerns regarding the possible yield and performance of 6k×6k CCDs. Conversations with experts at LBNL and DALSA indicated an expected yield for such devices in the 5-10% range, which would be insufficient for DAMIC-M's goals. As such, the baseline design of DAMIC-M CCDs was slightly modified in order to optimize yield, while still maintaining the equivalent desired size. Specifically, each module will feature four 6k×1.5k CCDs; this design has been integrated into the next pre-production phase of fabrication and testing for DAMIC-M.

An example of this updated DAMIC-M module can be seen in Fig. 7.3 (left). There are several challenges expected in the selection of science-grade devices from this batch. While previously we planned for the capability to package and test entire large-format CCDs, here it is unlikely that we will have science-grade performance across the four detectors of a single wafer. As such, the CCDs will be individually diced and cold-probed to get a preliminary read of performance, with the best CCDs grouped and glued to a silicon pitch adapter.

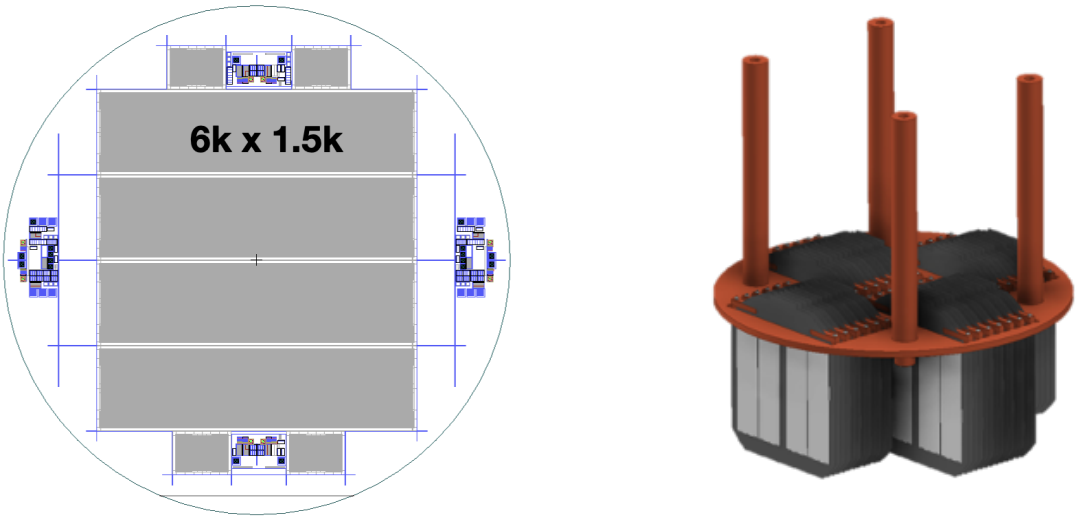

Figure 7.3: Left: Schematic of the wafer from which DAMIC-M 6k×1.5k CCDs will be diced. Right: Conceptual design of the final DAMIC-M detector core, a hanging tower configuration of modules consisting of four 6k×1.5k CCDs grouped atop a silicon pitch adapter.

7.2.2 DAMIC-M CCD Production

The first phase of DAMIC-M pre-production and testing is nearly complete, namely achieving sub-electron resolution with 1k×6k and 6k×4k CCDs and selecting output amplifier geometry. The second phase of pre-production, featuring 6k×1.5k CCDs, is underway; this phase has some overlap with the final planned production in terms of material and design. In February 2020, a silicon ingot was pulled at Topsil in Denmark; this material will be used for the CCDs of the latter two production cycles. Following surface-level transport without additional shielding, the ingot was wafered at Shin-Etsu Handotai Europe in Scotland. The wafers were then stored at Boulby Lab [127] in the United Kingdom: 22 wafers were directly shipped to DALSA by air for fabrication; 231 wafers for the final DAMIC-M production phase were placed in a shielding container and sent via surface-level transatlantic shipment for storage at SNOLAB; 58 wafers were kept at Boulby for eventual production of DAMIC-M silicon pitch adapters. The total surface-level exposure time of the wafers for DAMIC-M production was 14 d.

Half of the pre-production devices generated by DALSA will be dedicated to testing yield and performance of 6k×1.5k CCDs. Given four devices per wafer, this means that 44 devices will have to be packaged and then tested on a short timeline ($\sim$ 3 months) across the University of Chicago, LPNHE, and the University of Washington. The author's contributions to the construction of automated test systems and analysis tools will enable crucial pre-production studies prior to the scheduled start of DAMIC-M CCD production. The other half of devices will be used to explore different backside thinning techniques (e.g. delta doping [128]) in order to reduce the PCC region from $O(10\,\mu\text{m})$ to $O(10\,\text{nm})$.

Once process flows and design features are finalized, the wafers currently stored at SNOLAB will be moved to DALSA along with a shielding container. This will ensure that activation of detector materials is minimized during fabrication and other processing steps including wafer polishing at OMNISIL. The wafers will always be kept in a clean, nitrogen-flushed environment to further minimize radon exposure. We will perform all packaging, cold-probing, and testing of the final DAMIC-M CCDs underground. The cold-probing will be done at -45°C and follow the procedure of Ref. [129] to screen for defects.

A conceptual design for the DAMIC-M detector core can be seen in Fig. 7.3 (right). Achieving a low-background, kg-scale CCD dark matter detector with sub-electron resolution will be a major experimental feat. The projected physics reach for 1 kg-yr of exposure with DAMIC-M can be seen in Fig. 7.4 and Fig. 7.5; the experiment will be a leader in searching for dark matter beyond the heavy WIMP paradigm.

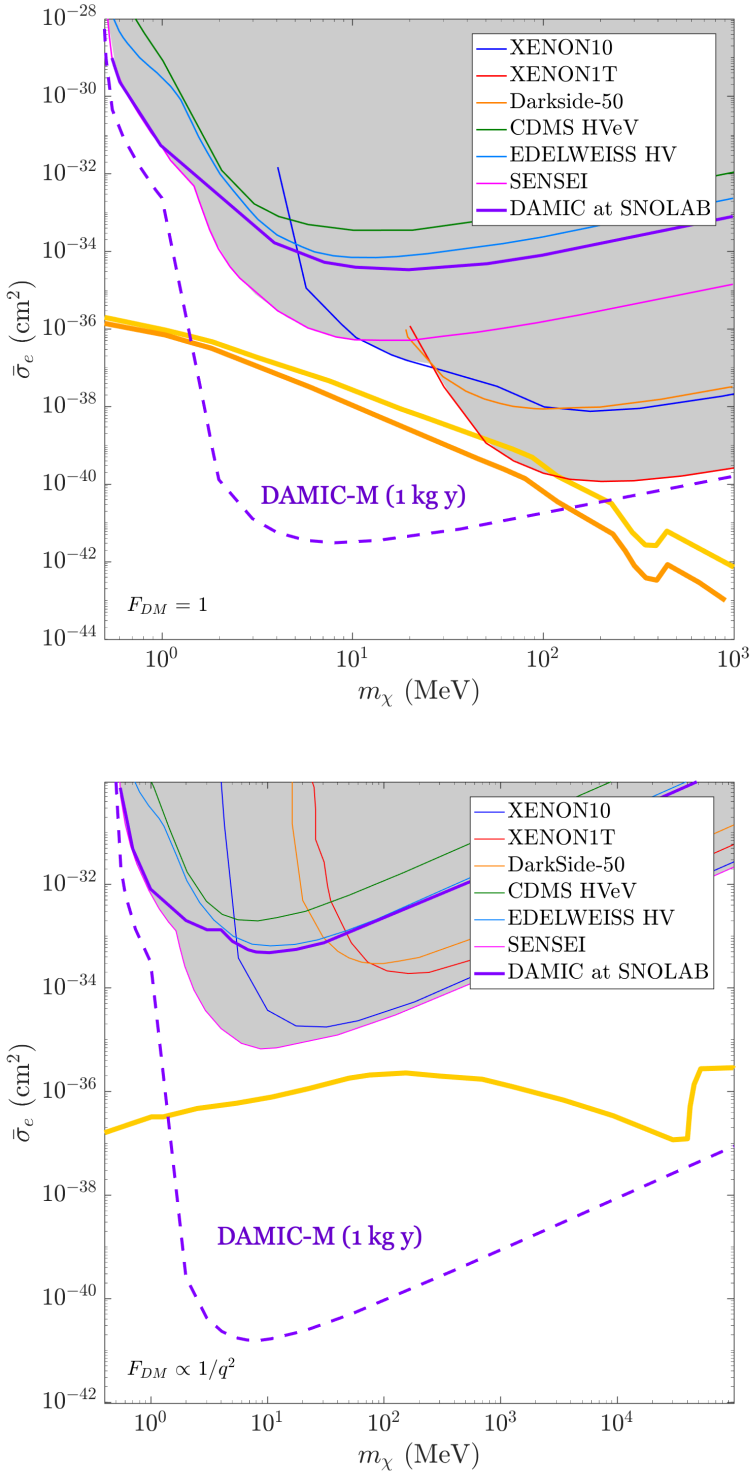

Figure 7.4: DAMIC-M projected constraints on the DM-e$^-$ free scattering cross-section for heavy (top) and light (bottom) mediators.

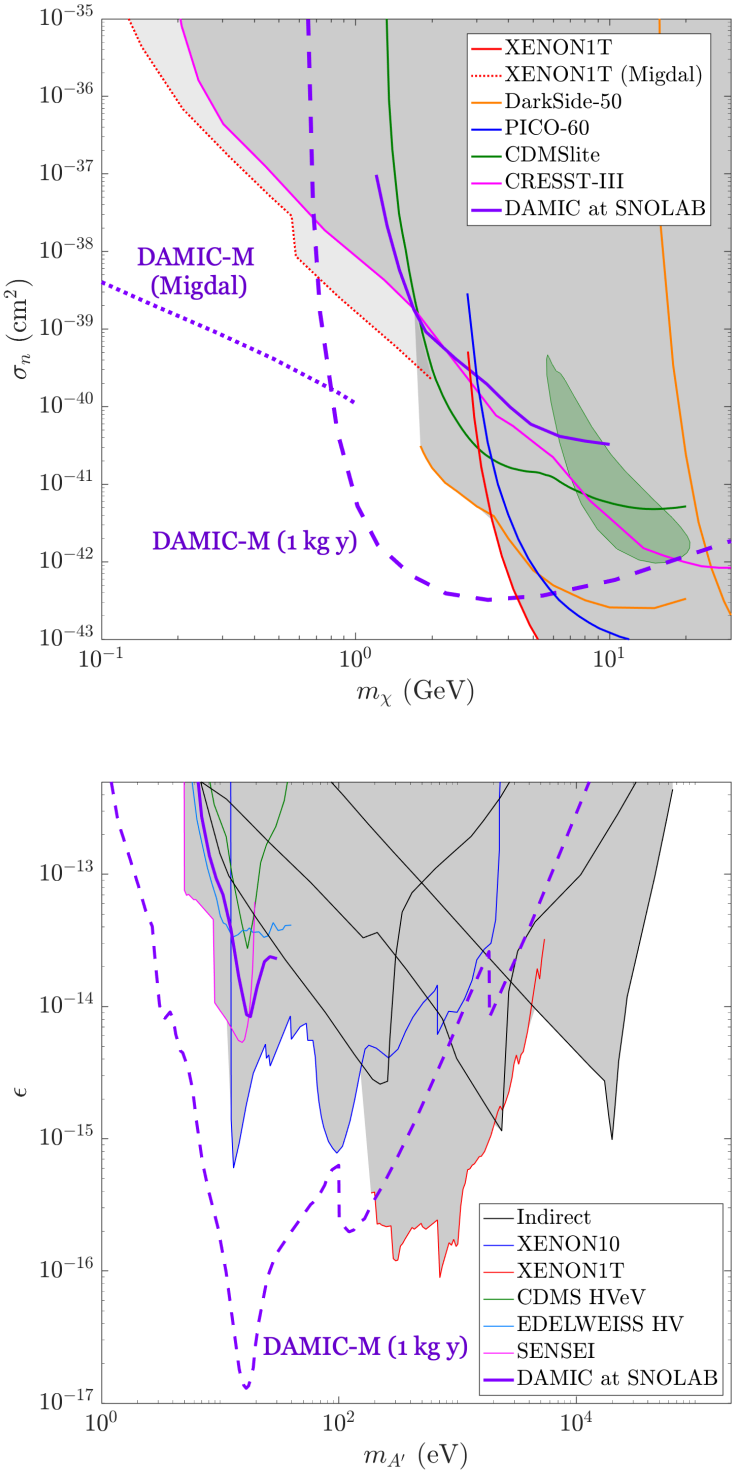

Figure 7.5: DAMIC-M projected constraints on spin-independent WIMP-nucleus elastic scattering (top) and the hidden-photon kinetic mixing parameter (bottom).

CONCLUSION

This work extensively reviews the DAMIC program's use of scientific-grade CCDs to search for light dark matter. It presents major achievements in improving the identification, mitigation, and rejection of radioactive backgrounds, as well as progress towards understanding and deployment of sub-electron resolution Skipper CCD technology in order to improve the sensitivity of next-generation dark matter direct-detection experiments.

We produced 500-μm thick p-i-n diodes at the Pritzker Nanofabrication Facility of the University of Chicago as a proof-of-concept for studying the microstructure and fabrication steps of scientific-grade CCDs. Probing these devices highlighted that key detector performance indicators, including low leakage current and full depletion at relatively low substrate bias voltages, could be demonstrated. This effort also informed additional studies of elemental compositions of CCD layers and process flow steps that affect CCDs' radioactivity.

We presented CCDs as successful dark matter detectors, in particular through results of the DAMIC at SNOLAB Experiment's search for WIMPs, as well as constraints on hidden-sector dark matter and light dark matter recoiling off electrons obtained by exploiting the extremely low, $O(10^{-22})\,\mathrm{A/cm^2}$, leakage current of DAMIC CCDs. The former placed the strongest exclusion limit on the WIMP-nucleon scattering cross section with a silicon target for $m_\chi < 9\ \mathrm{GeV}/c^2$. The latter established the best direct-detection limits on dark matter-electron scattering between 0.6-100 MeV/c^2 and hidden-photon dark matter for 1.2-9 eV/c^2.

We outlined the construction of a comprehensive radioactive background model for a CCD dark matter search, revealing a partial charge collection in DAMIC CCDs. We also reviewed the first-ever experimental measurement of the cosmogenic activation of silicon via the irradiation of DAMIC CCDs. Moreover, we presented a deep-dive into the powerful capability of DAMIC CCDs to measure problematic radiocontaminants including ^{32}Si ($140 \pm 30\,\mu\mathrm{Bq/kg}$) by utilizing their exquisite spatial resolution to identify correlated decay sequences over time. We proposed methods to improve future background mitigation.

Finally, we described the successful deployment of novel Skipper CCD technology, which will be used in the kg-scale DAMIC-M Experiment currently being developed. We provided detail on the construction of automated cryogenic CCD test chambers that enabled first results of characterization of DAMIC-M Skipper CCDs, in which a resolution of 0.07 e^- was achieved. These chambers further enabled electronics integration and hardware preparation for DAMIC-M and its prototype, the Low Background Chamber, experiments that will carve out new parameter space in the search for light dark matter and hidden-sector dark matter.

In summary, this thesis has shown the evolution of the use of CCDs as state-of-the-art dark matter detectors. The presented techniques surrounding reduction of backgrounds and improvement of detector resolution will be applied in future direct-detection experimental efforts in order to significantly improve sensitivity and hopefully lead to a serendipitous discovery that will unlock one of the greatest scientific mysteries in the Universe.

APPENDIX A

ANALYTICAL CALCULATION OF SEARCH EFFICIENCIES FOR MEASUREMENT OF RADIOCONTAMINANTS

Determining final contamination rates requires knowing the probability of identifying a daughter decay once its parent decay is observed within the 181.3 d data set. We refer to this probability, incorporating the live time of the given data set, as the "time efficiency" for a particular decay (ϵ_t). We denote the time range for the data set to span from $t = 0$ to $t = t_f$. Our probability depends on the search time ranges, which, among other factors, varies for different half-life values of relevant decays, and the possibility of one type of decay search overlapping with another. We denote the time bounds of searches as b_1 and b_2. For a half-life $t_{1/2}$, the mean lifetime is $\tau = \frac{t_{1/2}}{ln(2)}$; the normalized functional form for exponential decay is given by Eq. A.1.

$$F(t) = \frac{1}{\tau} e^{\frac{-t}{\tau}} \tag{A.1}$$

We analytically extend this form to consider several cases for the spatial-correlation analysis, in particular double or triple decay sequences. Despite DAMIC's high duty-cycle, there were breaks in data acquisition due to image readout and equipment maintenance.

A.1 Two Subsequent Decays

A.1.1 Continuous Case

We begin by considering the continuous case of two decays. The efficiency for this situation is be obtained by utilizing Equation A.1 within a double integral corresponding to the sequence of seeing a parent decay, and then seeing a daughter decay relative to the time when the parent decay occurs. This double integral is bound both by the overall data set range and by

the specific bounds of the given search – the outer integral corresponds to the parent decay occurring anywhere in the data set, and the inner incorporates the exponential distribution form of the daughter decay, as seen by Eq. A.2.

$$\epsilon = \frac{1}{t_f}\int_0^{t_f} dt \int_{t+b_1}^{t+b_2} dt' F(t'-t) \tag{A.2}$$

We use $F(t'-t)$ since we calculate within the search range relative to the time t when the parent decay occurs. We substitute the functional form of Eq. A.1 into Eq. A.2:

$$\epsilon = \frac{1}{t_f}\int_0^{t_f} dt \int_{t+b_1}^{t+b_2} dt' \Big(\frac{1}{\tau} e^{-(\frac{t'-t}{\tau})}\Big) = \frac{1}{t_f \tau}\int_0^{t_f} dt \Big(e^{\frac{t}{\tau}}\Big) \int_{t+b_1}^{t+b_2} dt' \Big(e^{\frac{-t'}{\tau}}\Big) \tag{A.3}$$

At this point, we can constrain and modify the expression in Eq. A.3. One issue is that, depending on when the parent decay occurs, search ranges can extend beyond the active data set. To address this, we split our integral:

$$\epsilon = \frac{1}{t_f}\Big[\underbrace{\int_0^{t_f-b_2} dt \Big(e^{\frac{t}{\tau}}\Big) \int_{t+b_1}^{t+b_2} dt' \Big(e^{\frac{-t'}{\tau}}\Big)}_{(A)} + \underbrace{\int_{t_f-b_2}^{t_f-b_1} dt \Big(e^{\frac{t}{\tau}}\Big) \int_{t+b_1}^{t_f} dt' \Big(e^{\frac{-t'}{\tau}}\Big)}_{(B)} + \underbrace{\cancel{\int_{t_f-b_1}^{t_f} dt \Big(e^{\frac{t}{\tau}}\Big) \int \dots}}_{(C)} \Big] \tag{A.4}$$

In (A), our integral bounds are 0 and $t_f - b_2$, ensuring the search range will always fall within the data set, and thus the inner integral bounds span the entire search range, $t + b_1$ to $t + b_2$. In (B), we see that the larger search bound $t + b_2$ can fall beyond the data set's end time, t_f, and so the inner integral bounds are $t + b_1$ to t_f. This ensures at least the lower search bound is within the data set. In (C), any parent decay's subsequent search range for seeing a daughter decay falls outside our data set, contributing zero to our efficiency. The reduced expression gives an efficiency without yet incorporating dead time in acquisition:

$$\epsilon = \frac{1}{t_f}\Big[\int_0^{t_f-b_2} dt\Big(e^{\frac{t}{\tau}}\Big)\int_{t+b_1}^{t+b_2} dt'\Big(e^{\frac{-t'}{\tau}}\Big) + \int_{t_f-b_2}^{t_f-b_1} dt\Big(e^{\frac{t}{\tau}}\Big)\int_{t+b_1}^{t_f} dt'\Big(e^{\frac{-t'}{\tau}}\Big)\Big] \tag{A.5}$$

Integrating and simplifying:

$$\boxed{\epsilon = \Big(\frac{\tau + b_2 - t_f}{t_f}\Big)\Big(e^{-\frac{b_2}{\tau}} - e^{-\frac{b_1}{\tau}}\Big) + \Big(\frac{b_2 - b_1}{t_f}\Big)\Big(e^{-\frac{b_1}{\tau}}\Big)} \tag{A.6}$$

Furthermore, we have a scaling for the effective dead time as $\epsilon_d = 1 - \frac{t_d}{t_f}$, where t_d is the total dead time across acquisition. This value has been obtained computationally for the current data set: $\epsilon_d \approx 0.89$. The overall time efficiency can thus be computed by:

$$\boxed{\epsilon_t = (\epsilon)(\epsilon_d)} \tag{A.7}$$

A.1.2 Discrete Case

The next step is to extend the result to more precisely incorporate the dead time in the data set. There are breaks in acquisition both from reading out the CCDs and from unplanned mechanical issues. It is necessary to add the contribution from each image's exposure to the efficiency, and so we sum across segments of the images' start time ($EXPSTART$) to stop time ($RDSTART$) within given search ranges. Furthermore, we want to ensure various cases of search ranges extending beyond total time of our data set are accounted for; this will be executed by utilizing Heaviside step functions. We denote start/end time of an individual image with a first decay by t^i_{start} and t^i_{stop}. We denote start/end times of subsequent images

with daughter decays by t^j_{start} and t^j_{stop}.

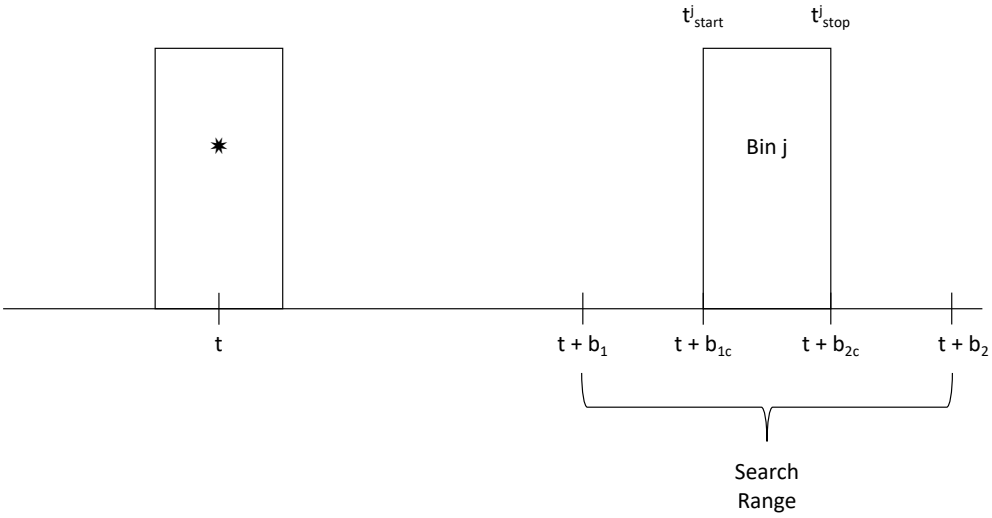

Figure A.1: Schematic for a 2-decay sequence (discrete case).

For a parent event in bin i, we search subsequent images denoted by bin j:

$$\begin{aligned} b_{1c} &= t^j_{start} - t \\ b_{2c} &= t^j_{stop} - t \end{aligned} \tag{A.8}$$

The modified form of Eq. A.2 is:

$$\epsilon_t = \frac{1}{t_f}\frac{1}{\tau}\sum_i^N \int_{t^i_{start}}^{t^i_{stop}} dt \sum_{j=i+1}^N \int_{t+b_{1c}}^{t+b_{2c}} dt' \left(e^{-(\frac{t'-t}{\tau})}\right) \tag{A.9}$$

which gives:

$$\boxed{\epsilon_t = \frac{\tau}{t_f} \sum_i A(i) \sum_j B(j)\, \Theta_1(i,j)\, \Theta_2(i,j)} \tag{A.10}$$

where

$$\begin{aligned} A(i) &= e^{(\frac{t^i_{stop}}{\tau})} - e^{(\frac{t^i_{start}}{\tau})} \\ B(j) &= e^{-(\frac{t^j_{start}}{\tau})} - e^{-(\frac{t^j_{stop}}{\tau})} \\ \Theta_1(i,j) &= \Theta_1\Big(t^j_{start} - (t^i_{stop} + b_1))\Big) \\ \Theta_2(i,j) &= \Theta_1\Big((t^i_{stop} + b_2) - t^j_{stop})\Big) \end{aligned} \tag{A.11}$$

A.2 Three Subsequent Decays

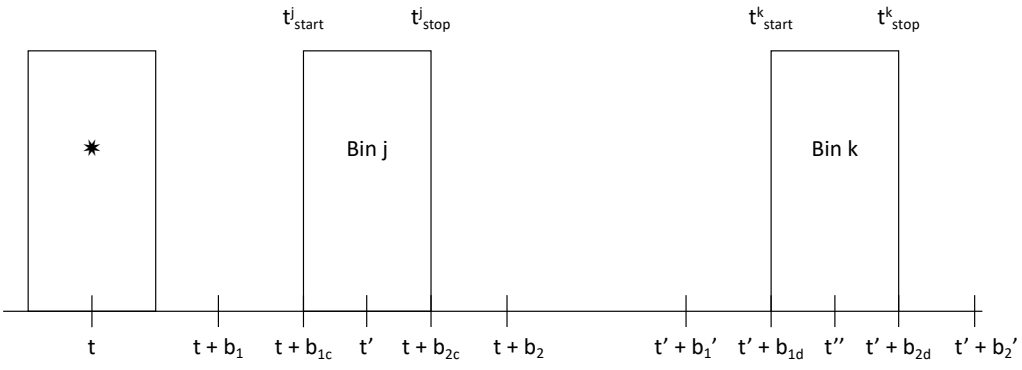

Figure A.2: Schematic for a 3-decay sequence (discrete case).

This form can further be extended to the case of searching for triple decay sequences (e.g. $\beta - \beta - \alpha$). We continue directly with the discrete case, since it will allow us to incorporate the aforementioned detector dead time into the final efficiency value. We denote the exponential time constants of the first and second decays as τ_1 and τ_2, respectively. The search range parameters for the first sequence remains b_1, b_2; the search parameter for the latter, for once a first daughter is detected, are represented by b_1', b_2'. The decay constants are τ_1 and τ_2. For some parent decay in bin i, we consider the first and second daughter decays within that chain as in bins j and k, respectively (see Fig. A.2):

$$\begin{aligned} b_{1c} &= t^j_{start} - t \\ b_{2c} &= t^j_{stop} - t \\ b_{1d} &= t^k_{start} - t' \\ b_{2d} &= t^k_{stop} - t' \end{aligned} \tag{A.12}$$

For convenience, we define the following expressions:

$$\tau' = \frac{\tau_1 \tau_2}{\tau_1 - \tau_2}$$

$$\begin{aligned} D(i) &= e^{(\frac{t^i_{stop}}{\tau_1})} - e^{(\frac{t^i_{start}}{\tau_1})} \\ E(j) &= e^{(\frac{t^j_{stop}}{\tau'})} - e^{(\frac{t^j_{start}}{\tau'})} \\ G(k) &= e^{-(\frac{t^k_{stop}}{\tau_2})} - e^{-(\frac{t^k_{start}}{\tau_2})} \end{aligned} \tag{A.13}$$

Extending the form of Eq. A.2 in similar fashion as before:

$$\epsilon_t = \frac{1}{t_f}\frac{1}{\tau_1\tau_2}\sum_i \int_{t^i_{start}}^{t^i_{stop}} dt \sum_{j=i+1} \int_{t+b_{1c}}^{t+b_{2c}} dt' \Big(e^{-(\frac{t'-t}{\tau_1})}\Big) \sum_{k=j+1} \int_{t'+b_{1d}}^{t'+b_{2d}} dt'' \Big(e^{-(\frac{t''-t'}{\tau_2})}\Big) \quad \text{(A.14)}$$

Integrating and evaluating the expression in the "k" sum gives:

$$\boxed{\epsilon_t = \frac{\tau'}{t_f}\sum_i D(i) \sum_j E(j)\,\Theta_1(i,j)\Theta_2(i,j) \sum_k G(k)\Theta'_1(j,k)\Theta'_2(j,k)} \quad \text{(A.15)}$$

where

$$\begin{aligned} \Theta'_1(j,k) &= \Theta_1\Big(t^k_{start} - (t^j_{stop} + b'_1))\Big) \\ \Theta'_2(j,k) &= \Theta_2\Big((t^j_{stop} + b'_2) - t^k_{stop})\Big) \end{aligned} \quad \text{(A.16)}$$

REFERENCES

[1] N. Aghanim et al., "Planck 2018 results. VI. Cosmological parameters," arXiv preprint arXiv:1807.06209 (2018).

[2] F. Zwicky, "Spectral displacement of extra galactic nebulae," Helv. Phys. Acta 6 (1933) 110.

[3] V.C. Rubin and W.K. Ford, Jr., "Rotation of the Andromeda Nebula from a Spectroscopic Survey of Emission Regions," Astrophys. J. 159 (1970) 379.

[4] K.G. Begeman, A.H. Broeils, and R.H. Sanders, "Extended rotation curves of spiral galaxies: Dark haloes and modified dynamics," Monthly Notices of the Royal Astronomical Society, 249(3):523–537 (1991).

[5] C. L. Bennett, M. S. Turner, and M. White, "The Cosmic Rosetta Stone," Physics Today 50(11), 32; DOI: 10.1063/1.881995 (1997).

[6] D. Clowe, et al., "A direct empirical proof of the existence of dark matter," The Astrophysical Journal, 648(2):L109–L113; DOI: 10.1086/508162 (2006).

[7] G. Bertone and D. Hooper, "History of dark matter," Rev. Mod. Phys. 90, 045002, arXiv:1605.04909v2 (2016).

[8] A. D. Lewis D. A. Buote, and J. D. Stocke, "Chandra Observations of A2029: The Dark Matter Profile Down to below $0.01r_{vir}$ in an Unusually Relaxed Cluster," The Astrophysical Journal, 586:135-142 (2003).

[9] B. D. Fields, P. Molaro, and S. Sarkar, "Big-Bang Nucleosynthesis," Review of Particle Physics 2014 by the Particle Data Group, DOI: 10.1088/1674-1137/38/9/090001, arXiv:1412.1408 (2014).

[10] M. Goodman and E. Witten, Phys. Rev. D 31, 3059 (1985).

[11] G. Jungman, M. Kamionkowski and K. Griest, "Supersymmetric dark matter," Phys. Rept. 267 195 (1996).

[12] J.D. Lewin and P.F. Smith, "Review of mathematics, numerical factors, and corrections for dark matter experiments based on elastic nuclear recoil," Technical report, SCAN-9603159 (1996).

[13] M. Battaglieri et al., "US Cosmic Visions: New Ideas in Dark Matter 2017: Community Report," arXiv:1707.04591 (2017).

[14] L. Necib, M. Lisanti, and V. Belokurov, "Inferred evidence for dark matter kinematic substructure with sdss–gaia," The Astrophysical Journal, 874(1):3 (2019).

[15] R. Essig et al., "Direct detection of sub-GeV dark matter with semiconductor targets," Journal of High Energy Physics volume 2016, Article number: 46 (2016).

[16] I. M. Bloch, et al., "Searching for dark absorption with direct detection experiments," Journal of High Energy Physics, 2017(6), Jun 2017. ISSN 1029-8479. DOI: 10.1007/jhep06(2017)087.

[17] T. Lin, "TASI lectures on dark matter models and direct detection," arXiv:1904.07915 (2019).

[18] H. Murayama, "Physics Beyond the Standard Model and Dark Matter," Les Houches Summer School - Session 86: Particle Physics and Cosmology: The Fabric of Spacetime, arXiv:0704.2276 (2007).

[19] J. L. Fend, "Dark Matter Candidates from Particle Physics and Methods of Detection," Annu. Rev. Astron. Astrophys. 48:495–545 (2010).

[20] T. Braine et al., "Extended search for the invisible axion with the axion dark matter experiment," Phys. Rev. Lett., 124:101303 (2020).

[21] F. Palmonari et al., "Search for Dark Matter in Cosmic Rays with the AMS-02 space spectrometer," J. Phys.: Conf. Ser. 335 012066 (2011).

[22] S.W. Allen, A.E. Evrard, and A.B. Mantz, "Cosmological Parameters from Observations of Galaxy Clusters," Annual Review of Astronomy and Astrophysics, vol. 49, issue 1, pp. 409-470 (2011).

[23] T.A Porter, R.P. Johnson, P.W. Graham, "Dark Matter Searches with Astroparticle Data," Annual Review of Astronomy and Astrophysics Vol. 49:155-194 (2011).

[24] ATLAS Collaboration, "Search for dark matter in events with missing transverse momentum and a Higgs boson decaying into two photons in pp collisions at $s = \sqrt{13}$ TeV with the ATLAS detector," arXiv:2104.13240 (2021).

[25] R. Bernabei et al., "First results from dama/libra and the combined results with DAMA/NAI," The European Physical Journal C, 56(3):333–355 (2008).

[26] C. Amole et al., "Dark matter search results from the pico-60 c3f8 bubble chamber," Physical Review Letters, 118(25) (2017).

[27] D.S. Akerib et al. (LUX Collaboration), "Results from a Search for Dark Matter in the Complete LUX Exposure," Phys. Rev. Lett. 118 (2017) 021303.

[28] E. Aprile et al. (XENON Collaboration), "Dark Matter Search Results from a One Ton-Year Exposure of XENON1T," Phys. Rev. Lett. 121 no.11, 111302 (2018).

[29] T. Saab, Dark matter limit plotter v5.16 (2021).

[30] G. Fisher, M. R. Seacrist and R. W. Standley, "Silicon Crystal Growth and Wafer Technologies," in Proceedings of the IEEE, vol. 100, no. Special Centennial Issue, pp. 1454-1474, doi: 10.1109/JPROC.2012.2189786 (2012).

[31] A. Aguilar-Arevalo et al. (DAMIC Collaboration), "Results on Low-Mass Weakly Interacting Massive Particles from an 11 kg-d Target Exposure of DAMIC at SNOLAB," Phys. Rev. Lett. 125, 241803 (2020).

[32] A. Aguilar-Arevalo et al. (DAMIC Collaboration), "Search for low-mass WIMPs in a 0.6 kg day exposure of the DAMIC experiment at SNOLAB," Phys. Rev. D 94 (2016) 082006.

[33] The Nobel Prize in Physics 2009. NobelPrize.org, https://www.nobelprize.org/prizes/physics/2009/summary/ , Nobel Prize Outreach AB (2021).

[34] J. Janesick, "Scientific Charge-Coupled Devices," Press Monographs (The International Society for Optical Engineering, Bellingham, WA, 2001).

[35] A. Drlica-Wagner et al., "Characterization of skipper CCDs for cosmological applications," Proceedings Volume 11454, X-Ray, Optical, and Infrared Detectors for Astronomy IX; 114541A, https://doi.org/10.1117/12.2562403 (2020).

[36] JD Ponz, RW Thompson, and JR Munoz, "The fits image extension," Astronomy and Astrophysics Supplement Series, 105:53–55, 1994.

[37] D. Rodrigues et al., "Absolute measurement of the Fano factor using a Skipper-CCD," Nuclear Instruments and Methods in Physics Research Section A: Accelerators, Spectrometers, Detectors and Associated Equipment, Vol. 1010 165511; arXiv:2004.11499 (2021).

[38] K. Ramanathan and N. Kurinsky, "Ionization Yield in Silicon for eV-Scale Electron-Recoil Processes," Phys. Rev. D 102 6, 063026, DOI: 10.1103/PhysRevD.102.063026; arXiv:200410709 (2020).

[39] G. F. Knoll, "Radiation Detection and Measurement, 3rd Edition," John, Wiley, & Sons, Inc. (Originally published: 1979).

[40] S. Holland et al., "Fully Depleted Charge-Coupled Devices," Proceedings, International Symposium On Detector Development For Particle, Astroparticle And Synchrotron Radiation Experiments (SNIC), SNIC-2006-0009 (2006).

[41] K. Honscheid et al., "The Dark Energy Camera (DECam)," Proceedings, 34th International Conference on High Energy Physics (2008).

[42] S.E. Holland et al., "Fully-Depleted, Back-Illuminated Charge-Coupled Devices Fabricated on High-Resistivity Silicon," IEEE Transactions on Electron Devices, Vol. 50, No. 1, 225-338, DOI: 10.1109/TED.2002.806476 (2003).

[43] S.E. Holland et al., "Fabrication of large format, fully depleted CCDs for the Dark Energy Survey Camera," Image Sensors Workshop (2013).

[44] S.E. Holland et al., "High-voltage-compatable fully depleted CCDs," Proceedings Vol. 6276, High Energy, Optical, and Infrared Detectors for Astronomy II; 62760B, https://doi.org/10.1117/12.672393 (2006).

[45] G.K. Teal and J.B. Little, Phys. Rev. 77 (1950) 809; 78 (1950) 647

[46] G.E. Jellison et al., "Optical functions of silicon determined by two-channel polarization modulation ellipsometry," Optical Materials Vol. 1, Issue 1, p. 41-47, https://doi.org/10.1016/0925-3467(92)90015-F (1992).

[47] S.E. Holland et al., "Development of Low Noise, Back-Side Illuminated Silicon Photodiode Arrays," IEEE Transactions on Nuclear Science, Vol. 44 No. 3, doi: 10.1109/23.603687 (1997).

[48] Horiba, "Lorentz Dispersion Model," Technical Note: Spectroscopic Ellipsometry (2006).

[49] S. Haque et al., "Design of Low-Noise Output Amplifiers for P-channel Charge-Coupled Devices Fabricated on High-Resistivity Silicon," Proceedings Vol. 8298, Sensors, Cameras, and Systems for Industrial and Scientific Applications XIII; 82980X https://doi.org/10.1117/12.905460 (2012).

[50] N.J.T. Smith, "The SNOLAB deep underground facility," The European Physical Journal Plus, 127(9):108 (2012).

[51] C. Jillings, "The SNOLAB Science Program," XIV International Conference on Topics in Astroparticle and Underground Physics, Journal of Physics: Conference Series 718 062028, doi:10.1088/1742-6596/718/6/062028 (2016).

[52] J. L. Orrell et al., "Assay methods for ^{238}U, ^{232}Th, and ^{210}Pb in lead and calibration of ^{210}Bi bremsstrahlung emission from lead," Journal of Radioanalytical and Nuclear Chemistry volume 309, pages1271–1281 (2016).

[53] K. Ramanathan, "Particles Taking Selfies: Investigations into Light Dark Matter Using Silicon Charge Coupled Devices," The University of Chicago, ProQuest Dissertations Publishing, 28150452 (2020).

[54] M. Stein, "Radon daughter plate-out measurements at SNOLAB for polyethylene and copper," Nuclear Instruments and Methods in Physics Research Section A: Accelerators, Spectrometers, Detectors and Associated Equipment, Vol. 880, p. 92-97, DOI: https://doi.org/10.1016/j.nima.2017.10.054 (2018).

[55] J. Castilla et al., "Readout electronics for the Dark Energy Camera," Proceedings of SPIE - The International Society for Optical Engineering, DOI: 10.1117/12.856852 (2010).

[56] A. Piers, "DAMIC at SNOLAB," Meeting of the Division of Particles and Fields of the American Physical Society (2019).

[57] M. M. Be, V. Chiste, C. Dulieu, et al., "Table of Radionuclides", vol. 8 of Monographie BIPM-5. Bureau International des Poids et Mesures, Pavillon de Breteuil, F-92310 Sevres, France, ISBN 978-92-822-2264-5 (2016).

[58] E. Aprile et al. (XENON Collaboration), "XENON1T Dark Matter Data Analysis: Signal Reconstruction, Calibration and Event Selection," Phys.Rev.D 100 (2019) 5, 052014, DOI: 10.1103/PhysRevD.100.052014 (2019).

[59] J. Zhou, "Direct dark matter detection with the DAMIC experiment at SNOLAB," The University of Chicago, ProQuest Dissertations Publishing, 3740101 (2015).

[60] K. Ramanathan et al., "Measurement of Low Energy Ionization Signals from Compton Scattering in a Charge-Coupled Device Dark Matter Detector," Phys.Rev.D 96 4, 042002, DOI: 10.1103/PhysRevD.96.042002 (2017).

[61] M. M. Bé et al., Table of Radionuclides, Vol. 1–A = 1 to 150 (Monographie BIPM-5, Sévres, 2004); Table of Radionuclides, Vol. 5–A = 22 to 244 (Monographie BIPM-5, S'evres, 2010).

[62] A. E. Chavarria et al., "Measurement of the ionization produced by sub-keV silicon nuclear recoils in a CCD dark matter detector," Phys. Rev. D 94, 082007 (2016).

[63] J. Lindhard, V. Nielsen, M. Scharff, and P. V. Thomsen, Mat. Fys. Medd. Dan. Vid. Selsk. 33, 10:1 (1963); J. Ziegler, J. Biersack, and U. Littmark, "The Stopping and Range of Ions in Solids, Stopping and Range of Ions in Matter," Vol. 1, Pergamon Press, New York (1985).

[64] J. Cuevas-Zepeveda, D. Norcini, and P. Privitera, "Measurement of Compton scattering on silicon atomic shell electrons with Skipper CCDs," APR21 Meeting of The American Physical Society (2021).

[65] A. Aguilar-Arevalo et al. (DAMIC Collaboration), "Constraints on Light Dark Matter Particles Interacting with Electrons from DAMIC at SNOLAB," Phys. Rev. Lett. 123, 181802 (2019).

[66] R. Essig et al. "Direct detection of sub-GeV dark matter with semiconductor targets," Journal of High Energy Physics Article no. 46 (2016).

[67] A. Aguilar-Arevalo et al. (DAMIC Collaboration), "First Direct-Detection Constraints on eV-Scale Hidden-Photon Dark Matter with DAMIC at SNOLAB," Phys.Rev.Lett. 118 14, 141803, DOI: 10.1103/PhysRevLett.118.141803 (2017).

[68] O. Abramoff et al. (SENSEI Collaboration), "SENSEI: Direct-Detection Constraints on Sub-GeV Dark Matter from a Shallow Underground Run Using a Prototype Skipper CCD," Phys. Rev. Lett. 122, 161801 (2019).

[69] T. Emken et al., "Direct Detection of Strongly Interacting Sub-GeV Dark Matter via Electron Recoils," Journal of Cosmology and Astroparticle Physics, Vol. 2019, DOI: 10.1088/1475-7516/2019/09/070 (2019).

[70] R. Agnese et al. "First Dark Matter Constraints from a SuperCDMS Single-Charge Sensitive Detector," Phys. Rev. Lett. 122, 069901 (2019).

[71] R. Essig, T. Volansky, and T. Yu, "New constraints and prospects for sub-GeV dark matter scattering off electrons in xenon," Phys. Rev. D 96, 043017 (2017).

[72] I. M. Bloch et al., "Searching for dark absorption with direct detection experiments," Journal of High Energy Physics volume 2017, Article number: 87 (2017).

[73] J. Suzuki, T. Horie, Y. Inoue, and M. Minowa, "Experimental search for hidden photon CDM in the eV mass range with a dish antenna," Journal of Cosmology and Astroparticle Physics, Volume 2015 (2015).

[74] H. An, M. Pospelov, J. Pradler, "New stellar constraints on dark photons," Physics Letters B Vol. 725, Issues 4–5, p. 190-195, https://doi.org/10.1016/j.physletb.2013.07.008 (2013).

[75] R. Agnese et al. (CDMS Collaboration), "Silicon Detector Dark Matter Results from the Final Exposure of CDMS II," Phys. Rev. Lett. 111, 251301 (2013).

[76] S. Agostinelli et al., "Geant4 — a simulation toolkit," Nuclear Instruments and Methods in Physics Research Volume 506, Issue 3 p. 250-303 (2003); J. Allison et al., "Recent developments in Geant4 Author links open overlay panel," Nuclear Instruments and Methods in Physics Research Section A: Accelerators, Spectrometers, Detectors and Associated Equipment, Vol. 835, p. 186-225 (2016).

[77] E. Aprile et al. (XENON Collaboration), Phys. Rev. Lett. 121, 111302 (2018), arXiv:1805.12562; R. Agnese et al. (SuperCDMS Collaboration), Phys. Rev. Lett. 120, 061802 (2018), arXiv:1708.08869; P. Agnes et al. (DarkSide Collaboration), Phys. Rev. Lett. 121, 081307 (2018), arXiv:1802.06994; R. Agnese et al. (SuperCDMS Collaboration), Phys. Rev. D 99, 062001 (2019), arXiv:1808.09098; C. Amole et al. (PICO Collaboration), Phys. Rev. D 100, 022001 (2019), arXiv:1902.04031; A. H. Abdelhameed et al. (CRESST Collaboration), Phys. Rev. D 100, 102002 (2019), arXiv:1904.00498; E. Aprile et al. (XENON Collaboration), Phys. Rev. Lett. 123, 251801 (2019), arXiv:1907.11485.

[78] T. Ichimiya A. Furuichi, "On the solubility and diffusion coefficient of tritium in single crystals of silicon," The International Journal of Applied Radiation and Isotopes, Vol. 19, Issue 7, p. 573-578, https://doi.org/10.1016/0020-708X(68)90067-7 (1968).

[79] A. Aguilar-Arevalo et al. (DAMIC Collaboration), "Measurement of the bulk radioactive contamination of detector-grade silicon with DAMIC at SNOLAB," Journal of Instrumentation, Vol. 16, https://doi.org/10.1088/1748-0221/16/06/P06019, arXiv:2011.12922 (2021).

[80] D.S. Leonard et al., "Systematic study of trace radioactive impurities in candidate construction materials for EXO-200," Nuclear Instruments and Methods in Physics Research Section A: Accelerators, Spectrometers, Detectors and Associated Equipment Vol. 591, Issue 3, p. 490-509, https://doi.org/10.1016/j.nima.2008.03.001 (2008).

[81] XMASS Collaboration "Identification of ^{210}Pb and ^{210}Po in the bulk of copper samples with a low-background alpha particle counter," Journal of Radioanalytical and Nuclear Chemistry 309(3): 1271-1281 (2016).

[82] A. P. Pocar, "Low background techniques and experimental challenges for Borexino and its nylon vessels," Princeton University Thesis (2003).

[83] J. P. Biersack, J. F. Ziegler, and M. D. Ziegler, "SRIM - The Stopping and Range of Ions in Matter," Nuclear Instruments and Methods in Physics Research Section B: Beam Interactions with Materials and Atoms Vol. 268, Issues 11–12, p. 1818-1823 (2010).

[84] I. Lawson, "Low Background Measurement Capabilities at SNOLAB" (2020).

[85] R. Saldanha et al., "Cosmogenic activation of silicon," Phys. Rev. D 102, 102006, DOI: https://doi.org/10.1103/PhysRevD.102.102006 (2020).

[86] C. Dunford, T. Burrows, Online nuclear data service (1998).

[87] C. E. Aalseth, R. Bonicalzi, M. G. Cantaloub, A. R. Day, L. E. Erikson, J. Fast, J. B. Forrester, E. S. Fuller, B. D. Glasgow, L. R. Greenwood, et al., "A shallow underground laboratory for low-background radiation measurements and materials development," Review of Scientific Instruments 83 113503 (2012).

[88] P. Lisowski, K. Schoenberg, The Los Alamos Neutron Science Center, Nuclear Instruments and Methods A 562 (2006) 910–914.; B. Takala, The ICE House, Los Alamos Science (2006).

[89] M.S. Gordon et al., "Measurement of the flux and energy spectrum of cosmic-ray induced neutrons on the ground," IEEE Transactions on Nuclear Science 51(6):3427 - 3434, DOI: 10.1109/TNS.2004.839134 (2005).

[90] A. Aguilar-Arevalo et al. (DAMIC Collaboration), "Measurement of radioactive contamination in the high-resistivity silicon CCDs of the DAMIC experiment," J. Instrum. 10 (2015) P08014.

[91] J. L. Orrell et al. "Assay methods for ^{238}U, ^{232}Th, and ^{210}Pb in lead and calibration of ^{210}Bi bremsstrahlung emission from lead," Journal of Radioanalytical and Nuclear Chemistry 309(3): 1271-1281 (2016).

[92] A. Aguilar-Arevalo et al., "Results on low-mass weakly interacting massive particles from a 11 kg-day target exposure of DAMIC at SNOLAB," Phys. Rev. Lett. 125, 241803 (2020).

[93] S. Holland et al., "Fully depleted, back-illuminated charge-coupled devices fabricated on high-resistivity silicon," IEEE Trans. Electron Devices 50 (2003), no. 1 225–238.

[94] J. Estrada, J. Molina, J. J. Blostein, and G. Fernandez, "Plasma effect in silicon charge coupled devices (CCDs)," Nucl. Instrum. Meth. Phys. Res. A 665 (2011) 90–93, [arXiv:1105.3229].

[95] E. Browne and J. K. Tuli, Nucl Data Sheets 108, 681 (2007). Data extracted from the ENSDF database (5 November 2020).

[96] C. Ouellet and B. Singh, Nucl Data Sheets 112, 2199 (2011). Data extracted from the ENSDF database (5 November 2020).

[97] K. Abusaleem, Nucl Data Sheets 116, 163 (2014); Data extracted from the ENSDF database (5 November 2020).

[98] J. L. Orrell et al. "Naturally occurring ^{32}Si and low-background silicon dark matter detectors," Astroparticle Physics 99 (2018): 9-20.

[99] M. Crisler et al., "SENSEI: First Direct-Detection Constraints on Sub-GeV Dark Matter from a Surface Run," Phys. Rev. Lett. 121, 061803 (2018).

[100] M. Settimo, "Search for low-mass dark matter with the DAMIC experiment," arXiv:2003.09497 (2020).

[101] R. Agnese et al. "Projected Sensitivity of the SuperCDMS SNOLAB experiment," Phys. Rev. D 95 (2017) 082002.

[102] N. Castelló-Mor, "DAMIC-M experiment: Thick, silicon CCDs to search for light dark matter," Nucl. Instrum. Methods A 958 (2020) 162933.

[103] S. Mader and K. N. Tu, "Microstructure of xenon-implanted silicon," Journal of Vacuum Science and Technology 12, 501 (1975).

[104] A. F. W. Willoughby, "Atomic diffusion in semiconductors," Rep. Prog. Phys. 41 (1978) 1665.

[105] L. Pattavina, "Radon-induced surface contaminations in neutrinoless double beta decay and dark matter experiments," Thesis, l'Università degli studi di Milano - Bicocca (2011).

[106] P. Mitra, "Single electron charge resolution with the first prototypes of DAMIC-M Skipper CCDs," KICP Seminar (2020).

[107] L. Khalil, "Optimisation de la lecture et du controle de CCD à très Bas bruit pour l'expérience DAMIC," Sorbonne Université (2019).

[108] J. M. Da Rocha, "Recherche de matière sombre légère avec des CCDs de l'expérience DAMIC à SNOLAB," Sorbonne Université (2019).

[109] T. Bond et al., "Integration and verification testing of the LSST camera," Conference: Modeling, Systems Engineering, and Project Management for Astronomy VIII, DOI: 10.1117/12.2314017 (2018).

[110] A.T.A.M. de Waele, "Basic Operation of Cryocoolers and Related Thermal Machines," J Low Temp Phys 164:179–236, DOI 10.1007/s10909-011-0373-x (2011).

[111] R. W. Leach and F. J. Low, CCD and IR array controllers," Optical and IR Telescope Instrumentation and Detectors, Vol. 4008, p. 337–343. International Society for Optics and Photonics (2000).

[112] C. Bebek and N. Roe, "4k × 2k and 4k × 4k CCD Users Manual," LBNL.

[113] V.P. Chechev and N.K. Kuzmenko, "Table de Radionucléides," Laboratoire Nationale Henri Becquerel (2000).

[114] National Institute of Standards and Technology XCOM: Element/Compound/Mixture Database, https://physics.nist.gov/PhysRefData/Xcom/html/xcom1.html.

[115] J. R. Janesick et al., "New advancements in charge-coupled device technology: sub-electron noise and 4096 x 4096 pixel CCDs," Proceedings Volume 1242, Charge-Coupled Devices and Solid State Optical Sensors; https://doi.org/10.1117/12.19452 (1990).

[116] J. Tiffenberg, "Counting electrons with the Skipper-CCD," DPF Meetig, Fermilab (2019).

[117] D. Wen, IEEE J. Solid-State Circuits 9, 410 (1974).

[118] P. Mitra, CCDDRone: Control a regular/DES or a Skipper CCD with a Leach system using C++, https://github.com/xtachx/CCDDrone (2021).

[119] J. Tiffenberg et al., "Single-Electron and Single-Photon Sensitivity with a Silicon Skipper CCD," Phys. Rev. Lett. 119, 131802, DOI: https://doi.org/10.1103/PhysRevLett.119.131802 (2017).

[120] G. F. Moroni, J. Estrada, et al., "Achieving sub-electron readout noise in Skipper CCDs," arXiv:1106.1839 (2011).

[121] P. Du, D. Egana-Ugrinovic, R. Essig, and M. Sholapurkar, "Sources of Low-Energy Events in Low-Threshold Dark Matter Detectors," arXiv:2011.13939 (2020).

[122] R. Thomas, "Cameras in the Dark: Direct Detection of Dark Matter with Charge-Coupled Devices," The University of Chicago, Thesis pre-print (2021).

[123] P. Antilogus et al., "ASPIC: LSST camera readout chip. Comparison between DSI and C&S," Publications du LPNHE, https://hal-emse.ccsd.cnrs.fr/LPNHE/in2p3-00420345 (2009).

[124] B. Schmidt et al. (EDELWEISS Collaboration), "Muon-induced background in the EDELWEISS dark matter search," Astroparticle Physics Vol. 44, p. 28-39, DOI: 10.1016/j.astropartphys.2013.01.014 (2013).

[125] V. Palusova et al., "Natural radionuclides as background sources in the Modane underground laboratory," J.Environ.Radioact. 216 106185, DOI: 10.1016/j.jenvrad.2020.106185 (2020).

[126] P. Loaiza, "Laboratoire Souterrain de Modane," Cygnus Workshop (2011).

[127] P.R. Scovell et al., "Low-background gamma spectroscopy at the Boulby Underground Laboratory," Astroparticle Physics, Vol. 97, p. 160-173, DOI: https://doi.org/10.1016/j.astropartphys.2017.11.006 (2018).

[128] P.W. Deelman et al., "Delta-doped CCDs with integrated UV coatings," Proceedings Volume 3965, Sensors and Camera Systems for Scientific, Industrial, and Digital Photography Applications, DOI: https://doi.org/10.1117/12.385471 (2000).

[129] S.E. Holland et al., "Fabrication of back-illuminated, fully depleted charge-coupled devices," Nuclear Instruments and Methods in Physics Research Section A: Accelerators, Spectrometers, Detectors and Associated Equipment, Vol. 579, Issue 2, p. 653-657, DOI: https://doi.org/10.1016/j.nima.2007.05.265 (2007).